# DISSERTATION | DOCTORAL THESIS

Titel | Title

Dissecting the role of UFMylation in endoplasmic reticulum-associated protein quality control

verfasst von | submitted by

Milica Mihailović MSc

angestrebter akademischer Grad | in partial fulfilment of the requirements for the degree of

Doctor of Philosophy (PhD)

Wien | Vienna, 2026

| | |
|---|---|
| Studienkennzahl lt. Studienblatt \| Degree programme code as it appears on the student record sheet: | UA 794 620 490 |
| Dissertationsgebiet lt. Studienblatt \| Field of study as it appears on the student record sheet: | Molekulare Biologie |
| Betreut von \| Supervisor: | Gülsün Elif Karagöz PhD |

## Acknowledgements

The last four yeast have been incredibly challenging, but also very rewarding. I feel extremely lucky to have been supported by many wonderful people during this time. I would first like to thank my PhD thesis advisor Elif for trusting me with this exciting project, leaving me the freedom to choose my own research topic, and for always prioritizing science.

My work was supported by FACS and MassSpec facilities at Max Perutz Labs, and I would like to thank Kitti and Markus for their patience and scientific input. The VBC campus is a great place to do science, and I would like to thank Yasin and the UFMylation team (Ni, Ranj, Bu) for the great collaboration over the years, sharing resources and having many scientific discussions. In addition, I am grateful to my TAC members, Andi Pauli and Marco Hein, for their valuable scientific input and continuous encouragement year after year.

My labmates have been a constant source of support, motivation and fun during long lab hours and many successful or failed experiments. I hope I will be able to find half as good a team in the future as we had during this time. Big thanks to Sanya, for teaching me many methods, selflessly sharing all the material, tips and tricks, and for many cool climbing sessions! I am so grateful to Asja, with whom I was always sharing all the good and bad news, coffee breaks in the sun, and many (mainly cheese-packed) dinners. Thanks to Paulina for the enthusiasm for science, fun conversations, and Propeller dinners! Thanks to Greg for all the movie nights, Harald for our pub quizzes, Sabina for Balkan level of understanding, Venja for all the fun discussion topics and all the others for making the lab so welcoming and lively.

I'd like to thank Otsuka lab members, especially Julia, Nina, and Tamara, for our engaging lunch breaks, feminist discussions and all the support, many times in form of cake and coffee. Thanks to my friends from campus, especially Julia for being a German course buddy and empathetic listener, Ana and Estela for many climbing sessions and outdoor hangouts. To Arda, Viktor, Nata and Johannes for many cool boardgame evenings and good beers.

Big thanks to my friends from Switzerland: Cécé, Kate, Sam, Larise, Alexey, Marco, Ana, Marion, Daniele, Cédric, Amélie, Fra, Mapy, Alessio, Laurence, Fabio, Nasim, Yahya, Paulina, Stefan, and many more, for all the fun times we had together, honest conversations about the PhD, and making me feel at home in Lausanne. I look forward to visiting you all around the world!

To my friends from home, especially Jovan, Marko, Peđa, Sonja, Mihailo, Jelena, Jana and Mimi, thank you for being here and staying true friends through many life phases.

Karo and Germain, thank you for understanding me in and between many languages, offering support in many possible and impossible ways and bringing my culinary experiences to another level. Bon bah, je suis la dernière quoi, c'était le temps, fin bref...

Merci à ma beautiful family, pour ma vrai deuxième maison!

Hvala mojoj Vikici, za razumevanje i podršku od studentskog doma i svih ispita, preko života u četiri različite države (za sad), i za sve buduće avanture! Za još mnogo životnih faza, slavlja, putovanja, dobrih koncerata i divnih druženja!

Hvala Nadi, Stevu, i Sandri za sve što su mi pružili i pokazali u Beču, za porodučnu atmosferu i sve divne nedeljne ručkove.

Hvala mojim roditeljima na negovanju kulture radoznalosti od malih nogu, na domu punom knjiga, topline i ljubavi. Hvala vam na stabilnom osloncu, odskočnoj dasci i verovanju da ne postoji ništa što neću moći da postignem. Hvala mom bratu na podršci od kad znam za sebe, otkrivanju sveta zajedno i nepresušnim diskusijama i interesovanjima. Hvala ti što uvek veruješ u mene iz sve snage.

And finally, thank you to my partner, biggest supporter and cheerleader, Thibaud. Thank you for unwavering support over many years and degrees, through a few countries and many travelled kilometers. Thank you for believing in me so hard that even the imposter syndrome couldn’t win.

## Contribution statement

This work was conducted at the Max Perutz Labs, Vienna BioCenter (VBC) campus, in the laboratory of Prof. Elif Karagöz.

During my PhD, I have dissected the previously elusive course of events upon ribosomal stalling at the ER. I have shown for the first time that the UFM1 E3 ligase recognizes post-split 60S-peptidyl-tRNA complexes and UFMylates them, which is necessary for downstream clearance of incomplete nascent peptides. I have shown that the ribosome recognition and rescue after ribosome stalling at the ER are prerequisite steps for UFMylation. Upon UFMylation of 60S-peptidyl-tRNA complexes, their connection to the translocon is loosened, facilitating access for RQC components and promoting degradation in a process that requires both the RQC and UFMylation pathways. UFMylation is therefore an essential factor in maintaining proteostasis at the ER.

I have conceptualized the research, performed a large part of the experiments, analyzed the data, and written and edited the manuscript for the first presented paper entitled “The coordinated action of UFMylation and the RQC pathways clears arrested polypeptides at the ER”. The groundwork for this project has been done by Aleksandra Anisimova, PhD, who has also performed selected experiments in the paper (establishment of siRNA assays and iCas9 cell lines, polysome profiling, selected western blots), analyzed the data, and edited the manuscript.

For the second presented paper, Dual regulation of the unfolded protein response by IGF2BP3 during ER stress, I established and optimized the aggresome assays, performed puromycin incorporation assays, analyzed the data, and edited the manuscript before submission.

## Abstract

Regulation of protein translation is crucial for maintaining cellular homeostasis. Various factors, such as aberrant mRNA processing, lack of translational components or rare codons, can cause ribosomal stalling during translation. In the cytosol, the factors that recognize and clear stalled ribosomes, collectively known as ribosome-associated quality control (RQC), are well-studied. However, the events following ribosome stalling during co-translational protein translocation into the endoplasmic reticulum (ER) remained poorly understood. Upon ribosome stalling at the ER, 60S ribosomal protein RPL26 was shown to be covalently modified by UFM1 (ubiquitin-fold modifier 1), a ubiquitin-like protein. Still, the precise role of UFMylation in ER protein quality control and its cross-talk with the RQC machinery have remained elusive.

In this work, I address this research gap by combining unbiased proteomics with biochemical and cellular assays. Proteomics of UFMylated ribosomes revealed that the RQC factors NEMF and LTN1 interacted with UFMylated ribosomes in a stalling-dependent manner.

Using cell biology, I found that, similar to cytosolic ribosomes, ER-stalled ribosomes are recognized by the E3 ligase ZNF598 and subsequently split by the ASC-1 complex. Importantly, these steps are necessary prerequisites for RPL26 UFMylation, in which the UFM1 E3 ligase recognizes post-split 60S-peptidyl-tRNA complexes as canonical substrates. UFMylation of RPL26 loosens the close interaction between the 60S-peptidyl-tRNA complex and the translocon, thereby allowing RQC components to access stalled nascent chains. In line with these results, impaired UFMylation weakens LTN1 binding to 60S-peptidyl-tRNA complexes, and depletion of either NEMF or LTN1 leads to the accumulation of UFMylated ribosomes, supporting the idea that these two machineries act on the same pathway and form a direct link to post-split ribosomal intermediates. Taken together, my work revealed that close collaboration between the RQC and UFMylation is necessary for the clearance of stalled ribosomes at the ER, thereby safeguarding cellular protein homeostasis.

## Zusammenfassung

Die Regulation der Proteinbiosynthese ist für die Aufrechterhaltung der zellulären Homöostase von entscheidender Bedeutung. Verschiedene Faktoren, wie beispielsweise eine fehlerhafte mRNA-Verarbeitung, das Fehlen von Translationskomponenten oder seltenen Codons, können während der Translation zu einem Ribosomenstillstand führen. Im Zytosol sind die Faktoren, die gestaute Ribosomen erkennen und beseitigen – zusammenfassend als ribosomassoziierte Qualitätskontrolle (RQC) bezeichnet – gut erforscht. Die Ereignisse, die auf ein Ribosomenstillstand während der co-translationalen Proteintranslokation in das endoplasmatische Retikulum (ER) folgen, waren jedoch bislang kaum verstanden. Nach dem Ribosomenstillstand am ER zeigte sich, dass das 60S-Ribosomprotein RPL26 durch UFM1 (Ubiquitin-Fold-Modifier 1), ein Ubiquitin-ähnliches Protein, kovalent modifiziert wird. Die genaue Rolle der UFMylierung bei der ER-Proteinqualitätskontrolle und ihre Wechselwirkung mit dem RQC-Apparat blieben jedoch bislang unklar.

In dieser Arbeit schließe ich diese Forschungslücke, indem ich unvoreingenommene Proteomik mit biochemischen und zellulären Assays kombiniere. Die Proteomik UFMylierter Ribosomen zeigte, dass die RQC-Faktoren NEMF und LTN1 in einer vom Stillstand abhängigen Weise mit UFMylierten Ribosomen interagierten.

Mithilfe der Zellbiologie konnte ich feststellen, dass im ER festsitzende Ribosomen – ähnlich wie zytosolische Ribosomen – von der E3-Ligase ZNF598 erkannt und anschließend vom ASC-1-Komplex gespalten werden. Wichtig ist, dass diese Schritte notwendige Voraussetzungen für die UFMylierung von RPL26 sind, bei der die UFM1-E3-Ligase die nach der Spaltung entstandenen 60S-Peptidyl-tRNA-Komplexe als kanonische Substrate erkennt. Die UFMylierung von RPL26 lockert die enge Wechselwirkung zwischen dem 60S-Peptidyl-tRNA-Komplex und dem Translokon und ermöglicht so den RQC-Komponenten den Zugang zu den angehaltenen Peptidketten. Im Einklang mit diesen Ergebnissen schwächt eine beeinträchtigte UFMylierung die Bindung von LTN1 an 60S-Peptidyl-tRNA-Komplexe, und der Abbau von entweder NEMF oder LTN1 führt zur Anreicherung von UFMylierten Ribosomen, was die Annahme stützt, dass diese beiden Mechanismen auf demselben Signalweg wirken und eine direkte Verbindung zu post-split Ribosomen-Zwischenprodukten herstellen. Insgesamt hat meine Arbeit gezeigt, dass eine enge Zusammenarbeit zwischen dem RQC und der UFMylierung für die Beseitigung blockierter Ribosomen am ER notwendig ist, wodurch die zelluläre Proteinhomöostase gesichert wird.

## Table of contents

Acknowledgements ..... 2
Contribution statement ..... 4
Abstract ..... 5
Zusammenfassung ..... 6
Table of contents ..... 7
1. Introduction ..... 10
1.1. Endoplasmic reticulum ..... 10
1.1.1. General structure of the ER ..... 10
1.1.2. Function of the ER ..... 11
1.1.3. Protein translation at the ER ..... 11
1.1.4. Unfolded protein response ..... 12
1.2. Ribosome-associated quality control ..... 13
1.3. UFMylation ..... 14
1.3.1. The UFMylation cascade and mechanism ..... 15
1.3.2. Insights from functional studies ..... 17
1.3.3. UFMylation substrates ..... 18
1.3.4. Link to autophagy and secretory pathways ..... 19
1.3.5. The role of UFMylation in cell cycle progression ..... 19
1.3.6. UFMylation in DNA damage response ..... 20
1.3.7. The role of UFMylation in antiviral response ..... 20
1.3.8. The role of UFMylation in ER quality control ..... 21
1.3.9. The cross-talk between UFMylation and ubiquitination ..... 21
1.4. Ribosome-associated quality control at the ER ..... 22
1.5. Aims ..... 22
2. Results ..... 24
2.1. The coordinated action of UFMylation and the RQC pathways clears arrested polypeptides at the ER ..... 24
2.1.1. Preamble ..... 24
2.1.2. Contribution statement ..... 24
2.2. Dual regulation of the unfolded protein response by IGF2BP3 during ER stress ..... 50
2.2.1. Preamble ..... 50
2.2.2. Contribution statement ..... 50
3. Discussion ..... 110
3.1. Ribosome rescue and RQC are implicated in ER protein quality control ..... 110
3.2. Both the RQC and UFMylation are needed for the clearance of RNCs at the ER ..... 110

3.3. Ribosome recognition and splitting upon stalling at the ER are prerequisites for UFMylation ..... 111
3.4. UFM1 E3 ligase binds 60S-peptidyl-tRNA complexes ..... 112
3.5. The effects of UFMylation in ER protein quality control ..... 113
3.6. The role of LTN1 in ER protein quality control ..... 113
3.7. The phylogenetic conservation of UFMylation's role in ER quality control ..... 114
4. Limitations and future perspectives ..... 115
5. References ..... 116
6. Abbreviations ..... 122
7. Appendix ..... 126
7.1. UFMylation anchors splicing factors at the ER to reprogram nuclear splicing ..... 126
7.1.1. Preamble ..... 126
7.1.2. Contribution statement ..... 126
7.2. Confirmation of manuscript status for "Dual regulation of the unfolded protein response by IGF2BP3 during ER stress ..... 162
7.3. Confirmation of manuscript status for "UFMylation anchors splicing factors at the ER to reprogram nuclear splicing" ..... 165

# 1. Introduction

## 1.1. Endoplasmic reticulum

Endoplasmic reticulum (ER) is a eukaryotic organelle consisting of a vast network of membrane sheets and tubules. This membrane-enclosed cellular compartment allows the maintenance of a specific biochemical environment and the localization of intracellular processes. The ER is the site of folding and maturation for a third of the proteome, including secretory and membrane proteins ranging from plasma membrane and other organellar membrane proteins to antibodies secreted by plasma cells[1,2]. Most mRNAs encoding for these proteins are brought to the ER on translating ribosomes for co-translational folding and maturation[3]. Nascent polypeptides that go through the ER before their final functional destination are subjected to extensive quality control during their maturation inside the ER lumen[4]. Apart from protein synthesis, the ER plays a major role in lipid synthesis and metabolism, serving as a cell-wide lipid reservoir that adjusts to cellular lipid needs[5]. The ER membrane is in continuity with the outer nuclear membrane, has extensive contacts with organelles such as mitochondria, lysosomes, endosomes, and chloroplasts, and serves as the major site for $Ca^{2+}$ storage[6]. Therefore, ER is crucial for cellular physiology and homeostasis.

### *1.1.1. General structure of the ER*

The ER is structurally divided into smooth ER, which has a tubular structure, and rough ER, with sheet-like architecture and ribosomes attached to the outer membrane[7]. ER sheets have the role in protein translation, translocation, folding, and maturation[8], while ER tubules are the place of lipid synthesis and formation of membrane contact sites with other organelles, through which ion transport, signaling, and organellar division are coordinated[9]. Depending on the cell type and physiological needs, the ratio of ER sheets to tubules can drastically change[8]. Cell types with high protein secretion, such as pancreatic cells secreting digestive enzymes or B cells actively secreting antibodies, have a vast network of ER sheets stacked by twisted membrane surfaces, allowing efficient packing in a limited intracellular space[10–12]. In contrast, cells with no high protein secretion need, such as neuronal cells, adrenal cells, and epithelial cells have highly developed intracellular tubular ER structures[13].

The structural and physiological division of the ER is established through integral membrane proteins that shape its architecture. For the correct formation of the tubular ER, high membrane curvature is required. This is done by reticulons and reticulon-like proteins, which form a hairpin structure from their hydrophobic domains, which are inserted like a wedge in the outer membrane layer of the ER, displacing the lipids and forming a curvature[14,15]. The loss of these proteins causes the reduction of tubular architecture, whereas their overexpression leads to expansion of ER tubules to longer structures, confirming the role of reticulons and reticulon-like proteins in shaping the ER tubules[15,16].

The proteins shaping the sheet ER architecture are, in contrast to reticulons, much less studied. The protein that stabilizes ER sheets was recently shown to be SigmaR1[17]. The stabilization of flat membranes is achieved through the insertion of trimeric SigmaR1 complexes into the inner layer of ER membrane, with 6 amphipatic helices lying in a flat architecture in the membrane and, therefore, supporting the non-curved sheet formation[17,18].

In cells depleted of SigmaR1, the levels of ER sheets are reduced, whereas SigmaR1 overexpression leads to ER sheet expansion[17]. Therefore, the ER sheet-to-tubules ratio is impacted by reticulons, SigmaR1, and membrane lipid composition. This dynamic regulation of ER structure provides its adaptability to current cellular needs and timely remodeling to fulfil protein or lipid synthesis demands.

### *1.1.2. Function of the ER*

The vast majority of lipid synthesis enzymes are localized to the ER, making it a central hub that regulates the lipid levels within membranes in the cell[5]. Major structural lipids, such as phosphatidylcholine and phosphatidylethanolamine, but also less abundant lipids involved in signaling, like phosphatidylinositol and sphingolipids, are all synthesized at the ER[5]. The lipids synthesized at the ER are subsequently transported to all other membranes either through vesicular transport through the Golgi, or directly shuffled to Golgi membrane through vesicle-associated membrane protein-associated proteins (VAPs) at ER-Golgi membrane contact sites[9]. VAPs interact with the FFAT (two phenylalanine in an acidic tract) motifs in proteins located in the non-ER membranes to facilitate the lipid shuffling[19].

The ER is a major intracellular $Ca^{2+}$ storage. The concentration of $Ca^{2+}$ ions in the cytosol is around 100 nM, whereas the concentration inside the ER lumen is between 100 and 800 µM[20]. Calcium gets released from the ER into the surrounding cytosol through inositol-1,4,5-triphosphate receptors ($IP_3Rs$)[20,21]. The released calcium ions can be subsequently imported into mitochondria through voltage-dependent anion-selective channel, or perform their function in intracellular signaling[20].

All the secretory and membrane proteins go through the ER for their proper folding and maturation. The following section describes this process in detail.

### *1.1.3. Protein translation at the ER*

The targeting of nascent proteins to the ER mostly occurs co-translationally, after the N-terminal signaling peptide or the first hydrophobic transmembrane domain (TMD) emerges from the peptide exit tunnel[3]. The signal recognition particle (SRP), a highly conserved ribonucleoprotein complex, recognizes the signal peptide or TMD and targets the actively translating ribosome to the ER membrane[22]. SRP's subunit SRP54 recognizes the 60S ribosomal subunit, directly binding both the ribosome next to the peptide exit channel and the signal peptide or the TMD[3,22]. The Alu domain of SRP then engages the GTPase center of the ribosome, likely slowing down translation rates during ER targeting[3]. SRP then hands over the ribosome-nascent chain complex (RNC) to the SRP receptor at the ER membrane[22,23], the interaction mediated by the GTPase domain of SRP54 and GTPase domain of the α subunit of SRP receptor (SRα)[24]. This binding triggers GTP hydrolysis in both proteins and the subsequent release of SRP from its receptor[25]. The RNC subsequently docks on the Sec61α subunit of the conserved heterotrimeric translocation complex SEC61[3]. Sec61α forms a lateral gate through which the emerging peptide gets translocated into the ER lumen, and additionally allowing hydrophobic domains to be directly inserted inside the ER membrane[25].

Apart from the majority of proteins targeted to the ER via an N-terminal signal sequence or TMD, there is another group of proteins whose single TMD is located near the C-terminus,

collectively called tail-anchored (TA) proteins[3]. As their hydrophobic domain is translated only near the end of translation, TA proteins are targeted to the ER membrane post-translationally[26]. TA proteins can be inserted into ER membrane by two distinct mechanisms: through guided entry of TA (GET) pathway or through ER membrane protein complex (EMC). In the GET pathway, nascent TA proteins are captured by SGTA chaperone in the cytosol, get loaded to another cytosolic chaperone GET3, which interacts with TMD insertase GET1/2 in the ER membrane, a process dependent on ATP hydrolysis[27,28]. The alternative EMC pathway directly inserts TA proteins into the ER membrane, without the need of a cytosolic factor[29]. Disruption of the GET pathway leads to mislocalization of TA proteins to the mitochondrial membrane[30], underlying the importance of the ER targeting regulation for keeping cellular proteostasis.

*1.1.4. Unfolded protein response*

Disbalance of ER function in folding and maturation of secretory and membrane proteins can cause the accumulation of partially unfolded or misfolded proteins, a condition termed ER stress[31]. ER stress can result from external stressors, such as oxidative stress, physical or chemical stressors, calcium depletion, or internal disruptions in protein folding[32]. It is the underlying cause of many pathophysiological processes and disease development, such as cystic fibrosis[33] and cancer[34]. A conserved set of signaling cascades that regulate ER homeostasis and, upon protein folding imbalance, activate the restoring mechanisms, are collectively called unfolded protein response (UPR)[35,36].

UPR consists of three branches: the inositol-requiring enzyme 1 (IRE1), PKR-like kinase (PERK), and the activating transcription factor 6 (ATF6)[4]. IRE1 is a transmembrane protein consisting of an ER luminal domain and cytosolic kinase and RNase domains. Upon accumulation of misfolded proteins in the ER lumen, IRE1 oligomerizes, activating its kinase domain[37]. The trans-autophosphorylation allosterically activates the RNase domain, which initiates the unconventional splicing of its main target mRNA *XBP1* by cleaving two similar stem-loop endomotifs, removing its intron[37]. The cleaved 5'- and 3'-ends of *XBP1* mRNA are then ligated by the RtcB complex, generating *XBP1* spliced mRNA[38]. The spliced *XBP1* encodes for a transcription factor that activates the expression of ER chaperons, lipid remodeling enzymes and ER protein degradation factors, through which the folding burden gets alleviated[39].

The second conserved branch of the UPR is through PERK signaling. PERK is an ER transmembrane kinase with a structurally similar ER luminal sensor domain as IRE1[4]. Similarly to IRE1 activation mechanism, upon ER stress PERK oligomerizes, which activates its trans-autophosphorylation and subsequent activation[40]. PERK then phosphorylates the eukaryotic translation initiation factor eIF2α, leading to a cell-wide temporary translational shutdown[41]. This downregulation of cellular translation levels provides increased time span for the restorative mechanisms to take place, while decreasing the protein synthesis load into the ER. The phosphorylation of eIF2α drives the selective translation of transcription factor ATF4, which in turn activates the expression of amino acid synthesizing enzymes and transporters, chaperons such as heat shock proteins, and autophagy genes[42].

The last branch of UPR is mediated through ATF6. Upon ER stress, the disulfide bridges in the ATF6 dimers get reduced, causing a change in localization of ATF6 from the ER membrane to

the Golgi[43]. In the Golgi, the transmembrane domain of ATF6 is proteolytically cleaved by Site 1P and Site 2P proteases, releasing the leucine zipper transcription factor domain, ATF6(N)[44]. Upon subsequent translocation to the nucleus, ATF6(N) drives the expression of UPR target genes, including ER chaperons, lipid synthesis enzymes, and XBP1[45].

## 1.2. Ribosome-associated quality control

Various factors during protein translation can induce elongating ribosomes to stall. The translational arrest can be caused by aberrant mRNA processing, with excessive secondary structures[46], rare codons[47], or truncated mRNAs[48,49], by a lack of translational components[50], a lack of stop codons causing translation into poly(A) tail[51,52], or oxidative damage to mRNAs[53]. The resulting stalled ribosomes have to be promptly recognized and cleared, since the incomplete peptides have a high tendency for misfolding and aggregation[54].

Depending on the localization of the stalled ribosomes on the mRNA, namely at the truncated 3'-end of mRNAs or internally within the coding sequence, two distinct recognition mechanisms can take place. During canonical translation termination, the stop codon in the A-site is recognized by eukaryotic release factor 1 (eRF1), which catalyzes the peptide-tRNA cleavage, therefore releasing the nascent protein[55]. eRF1's translational termination is dependent on eRF3's GTPase activity[56]. Since the truncated mRNAs lead to stalled ribosomes with an empty A-site[49], the same release factors can't recognize these ribosomes. Instead, the eRF1 homolog is recruited to stalled ribosomes with an empty A-site is Pelota (Dom34 in yeast)[49,57]. This recruitment depends on an eRF3 homolog, GTPase Hbs1L (Hbs1 in yeast)[58]. Similar to canonical translation termination, the subsequent ribosome splitting is mediated by ATPase ABCE1 (Rli1 in yeast)[57]. An important distinction from the termination is that Pelota, unlike eRF1, is incapable of cleaving the tRNA from the nascent polypeptide due to its lack of GGQ (Gly-Gly-Gln) motif, resulting in a 60S-peptidyl-tRNA complex after ribosome splitting by ABCE1. Therefore, the presence of 60S-peptidyl-tRNA is a unique signal for initiation of downstream quality control.

In the alternative case of ribosomes stalled internally within the mRNA coding sequence, Pelota cannot be recruited to the stall site due to the occupied A-site. The first factor that recognizes these stalled ribosomes, more specifically their 40S-40S collided interface, is E3 ligase ZNF598 (Hel2 in yeast[59])[60,61], represented in Figure 1. 40S ribosomal proteins RPS10 and RPS20 are primary ubiquitination targets of ZNF598, both positioned at the collided ribosomal interface[60]. This ubiquitination is required for terminal stalling of the ribosomes and is a necessary prerequisite for the activation of the downstream quality control pathways[60]. Upon 40S ribosomal protein ubiquitination by ZNF598, the ASC-1 complex gets recruited to the stalled ribosomes (RQT complex in yeast[62])[63]. ASC-1 complex consists of helicase ASCC3 (Slh1 in yeast), zinc-finger protein ASC-1 or TRIP4 (Rqt4 in yeast), ubiquitin-binding protein ASCC2 (Cue3 in yeast) and ASCC1 (no known homolog in yeast)[62,63]. ASC-1 complex splits the leading ribosome in a reaction dependent on ATP and ASCC3's activity[63]. This ribosomal splitting happens only after collided ribosomes have been recognized and ubiquitinated by ZNF598, while the splitting by Pelota-Hbs1 and ABCE1 happens only upon stalling at truncated mRNAs[63]. Both pathways release 60S-peptidyl-tRNA, a complex recognized by the

downstream components, collectively termed the ribosome-associated quality control (RQC) machinery.

The splitting of the ribosome upon stalling leaves the P-site occupied with tRNA connected to the nascent polypeptide, unlike the post-termination empty 60S subunit. This specific interface is recognized by NEMF (Rqc2 in yeast), whose binding facilitates the recruitment of E3 ligase LTN1[48,48,64]. NEMF catalyzes the extension of nascent polypeptide by adding non-templated C-terminal alanine and threonine extensions (CAT-tails)[65]. The role of CAT-tails is to, by extension of the polypeptide length, expose the lysines (Lys) which can potentially be buried within the peptide exit channel of the ribosome, and increase the likelihood of finding a target Lys residue for ubiquitination by LTN1[65]. LTN1 then binds to the 60S-peptidyl-tRNA complexes in a way that its catalytic RING domain is positioned close to the ribosome exit tunnel, in proximity to the target nascent peptide[64,66]. The formation of K48-linked ubiquitin chains is promoted by TCF25 (Rqc1 in yeast)[67]. The resulting poly-ubiquitinated nascent chains are cleaved from the 60S subunit by the endonuclease ANKZF1 (Vms1 in yeast)[68,69], extracted by ATPase VCP (Cdc48 in yeast), and further degraded by the proteasome[70,71].

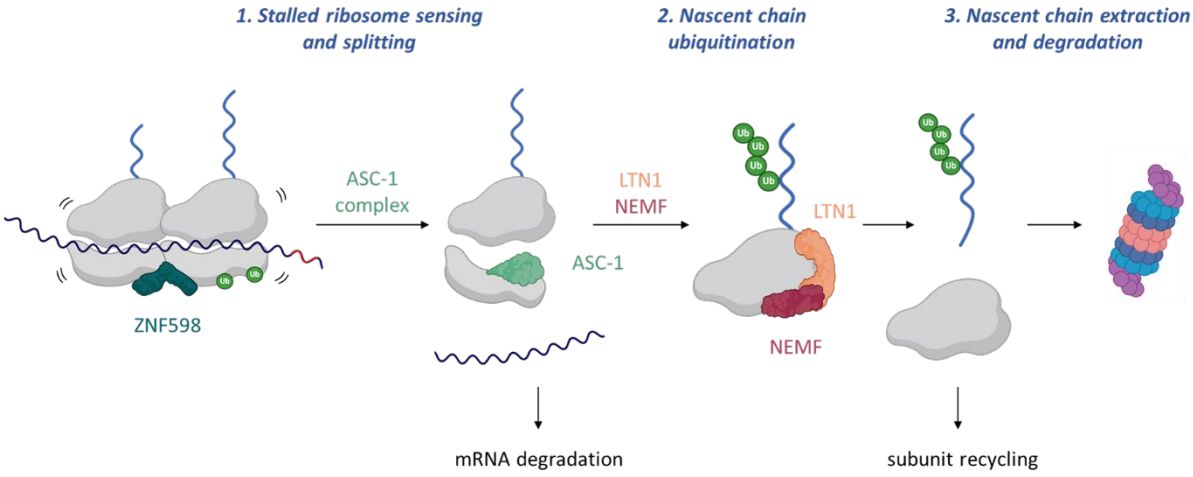



*Figure 1. Schematic representation of ribosome-associated quality control process upon internal ribosome stalling*

Compared to the extensively studied cytosolic RQC, the required factors for recognition and clearance of the ribosomes stalled during co-translational targeting to the ER are not well understood. In case of ribosome stalling at the ER, the target of RQC, incomplete nascent chain, is physically separated in the ER lumen from the cytosolic quality control factors. Additionally, since the nascent chain is threaded through the translocon embedded inside the ER membrane, the complex is more rigid and could be more challenging to access by the canonical machinery. Therefore, the mechanism and players responsible for the clearance of ER-bound stalled ribosomes are unclear.

### 1.3. UFMylation

Ubiquitin-like proteins (Ubl's) are a protein family that shares the ubiquitin fold and is evolutionarily related to ubiquitin[72]. The conjugation of Ubl's to target proteins or lipids alters their stability, activity, subcellular localization, or protein interactions[72].

UFM1 (ubiquitin-fold modifier 1) is a Ubl that covalently modifies its targets through a process termed UFMylation[73]. In a similar fashion to ubiquitin conjugation, UFMylation happens in an enzymatic sequence catalyzed by E1 activating enzyme (UBA5), E2 conjugating enzyme (UFC1) and E3 ligating enzyme (a complex consisting of UFL1, DDRGK1, and CDK5RAP3). In contrast to the variety of E1 (~10), E2 (~50), and especially E3 enzymes (~600) in the ubiquitin-conjugating system[74,75], the UFMylation cascade consists of single enzymes for each step.

The UFMylation system is highly conserved in eukaryotes, except in fungi[76]. UFM1 post-translationally modifies a wide range of substrates, therefore modifying various cellular processes such as endoplasmic reticulum (ER) homeostasis[77–81], translation initiation[82], DNA damage[83,84], hematopoiesis[85], and possibly many more to be discovered in the future. Complete loss of components of the UFMylation cascade (UFM1, UBA5, UFL1, CDK5RAP3, DDRGK1) is lethal in mice, underlining their indispensability in hematopoietic development[85–88]. Mutations in UFMylation cascade give rise to pathologies in humans including neurodevelopmental disorders[89–92], skeletal dysplasia[93,94], and cancer[95,96]. Therefore, it is of high importance to understand the molecular mechanisms upon target protein UFMylation.

The main target of UFMylation is 60S ribosome protein RPL26[79,80,97]. Mammalian cells in homeostatic conditions show a low baseline level of RPL26 UFMylation, with a strong increase upon ribosome stalling at the ER[79,97]. This modification is necessary for the degradation of arrested peptides at the ER, as the inability to UFMylate RPL26, either through UFM1 KO, or through deletion of the C-terminus of RPL26, which contains UFMylation sites, stabilizes the ER stalling reporter[97]. This modification is important for maintaining ER homeostasis; however, the precise role, regulation, and the mechanistic details of RPL26 UFMylation remained elusive.

*1.3.1. The UFMylation cascade and mechanism*

UFM1 gets covalently attached to target substrates through an enzymatic cascade which is conceptually similar to the ubiquitination enzymatic mechanism (Figure 2). UFM1 gets synthesized in a pro-form and it requires proteolytic cleavage of the last 2 amino acids, $Ser^{84}$-$Cys^{85}$, on the C-terminus in order to be conjugation-competent. The cysteine proteases that are a part of UFMylation system are UFSP1 and UFSP2. UFSP1 is the main protease that catalyzes the C-terminal amino acid cleavage for UFM1 maturation, and it also removes UFM1 from UFC1, serving as a release of an autoinhibitory mechanism[98]. In contrast, UFSP2's main role is in cleaving UFM1 from the substrate, however it can also contribute to the proteolytic cleavage of pro-UFM1[99]. Cells with UFSP2 KOs show increased UFMylation due to their inability to recycle UFM1 upon UFMylation[79].

UFMylation cascade involves 3 steps: the activation step by E1 enzyme UBA5 (UFM1-activating enzyme 5), the conjugating step by E2 enzyme UFC1 (UFM1-conjugating enzyme 1), and the ligating step by UFM1 E3 ligase, the ER-tethered complex consisting of UFL1 (UFM1 specific ligase 1), DDRGK1, and CDK5RAP3[73,77,78].

Initially named due to its homology to ubiquitin E1 enzyme UBA1, UBA5 consists of adenylation domain, which contains the catalytic cysteine that activates UFM1 and the ATP-binding site, UFM1-interacting motif (UFIM), and E2 recognition site (UFC1-binding sequence, UBS)[100–102]. Dimerization of UBA5 is necessary for UFM1 activation, and the active complex consists of two UBA5 and two UFM1 molecules[103]. Each UFM1 interacts with both UBA5 molecules in a homodimer, through the UFIM domain on one, and the adenylation domain in the other subunit[103]. The activation mechanism, therefore, happens *in trans* with one UBA5 subunit binding UFM1 and the other subunit catalyzing its activation and subsequent transfer to the E2 enzyme UFC1[103].

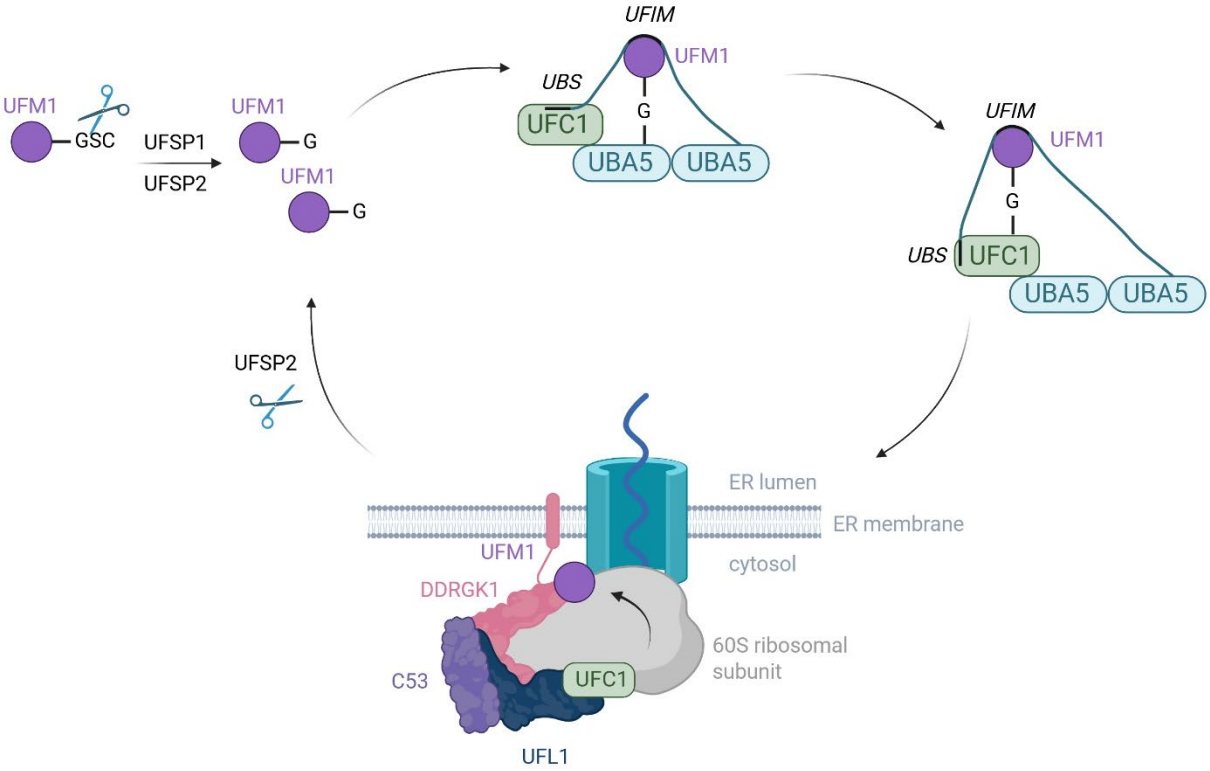



*Figure 2. Schematic representation of the UFMylation cycle*

Interestingly, the binding surface of UFC1 that is responsible for its interaction with UBA5 doesn't exist in other E2 enzymes, making the transfer of UFM1 specific from UBA5 to UFC1[73,101]. UFC1 contains an N-terminal helix and a core UBC (ubiquitin-conjugating) domain[101]. In order to accept the activated UFM1, UFC1 binds the $(UBA5)_2$-$(UFM1)_2$ tetramer, in a *trans*-binding mechanism where UFC1 binds one UBA5 subunit and acquires activated UFM1 from the other UBA5 subunit[101]. The binding surface of UFC1 to E2 recognition UBS site on UBA5 is a hydrophobic pocket opposite of a catalytic Cysteine[116], a unique pocket that ensures UFM1 E1/E2 specificity and incompatibility with other E2 enzymes in the ubiquitin pathway[101].

The UFM1 E3 ligase complex consists of three proteins: UFL1, the catalytic subunit, DDRGK1 (also known as UFBP1), and CDK5RAP3[77,78]. The complex is tethered through DDRGK1 to the ER-membrane, keeping it in close proximity to the main UFMylation target, RPL26 upon ribosome stalling at the ER[79,97,104]. UFM1 E3 ligase acts similarly to scaffold-type RING E3 ligases, with the UFM1 transfer happening directly from UFC1, the E2 enzyme, to target

proteins[104]. UFL1 consists of a short N-terminal helix, followed by a partial winged-helix (pWH), five winged-helix (WH) motifs, a disordered region consisting of a bipartite coiled-coil (CC) domain and a PTC (peptidyl transferase center) loop, and the C-terminal globular domain. DDRGK1 contains a transmembrane domain (TM) on the N-terminus, followed by a flexible linker region, a long α-helix, a WH and a pWH motif. Finally, CDK5RAP3 consists of N-terminal globular domain, a CC domain and another globular domain intersected by a disordered region[77,78].

The minimal requirement for UFM1 E3 ligase activity is UFL1-DDRGK1 complex[104]. The C-terminal partial WH motif combines with N-terminal pWH motif of UFL1 to form a full WH motif and stabilize the core complex[77]. UFM1 binds DDRGK1 directly through its UFM1-interacting motif (UFIM)[77]. Recent structural data show that the UFM1 E3 ligase complex forms a C-shape around the empty 60S subunits in a manner that is incompatible with the binding of tRNA, 40S subunit, or the translocon[77,78]. However, whether this way of binding is the only canonical ribosomal state recognized by the UFM1 E3 ligase remains to be discovered.

*1.3.2. Insights from functional studies*

UFMylation has been implicated in a vast variety of developmental processes and physiological functioning of many tissues and organs. Here I present an overview of the main functional roles of the UFMylation machinery.

Uba5 is essential for development of erythroid cell lineage, with the Uba5 knockout mice exhibiting embryonic lethality due to severe anaemia[87]. In addition, loss of Ddrgk1 or Ufl1 show the same phenotype of impaired erythroid development and hematopoiesis, mechanistically through increased ER stress and unfolded protein response (UPR) activation, leading to hematopoietic progenitor cell death[85,88]. The lethal outcome of the loss of UFMylation machinery in mice is largely associated with the impaired hematopoietic development, underlying its major role in development.

Mice with neuron-specific loss of Ufl1 and Ddrgk1 develop microcephaly, significant cortical and hippocampal neuronal loss and cell death[105]. Loss of these two proteins also led to an increased inflammatory response[105]. Neuronal-specific deficiency of Cdk5rap3 in mice similarly led to encephalo-dysplasia, abnormal brain structure and neuronal death, resulting in lethality during lactation period[106].

Liver-specific knockout of UFM1 E3 ligase components (Ufl1 and Ddrgk1) in mice causes early liver damage, progressive fibrosis and hepatocyte steatosis[107]. In addition, over 50% of the mice exhibited spontaneous hepatocellular carcinoma[107]. In another study, liver-specific loss of Cdk5rap3 decreases hepatocyte proliferation and maturation, leading to liver hypoplasia in mice[86]. These findings underline the importance of the UFMylation system in liver development and homeostasis.

Loss of Ddrgk1 in early mesenchymal cells resulted in severe limb shortening and limb deformations in mice, due to abnormal growth plate development[108]. Additionally, Ddrgk1 conditional knockout in the intervertebral disc reduced spinal development and induced disc degeneration[109].

Findings from cardiomyocyte-restricted Ufl1 knockout mice show that Ufl1 is necessary for physiological cardiac growth and maintenance of cardiac function[110]. Also, Ufl1 has a protective role against pathological remodeling of the heart due to pressure overload, and therefore protects against heart failure[110].

Taken together, the findings from multiple studies in murine models show that UFMylation machinery is indispensable for embryogenesis and the development of multiple tissues and organs, and crucial for adult cellular homeostasis of neurons, hepatocytes, erythrocytes, and skeletal cells.

*1.3.3. UFMylation substrates*

The main substrate of UFMylation is ribosomal protein RPL26[79,97]. RPL26 is UFMylated at its C-terminus, on two conserved lysines, K132 and K134[79,97]. Interestingly, K132 substitution to arginine abolished di-UFMylation and did not affect the mono-UFMylation, while the K134R substitution greatly decreased both UFMylated RPL26 species[79,97], showing that K134 UFMylation might be a prerequisite for K132 modification. RPL26 was shown to be strongly UFMylated upon ribosome stalling at the ER[80,97] and the deletion of C-terminal tail of RPL26, which abrogates RPL26 UFMylation, stabilized the incomplete nascent chains at the ER[80]. Therefore, RPL26 UFMylation is indispensable for protein quality control at the ER.

UFM1 E3 ligase was shown to be recognizing empty 60S subunits upon translation termination at the ER[77,78]. The role of UFMylation upon the termination of ER-localized translation is to recycle the empty 60S subunits from the ER membrane, in order to make them available for next cycle of translation[77,78]. In particular, DDRGK1's α-helix is positioned at the ribosome exit tunnel, which dislocates the 60S subunit from the tight interaction with the translocon and, therefore, releases the 60S from the ER membrane[77,78].

This role of UFMylation and mode of binding of UFM1 E3 ligase did not explain the phenotype of incomplete nascent chain accumulation at the ER in cells with impaired UFMylation[80,97]. From this data, an alternative role in protein-associated quality control and, potentially, a distinct mode of binding is highly likely, but so far has not been studied.

Apart from the main UFMylation target RPL26, there have been other ribosomal proteins reported to be UFMylated. Upon His-UFM1 overexpression and IP-MS analysis, uS3 and uS10 were identified to be UFMylation substrates[111]. These 40S ribosomal proteins are solvent-exposed and in close proximity of RPL26, but the role of their UFMylation is yet to be elucidated.

Since the UFM1 E3 ligase is tethered to the ER, the mechanism of UFM1 transfer to non-ER-resident targets (further discussed in Chapters 1.3.5, 1.3.6, and 1.3.7) is not properly understood. Given that some of the confirmed targets include the nuclear-resident histone H4[84] and double strand break repair protein MRE11[83] (the role of UFMylation in DNA damage response explained further in Chapter 1.3.6), and that the minimal active UFM1 E3 ligase complex consists of UFL1 and DDRGK1[104], both attached to the ER membrane, there is a localization incompatibility of the catalytic E3 ligase and its targets. Even though UFM1 itself was shown to have a predominantly nuclear localization[73], for the efficient modification, the E3 ligase has to simultaneously bind UFM1 and the target protein, however brief that

interaction might be. Apart from localization, the UFM1 E3 ligase complex recognizes 60S ribosomal subunits by many points of contact along all three components of the ligase complex[77,78], raising the question of target recognition of non-ribosomal proteins.

The next 4 sections provide an overview of UFMylation targets apart from RPL26 and the physiological consequences of their UFMylation.

*1.3.4. Link to autophagy and secretory pathways*

An unbiased ER-phagy CRISPRi screen identified UFMylation pathway as its positive regulator[112]. Specifically, the loss of DDRGK1 or UFL1 impairs the starvation-induced autophagy of ER sheets, through the sheet-localized autophagy receptor FAM134B[112]. Additionally, CDK5RAP3 was identified as an ER-phagy receptor, interacting with ATG8 by a non-canonical shuffled ATG8 interacting motifs both in mammalian and plant cells[113]. CDK5RAP3-mediated ER-phagy is activated through phosphate starvation[114] and subsequent induction of ER stress[113]. In contrast to DDRGK1 and UFL1[112], the CDK5RAP3-mediated ER-phagy was not induced by carbon or nitrogen starvation[113]. Therefore, the UFMylation machinery is a positive regulator of ER-phagy and serves as an important protector against ER stress.

The main substrate of UFMylation machinery is RPL26, which gets modified upon ribosome stalling at the endoplasmic reticulum[79,80,97]. It is of high importance that the aggregation-prone incomplete nascent chains at the stalled ribosomes are promptly degraded, so that the risk of possible aggregation-induced homeostasis perturbation is alleviated. These incomplete peptides at the ER-localized translation have been reported to be degraded mainly in a proteasome-dependent manner[80,115], but lysosomal degradation inhibitors also had a stabilizing effect[97,115]. Additionally, Brefeldin A treatment, which impairs ER-to-Golgi trafficking, stabilized ER stalling reporter ERK20[97]. Another study uncovered a novel regulator, SAYSD1, which recognizes clogged translocons and routes the incomplete nascent chains through Golgi to be ultimately degraded by the lysosomal system[116].

Since the degradation by the proteasome involves retrotranslocation into the cytosol, it is plausible that a presence of a bulky folded domain inside the ER lumen, such as GFP in the reporter ERK20[97], would render the cytosolic degradation less probable, and favor lysosomal degradation. However, one study found that when a small VHP domain was changed into GFP, it was similarly stabilized by proteasomal inhibition compared to lysosomal proteolysis inhibition[80].

These results can be explained by a redundancy in degradation pathways, and a possible rerouting to lysosomal degradation in the context of impaired proteasomal activity. Additionally, since these experiments were conducted in different cell lines, the degradation pathways could be cell-specific.

*1.3.5. The role of UFMylation in cell cycle progression*

Various phenotypes that arise from the loss of UFMylation machinery, such as defects in haematopoiesis, microcephaly, hepatocellular carcinoma, can be caused by impaired cell cycle progression. Indeed, the impairment of UFMylation machinery has been shown to reduce

Cyclin D1 levels on the transcriptional and translational level, and, therefore, block the G1 checkpoint and the progress into the S phase of cell cycle[82]. The proposed mechanism includes the regulation of translational initiation through UFMylation of eukaryotic initiation factor eIF4G1 on K729 and K726, which in turn allows binding of eIF4A1 and the assembly of 48S pre-initiation complex (PIC)[82]. In cells with impaired UFMylation, the 48S PIC is not properly formed, leading to the cell-wide translational shutdown, which directly affects Cyclin D1 levels due to its short half-life, and results in the G1 checkpoint block[82].

CDK5RAP3, the component of UFM1 E3 ligase, was shown to be important for G2/M cell cycle progression[117]. Overexpression of CDK5RAP3 caused the increased enzymatic activity of Cdk1-cyclin B1 and its nuclear accumulation, a positive signal for cell cycle progression[117]. In contrast, depletion of CDK5RAP3 caused increased retention of Cdk1-cyclin B1 in the cytoplasm and the G2/M cell cycle arrest[117]. Another evidence of regulation of the G2/M cell cycle through UFMylation system is through stabilization of p53[118]. UFMylation of p53 antagonizes its ubiquitination, and stabilizes p53[118]. Stabilization of p53 leads to G2/M cell cycle arrest and promotion of DNA damage repair mechanisms[119]. Therefore, UFMylation system regulates cell cycle progression both in G1 and G2/M checkpoints and is necessary for proliferation.

### *1.3.6. UFMylation in DNA damage response*

One of the targets of UFMylation is the double-strand break repair protein MRE11[83]. MRE11 is a part of MRN complex which activates ATM kinase, the main driver of DNA damage repair[120]. MRE11 is UFMylated on K282, which is required for the correct assembly of the MRN complex and the activation of ATM kinase, leading to double-strand break DNA repair[83]. The MRN complex recruits UFM1 E3 ligase catalytic component UFL1 to the double-strand breaks, which, apart from UFMylating integral complex component MRE11, also UFMylates histone H4 as a response to DNA damage[121]. Histone H4 UFMylation enhances the recruitment of Suv39h1 and Tip60 to DNA break sites, which activates the ATM kinase, ensuring an additional point of activation of the DNA damage repair mechanism[121].

In response to DNA damage, p53 also gets UFMylated, causing its accumulation[118]. p53 is then orchestrating the response to DNA damage through its transcriptional activation of DNA damage response genes, but also through cell cycle arrest, which allows time for the repair to happen before cell cycle progression into mitosis[122]. Therefore, UFMylation regulates DNA damage response on multiple levels, and the defects in the UFMylation system compromise genome integrity.

### *1.3.7. The role of UFMylation in antiviral response*

UFMylation has been implicated in the antiviral response. Upon Epstein-Barr virus (EBV) infection, the viral G-protein-coupled receptor BILF1 recruits UFL1 through its C-terminal tail. UFL1 then UFMylates mitochondrial antiviral-signaling protein (MAVS) at K461, causing the translocation of MAVS from mitochondria to lysosome and its subsequent degradation[123]. This prevents the activation of NRLP3 inflammasome and, therefore, dampens the antiviral response[123]. A separate study showed that UFMylation of RPL26 promoted the viral

translation of hepatitis A virus[124], showing an additional role of UFMylation in promoting the viral infection, albeit without a detailed mechanistic insight.

In contrast, another piece of evidence showed that UFMylation plays a role in promoting antiviral response. Upon RNA viral infection, UFL1 gets recruited to 14-3-3ε protein, which increases the interaction of 14-3-3ε with antiviral innate immune receptor and RNA sensor RIG-I, keeping MAVS at the mitochondrial membrane and therefore activating the downstream interferon production and the antiviral signaling[125]. Taken together, there is emerging evidence of a dual role of UFMylation in antiviral response, which can be either promoting the viral infection of activating the cellular antiviral mechanisms. The exact circumstances leading to the activation of either responses are, however, yet to be elucidated.

*1.3.8. The role of UFMylation in ER quality control*

UFMylation machinery is invaluable for ER homeostasis. Knockout of UBA5, UFL1, or DDRGK1 in cells of various stages in hematopoietic development causes an increased eIF2α phosphorylation and increased XBP1 splicing, the hallmarks of ER stress through activated unfolded protein response (UPR)[85,88]. DDRGK1 knockout in intestinal epithelial cells also causes activation of both the IRE1 and PERK branches of the UPR, as well as an increase in eIF2α phosphorylation[126]. Induction of ER stress by thapsigargin (TG), an inhibitor of ER-resident $Ca^{2+}$ ATPase[127], causes upregulation of UFM1 and its conjugation machinery both on the mRNA and on the protein level[128,129]. Furthermore, UFM1 and DDRGK1 are required for prevention of apoptosis induced by unfolded protein stress in the ER in pancreatic beta cells[129]. Therefore, UFMylation system is necessary to protect the cells from ER stress and keep ER homeostasis.

UFMylation has a major role in recycling empty 60S subunits from the ER membrane following translation termination at the ER[77,78]. As ER-targeted translation happens through the translocon, it is crucial that upon completed targeting of secretory and membrane proteins to the ER, the remaining 60S subunits are timely recycled, to avoid translocon obstruction and ensure the optimal folding capacity. Upon UFMylation of empty 60S subunits, the positioning of DDRGK1's α-helix over the peptide exit tunnel of the ribosome, which is in close contact with the translocon during co-translational protein translocation into the ER, allows the release of 60S subunits from the ER membrane[77,78]. This renders the translocon unobstructed and ready for the next cycle of protein translation at the ER.

Apart from its role in physiological translation at the ER, UFMylation also has been implicated in protein-associated quality control upon co-translational ribosomal stalling at the ER, as the incomplete peptides are not degraded in cells without RPL26 UFMylation[80,97]. However, the signaling pathways following RPL26 UFMylation and its direct role in ER quality control have remained elusive.

In summary, UFMylation is crucial for regulation of translational termination at the ER, ribosome-associated protein quality control at the ER, and for maintaining ER homeostasis.

*1.3.9. The cross-talk between UFMylation and ubiquitination*

Recently, there has been emerging evidence of the same protein targets of both UFMylation and ubiquitination modifications. Tumor suppressor p53 was shown to be stabilized by UFMylation by antagonizing its ubiquitin-mediated degradation[118]. Depletion of Ufl1 or Ddrgk1 in mouse colon cancer xenograft experiment increased tumor size and weight in a p53-dependent manner, therefore underlining p53's oncoprotective role through its increased stability upon UFMylation[118]. Interestingly, a DNA damage regulator and oncogene NONO can also get both UFMylated and ubiquitinated, and its UFMylation promotes ubiquitination-dependent protein degradation by the proteasome[130]. The decreased stability of NONO through its UFMylation serves as an oncoprotective mechanism preventing hepatocellular tumor growth and metastasis[130]. Another example of increased degradation upon UFMylation is PD-L1, the programmed cell death protein 1[131]. UFL1 expression is negatively correlated with PD-L1 levels in human melanoma and liver cancer patients, with the low expression of UFL1 closely correlating with poorer overall survival[131]. Even though UFMylation of p53 on one side and NONO and PD-L1 on the other side results in opposite phenotypes in protein stability (increased stability or degradation, respectively), it serves as a tumor-suppressing mechanism in all reported cases. This emphasizes a role of UFMylation machinery in preventing tumor progression, and an attractive future therapeutic target.

### 1.4. Ribosome-associated quality control at the ER

Even though the ribosome-associated protein quality control in the cytosol is well studied, the details of this process upon co-translational ribosome stalling at the ER are less understood. As explained in Chapter 1.1.2, secretory and membrane proteins are co-translationally translocated inside the ER lumen during their synthesis. The same factors that can induce ribosome stalling in the cytosol, can also cause translational halts during the protein synthesis at the ER. Given that the nascent peptide that is being translocated inside the ER is physically separated from the cytosolic quality control machinery, it is unclear whether the same factors are sufficient for the clearance of ER-stalled ribosomes.

Upon ribosome stalling at the ER, the cytosolic RQC machinery (NEMF and LTN1) was shown to be able to recognize the 60S-peptidyl-tRNA complexes on the Sec61 translocon[132,133]. LTN1 can ubiquitinate the incomplete polypeptides at the ER with a minimum exposure of 12-25 residues to the cytosol[132]. However, the process of stalled ribosome recognition and rescue, as well as the release of 60S subunit upon nascent chain clearance is still elusive.

UFMylation of RPL26 allows the empty, post-termination 60S subunits upon translation at the ER to be detached from the translocon and recycled for the next translation cycle[77,78]. However, since UFMylation of RPL26 is increased upon ribosome stalling at the ER[79,80,97], an alternative role in ER quality control is likely.

### 1.5. Aims

Quality control of stalled ribosomes at the ER, unlike the cytosolic stalled ribosomes, is not well understood. UFMylation of RPL26 increases upon ribosome stalling at the ER and is necessary for the clearance of ER-stalled ribosomes[79,97], however, the precise role, timing and regulation of this modification in the ER quality control was elusive. During my PhD work, I addressed two main open questions:

1. How do cells recognize and clear UFMylated ribosomes at the ER?
2. How do UFMylation and RQC pathways crosstalk to clear stalled ribosomes at the ER?

To answer the first question, I used an unbiased proteomics approach to detect the pathways that recognize UFMylated ribosomes. I have identified the RQC factors to be specifically associating with UFMylated ribosomes and demonstrated that the same ribosome rescue factors ZNF598 and ASC-1 complex are required for ribosome recognition and splitting, respectively, upon ribosome stalling at the ER (Chapter 2.1, Figures 1 and 2).

To address the second question, I combined biochemical and cell biology methods to reveal that the ribosomal recognition and splitting are necessary prerequisites for RPL26 UFMylation. UFM1 E3 ligase recognizes post-split 60S-peptidyl-tRNA subunits and UFMylates them, therefore destabilizing the association of 60S-peptidyl-tRNA complexes to the translocon. This in turn allows easier access of LTN1 to the complex, indicated by a decrease in LTN1's association to the 60S-peptidyl-tRNA complexes in UFM1 KO cells (Chapter 2.1, Figures 3-6). UFM1 E3 ligase and RQC factors can, therefore, recognize the same 60S-peptidyl-tRNA complexes, and act in coordination to clear the 60S-peptidyl-tRNA complexes, unblocking the translocon and therefore actively keeping the ER proteostasis.

Additionally, Chapter 2.2. provides a mechanistic insight into the dual regulation of ER proteostasis through RNA-binding protein IGF2BP3, which promotes mRNA degradation to reduce the translational and folding burden on the ER, and also supports the transcriptional activation of the unfolded protein response (UPR), resulting in ER proteostasis maintainance.

# 2. Results

## 2.1. The coordinated action of UFMylation and the RQC pathways clears arrested polypeptides at the ER

### *2.1.1. Preamble*

This paper investigates the mechanistic details of ribosome quality control upon ribosome stalling at the ER. Ribosomes stalled during co-translational translocation into the ER can give rise to aggregation-prone incomplete peptides, clog the translocon and impair ER homeostasis. The quality control following cytosolic ribosome stalling has been extensively studied, however, the regulation of ribosomes stalled at the ER is not well understood. It was shown that 60S ribosomal protein RPL26 gets UFMylated upon ribosomal stalling at the ER and that this modification is necessary for the degradation of incomplete peptides at the ER. However, the functional role of this modification, the timing of this process during events upon ribosome stalling at the ER, and the cross-regulation between the RQC and UFMylation remained unclear.

This work identified that ribosome recognition by ZNF598 and ribosome splitting by the ASC-1 complex are prerequisites for RPL26 UFMylation. UFM1 E3 ligase recognizes post-split 60S-peptidyl-tRNA complexes as canonical substrates, and releases the tightly bound 60S subunits from the translocon, facilitating the access of E3 ligase LTN1 to the complex. Both the RQC and UFMylation are thus needed to act in concert to clear ribosomes stalled at the ER and keep ER proteostasis.

This manuscript represents the majority of my PhD work and addresses both aims of my thesis.

This work has been published in *EMBO Journal* on March 25th, 2026 under the doi: https://doi.org/10.1038/s44318-026-00753-9.

### *2.1.2. Contribution statement*

I have formulated the hypothesis, designed and conducted a major part of the experiments, analyzed the results, and written and edited the manuscript presented. The groundwork for this project was done by my colleague, Aleksandra Anisimova, PhD, who has established selected inducible knock-out cell lines, performed and analyzed siRNA experiments, polysome profiling, and selected western blots.

Article

SOURCE DATA | TRANSPARENT PROCESS | OPEN ACCESS | CHECK FOR UPDATES

THE EMBO JOURNAL

# The coordinated action of UFMylation and the RQC pathways clears arrested polypeptides at the ER

Milica Mihailovic [1,2,7], Aleksandra S Anisimova [1,2,7], Bu Erte [3], Ni Zhan[3], Ioanna Styliara[1,4], Yasin Dagdas [3,5]✉ & Gülsün Elif Karagöz [1,6]✉

## Abstract

**Clearance of arrested nascent polypeptides resulting from ribosomal stalling is essential for proteostasis. Stalled endoplasmic reticulum (ER)-bound ribosomes are marked by ubiquitin-fold modifier 1 (UFM1) on the large ribosomal subunit protein RPL26, but the precise role of this modification in ribosome-associated quality control (RQC) remains poorly understood. Here, we define the interplay between the UFMylation machinery and the RQC in clearing arrested polypeptides upon ribosome stalling at the ER. Proteomic analysis shows that RQC factors associate with UFMylated ribosomes. Functional assays demonstrate that ribosome rescue factors ZNF598 and ASC-1 recognize and split stalled ribosomes at the ER, a prerequisite for RPL26 UFMylation. The UFM1 E3 ligase complex then binds and UFMylates the post-split 60S-peptidyl-tRNA complex, facilitating access of RQC factors. Depletion of the NEMF/LTN1 complex leads to accumulation of UFMylated ribosomes, whereas impaired UFMylation weakens NEMF/LTN1 binding to ER-stalled ribosomes, supporting a physical link between these pathways. These findings demonstrate that RQC cooperates with the UFMylation machinery to overcome the topological constraints of clearing the arrested polypeptides at the ER.**

**Keywords** UFMylation; Ribosome-associated Quality Control; Translation; Endoplasmic Reticulum; Ribosome Stalling
**Subject Categories** Post-translational Modifications & Proteolysis; Translation & Protein Quality
https://doi.org/10.1038/s44318-026-00753-9
Received 25 April 2025; Revised 6 February 2026; Accepted 25 February 2026
Published online: 25 March 2026

## Introduction

To maintain cellular protein homeostasis, protein translation is constantly monitored by quality control factors. Distinct secondary mRNA structures, incompletely processed mRNAs, rare codons, or translation into poly(A) tail can lead to prolonged translational pausing and ribosomal stalling (Shoemaker and Green, 2012; Choe et al, 2016; Doma and Parker, 2006; Letzring et al, 2013; Juszkiewicz and Hegde, 2017). Like a traffic jam, stalled ribosomes lead to ribosomal collisions and impaired translation (Chandrasekaran et al, 2019; Tesina et al, 2020). Also, arrested nascent polypeptides are prone to aggregation, which perturbs homeostasis (Choe et al, 2016). The highly conserved ribosome rescue and ribosome-associated quality control (RQC) pathways recognize and recycle stalled ribosomes and degrade incomplete nascent chains to maintain proteostasis (Filbeck et al, 2022).

The mechanisms involved in clearing stalled ribosomes in the cytosol have been studied in depth (reviewed (Joazeiro, 2017, 2019; Filbeck et al, 2022; Inada and Beckmann, 2024)). Collided ribosomes are recognized by the E3 ligase ZNF598, which ubiquitinates 40S ribosomal proteins and halts translation (Juszkiewicz and Hegde, 2017; Sundaramoorthy et al, 2017; Juszkiewicz et al, 2018). This is followed by the binding of the ribosome splitting factors ASC-1 complex/Pelota that recognize ubiquitinated stalled ribosomes (Juszkiewicz et al, 2020; Hashimoto et al, 2020) and split the leading ribosome to release the 60S-peptidyl-tRNA complex. After splitting, the 60S-peptidyl-tRNA complex is recognized by the RQC machinery, NEMF/LTN1 complex. NEMF adds template-independent C-terminal alanine and threonine extensions (CAT-tails) to the stalled nascent chain, which facilitates the exposure of the nascent chains out of the ribosome tunnel for ubiquitination by the E3 ligase LTN1 (Shen et al, 2015; Bengtson and Joazeiro, 2010; Kostova et al, 2017; Chu et al, 2009; Lyumkis et al, 2013). Subsequently, the nascent chain is released from the ribosome after tRNA cleavage by ANKZF1, extracted from the 60S ribosomal subunit by AAA ATPase VCP, and finally targeted for proteasomal degradation (Kuroha et al, 2018; Brandman et al, 2012; Meyer et al, 2012). The released 60S subunit is recycled and ready for translation initiation.

Translation into the endoplasmic reticulum (ER) membrane or the ER lumen poses topological and steric challenges for the RQC machinery to access the nascent chains on ER-bound ribosomes upon stalling. These nascent chains also obstruct the translocon, hindering the synthesis and maturation of other proteins at the ER, which causes an additional burden on proteostasis (Izawa et al, 2012; Phillips and Miller, 2020). Recent studies showed that

[1]Max Perutz Laboratories Vienna, Vienna BioCenter, Vienna, Austria. [2]Vienna BioCenter PhD Program, Doctoral School of the University of Vienna and Medical University of Vienna, Vienna, Austria. [3]Gregor Mendel Institute (GMI), Vienna BioCenter, Vienna, Austria. [4]University of Vienna, Vienna, Austria. [5]Heidelberg University, Centre for Organismal Studies (COS), Heidelberg, Germany. [6]Medical University of Vienna, Vienna, Austria. [7]These authors contributed equally: Milica Mihailovic, Aleksandra S Anisimova. ✉E-mail: yasin.dagdas@cos.uni-heidelberg.de; guelsuen.karagoez@meduniwien.ac.at

© The Author(s)

ribosomes stalled at the ER are marked by UFM1 (ubiquitin-fold modifier 1) at the large ribosomal subunit protein RPL26 (Wang et al, 2020; Walczak et al, 2019), and impairing UFMylation results in the accumulation of arrested polypeptides at the ER (Scavone et al, 2023). Similar to ubiquitination, UFMylation proceeds through a cascade of enzymatic reactions catalyzed by an E1-activating enzyme (UBA5), an E2-conjugating enzyme (UFC1), and an E3-ligating enzyme complex (UFM1 E3 ligase complex) (Kumar et al, 2021; Komatsu et al, 2004; Gavin et al, 2014; Stephani et al, 2020; Tatsumi et al, 2010). The UFM1 E3 ligase complex consists of three components: UFL1, DDRGK1, and CDK5RAP3 (C53), and is tethered to the ER by the ER-membrane protein DDRGK1. UFMylation is essential for ER homeostasis, and it is implicated in ER-phagy and RQC (Wang et al, 2020; Scavone et al, 2023; Stephani et al, 2020). Yet, due to a lack of biochemical and structural work, our understanding of the clearance of the ER-bound ribosomes that co-translationally translocate nascent chains into the ER remained incomplete (Karagöz et al, 2019; Lakshminarayan et al, 2020). More specifically, it is unclear whether UFMylation and RQC directly interact or act independently.

Accumulating evidence supports two models, not necessarily mutually exclusive, that explain the role of UFMylation in ER-localized translation. The first model suggests that ribosomal stalling at the ER induces RPL26 UFMylation, and UFMylation is involved in the clearance of arrested polypeptides resulting from ribosomal stalling (Wang et al, 2020; Scavone et al, 2023). The second, more recent model proposes that UFMylation releases the 60S ribosomal subunit from the translocon following the canonical translation termination at the ER (DaRosa et al, 2024; Makhlouf et al, 2024). The second model emerged from recent structural work showing that the UFM1 E3 ligase complex binds to an empty 60S subunit that sterically clashes with the translocon and a tRNA at the P-site. However, this novel binding mode cannot explain how the depletion of the UFMylation machinery leads to the accumulation of arrested polypeptides in the cell.

To reveal how UFMylation machinery clears arrested peptides at the ER, we dissected the interplay between the RQC and UFMylation machinery in this process. We show that the UFM1 E3 ligase complex loads onto the 60S-peptidyl-tRNA complex after ribosomal splitting by ribosome rescue factors. Through close collaboration with the RQC factors NEMF/LTN1, the UFM1 E3 ligase complex facilitates the clearance of stalled peptides by enabling better access of RQC factors to the nascent chain. Altogether, our findings underline the crucial role of the UFMylation-RQC crosstalk for clearing arrested polypeptides at the ER.

## Results

### RQC factors associate with and act on UFMylated ribosomes

To discover the pathways involved in the clearance of UFMylated ribosomes, we isolated them from mammalian cells for mass spectrometry (MS) analysis. To efficiently pull down UFMylated ribosomes, we generated an HCT116 cell line with endogenously tagged FLAG-UFM1 using the CRISPR-Cas9 gene editing approach. We enriched ribosomes by pelleting them using sucrose cushion sedimentation under control conditions or after inducing ribosomal stalling with anisomycin (ANS), which impairs ribosomal peptidyl transferase activity (Hansen et al, 2003). UFMylated ribosomes were subsequently pulled down by FLAG immunoprecipitation and subjected to MS (Fig. 1A). The MS analyses showed enrichment of UFM1 E3 ligase complex components (UFL1, CDKRAP53, DDRGK1) in FLAG-immunoprecipitated samples from FLAG-UFM1 cells treated with anisomycin, compared to the IgG control, and to untreated cells as a control (Fig. 1B,C; complete list in Dataset EV1). In addition to the components of the UFM1 E3 ligase complex, we found that the RQC component NEMF specifically associated with UFMylated ribosomes in a stalling-dependent manner (Fig. 1B,C). FLAG-UFM1 IPs followed by western blot analyses showed efficient enrichment of UFMylated RPL26 in the pulldowns relative to lysates and to non-modified RPL26, which further increased upon ribosomal stalling (Fig. 1D,E). Under those conditions, we observed a stalling-dependent association of UFM1 E3 ligase components, as well as NEMF and LTN1 in FLAG-UFM1 pulldowns, confirming our MS results (Figs. 1D,E and EV1A). IP of Sec61β in control conditions and upon ANS treatment showed stalling-dependent increase in association of UFMylated RPL26 with the translocon, supporting the notion that ER-bound ribosomes are UFMylated (Fig. EV1B).

NEMF/LTN1 associates with the peptidyl-tRNA-60S after splitting of stalled ribosomes (Shao et al, 2015; Shao and Hegde, 2014). To assess whether NEMF and UFL1 co-migrate at similar ribosomal fractions, we performed polysome profiling. Supporting structural and biochemical data, NEMF/LTN1 migrated primarily with the 60S ribosomal subunit in polysome profiles. Instead, UFL1 showed a broad distribution across 40S, 60S, and 80S fractions in two cell lines (HCT116 and HEK293T; Figs. 1F,G and EV1C). Notably, unlike UFL1, the majority of UFM1-conjugated RPL26 co-migrated with the 60S subunit, with a small fraction co-migrating with the 80S, as shown previously (Wang et al, 2020; DaRosa et al, 2024) (Figs. 1F,G and EV1C). This is consistent with our FLAG-UFM1 pulldowns, in which small ribosomal proteins were not enriched (Figs. 1E and EV1A). Additionally, we detected ZNF598-dependent ubiquitination of 40S ribosome protein RPS10 on disomes by polysome profiling in HCT116 cells treated with ANS. At the same time, UFMylation was mainly enriched in the 60S fractions, suggesting that early ZNF598 ubiquitination and UFMylation target distinct substrates (Fig. EV1D).

The association of RQC components with the UFMylated ribosomes supports their role in clearing ribosomes stalled at the ER. Together, these findings suggest a crosstalk between the RQC and the UFMylation machinery in resolving stalled ribosomes at the ER.

### Ribosome rescue factors recognize and mark ER-stalled ribosomes

To further assess the functional role of ribosome rescue factors in recognizing and recycling the ribosomes stalled at the ER, we monitored the translational readthrough of well-characterized stalling cytosolic or ER-targeted reporters (Wang et al, 2020) (Fig. 2A) in a fluorescence-activated cell sorting (FACS) assay (Fig. 2B,C). The ERK20 reporter consists of an N-terminal signal sequence, an N-glycosylation site, followed by EGFP and a poly-

 © The Author(s)

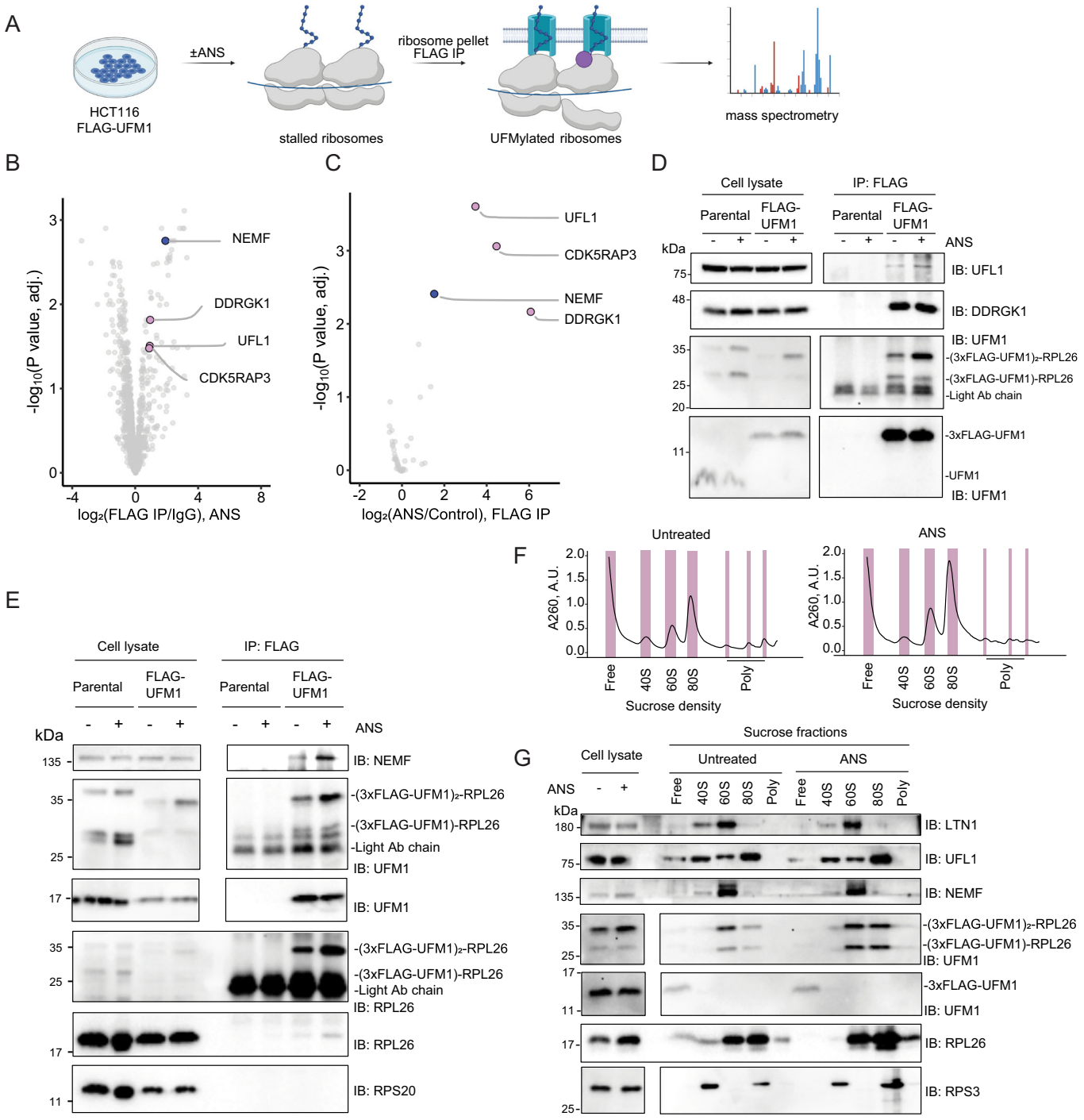



**Figure 1. RQC factors directly associate with UFMylated ribosomes.**

(**A**) Scheme of mass spectrometry analysis of UFMylated ribosomes. (**B**) Volcano plot of proteins co-enriched with UFMylated ribosomes in FLAG IP over control IgG IP upon 1 h 200 nM ANS treatment in HCT116 FLAG-UFM1 cells, identified by mass spectrometry experiment from (**A**), $n = 3$. (**C**) Volcano plot of enrichment of FLAG-eluates from ANS-treated HCT116 FLAG-UFM1 cells over FLAG-eluates from untreated control HCT116 FLAG-UFM1 cells, identified by mass spectrometry experiment from (**A**), $n = 3$. Proteins enriched 1.5 times in FLAG IP over IgG IP in ANS condition ($P$ value adj. <0.05) are shown, calculated with limma-moderated Benjamini–Hochberg-corrected two-sided $t$-test. (**D**, **E**) Immunoblot analysis of FLAG IP eluates upon 200 nM 1 h ANS treatment or from untreated HCT116 parental or HCT116 FLAG-UFM1 cells. (**F**) Polysome profiling of HCT116 FLAG-UFM1 cell lysates upon 200 nM 1 h ANS treatment or from untreated control condition. (**G**) Immunoblot analysis of selected sucrose fractions from (**F**). Source data are available online for this figure.

© The Author(s)

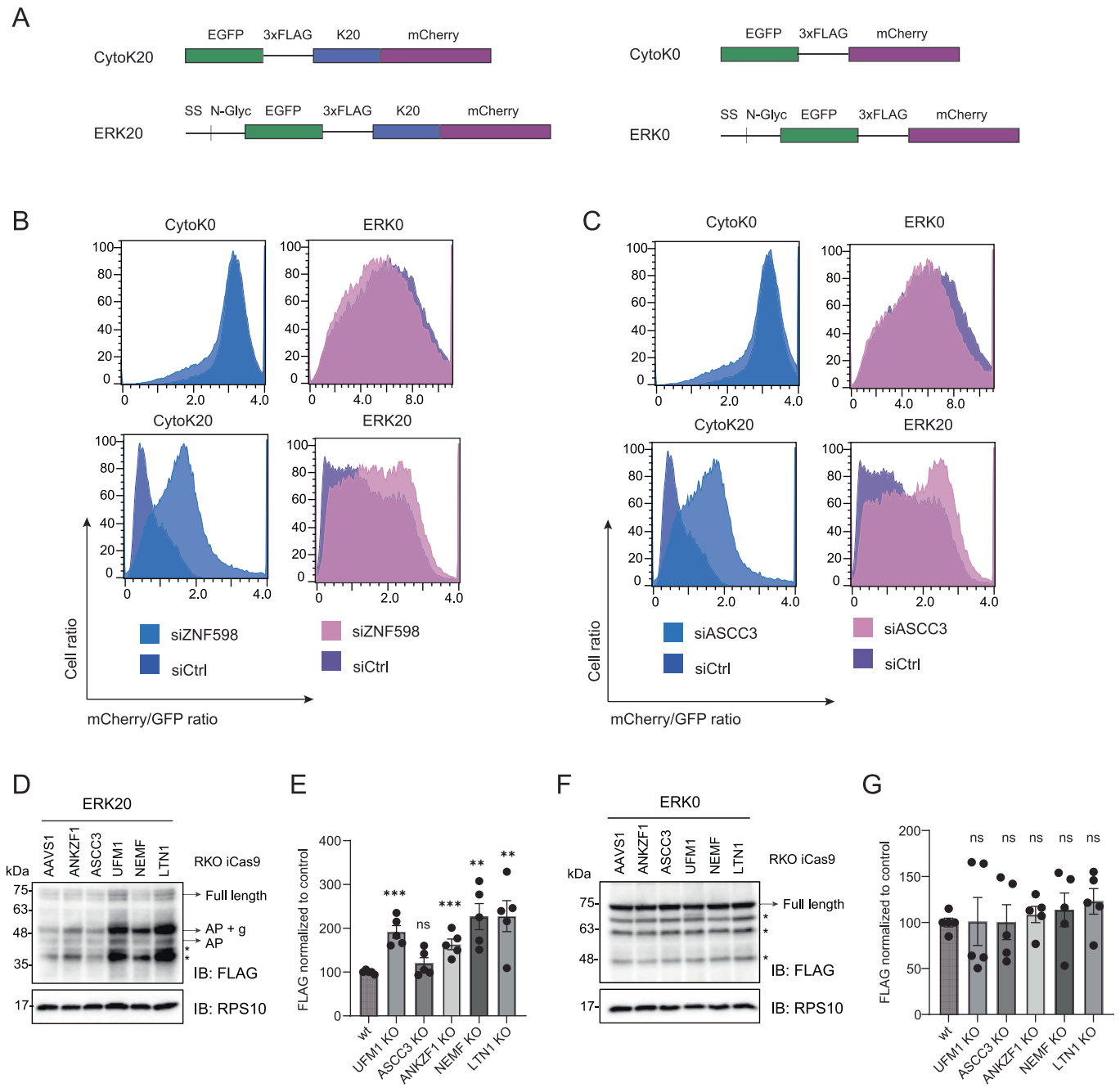



**Figure 2. RQC and UFMylation machinery are needed to clear stalled peptides at the ER.**

**(A)** Schematic representation of control (K0) and stalling (K20) cytosolic and ER reporters. **(B, C)** Readthrough of reporters from **(A)** shown by mCherry/GFP ratio measured by FACS after 24 h expression in HCT116 cells upon siRNA-mediated knockdown of ZNF598 **(B)** or ASCC3 **(C)** compared to non-targeting control siRNA. **(D, F)** Reporter accumulation shown by FLAG immunoblot in RKO iCas9 KO cell lysates upon 48 h dox treatment to induce AAVS1 (non-targeting control), ANKZF1, ASCC3, UFM1, NEMF or LTN1 knockout, upon 24 h ERK20 **(D)** or ERK0 expression **(F)** normalized to RPS10 loading control. **(E)** Quantification of **(D)** with unpaired two-sided Student *t*-test, $n = 5$. Error bars represent standard error of the mean (SEM). $^{****}P \leq 0.0001$, $^{***}P \leq 0.001$, $^{**}P \leq 0{,}01$, $^{*}P \leq 0.05$. List of complete *P* values available in Dataset EV2. **(G)** Quantification of **(F)** with unpaired two-sided Student *t*-test, $n = 5$. Error bars represent SEM. AP arrested peptide, g glycosylation, * degradation products. Source data are available online for this figure.

lysine stretch that mimics translation into polyA tail, and a C-terminal mCherry. In contrast, the cytosolic stalling reporter CytoK20 lacks the ER-targeting signal sequence and glycosylation site, while having the same domain organization and sequence (Fig. 2A). We used siRNA to deplete ZNF598 and ASCC3, a component of the ASC-1 complex (Fig. EV2A) as the depletion of ASCC3 leads to the 80% destabilization of the whole complex (Juszkiewicz et al, 2020). Both the cytosolic (as shown earlier (Juszkiewicz et al, 2018)) and ER stalling reporters exhibited increased readthrough upon loss of ZNF598 and ASCC3 (Fig. 2B,C).

 © The Author(s)

In contrast, control cytosolic CytoK0 and ER-targeted ERK0 reporters, which lack the stalling-inducing poly-lysine sequence, did not show a difference in readthrough upon depletion of the ribosome rescue factors (Fig. 2B,C). Importantly, the loss of Pelota, which acts specifically on ribosomes stalled at the 3'-end of the RNA (Izawa et al, 2012; Guydosh and Green, 2014), did not impact the readthrough of our internal ribosomal stalling reporters, validating our findings (Fig. EV2B). These results suggest that, as observed for cytosolic ribosomes, the ribosome rescue factors ZNF598 and the ASC-1 complex are involved in the recognition and splitting of ribosomes stalled at the ER, indicating that they can access and act on the ER-bound ribosomal pool.

## Both the RQC and the UFMylation machinery clear stalled polypeptides at the ER

After demonstrating that ribosome rescue components are involved in the clearance of ER-stalled ribosomes, we next investigated the interplay among ribosome rescue, RQC, and the UFMylation machinery in the clearance of the model ER stalling substrate, ERK20. To deplete those factors efficiently, we used RKO cell lines that stably express doxycycline-inducible Cas9 (iCas9) (de Almeida et al, 2021). Using lentiviral transduction, we introduced either specific guide RNAs (gRNAs) targeting the ribosome rescue and RQC components (ANKZF1, ASCC3, NEMF, LTN1) or the non-coding control locus AAVS1. In parallel, we used UFM1 iCas9 cells to impair UFMylation. Treatment of cells with doxycycline for 48 h resulted in efficient depletion of the ribosome rescue and RQC factors or UFM1 (96% ANKZF1, 71% ASCC3, 75% NEMF, 69% LTN1, and 93% UFM1, Fig. EV2C). Supporting earlier evidence (Wang et al, 2020; Scavone et al, 2023), the depletion of NEMF, LTN1, and UFM1 significantly stabilized the ER stalling reporter ERK20 (Fig. 2D,E). Moreover, while less efficiently, depletion of ANKZF1 also led to stabilization of ERK20 (Fig. 2D,E). Instead, depletion of ASCC3 did not impact the levels of the ERK20 reporter. This is expected since the ASC-1 complex mediates ribosome splitting, and its depletion results in less efficient stalling and increased read-through. Importantly, depletion of any of these genes did not cause accumulation of the control ER reporter ERK0 (Fig. 2F,G), validating the direct role of these factors on the clearance of arrested polypeptides generated by ribosome stalling at the ER.

Next, we tested the downstream degradation pathway of cytosolic and ER stalling reporters through proteasomal inhibition by MG132 or inhibition of lysosomal degradation by bafilomycin treatment. Both reporters were stabilized by the inhibition of the proteasome and lysosomal degradation machinery. Yet, the proteasomal inhibition showed a higher accumulation of the reporters, indicating its major contribution to their clearance (Fig. EV2D). Taken together, we show that the UFMylation and the RQC machinery are necessary for clearing arrested nascent peptides on stalled ribosomes at the ER.

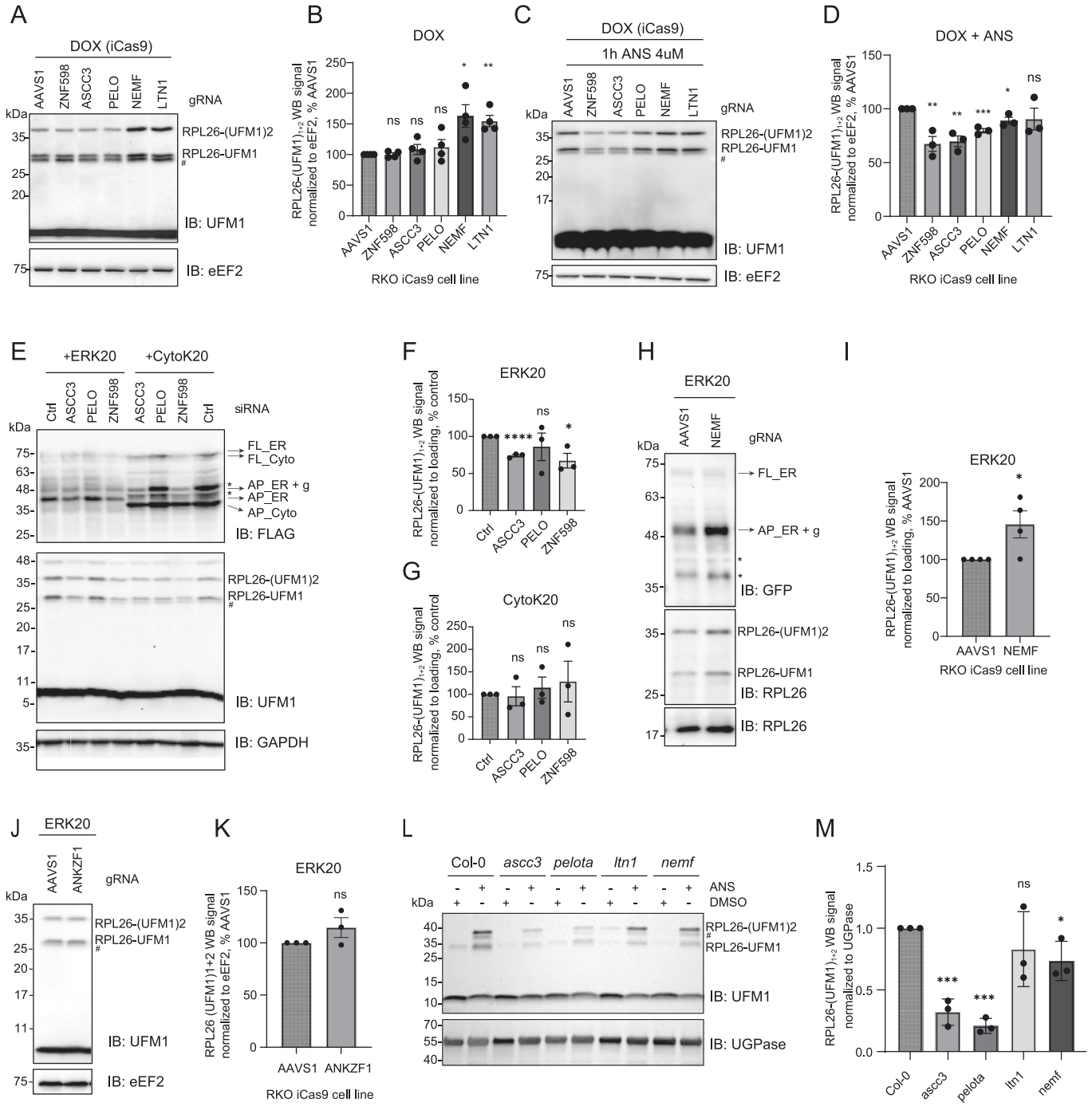
## Recognition and splitting of the ER-stalled ribosomes precedes RPL26 UFMylation

Next, we investigated the crosstalk between the RQC and UFMylation. To reveal the order of events and the interdependence of these pathways, we first assessed whether the loss of ribosome rescue or RQC components impacts UFMylation of the ER-stalled ribosomes. To this end, we used RKO iCas9 cell lines expressing gRNAs against those components (Fig. EV2C). Under steady-state conditions, depletion of ZNF598, ASCC3, or Pelota did not impact UFMylation levels (Figs. 3A, lanes 1–4 and 3B). However, upon ANS treatment, we noticed a significant decrease in UFMylation levels upon depletion of ZNF598, ASCC3, or Pelota compared to control (AAVS1) (Figs. 3C, lanes 1–4 and 3D). These results were corroborated in the HCT116 cell line using siRNA-mediated depletion (Fig. EV3A,B). These data indicate that ribosome splitting is required for UFMylation of ribosomes at RPL26 after ribosomal stalling. Recent work showed that RPL26-UFMylation also occurs after canonical translation termination at the ER, releasing free 60S from the translocon (DaRosa et al, 2024; Makhlouf et al, 2024). We anticipate that RPL26 UFMylation at steady-state conditions is governed by two main events: i. translation termination at the ER following ribosome splitting via translation termination factors, and ii. ribosomal stalling at the ER followed by ribosomal splitting via ASC-1 or Pelota, depending on the type of mRNA lesion. Therefore, the depletion of ASCC3 or ZNF598 has only a partial effect in our assays.

Notably, the depletion of RQC factors NEMF and LTN1, which facilitate ubiquitination and clearance of the nascent chain, increased RPL26 UFMylation levels under steady-state conditions (Figs. 3A, lanes 5, 6 and 3B), suggesting that RQC continuously surveils aberrant translation, supporting earlier work that revealed that LTN1 depletion impacts RPL26 UFMylation in neurons (Endo et al, 2023). We anticipate that depletion of NEMF and LTN1 impairs the clearance of stalled ribosomes at the ER (as shown in Fig. 2D,E), leading to the accumulation of UFMylated 60S-peptidyl-tRNA complex intermediates. Surprisingly, NEMF and LTN1 depletion did not significantly affect RPL26 UFMylation upon ANS treatment (Figs. 3C, lanes 5, 6 and 3D). Compared to steady-state conditions in Fig. 3A, this difference may be due to cell-wide ribosomal stalling induced by ANS treatment, which exhausts the UFMylation machinery. These data suggest that during ANS treatment, the UFMylation machinery operates at capacity; therefore, the depletion of NEMF and LTN1 does not result in a further increase under these conditions.

To dissect these mechanisms in experimental settings differentiating cytosolic and stalled ribosomes at the ER, we tested the effect of their loss in cells expressing the cytosolic or ER stalling reporters ERK20 and CytoK20. As shown before (Wang et al, 2020), while ERK20 expression increased RPL26 UFMylation, CytoK20 did not (Fig. 3E). The siRNA-mediated knockdowns of ZNF598 and ASCC3 resulted in a significant decrease in RPL26 UFMylation levels in cells expressing ERK20, compared to control siRNA, while PELO knockdown did not impact UFMylation (Figs. 3E, lanes 1–4 and 3F). In contrast, cells expressing CytoK20 showed no difference in RPL26-UFMylation levels upon knockdowns of ribosome rescue factors ZNF598 and ASCC3 (Fig. 3E, lanes 5–8 and 3G). Similarly, their depletion did not impact UFMylation levels in cells expressing control ERK0 reporter (Fig. EV3C,D). Therefore, the depletion of ZNF598 and ASC-1 complex decreases UFMylation, specifically in cells expressing ER stalling reporter ERK20. We also noticed an increase in UFMylation upon NEMF depletion in RKO iCas9 cells expressing the ERK20 reporter (Fig. 3H,I), indicating that UFMylation of RPL26 is not dependent on NEMF, consistent with our data showing that

© The Author(s)




NEMF binds to already UFMylated 60S. However, we did not observe a significant increase in RPL26-UFMylation upon ANKZF1 depletion (Fig. 3J,K). This is in contrast to the increased stability of the ERK20 stalling reporter upon ANKZF1 depletion (Fig. 2D), suggesting that deUFMylation of RPL26 might precede ANKZF1-mediated hydrolysis of the peptidyl-tRNA bond.

Given the conservation of the UFMylation system across higher eukaryotes, we next investigated its evolutionary conservation in plants. To this end, we evaluated the effect of RQC machinery on RPL26 UFMylation using *Arabidopsis thaliana* mutant lines. UFMylation levels were assessed upon ANS treatment in *ascc3*, *pelota*, *ltn1*, and *nemf* mutant lines compared to wt (Columbia Col-0 ecotype). Knocking out *ascc3* and *pelota* significantly decreased UFMylation levels upon ANS-induced stalling compared to the wild-type (Fig. 3L,M). Additionally, we noticed a slight decrease in the *nemf* mutant line (Fig. 3L,M). These results confirm our hypothesis that the order of events upon ribosome stalling at the ER is conserved across eukaryotes. Interestingly, in plants, we observed a more substantial effect of Pelota depletion on RPL26 UFMylation than in human cell lines. We speculate that differences in RNase

 © The Author(s)

**Figure 3. RPL26 is UFMylated on post-split 60S subunit upon ribosomal stalling at the ER.**

(**A**, **C**) UFMylation levels visualized by UFM1 immunoblot in RKO iCas9 cells upon 48 h dox treatment to induce RQC components or non-targeting AAVS1 knockout in untreated (**A**) or 1 h 4 μM ANS treated cells (**C**). (**B**) Quantification of (**A**) with unpaired two-sided Student *t*-test, $n = 4$. Error bars represent SEM. (**D**) Quantification of (**C**) with unpaired two-sided Student *t*-test, $n = 3$. Error bars represent SEM. (**E**) UFMylation levels visualized by UFM1 immunoblot in HCT116 cells upon 72 h siRNA-mediated knockdown of RQC components or non-targeting control, and 24 h expression of ERK20 or CytoK20. (**F**, **G**) Quantification of (**E**) for cells expressing ERK20 (**F**) or CytoK20 (**G**) shown by FLAG signal normalized to loading control with unpaired two-sided Student *t*-test, $n = 3$. Error bars represent SEM. (**H**) UFMylation levels visualized by RPL26 immunoblot in RKO iCas9 cells upon 48 h dox treatment to induce non-targeting AAVS1 or NEMF knockout upon 24 h expression of ERK20 reporter. (**I**) Quantification of (**H**) with unpaired two-sided Student *t*-test, $n = 4$. Error bars represent SEM. (**J**) UFMylation levels visualized by UFM1 immunoblot in RKO iCas9 cells upon 48 h dox treatment to induce non-targeting AAVS1 or ANKZF1 knockout upon 24 h expression of ERK20 reporter. (**K**) Quantification of (**J**) with unpaired two-sided Student *t*-test, $n = 3$. Error bars represent SEM. (**L**) Seven-day-old *Arabidopsis* seedlings of wild-type (Col-0) and RQC component mutant (*ascc3*, *pelota*, *ltn1*, *nemf*, *rqc1*, *edf1*) were treated with either DMSO or 100 μM ANS for 16 h. The UFMylation level was tested via immunoblotting using anti-UFM1 antibody, with UGPase was introduced as loading control. The data shown are representative of three biological replicates. (**M**) Quantification of (**L**) for ANS-treated samples with unpaired two-sided Student *t*-test, $n = 3$. Error bars represent standard deviation. $^{****}P \le 0.0001$, $^{***}P \le 0.001$, $^{**}P \le 0.01$, $^{*}P \le 0.05$. List of complete *P* values available in Dataset EV2. FL full length, AP arrested peptide, g glycosylation, # - UFC1-UFM1 complex (Kumar et al, 2021), *degradation products. Source data are available online for this figure.

activity in plants may create 3'-ends, inducing ribosome-stalling that are primarily resolved by Pelota (Yu et al, 2016; Tanaka et al, 2025).

Our data show that RPL26 UFMylation is diminished in the absence of either ZNF598 or ASC-1 complex, suggesting that recognition of collisions (mediated by ZNF598 (Juszkiewicz et al, 2018)) and subsequent ribosome splitting (mediated by ASC-1 complex (Juszkiewicz et al, 2020)) precede and are prerequisites for RPL26 UFMylation. At the same time, the depletion of the RQC components NEMF and LTN1, which are involved in the clearance of the arrested peptides on the 60S, does not impair the UFMylation of RPL26. These results indicate that the nascent polypeptide release is not necessary for the UFM1 E3 ligase complex to access and UFMylate the 60S. Taken together, we mechanistically show that translational stalling at the ER induces UFMylation of post-split 60S-peptidyl-tRNA complexes, and this mechanism is evolutionarily conserved in plants and mammals.

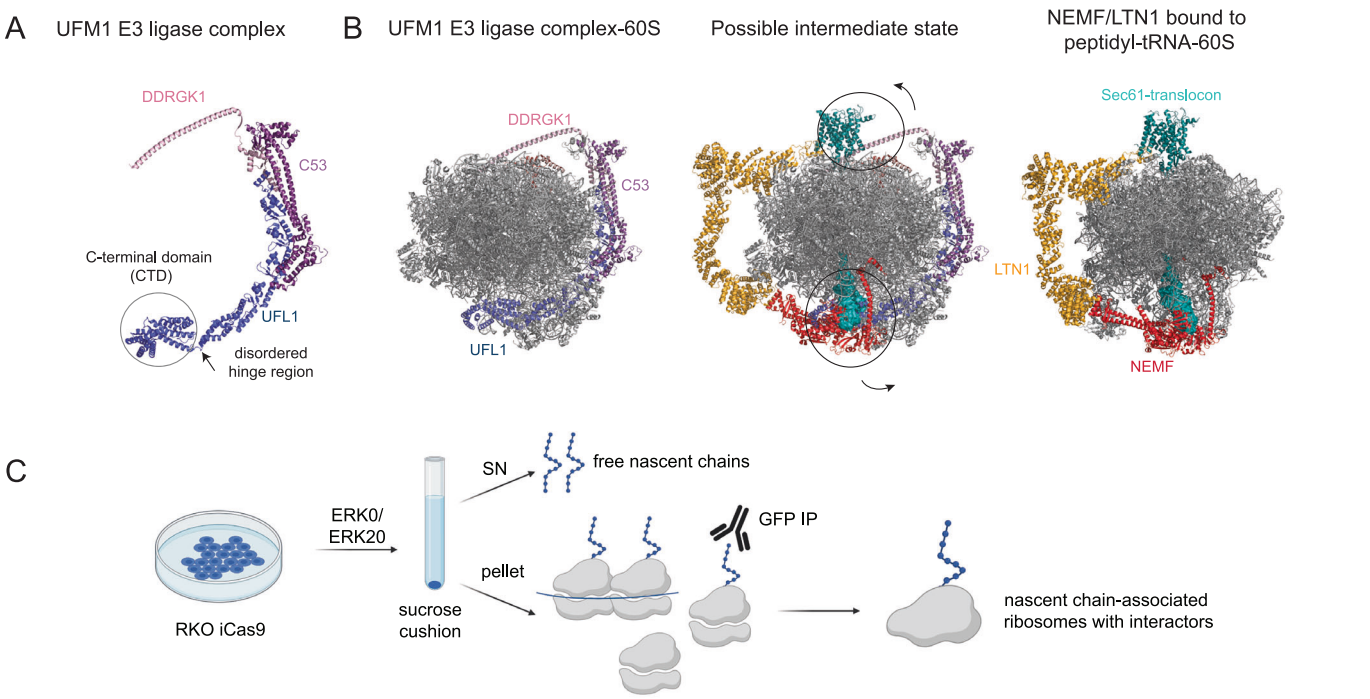
## UFM1 E3 ligase complex binds the nascent chain-associated 60S-peptidyl-tRNA complex at the ER

The cryo-electron microscopy structures of UFM1 E3 ligase complex bound to 60S ribosomes revealed that it forms extensive contacts with the 60S in a clamp-like architecture extending from tRNA-binding sites to the peptide exit tunnel, with all three subunits of the complex contributing to this interaction (DaRosa et al, 2024; Makhlouf et al, 2024). Based on these structures, it was proposed that UFL1 binding blocks the tRNA-binding site, and these two binding events are mutually exclusive. However, those structures cannot explain how the loss of the UFM1 E3 ligase components leads to the accumulation of ER-stalling reporters. Namely, it is not clear how the loss of machinery that only works on post-termination ribosomes could result in the accumulation of the arrested nascent polypeptides (Fig. 2D,E). To this end, we next dissected whether binding of the UFM1 E3 ligase complex occurs before or after nascent chain release from ER-bound 60S subunits.

Depletion of the RQC factors involved in the nascent chain clearance increased UFMylation of RPL26, suggesting that the UFM1 E3 ligase complex can access and UFMylate nascent chain-associated 60S subunits (Fig. 3A,B,L,M). The catalytic component of the UFM1 E3 ligase complex, UFL1, forms the central scaffold of the UFM1 E3 ligase complex and forms extensive contacts with the other two components of the E3 ligase complex and the 60S (DaRosa et al, 2024; Makhlouf et al, 2024). The structural model of UFL1 displays a short N-terminal α-helix followed by one partial winged-helix (pWH), five WH motifs, a bipartite coiled-coil (CC) domain with a disordered region and a C-terminal globular domain (CTD), which contacts the 28S ribosomal RNA (rRNA), occluding all three tRNA-binding sites (Fig. 4A,B) (DaRosa et al, 2024; Makhlouf et al, 2024). Based on our data and data from others (DaRosa et al, 2024; Makhlouf et al, 2024), we hypothesized that the extensive contacts formed between the UFM1 E3 ligase complex and the 60S would allow for sufficient affinity for this interaction to occur even though the tRNA at the P-site is occupied. Notably, the structural models of the UFL1 show that CTD displays a high degree of conformational freedom due to it being connected to the rest of the protein with a disordered segment (Fig. 4A). Overlaying the published structures of 60S ribosomes with UFL1 complex and NEMF/LTN1 shows a possibility of a hybrid state with a possible rearrangement of the CTD of UFL1 and NEMF/LTN1 at the P-site (Fig. 4B). Supporting this, deletion of the CTD of UFL1 does not entirely abolish UFMylation of RPL26 in cells (DaRosa et al, 2024). Therefore, we speculated that UFL1 could undergo conformational rearrangements to enable its binding to the 60S-peptidyl-tRNA complex (Fig. 4B).

To experimentally test this model, we assessed whether the UFM1 E3 ligase complex associates with the 60S-peptidyl-tRNA complex. To this end, we enriched nascent chain-bound ribosomes by immunoprecipitating ER stalling reporter ERK20 or control ER reporter ERK0 in RKO cells (Fig. 4C). To enrich for the ribosome-associated nascent chains, we first isolated ribosomes via sucrose cushions and performed immunoprecipitation (Fig. 4C). We found that UFL1 specifically associates with ERK20 on nascent chain-bound ribosomes, whereas we did not observe UFL1 binding to ERK0 (Fig. 4D). Quantification of three independent replicates showed a significant difference in binding between ERK0 and ERK20, showing that UFL1 binding depends on ribosome stalling at the ER (Fig. 4E). Importantly, we also observed an enrichment of the UFMylated RPL26 in the eluates from ERK20-expressing cells (Fig. 4D, lanes 3–5). These data suggest that the UFM1 E3 ligase complex can bind and actively UFMylate the 60S-peptidyl-tRNA complex with arrested nascent chains at the ER. Similarly, as expected, we found that under those conditions, NEMF specifically associated with ERK20-containing ribosomes, validating our biochemical approach (Fig. 4F,G).

© The Author(s)


A
UFM1 E3 ligase complex
DDRGK1
C53
C-terminal domain (CTD)
UFL1
disordered hinge region
B
UFM1 E3 ligase complex-60S
Possible intermediate state
NEMF/LTN1 bound to peptidyl-tRNA-60S
DDRGK1
C53
UFL1
Sec61-translocon
LTN1
NEMF
C
RKO iCas9
ERK0/ ERK20
sucrose cushion
SN
free nascent chains
pellet
GFP IP
nascent chain-associated ribosomes with interactors
D
Cell lysate
IP: GFP
ERK0
ERK20
ERK20
ERK20 1.5x
ERK0
kDa
75
63
48
35
35
25
17
75
FL_ERK20
FL_ERK0
AP_ER + g
IB: GFP
RPL26-(UFM1)2
RPL26-UFM1
IB: RPL26
IB: RPL26
IB: UFL1
F
Cell lysate
IP: GFP
ERK0
ERK20
ERK0
ERK20
kDa
135
75
63
48
35
35
25
17
17
IB: NEMF
FL_ERK20
FL_ERK0
AP_ERK20 + g
IB: GFP
RPL26-(UFM1)2
RPL26-UFM1
IB: RPL26
IB: RPL26
IB: RPS10
H
Ribosomal pellet
IP:GFP
ERK20
ERK20
AAVS1
NEMF
UFM1
AAVS1
NEMF
UFM1
kDa
75
63
48
35
35
25
17
180
75
FL_ER
AP_ER + g
IB: GFP
RPL26-(UFM1)2
RPL26-UFM1
IB: RPL26
IB: RPL26
IB: LTN1
IB: UFL1
E
UFL1 association
UFL1/GFP signal normalized to ERK20
150
100
50
0
**
ERK20
ERK0
Reporter
G
NEMF association
NEMF/GFP signal, % ERK20 DMSO
150
100
50
0
**
ERK0
ERK20
Reporter
I
UFL1 association
UFL1/GFP signal, normalized to AAVS1 KO
150
100
50
0
ns
ns
AAVS1 KO
NEMF KO
UFM1 KO
J
LTN1 association
LTN1/GFP signal, normalized to AAVS1 KO
150
100
50
0
**
***
AAVS1 KO
NEMF KO
UFM1 KO


© The Author(s)

**Figure 4. UFL1 UFMylates nascent chain-bound 60S subunits.**

**(A)** The cryostructural model of UFM1 E3 ligase complexes shows flexibility around the CTD region of UFL1 (pbd: 8ohd). **(B)** Left: The structure of UFM1 E3 ligase complex bound to 60S subunit (pbd: 8ohd), right: the structure of NEMF/LTN1 complex bound to peptidyl-tRNA-60S complex (pdb: 3j92, 8agw) docked on translocon (pdb:3j7r), middle: overlay of two structures shows a possible hybrid state with conformational rearrangements of UFL1 and DDRGK1. **(C)** Experimental approach for detecting interactors of nascent chain-associated ribosomes. **(D)** Ribosomal pellet was obtained by sucrose cushion centrifugation followed by GFP immunoprecipitation from RKO iCas9 parental cell line upon 24 h expression of ERK0 or ERK20 reporter. Protein levels are analyzed by immunoblotting. **(E)** Quantification of UFL1 association normalized to eluate nascent chain levels from **(D)** with unpaired two-sided Student *t*-test, $n = 3$. Error bars represent SEM. **(F)** Ribosomal pellet was obtained by sucrose cushion centrifugation followed by GFP immunoprecipitation from RKO iCas9 AAVS1 (non-targeting control) cell line upon 24 h expression of ERK0 or ERK20 reporter. Protein levels are analyzed by immunoblotting. **(G)** Quantification of NEMF association normalized to eluate nascent chain levels from **(I)** with unpaired two-sided Student *t*-test, $n = 3$. Error bars represent SEM. **(H)** Ribosomal pellet was obtained by sucrose cushion centrifugation followed by GFP immunoprecipitation from RKO iCas9 AAVS1 (non-targeting control), NEMF or UFM1 KO cell line upon 24 h expression of ERK20 reporter. Protein levels are analyzed by immunoblotting. **(I)** Quantification of UFL1 association normalized to eluate nascent chain levels from **(H)** with unpaired two-sided Student *t*-test, $n = 3$. Error bars represent SEM. **(J)** Quantification of LTN1 association normalized to eluate nascent chain levels from **(H)** with unpaired two-sided Student *t*-test, $n = 3$. Error bars represent SEM. $^{****}P \leq 0.0001$, $^{***}P \leq 0.001$, $^{**}P \leq 0.01$, $^{*}P \leq 0.05$. List of complete *P* values available in Dataset EV2. FL full length, AP arrested peptide, # - UFC1-UFM1 complex (Kumar et al, 2021), * degradation products. Source data are available online for this figure.

To assess whether the association of NEMF/LTN1 with the 60S is required for UFL1 binding to the 60S-peptidyl-tRNA complex at the ER, we conducted similar experiments upon NEMF depletion in RKO iCas9 cells expressing ERK20 reporter (Fig. 4C). The IP analyses showed that UFL1 binding was unaffected by NEMF depletion, supporting the evidence that UFMylation precedes the activity of the late RQC components (Fig. 4H,I). Notably, upon NEMF depletion, EK20 pulldowns displayed higher levels of UFMylated RPL26, further supporting our model that the UFM1 E3 ligase complex binds to and UFMylates the 60S-peptidyl-tRNA complex before nascent chain release (Fig. 4H, lanes 4, 5). The UFM1 depletion did not impair the association of UFL1 with ERK20-expressing ribosomes, indicating that UFMylation of RPL26 does not largely stabilize UFL1 binding (Figs. 4H, lanes 4, 6 and 4I). We also noticed a NEMF-dependent association of LTN1 to the 60S-peptidyl-tRNA complexes for ER-stalled ribosomes (Fig. 4H,J), in accordance with previous data shown for cytosolic stalled ribosomes (Shao et al, 2015). Interestingly, we discovered that LTN1 binding decreases upon UFM1 KO for ER-stalled ribosomes (Fig. 4H,J). These data indicate that the UFM1 E3 ligase complex facilitates the binding of RQC components to the 60S peptidyl-tRNA at the ER. We envision that, as shown for the empty 60S-translocon interaction (DaRosa et al, 2024; Makhlouf et al, 2024), the UFMylation machinery destabilizes the translocon-60S interface. This would facilitate LTN1's access to the nascent chain and would allow positioning of LTN1's C-terminus, which contains the RING domain, in its canonical binding site near the exit tunnel. This thereby stabilizes LTN1's interaction with the complex (Fig. 4B).

This model predicts that impairment of RPL26 UFMylation would reduce LTN1's access to nascent chains and diminish LTN1-mediated ubiquitination of arrested polypeptides. To test whether impairing UFMylation affects LTN1-mediated ubiquitination of arrested polypeptides, we used tandem ubiquitin-binding entity (TUBE) pulldowns under control conditions and upon UFM1 or LTN1 depletion. In these assays, we expressed either the ERK0 control or the ERK20 stalling reporter, then enriched for ubiquitinated proteins using TUBEs. Surprisingly, those assays showed no consistent decrease in ERK20 ubiquitination upon depletion of either UFM1 or LTN1, under both steady-state conditions and in the presence of proteasome inhibitors (Figs. 5A,B and EV4A–D). Given the clear accumulation of ERK20 upon depletion of LTN1 and UFM1, we speculate that other ER-localized E3 ligases might ubiquitinate the ER stalling reporter when canonical clearance mechanisms are impaired, thereby masking the effects of LTN1 or the UFM1 machinery. An unbiased genome-wide genetic screen that used accumulation of an ER-stalling reporter as a readout identified LTN1 as one of the top hits but did not identify any other well-characterized ER-localized E3 ligases (Wang et al, 2023). Similarly, depletion of different E3 ligases involved in ER-associated degradation (ERAD) does not stabilize ER-stalling reporters in either mammals or yeast (Scavone et al, 2023; Crowder et al, 2015). Altogether, these data converge on the model that while other E3 ligases might ubiquitinate stalled polypeptides at the ER, the RQC is the primary path for nascent chain degradation upon ribosomal stalling at the ER.

## DeUFMylation of RPL26 is not required for LTN1 binding

Recent structures of the UFM1 E3 ligase in complex with empty 60S suggested that upon UFMylation of RPL26, the UFM1 E3 ligase complex associates more stably with the 60S and deUFMylation of RPL26 is required for the disassembly of the UFM1 E3 ligase from the 60S ribosomal subunit (DaRosa et al, 2024; Makhlouf et al, 2024). We wondered whether deUFMylation is necessary for LTN1 association with the 60S-peptidyl-tRNA complex. To test this, we compared association of LTN1 with 60S-peptidyl-tRNA complexes under control conditions and upon depletion of deUFMylase UFSP2 using nascent chain pulldowns. To avoid adaptation of cells to long-term depletion of UFSP2, we used the iCas9 system. As expected, depletion of UFSP2 led to increased levels of UFMylated RPL26 (Fig. 5C). However, we did not observe a significant impact of UFSP2 depletion on LTN1 association with the 60S-peptidyl-tRNA complex, indicating that deUFMylation is not necessary for LTN1 association (Fig. 5C–E).

In summary, our data suggest that the UFM1 E3 ligase complex binds to the 60S-peptidyl-tRNA complexes after ribosome splitting at the ER. The spatial proximity of the ER-tethered UFM1 E3 ligase allows it to access the post-split ribosomes at the ER to perform UFMylation. This interaction does not depend on the binding of RQC components (NEMF/LTN1 complex), suggesting that it can precede RQC binding. Instead, RPL26 UFMylation facilitates the subsequent association of the RQC machinery with 60S-peptidyl-tRNA complexes, allowing the clearance of arrested polypeptides on ER-stalled ribosomes.

© The Author(s)

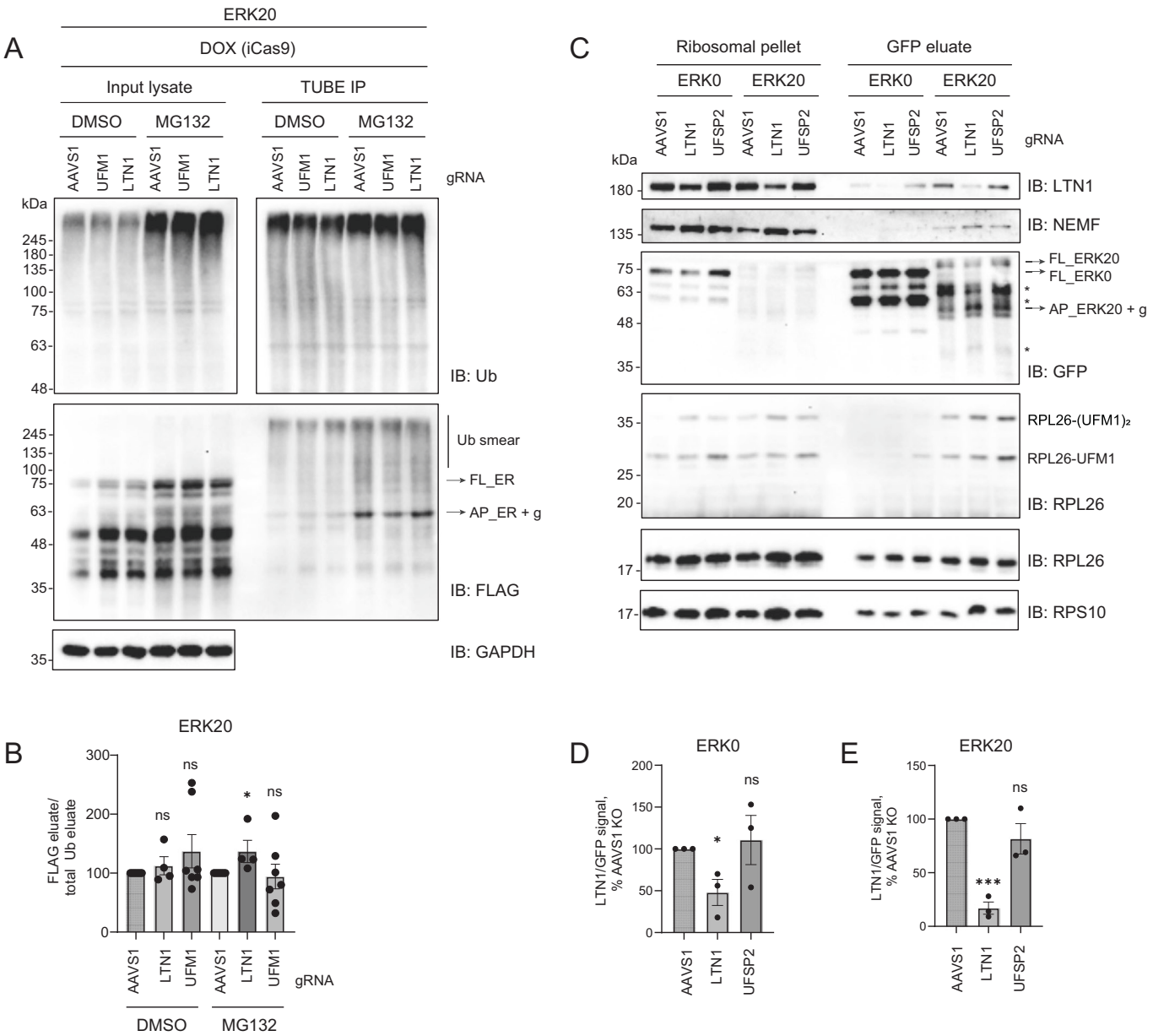



**Figure 5. UFSP2 does not impact LTN1 binding to 60S-peptidyl-tRNA complexes.**

(**A**) TUBE assays were performed from RKO iCas9 AAVS1 (non-targeting control), LTN1 or UFM1 KO cell line upon 24 h expression of ERK20 reporter and 3 h treatment with 20 μM proteasome inhibitor MG132 or DMSO as control. Protein levels are analyzed by immunoblotting. (**B**) Quantification of (A) with unpaired two-sided Student *t*-test, $n = 7$. Error bars represent SEM. (**C**) Ribosomal pellet was obtained by sucrose cushion centrifugation followed by GFP immunoprecipitation from RKO iCas9 AAVS1 (non-targeting control), LTN1 or UFSP2 KO cell line upon 24 h expression of ERK0 or ERK20 reporter. Protein levels are analyzed by immunoblotting. (**D**, **E**) Quantification of LTN1 association normalized to eluate nascent chain levels from (**C**) for cells expressing ERK0 (**D**), or ERK20 (**E**) with unpaired two-sided Student *t*-test, $n = 3$. Error bars represent SEM ****$P \le 0.0001$, ***$P \le 0.001$, **$P \le 0.01$, *$P \le 0.05$. List of complete *P* values available in Dataset EV2. FL full length, AP arrested peptide, g glycosylation, * degradation products. Source data are available online for this figure.

## Discussion

The best-described substrate of the UFMylation machinery is the large ribosomal subunit protein RPL26, initially discovered to be increasingly UFMylated upon ribosomal stalling at the ER (Wang et al, 2020; Walczak et al, 2019). However, the primary function of this event has remained poorly understood. Recent cryo-EM structures uncovered a novel function of the UFMylation machinery in recycling the 60S subunits after translational termination at the ER by releasing them from the translocon (DaRosa et al, 2024; Makhlouf et al, 2024). These structures also showed that UFL1 occupies the tRNA binding sites at the 60S, suggesting that the UFM1 E3 ligase binds to 60S after translation termination (DaRosa et al, 2024; Makhlouf et al, 2024). Therefore, the role of UFMylation in clearing the nascent polypeptides arrested at the ER-stalled ribosomes remained unclear.

 © The Author(s)

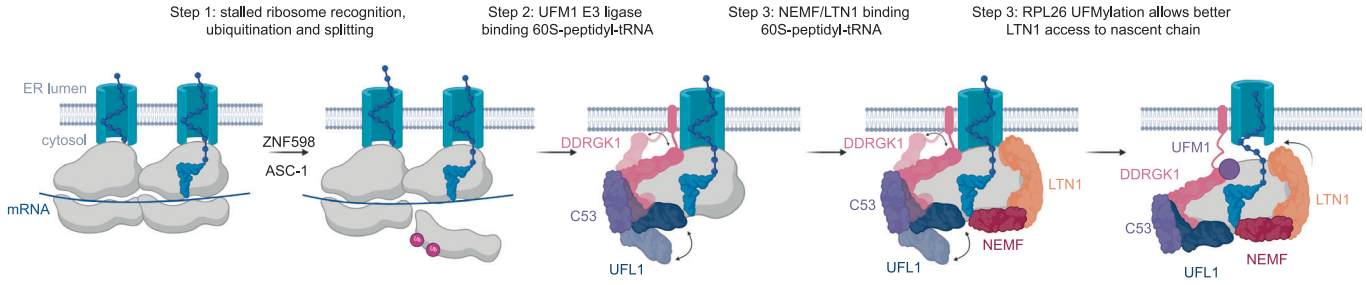



**Figure 6. UFMylation machinery acts together with RQC to clear arrested peptides at the ER.**

Upon ribosomal stalling at the ER, ZNF598 recognizes and ubiquitinates 40S proteins, followed by ASC-1 complex-mediated splitting of the leading ribosome. The 60S-peptidyl-tRNA complex is recognized and UFMylated by the UFM1 E3 ligase complex, independently of downstream RQC factors. NEMF binds UFMylated 60S-peptidyl-tRNA complexes and brings in LTN1. UFMylation-induced translocon release from 60S-peptidyl-tRNA complexes allows LTN1 to access the nascent chain. LTN1 then ubiquitinates the arrested nascent chains. The nascent chain is released and subsequently degraded by the proteasome, while the 60S subunit is recycled.

Here, using IP analyses coupled to MS and Western blotting, we found that the RQC components are associated with the UFMylated ribosomes, indicating a direct physical link between these two pathways (Fig. 1A–E). To confirm the role of RQC factors in clearing the nascent polypeptides arrested at the ER-stalled ribosomes, we used genetic depletion of ribosome rescue and RQC machinery and found that ribosomes stalled upon ERK20 expression recruit the RQC E3 ligase ZNF598 and the ribosome-splitting factor ASC-1 complex (Figs. 2B,C and 3E,F). Similar to RQC events upon cytosolic stalling, the stalled ribosomes at the ER required the activity of ANKZF1, NEMF and LTN1 for clearance of arrested polypeptides since the loss of these components stabilized the ER stalling reporter (Fig. 2D,E and 3H,I). Likewise, impaired UFMylation specifically stabilized ERK20 substrate, in line with the published work (Fig. 2D,E) (Wang et al, 2020), indicating that both the RQC and the UFMylation machinery are involved in the clearance of the arrested polypeptides at the ER.

After demonstrating the role of the RQC and the UFMylation machinery in the clearance of the nascent chains arrested at the ER-stalled ribosomes, we assessed the sequence of events and interdependence of these pathways by testing the impact of the loss of ribosome rescue and RQC factors on RPL26 UFMylation upon ribosome stalling. The RPL26 UFMylation levels decreased upon knockdown or knockout of ZNF598 or ASCC3 in cells treated with anisomycin, a drug inducing ribosomal stalling (Figs. 3C,D and EV3A,B) as well as upon expression of the specific ER stalling reporter ERK20 (Fig. 3E,F). Experiments performed in plants (*Arabidopsis thaliana*) validated those findings (Fig. 3L,M), confirming that UFMylation happens on post-split 60S ribosomes upon ribosomal stalling at the ER and that this mechanism is conserved from plants to mammals.

Previous structural data showed that UFL1 binds to the 60S ribosomal subunit in a way that clashes with the binding of the 40S subunit, translocon, or tRNA (DaRosa et al, 2024; Makhlouf et al, 2024). These data cannot be reconciled with the data showing increased UFMylation of RPL26 upon ribosome stalling. We showed that UFL1 associates with 60S subunits upon translation of the ER stalling reporter ERK20, but not the ER-targeted control reporter ERK0 (Fig. 4D,E). Immunoprecipitation of the ribosome-attached ERK20 stalling reporter showed that these ribosomes were already UFMylated at RPL26, demonstrating that UFM1 E3 ligase can act on nascent chain-loaded ribosomes with occupied tRNA at the P-site, contradicting the previous model (Fig. 4D,E) (DaRosa et al, 2024; Makhlouf et al, 2024). Supporting our findings, single particle cryo-electron microscopy studies of the native UFM1 E3 ligase complexes isolated from cells showed a small population of 60S with a weak extra density in the peptide exit tunnel, which could represent a nascent polypeptide chain (DaRosa et al, 2024). Importantly, the depletion of NEMF did not impact UFL1 binding to the nascent chain-containing 60S-peptidyl-tRNA complexes (Fig. 4H,I). In line with those results, we readily detected UFMylated RPL26 in the nascent chain immunoprecipitates from NEMF KO cells, showing that UFMylation does not depend on NEMF activity. Instead, NEMF depletion led to the accumulation of stalled ribosomes at the ER, observed by increased RPL26 UFMylation (Fig. 4H). These results indicated that UFMylation occurs before the clearance of the arrested polypeptides. To sum up, we found that the 60S-peptidyl-tRNA complex formed upon ribosome splitting is a canonical substrate for UFM1 E3 ligase complex and that the NEMF/LTN1-dependent release of the nascent chain is not necessary for RPL26 UFMylation. Instead, NEMF/LTN1 binds to the UFMylated ribosomes to clear arrested nascent chains and complete the ribosome rescue and RQC cycle. Supporting our findings, during the revision of our manuscript, a single-particle cryo-EM structure was published, demonstrating that the UFM1 E3 ligase complex associates with NEMF and LTN1 (Penchev et al, 2025). Notably, the structure revealed that the CTD of UFL1 adopts a novel conformation to allow its binding to the 60S-peptidyl-tRNA complex and NEMF (Penchev et al, 2025). Our data and those of others show that cells evolved intricate coordination between two distinct quality control pathways to enable efficient clearance of stalled polypeptides at the ER.

On cytosolic ribosomes, LTN1 binds close to the ribosome exit tunnel in proximity to the stalled nascent polypeptides emerging from the ribosome (Shao et al, 2015). On the ER-bound ribosomes, the exit tunnel is occupied by the translocon (Lewis et al, 2024; Voorhees et al, 2014). The LTN1 was proposed to access arrested polypeptides via their exposure to the cytosol by a gap at the ribosome-translocon contact site (von der Malsburg et al, 2015). As impaired UFMylation stabilizes the arrested nascent chains (Fig. 2D,E), and diminishes the binding of LTN1 to 60S at the ER (Fig. 4H,J), we speculate that, similar to what has been proposed

© The Author(s)

for the post-termination empty 60S subunits (DaRosa et al, 2024; Makhlouf et al, 2024), binding of the UFM1 E3 ligase complex destabilizes the 60S-translocon interactions and allows the E3 ligase LTN1 to access the arrested nascent chain for ubiquitination and subsequent degradation (Fig. 4B).

Both the ubiquitin-proteosome system and lysosomal degradation were proposed to be involved in the clearance of stalled nascent peptides at the ER (Wang et al, 2020; Stephani et al, 2020; Scavone et al, 2023). Notably, the previous work on the ERK20 reporter used here showed that it is mainly degraded by lysosomes and neither proteosome inhibition nor NEMF depletion stabilized the reporter (Wang et al, 2020). However, we show a clear stabilization of the same reporter preferentially by proteosome inhibition (Fig. EV2D), and NEMF depletion (Fig. 2D,E). Supporting our results, an alternative ER stalling reporter containing a folded VHP domain and a poly-lysine stretch was degraded primarily by the proteasome and showed NEMF-dependent stabilization (Scavone et al, 2023). We therefore conclude that while the RQC and ubiquitin-proteasome system play the major role in clearing stalled ribosomes, depending on the cell type and expression levels, arrested polypeptides at the ER can be cleared by complementary degradation pathways, including ER-phagy and lysosomal pathways (Inada and Beckmann, 2024; Bengtson and Joazeiro, 2010; Wang et al, 2020; Stephani et al, 2020).

Altogether, our data converge on the following model: stalling of the ER-bound ribosomes recruits canonical ribosome rescue and ribosome-associated quality control machinery. First, the E3 ligase ZNF598 recognizes the collided ribosomes and stabilizes them by ubiquitinating small subunit proteins (Juszkiewicz et al, 2018). This is followed by the binding of the ASC-1 complex that splits the leading ribosome, leaving a 60S-peptidyl-tRNA complex (Fig. 6). The 60S-peptidyl-tRNA complex is then recognized and UFMylated by the UFM1 E3 ligase complex. The association of the UFM1 E3 ligase complex destabilizes 60S-peptidyl-tRNA-translocon interactions, allowing the RQC components NEMF and LTN1 to bind and access the nascent chain, which is ubiquitinated and targeted for downstream proteasomal degradation to restore cellular proteostasis. This process shows high evolutionary conservation in plants and mammals. Our work highlights a fine collaboration between two distinct processes to maintain translational fidelity by overcoming the unique challenges posed by the spatial separation of arrested nascent chains from the ribosome at the ER.

## Methods

**Reagents and tools table**

| Reagent/resource | Reference or source | Identifier or catalog number |
|---|---|---|
| **Experimental models** | | |
| RKO-Dox-Cas9 (iCas9) | Hornegger et al, 2024, de Almeida et al, 2021 | |
| RKO-Dox-Cas9 (iCas9) 3xFLAG-UFM1 | This study | |
| RKO-Dox-Cas9 (iCas9) PELO KO | This study | |
| RKO-Dox-Cas9 (iCas9) LTN1 KO | This study | |
| RKO-Dox-Cas9 (iCas9) NEMF KO | This study | |
| RKO-Dox-Cas9 (iCas9) ASCC3 KO | This study | |
| RKO-Dox-Cas9 (iCas9) ZNF598 KO | This study | |
| RKO-Dox-Cas9 (iCas9) UFM1 KO | This study | |
| RKO-Dox-Cas9 (iCas9) ANKFZ1 KO | This study | |
| RKO-Dox-Cas9 (iCas9) UFSP2 KO | This study | |
| HCT116 tetON OsTIR1 | Natsume et al, 2016 | |
| HCT116 tetON OsTIR1 3xFLAG-UFM1 | This study | |
| HEK293T cells | Shotaro Otsuka lab | CRL-11268 (ATCC) |
| HEK293T splitGFP parental | Leonetti et al, 2016 | |
| HEK293T Sec61β splitGFP | Leonetti et al, 2016 | |
| *ascc3* mutant (*A. thaliana*) | NASC | AT5G61140 |
| *pelota* mutant (*A. thaliana*) | NASC | AT4G27650 |
| *nemf* mutant (*A. thaliana*) | NASC | AT5G49930 |
| *ltn1* mutant (*A. thaliana*) | NASC | AT5G58410 |
| **Recombinant DNA** | | |
| Hygro-P2A-mAID-mClover | Addgene | #121179 |
| BSD-P2A-3xFLAG HDR | This study | |
| Hygro-P2A-3xFLAG HDR | This study | |
| Dual-sgRNA_hU6-mU6 | de Almeida et al, 2021 | |
| pSpCas9 (BB)-2A-GFP (PX458) | Addgene | Cat #48138 |
| 6His-TEVb-HaloTR-TUBE | MRC PPU Dundee | Cat #DU23799 |
| CytoK0 | Wang et al, 2020 | |
| CytoK20 | Wang et al, 2020 | |
| ERK0 | Wang et al, 2020 | |
| ERK20 | Wang et al, 2020 | |
| **Antibodies** | | |
| Rabbit anti-ANKZF1 | Proteintech | 20447-1-AP |
| Rabbit anti-ASCC3 | Bethyl laboratories | A304-014A-T |
| Rabbit anti-DDRGK1 | Proteintech | 21445-1-AP |
| Rabbit anti-eEF2 | Proteintech | 20107-1-AP |
| Mouse anti-FLAG | Sigma | F1804-5MG |


© The Author(s)

| Reagent/resource | Reference or source | Identifier or catalog number |
|---|---|---|
| Rabbit anti-GAPDH | Proteintech | 10494-1-AP |
| Mouse anti-GFP | Roche | 11814460001 |
| Rabbit anti-LTN1 | Proteintech | 28452-1-AP |
| Rabbit anti-NEMF | Proteintech | 11840-1-AP |
| Rabbit anti-Pelota | Proteintech | 10582-1-AP |
| Rabbit anti-RPL26 | Abcam | ab59567 |
| Rabbit anti-RPS10 | Abcam | ab151550 |
| Rabbit anti-RPS20 | Abcam | ab133776 [EPR8716] |
| Rabbit anti-RPS3 | Proteintech | 11990-1-AP |
| Mouse anti-Sec61α | Santa Cruz | sc-393182 sample |
| Mouse anti-Ub | Santa Cruz | sc-8017 |
| Rabbit anti-UFL1 | Proteintech | 26087-1-AP |
| Rabbit anti-UFM1 | Abcam | ab109305 |
| Rabbit anti-UGPase | Agrisera | AS14 2813 |
| Mouse anti-Vinculin | Proteintech | 6305-1-Ig |
| Rabbit anti-ZNF598 | Sigma-Aldrich | HPA041760-25UL |
| **Oligonucleotides and other sequence-based reagents** | | |
| Single guide RNAs | This study | Dataset EV2 |
| Primers | This study | Dataset EV2 |
| ASCC3 siRNA | Dharmacon | L-012757-01-0005 |
| PELO siRNA | Dharmacon | L-019068-01-0005 |
| ZNF598 siRNA | Dharmacon | L-007104-00-0005 |
| Control siRNA | Dharmacon | D-001810-10-05 |
| **Chemicals, enzymes and other reagents** | | |
| digitonin | Carl Roth | 4005.4 |
| Anisomycin | Sigma-Aldrich | A9789-5MG |
| Doxycycline | Sigma-Aldrich | D5207-5G |
| MG132 | Santa Cruz Biotechnology | sc-201270 |
| Bafilomycin A1 | Szabo Scandic | AVIOOMC00028-1 |
| **Software** | | |
| GraphPad Prism 10 | https://www.graphpad.com/ | |
| Adobe Illustrator 2023 | https://www.adobe.com/products/illustrator.html | |
| BioRender | https://www.biorender.com/ | |
| FlowJo v10.9.0 | https://www.flowjo.com/ | |
| Pymol v 3.1.5.1 | https://www.pymol.org/ | |
| **Other** | | |
| Dynabeads™ Protein G | Invitrogen | 10004D |
| GFP-Trap® Magnetic Particles | ChromoTek | gtma-20 |
| Magne® HaloTag® Beads | Promega | G7281 |

## Mammalian cell culture

HCT116 tetON (doxycycline-inducible) OsTIR1 cells obtained the Masato Kanemaki lab (Natsume et al, 2016) were cultured in McCoy's 5 A (modified) medium (Sigma, M9309) supplemented with 10% fetal bovine serum (Gibco, 10437028), 2 mM L-Glutamine (Sigma, G7513), 1% Pen/Step (Sigma, P0781). RKO-Dox-Cas9 cells (expressing doxycycline-inducible Cas9), a kind gift from from Johannes Zuber lab (de Almeida et al, 2021) were cultured in RPMI-1640 media (Sigma, R8758) supplemented with 10% fetal bovine serum (Gibco, 10437028), 2 mM L-Glutamine (Sigma, G7513), 1% Pen/Step (Sigma, P0781), 1× non-essential amino acids (Thermo Scientific, 11140050), and 1 mM sodium pyruvate (Gibco, 11360070). HEK293T cells, a kind gift from Shotaro Otsuka lab, were cultured in DMEM medium (Sigma, D5796) supplemented with 10% fetal bovine serum (Gibco, 10437028), 2 mM L-Glutamine (Sigma, G7513), 1% Pen/Step (Sigma, P0781). Cell lines were grown in a humidified incubator at 37 °C and 5% $CO_2$. All cell lines were regularly tested for *Mycoplasma* infection with the EZ-PCR™ Mycoplasma Detection Kit (Biological Industries).

## Mammalian cell line generation

RKO-Dox-Cas9 (iCas9) cell lines for doxycycline inducible knock-out of the genes encoding RQC components were established using lentiviral transduction with lentiviral particles (produced as described in (Hornegger et al, 2024) containing Dual-sgRNA_hU6-mU6 vectors described in (de Almeida et al, 2021) expressing two sgRNAs (Dataset EV2) from human and mouse U6 promoters and eBFP2 from a PGK promoter. The eBFP2-positive cells were FACS sorted at BD FACSMelody™ Cell Sorter at Max Perutz Labs BioOptics FACS Facility.

To endogenously tag UFM1 with N-terminal 3xFLAG sequence human UFM1 N-terminal homology arms sequence was amplified using HindIII_UFM1_N_HAs_F and XhoI_UFM1_N_HAs_R primers. The UFM1 homology arms were inserted into the pMK344 plasmid backbone (Addgene #121179) using HindIII and XhoI restriction sites. To remove the BamHI site the plasmid was treated with HindIII and XbaI restriction enzymes and ligated through annealed overlapping oligos (pMK344_oligo_HindIII_XbaI_F/R). The BamHI and SalI restriction sites were introduced to the homology arms using BamHI_UFM1_N-HA and SalI_UFM1_N-HA primers. The BSD-P2A-3xFLAG sequence was cloned using the pMK347 (BSD-P2A-mAID) plasmid (Addgene #121181) which was digested with the Esp3I and BamHI enzymes to remove P2A-mAID and ligated using P2A-3xFLAG template made from annealed oligos (3xFLAG_pMK347_F/R) with cohesive ends. The BSD-P2A-3xFLAG sequence was inserted into the plasmid with N-terminal homology arms of UFM1 using SalI and BamI restriction sites resulting in the HDR template. The PAM sites were mutated in the HDR template using site-directed mutagenesis with a primer pair UFM1_gRNA_517_PAM_mut_F/R. To clone the Hygro-P2A-3xFLAG HDR template Hygro-P2A-3xFLAG was amplified from pMK344 with KS_F and P2A_3xFLAG_BamHI_R primers and cloned to replace the BSD-P2A-3xFLAG in the final UFM1 HDR template with mutated PAM sites. All primer sequences are listed in Dataset EV2.

© The Author(s)

To introduce the 3xFLAG tag to the N-terminus of the endogenous UFM1 HCT116 tetON OsTIR1 (Natsume et al, 2016) or RKO-Dox-Cas9 (iCas9) (Hornegger et al, 2024) cells were transiently transfected with 1:1:2 ratio mixture of the BSD-P2A-3xFLAG HDR, Hygro-P2A-3xFLAG HDR template plasmids and pSpCas9 (BB)-2A-GFP (PX458) (plasmid #48138, Addgene) (Ran et al, 2013) targeting the first exon of the UFM1 gene (Dataset EV2) using the Fugene HD (Promega) reagent according to the manufacturer's instructions. 24 h after transfection cell were collected by trypsinization and plated in 1:200 dilution in standard culture media (McCoy's 5 A (modified) with 10% FBS, 2 mM L-Glutamine, 1% Pen/Step). On the next day the media was supplemented with 100 µg/mL of Hygromycin B Gold (InvivoGen, #ant-hg) and 10 µg/mL of Blasticidin S Hydrochloride (InvivoGen, #ant-bl-05). Cells were grown in selection media until visible colonies were formed and expanded in 96-well plates. The homozygous insertion was verified using western blotting with anti-UFM1 (ab108062, Abcam) and anti-GAPDH (10494-1-AP, Proteintech) antibodies and genotyped using DirectPCR Lysis-Reagent Cell (Peqlab, VWR) with hsUFM1_HAs_F, hsUFM1_HAs_R, HygR_F, and BSDR_F primers.

## Co-immunoprecipitation mass spectrometry of 3xFLAG-UFM1

### *Sample processing*

For MS analysis of 3xFLAG-UFM1 co-immunoprecipitation (co-IP), four ⌀15 cm dishes of ~80% confluent 3xFLAG-UFM1 HCT116 cells per condition were used. Media was changed 16 h before collection. Ribosome stalling was induced with 200 nM anisomycin for 1 h. Cells were washed with warm PBS + 100 µg/mL cycloheximide (CHX), lysed on ice in buffer (20 mM HEPES pH 7.3, 120 mM KCl, 15 mM $MgCl_2$, 1.5% digitonin, 100 mg/mL CHX, 0.5 mM DTT, 1x protease inhibitor Roche), scraped, and incubated on ice with vortexing. Lysates were passed through a 27 G needle and centrifuged (20,000× *g*, 20 min, 4 °C). Clarified lysates (2.55 mL) were layered onto 850 µL of 25% sucrose cushions and centrifuged (100,000× *g*, 1.5 h, 4 °C, TLA100.3 rotor). Ribosomal pellets were resuspended in 1 mL of lysis buffer (20 mM HEPES pH 7.3, 120 mM KCl, 15 mM $MgCl_2$, 1.5% digitonin, 100 mg/mL CHX, 0.5 mM DTT, 1× protease inhibitor Roche). For co-IP, 40 µg anti-FLAG M2 antibody or IgG control were coupled to 160 µL protein G Dynabeads in 1 mL lysis buffer (without DTT/CHX), washed, and added to 450 µL resuspended ribosomes. After 2 h incubation (4 °C), beads were washed three times with (20 mM HEPES pH 7.3, 195 mM KCl, 5 mM $MgCl_2$, 0.5% digitonin, 100 mg/mL cycloheximide, 0.1 mM DTT, 1× EDTA-free protease inhibitor cocktail), followed by three washes with (20 mM HEPES pH 7.3, 195 mM KCl, 5 mM $MgCl_2$), then resuspended in 50 µL of 100 mM ammonium bicarbonate (ABC), supplemented with 300 ng trypsin (Trypsin Gold, Promega) and incubated for 4 h on a Thermo-shaker with 1200 rpm at 37 °C. The supernatant was transferred to a fresh tube and reduced with 0.5 mM Tris 2-carboxyethyl phosphine hydrochloride (TCEP, Sigma) for 30 min at 60 °C and alkylated in 3 mM methyl methanethiosulfonate (MMTS, Fluka) for 30 min at room temp protected from light. Subsequently, the sample was digested with another 300 ng of trypsin at 37 °C overnight. The digest was acidified by addition of trifluoroacetic acid (TFA, Pierce) to 1%. A similar aliquot of each sample was analyzed by LC-MS/MS. Total protein concentration of the lysate and ribosomal pellet inputs was measured using Pierce™ BCA Protein Assay Kit (Reducing Agent Compatible). Aliquots containing 25 µg of total protein were tryptic digested, using the iST kit (PO 00001, PreOmics) according to the manufacturer's instructions. Offline sample desalting using the OASIS MCX 96-well uElution Plate 30 µm (Waters), 2 µl sorbent per well, was performed in a centrifuge spinning at 200×*g* for 3 min at each step. Samples were brought to a concentration of 2% H3PO4 in 100 mM Ammonium Formate and loaded to dry wells of the OASIS plate. Bound peptides were washed 2× with 200 µl of 2% formic acid in 100 mM Ammonium Formate and 2 ×200 µl of 100% methanol. Elution of peptides was performed by applying 2×25 µl of 5% NH4OH in 80% methanol, followed by vacuum centrifugation to dryness and reconstitution in 20 µl of 2% acetonitrile in 0.1% TFA. 250 ng of each peptide sample each sample was analyzed by LC-MS/MS. The nano HPLC system (Vanquish Neo UHPLC-System, Thermo Scientific) was coupled to an Orbitrap Astral mass spectrometer, equipped with a Nanospray Flex ion source (all parts Thermo Scientific). Peptides were loaded onto a trap column (PepMap Acclaim C18, 5 mm × 300 µm ID, 5 µm particle size, 100 Å pore size, Thermo Scientific) at a flow rate of 25 µl/min using 0.1% TFA as mobile phase. After 5 min, the trap column was switched in line with the analytical column (Aurora Ultimate C18 25 cm × 75 µm ID, 1.7 µm particles, 120 Å, Ionopticks operated at 50 °C). Peptides were eluted using a flow rate of 300 nl/min, starting with the mobile phases 98% A (0.1% formic acid in water) and 2% B (80% acetonitrile, 0.1% formic acid) and linearly increasing to 35% B over the next 60 min, followed by an increase to 95% B in 1.7 min, a 4-min hold at 95% B, and re-equilibration with 2% B for three column volumes (equilibration factor of 3.0). The Orbitrap Astral was operated in data-dependent mode, performing a full scan in the Orbitrap every 0.7 s (*m/z* range 375–1500 *m/z*; resolution 240,000; standard AGC target, maximum injection time 10 ms, minimum intensity 5000). MS/MS spectra were acquired in the Astral analyser by isolating 1.6 Da windows and fragmenting precursor ions with normalized HCD collision energy of 30% with a maximum injection time of 5 or 10 ms correspondingly or until a standard AGC target was reached. Fragment ions ranging from 150 to 2000 *m/z* were acquired. Precursor ions selected for fragmentation (include charge state 2–6) were put on a dynamic exclusion list for 30 s.

### *Data processing*

For peptide identification from DDA data, the RAW-files were loaded into Proteome Discoverer (version 3.2.0.450, Thermo Scientific). All MS/MS spectra were searched using MSAmanda version 3.2.22.93 (Dorfer et al, 2014). The peptide and fragment mass tolerance was set to ±10 ppm, the maximum number of missed cleavages was set to 2, using tryptic enzymatic specificity without proline restriction. The RAW-files were searched against the uniprot reference database, using human as sub-organism (20,586 sequences; 11,456,034 residues), supplemented with common contaminants using the following modifications: Carbamidomethylation of cysteine was set as fixed modification and oxidation of methionine, UFMylation residues VG and DRVG each on Lysine, deamidation of asparagine and glutamine, glutamine to pyro-glutamate conversion at peptide N-terminal glutamine and acetylation on the protein N-terminus were set as variable

 © The Author(s)

modifications. The localization of the post-translational modification sites within the peptides was performed with the tool ptmRS, based on the tool phosphoRS (Taus et al, 2011). The result was filtered to 1% FDR on PSM and protein level using the Percolator algorithm (Käll et al, 2007) integrated in Proteome Discoverer. Additionally, an Amanda score cut-off of at least 150 was applied. Proteins were filtered to be identified by a minimum of 2 PSMs in at least 1 sample. Protein areas were computed in IMP-apQuant (Doblmann et al, 2019) by summing up unique and razor peptides. Resulting protein areas were normalized using iBAQ (Schwanhäusser et al, 2011). Match-between-runs (MBR) was applied for peptides with high confident peak area that were identified by MS/MS spectra in at least one run. Proteins were filtered to be identified by a minimum of 3 quantified peptides. Statistical significance of differentially expressed proteins was determined using limma (Smyth, 2004).

## Mammalian siRNA and plasmid transfections

For reporter accumulation experiments, RKO iCas9 cells were seeded in 6-well plates and treated with 450 nM doxycycline for 48 h to induce expression of Cas9. The cells were then transfected with 2 µg plasmid using jetOPTIMUS® reagent according to the manufacturer's instructions (Avantor, 101000051). Cells were washed with cold PBS buffer and collected on plate in RIPA buffer (150 mM NaCl, 1% NP-40, 0.5% Sodium deoxycholate, 0.1% SDS, and 25 mM TRIS pH 7.4) with 1× EDTA-free protease inhibitor cocktail (Roche, 11873580001). Cell lysate was clarified on a table-top centrifuge at maximum speed (20,000 g) for 20 min at 4 °C.

To test the effect of RQC components' loss on UFMylation, HCT116 tetON OsTIR1 cells were seeded in 24-well plates and transfected with Dharmacon ON-TARGETplus Human siRNA SMARTpools at 10 nM against ASCC3 (L-012757-01-0005) and at 25 nM against PELO (L-019068-01-0005) and ZNF598 (L-007104-00-0005). ON-TARGETplus Non-targeting Control Pool (D-001810-10-05) at 25 nM was used as a control. Cells were passed to 6-well plates and either transfected with 2 µg of plasmids containing CytoK0, CytoK20, ERK0, or ERK20 reporters (Wang et al, 2020) for 24 h using jetOPTIMUS® reagent (Avantor, 101000051) according to the manufacturer's instructions or treated with 4 µM anisomycin dissolved in DMSO for 1 h before collection.

RKO iCas9 cells were seeded in ø10 cm dishes in media supplemented with 450 nM doxycycline for 48 h to induce expression of Cas9. Cells were then either transfected with 10 µg of plasmids containing CytoK0, CytoK20, ERK0, or ERK20 reporters (Wang et al, 2020) for 24 h using jetOPTIMUS® reagent according to the manufacturer's instructions (Avantor, 101000051), or treated with 4 µM anisomycin dissolved in DMSO for 1 h before collection.

## Flow cytometry analysis

HCT116 tetON OsTIR1 cells were seeded in 24-well plates and transfected with Dharmacon ON-TARGETplus Human siRNA SMARTpools for 72 h total as described in "Mammalian siRNA and plasmid transfections". Cells were passed to 6-well plates and transfected with 2 µg of pEGFP-N1 plasmid containing CytoK0, CytoK20, ERK0, or ERK20 reporters (Wang et al, 2020) for 24 h using jetOPTIMUS® reagent according to the manufacturer's instructions (Avantor, 101000051). Cells were harvested in trypsin, resuspended in full media and analyzed by flow cytometry (BD LSRFortessa™ Cell Analyser). Data was analyzed in FlowJo software.

## Sucrose density gradient fractionation

For polysome sucrose density fractionation, four ø15 cm dishes of ~80% confluent HCT116 3xFLAG-UFM1 cells were used per condition. Ribosome stalling was induced with 200 nM anisomycin for 1 h. Cells were washed in cold PBS supplemented with 100 µg/mL cycloheximide, lysed on the plate with 300 µL of ice-cold lysis buffer (20 mM HEPES pH 7.3, 120 mM KCl, 15 mM $MgCl_2$, 1.5% digitonin, 100 µg/mL cycloheximide, 0.5 mM DTT, 1× EDTA-free protease inhibitor cocktail). Cell lysates were further incubated on ice for 10 min with intermittent vortexing, passed three times through the 27 G needle, and clarified on a table-top centrifuge at maximum speed (20,000× *g*) for 10 min at 4 °C. In total, 1700 µL of the clarified lysate were layered on top of 10–35% sucrose gradient (gradient buffer composition: 20 mM HEPES pH 7.3, 120 mM KCl, 5 mM $MgCl_2$, 100 µg/mL cycloheximide, 0.5 mM DTT) and centrifugated at 35,000× *g* for 3 h at 4 °C using SW32Ti rotor. Polysome fractions were separated on a BioComp fractionator and 500 µL fractions were collected. Western blot analysis was performed following trichloroacetic acid (TCA) precipitation. Protein pellets were dissolved in 1× Leammli sample buffer. Fractions corresponding to the migration peaks of ribosomal subunits used for Western blotting were separated by at least four fractions.

For polysome sucrose density fractionation of HEK293T cells, one ø15 cm dish at ~80% confluency was used per condition. The experiment was performed similarly to that in HCT116 3xFLAG-UFM1 cells, with the following modifications: 250 µL of clarified lysate were layered onto a 10–35% sucrose gradient and centrifuged using an SW40Ti rotor. Fractions of 200 µL were collected. Fractions corresponding to the migration peaks of ribosomal subunits used for Western blotting were separated by at least four fractions.

## Cell lysis and immunoblotting

Clear cell lysates were collected in RIPA buffer with 1× EDTA-free protease inhibitor cocktail (Roche, 11873580001), clarified on a table-top centrifuge at maximum speed (20,000× *g*) for 20 min at 4 °C, and analyzed on 10%, 12% or 15% SDS-polyacrylamide gels, followed by a semi-dry transfer (BioRad blotter) or wet transfer (120 V, 1 h 20 min on a BioRad blotter) on a 0.2 µm nitrocellulose membrane. Membrane was blocked in 1×TBS buffer with 0.1% Tween containing 5% milk for 1 h at room temperature. Primary antibody (listed in Dataset EV2) was diluted in 2.5% milk 1× TBS-0.1% Tween buffer and incubated either 1 h at room temperature or at 4 °C overnight, followed by three washes with 1× TBS-0.1% Tween buffer. Secondary antibody conjugated with horseradish peroxidase (Promega) was diluted in 2.5% milk 1× TBS-0.1% Tween buffer and incubated for 1 h at room temperature, followed by three washes with 2.5% milk 1× TBS-0.1% Tween buffer. The blots were developed using chemiluminescent detection on iBright ThermoFisher machine and quantified in iBright Analysis Software (ThermoFisher).

© The Author(s)

## Immunoprecipitations

### GFP IP from sucrose cushions

For detecting UFL1 and RQC factors binding to nascent chain-containing 60S ribosomes, RKO iCas9 cell lines expressing gRNA against AAVS1 (non-targeting control), NEMF, or UFM1 (gRNA sequences are listed in Dataset EV2) were seeded in ⌀10-cm dishes (2 dishes per condition) in media supplemented with 450 nM doxycycline for 48 h to induce expression of Cas9. Cells were then transfected with 10 µg of plasmids containing CytoK20, or ERK20 reporters (Wang et al, 2020) for 24 h using jetOPTIMUS® reagent according to the manufacturer's instructions (Avantor, 101000051). Cells were then washed in cold PBS supplemented with 100 µg/mL cycloheximide, lysed on the plate with ice-cold lysis buffer (20 mM HEPES pH 7.3, 120 mM KCl, 5 mM $MgCl_2$, 1% NP-40, 100 µg/mL cycloheximide, 0.5 mM DTT, 1× EDTA-free protease inhibitor cocktail). Cell lysates were further incubated on ice for 10 min with intermittent vortexing, passed three times through the 27 G needle, and clarified on a table-top centrifuge at maximum speed (20,000× *g*) for 20 min at 4 °C. 700 µL of the lysate was layered on top of 233 µL of sucrose cushion (1 M sucrose, 20 mM HEPES pH 7.3, 120 mM KCl, 5 mM $MgCl_2$, 100 µg/mL cycloheximide, 0.5 mM DTT). Ribosomes were pelleted by centrifugation at 100,000× *g* for 1.5 h at 4 °C in a TLA100.3 rotor. After the supernatant was removed, the ribosomal pellet was resuspended with 150 µL of lysis buffer. Immunoprecipitations were performed with 40 µL of resuspended GFP-Trap® Magnetic Particles (ChromoTek, gtd-20) per condition, the mixture was incubated on a rotator at +4 °C for 1 h, washed 3 times with wash buffer (20 mM HEPES pH 7.3, 195 mM KCl, 5 mM $MgCl_2$, 0.5% NP-40, 100 µg/mL cycloheximide, 0.1 mM DTT, 1× EDTA-free protease inhibitor cocktail), and eluted in 30 µL of 1× SDS sample buffer without DTT. Samples were incubated at 70 °C for 10 min, the eluate was separated from the magnetic particles, DTT was added to the final concentration of 10 mM, samples were incubated at 95 °C for 5 min and loaded on a SDS-PAGE gel followed by western blotting.

### FLAG IP from cell lysate

HCT116 tetON OsTIR1 3xFLAG-UFM1 or RKO iCas9 3xFLAG-UFM1 cell lines or their respective parental cell lines were seeded in ⌀15-cm dishes (2 dishes per condition) and treated with 200 nM ANS for 1 h before collection, or untreated as a control. Cells were washed with cold PBS and lysed on plate with ice-cold lysis buffer (20 mM HEPES pH 7.3, 120 mM KCl, 15 mM $MgCl_2$, 1.5% w/v digitonin, 100 µg/mL cycloheximide, 0.5 mM DTT, 1× EDTA-free protease inhibitor cocktail). Cell lysates were further incubated on ice for 10 min, passed three times through the 27 G needle, and clarified on a table-top centrifuge at maximum speed (20,000× *g*) for 20 min at 4 °C. For co-IP, 10 µg anti-FLAG M2 antibody was coupled to 40 µL protein G Dynabeads (per 15-cm dish) in 1 mL lysis buffer (without DTT/CHX) and coupled for 20 min at room temperature on an end-over-end rotator. Beads were washed three times with lysis buffer without DTT. Co-IP was performed from 700 µL of cleared cell lysates for 2 h at 4 °C on an end-over-end rotator. Beads were washed three times with the wash buffer (20 mM HEPES pH 7.3, 195 mM KCl, 5 mM $MgCl_2$, 0,5% w/v digitonin, 100 µg/mL cycloheximide, 0.1 mM DTT, 1× EDTA-free protease inhibitor cocktail) and eluted in 30 µL of 1× SDS sample buffer without DTT. Samples were incubated at 70 °C for 10 min, the eluate was separated from the magnetic particles, DTT was added to the final concentration of 10 mM, samples were incubated at 95 °C for 5 min and loaded on a SDS-PAGE gel followed by western blotting.

### GFP IP from split GFP cells

HEK293 Sec61β split GFP or parental cell lines (Leonetti et al, 2016), a kind gift from Leonetti lab were seeded in 15-cm dishes (2 dishes per condition) and treated with 4 µM ANS for 3 h before collection, or untreated as control. Cells were washed with cold PBS and lysed on plate with ice-cold lysis buffer (20 mM HEPES pH 7.3, 150 mM KCl, 5 mM $MgCl_2$, 1,5% w/v digitonin, 0.5 mM DTT, 1× EDTA-free protease inhibitor cocktail). Cell lysates were further incubated on ice for 10 min, passed three times through the 27 G needle, and clarified on a table-top centrifuge at maximum speed (20,000× *g*) for 20 min at 4 °C. Cleared cell lysates were treated with 2.5 µg RNase A (Thermo Scientific, EN0531) per 750 ng total RNA for 20 min at 25 °C at 750 rpm. Immunoprecipitations were subsequently performed with 25 µL of resuspended GFP-Trap® Magnetic Particles (ChromoTek, gtma-20) per dish, the beads were incubated with 830 µL of cell lysate on a rotator at +4 °C for 2 h, washed three times with wash buffer (20 mM HEPES pH 7.3, 150 mM KCl, 5 mM $MgCl_2$, 0.5% w/v digitonin, 0.1 mM DTT, 1× EDTA-free protease inhibitor cocktail), and eluted in 25 µL of 1× SDS sample buffer with 10 mM DTT, boiled at 95 °C for 5 min and loaded on a SDS-PAGE gel followed by western blotting.

## TUBE assays

For detecting polyubiquitinated proteins, RKO iCas9 cell lines expressing gRNA against AAVS1 (non-targeting control), UFM1, or LTN1 (gRNA sequences are listed in Dataset EV2) were seeded in ⌀10 cm dishes (1 dish per condition) in media supplemented with 450 nM doxycycline for 48 h to induce expression of Cas9. Cells were then transfected with 10 µg of plasmids containing ERK0, or ERK20 reporters (Wang et al, 2020) for 24 h using jetOPTIMUS® reagent according to the manufacturer's instructions (Avantor, 101000051). Before collection, cells were treated with 20 µM proteasome inhibitor MG132 or DMSO as a control for 3 h. For collection, cells were washed in cold PBS, lysed on the plate with ice-cold lysis buffer (20 mM HEPES pH 7.3, 120 mM KCl, 5 mM $MgCl_2$, 1% NP-40, 1× EDTA-free protease inhibitor cocktail) supplemented with 10 mM N-ethylmaleimide (NEM). Cell lysates were further incubated on ice for 10 min with intermittent vortexing, passed through a 27 G needle three times, and clarified in a tabletop centrifuge at maximum speed (20,000× *g*) for 20 min at 4 °C. TUBE was inducibly expressed in *E. coli* Rosetta cells from 6His-TEVb-HaloTR-TUBE plasmid in pET28a backbone (MRC PPU Dundee, obtained from MRC PPU reagents, https://mrcppureagents.dundee.ac.uk/product/37522, DU23799) at 16 °C overnight, bacterial pellet was lysed in lysis buffer (25 mM HEPES, pH 7.4, 150 mM NaCl, 0.5% NP-40 1× EDTA-free protease inhibitor cocktail) supplemented with benzonase, sonicated and cleared by 20,000× *g* centrifugation for 30 min at 4 °C. The cleared bacterial lysate was conjugated to Halo beads (Promega, G7281) overnight at 4 °C on an end-over-end rotator, washed five times with wash buffer (25 mM HEPES, pH 7.4, 1 M NaCl, 0.5% NP-40 1× EDTA-free protease inhibitor cocktail) and once with cell lysis buffer (20 mM HEPES pH 7.3, 120 mM KCl, 5 mM $MgCl_2$, 1% NP-

 © The Author(s)

40, 1× EDTA-free protease inhibitor cocktail, 10 mM NEM). Cleared cell lysates were incubated with conjugated Halo-TUBE beads for 3 h at 4 °C on an end-over-end rotator, washed three times with wash buffer (20 mM HEPES pH 7.3, 495 mM KCl, 5 mM $MgCl_2$, 1% NP-40, 1× EDTA-free protease inhibitor cocktail) supplemented with 10 mM N-ethylmaleimide (NEM) and eluted at 95 °C for 5 min in 1× SDS sample buffer with DTT added to a final concentration of 10 mM.

### Plant experiments

All *Arabidopsis thaliana* lines used in this study originate from the Columbia (Col-0) ecotype. Mutant lines used in this study are listed in Dataset EV2. Seedlings were grown in liquid 1/2 MS medium containing 1% sucrose under 16 h light/8 h dark photoperiod for 7 days with shaking at 80 rpm. Seven-day-old seedling grown in liquid 1/2 MS medium were treated with 100 µM anisomycin (ANS) for 16 h under continuous light with shaking at 80 rpm. An equal volume of pure dimethyl sulfoxide (DMSO) was added as control. Subsequently, seedlings were then frozen in liquid nitrogen after chemical treatment and homogenized for western blotting. The total protein was extracted with Grinding Buffer (50 mM Tris-HCl, 150 mM NaCl, 1% glycerol, 0.5% NP-40, 1.5 mM $MgCl_2$, 1× protease inhibitor cocktail). The SDS loading buffer was added to lysates, and the samples then were boiled at 95 °C for 10 min. 10 µg of sample was loaded per lane. SDS-PAGE was performed using gradient 4–20% Mini-PROTEAN TGX Precast Protein Gels (BioRad). Blotting on nitrocellulose membranes was performed using a semi-dry Turbo Transfer Blot System (BioRad). The membranes were blocked with 5% skimmed milk in TBS and 0.1% Tween 20 (TBS-T) for 1 h at room temperature. Subsequently, the membranes were incubated with primary antibody, followed by incubation with secondary antibody conjugated to horseradish peroxidase (HRP). After three times 10 min washes with TBS-T, the immune-reaction was developed using ECL SuperSignal West Femto (Thermo) and detected with iBright Imaging System (Thermo). Protein bands intensity was quantified using the iBright Imaging analysis System (Thermo). The average relative intensities and a standard error were calculated from three biological replicates.

#### *Graphics*

Figs. 1A, 4C, 6 and synopsis were created with BioRender.com.

### Statistical analysis and reproducibility

All experiments were performed at least three times unless otherwise indicated in figure legends. Statistical analysis was performed in GraphPad Prism 10 software using unpaired two-sided Student *t*-test.

## Data availability

Mass spectrometry proteomics data have been deposited at the ProteomeXchange Consortium via the PRIDE partner repository (Perez-Riverol et al, 2022) with the dataset identifier PXD071028.

The source data of this paper are collected in the following database record: biostudies:S-SCDT-10_1038-S44318-026-00753-9.

Expanded view data, supplementary information, appendices are available for this paper at https://doi.org/10.1038/s44318-026-00753-9.

## Peer review information

A peer review file is available at https://doi.org/10.1038/s44318-026-00753-9

## References

Bengtson MH, Joazeiro CAP (2010) Role of a ribosome-associated E3 ubiquitin ligase in protein quality control. Nature 467:470–473

Brandman O, Stewart-Ornstein J, Wong D, Larson A, Williams CC, Li G-W, Zhou S, King D, Shen PS, Weibezahn J et al (2012) A ribosome-bound quality control complex triggers degradation of nascent peptides and signals translation stress. Cell 151:1042–1054

Chandrasekaran V, Juszkiewicz S, Choi J, Puglisi JD, Brown A, Shao S, Ramakrishnan V, Hegde RS (2019) Mechanism of ribosome stalling during translation of a poly(A) tail. Nat Struct Mol Biol 26:1132–1140

Choe Y-J, Park S-H, Hassemer T, Körner R, Vincenz-Donnelly L, Hayer-Hartl M, Hartl FU (2016) Failure of RQC machinery causes protein aggregation and proteotoxic stress. Nature 531:191–195

Chu J, Hong NA, Masuda CA, Jenkins BV, Nelms KA, Goodnow CC, Glynne RJ, Wu H, Masliah E, Joazeiro CAP et al (2009) A mouse forward genetics screen identifies LISTERIN as an E3 ubiquitin ligase involved in neurodegeneration. Proc Natl Acad Sci USA 106:2097–2103

Crowder JJ, Geigges M, Gibson RT, Fults ES, Buchanan BW, Sachs N, Schink A, Kreft SG, Rubenstein EM (2015) Rkr1/Ltn1 ubiquitin ligase-mediated degradation of translationally stalled endoplasmic reticulum proteins. J Biol Chem 290:18454–18466

DaRosa PA, Penchev I, Gumbin SC, Scavone F, Wąchalska M, Paulo JA, Ordureau A, Peter JJ, Kulathu Y, Harper JW et al (2024) UFM1 E3 ligase promotes recycling of 60S ribosomal subunits from the ER. Nature 627:445–452

de Almeida M, Hinterndorfer M, Brunner H, Grishkovskaya I, Singh K, Schleiffer A, Jude J, Deswal S, Kalis R, Vunjak M et al (2021) AKIRIN2 controls the nuclear import of proteasomes in vertebrates. Nature 599:491–496

Doblmann J, Dusberger F, Imre R, Hudecz O, Stanek F, Mechtler K, Dürnberger G (2019) apQuant: accurate label-free quantification by quality filtering. J Proteome Res 18:535–541

Doma MK, Parker R (2006) Endonucleolytic cleavage of eukaryotic mRNAs with stalls in translation elongation. Nature 440:561–564

Dorfer V, Pichler P, Stranzl T, Stadlmann J, Taus T, Winkler S, Mechtler K (2014) MS Amanda, a universal identification algorithm optimized for high accuracy tandem mass spectra. J Proteome Res 13:3679–3684

Endo R, Chen Y-K, Burke J, Takashima N, Suryawanshi N, Hui KK, Miyazaki T, Tanaka M (2023) Dysregulation of ribosome-associated quality control elicits cognitive disorders via overaccumulation of TTC3. Proc Natl Acad Sci USA 120:e2211522120

Filbeck S, Cerullo F, Pfeffer S, Joazeiro CAP (2022) Ribosome-associated quality-control mechanisms from bacteria to humans. Mol Cell 82:1451–1466

Gavin JM, Hoar K, Xu Q, Ma J, Lin Y, Chen J, Chen W, Bruzzese FJ, Harrison S, Mallender WD et al (2014) Mechanistic study of Uba5 enzyme and the Ufm1 conjugation pathway. J Biol Chem 289:22648–22658

Guydosh NR, Green R (2014) Dom34 rescues ribosomes in 3′ untranslated regions. Cell 156:950–962

Hansen JL, Moore PB, Steitz TA (2003) Structures of five antibiotics bound at the peptidyl transferase center of the large ribosomal subunit. J Mol Biol 330:1061–1075

© The Author(s)

Hashimoto S, Sugiyama T, Yamazaki R, Nobuta R, Inada T (2020) Identification of a novel trigger complex that facilitates ribosome-associated quality control in mammalian cells. Sci Rep 10:3422

Hornegger H, Anisimova AS, Muratovic A, Bourgeois B, Spinetti E, Niedermoser I, Covino R, Madl T, Karagöz GE (2024) IGF2BP1 phosphorylation in the disordered linkers regulates ribonucleoprotein condensate formation and RNA metabolism. Nat Commun 15:9054

Inada T, Beckmann R (2024) Mechanisms of translation-coupled quality control. J Mol Biol 436:168496

Izawa T, Tsuboi T, Kuroha K, Inada T, Nishikawa S, Endo T (2012) Roles of dom34:hbs1 in nonstop protein clearance from translocators for normal organelle protein influx. Cell Rep 2:447–453

Joazeiro CAP (2017) Ribosomal stalling during translation: providing substrates for ribosome-associated protein quality control. Annu Rev Cell Dev Biol 33:343–368

Joazeiro CAP (2019) Mechanisms and functions of ribosome-associated protein quality control. Nat Rev Mol Cell Biol 20:368–383

Juszkiewicz S, Chandrasekaran V, Lin Z, Kraatz S, Ramakrishnan V, Hegde RS (2018) ZNF598 is a quality control sensor of collided ribosomes. Mol Cell 72:469–481.e7

Juszkiewicz S, Hegde RS (2017) Initiation of quality control during poly(A) translation requires site-specific ribosome ubiquitination. Mol Cell 65:743–750.e4

Juszkiewicz S, Speldewinde SH, Wan L, Svejstrup JQ, Hegde RS (2020) The ASC-1 complex disassembles collided ribosomes. Mol Cell 79:603–614.e8

Käll L, Canterbury JD, Weston J, Noble WS, MacCoss MJ (2007) Semi-supervised learning for peptide identification from shotgun proteomics datasets. Nat Methods 4:923–925

Karagöz GE, Acosta-Alvear D, Walter P (2019) The unfolded protein response: Detecting and responding to fluctuations in the protein-folding capacity of the endoplasmic reticulum. Cold Spring Harbor Perspect Biol 11:a033886

Komatsu M, Chiba T, Tatsumi K, Iemura S, Tanida I, Okazaki N, Ueno T, Kominami E, Natsume T, Tanaka K (2004) A novel protein-conjugating system for Ufm1, a ubiquitin-fold modifier. EMBO J 23:1977–1986

Kostova KK, Hickey KL, Osuna BA, Hussmann JA, Frost A, Weinberg DE, Weissman JS (2017) CAT-tailing as a fail-safe mechanism for efficient degradation of stalled nascent polypeptides. Science 357:414–417

Kumar M, Padala P, Fahoum J, Hassouna F, Tsaban T, Zoltsman G, Banerjee S, Cohen-Kfir E, Dessau M, Rosenzweig R et al (2021) Structural basis for UFM1 transfer from UBA5 to UFC1. Nat Commun 12:5708

Kuroha K, Zinoviev A, Hellen CUT, Pestova TV (2018) Release of ubiquitinated and non-ubiquitinated nascent chains from stalled mammalian ribosomal complexes by ANKZF1 and Ptrh1. Mol Cell 72:286–302.e8

Lakshminarayan R, Phillips BP, Binnian IL, Gomez-Navarro N, Escudero-Urquijo N, Warren AJ, Miller EA (2020) Pre-emptive quality control of a misfolded membrane protein by ribosome-driven effects. Curr Biol 30:854–864.e5

Leonetti MD, Sekine S, Kamiyama D, Weissman JS, Huang B (2016) A scalable strategy for high-throughput GFP tagging of endogenous human proteins. Proc Natl Acad Sci 113:E3501–E3508

Letzring DP, Wolf AS, Brule CE, Grayhack EJ (2013) Translation of CGA codon repeats in yeast involves quality control components and ribosomal protein L1. RNA 19:1208–1217

Lewis AJ, Zhong F, Keenan RJ, Hegde RS (2024) Structural analysis of the dynamic ribosome-translocon complex. eLife 13:RP95814

Lyumkis D, Doamekpor SK, Bengtson MH, Lee J-W, Toro TB, Petroski MD, Lima CD, Potter CS, Carragher B, Joazeiro CAP (2013) Single-particle EM reveals extensive conformational variability of the Ltn1 E3 ligase. Proc Natl Acad Sci USA 110:1702–1707

Makhlouf L, Peter JJ, Magnussen HM, Thakur R, Millrine D, Minshull TC, Harrison G, Varghese J, Lamoliatte F, Foglizzo M et al (2024) The UFM1 E3 ligase recognizes and releases 60S ribosomes from ER translocons. Nature 627:437–444

Meyer H, Bug M, Bremer S (2012) Emerging functions of the VCP/p97 AAA-ATPase in the ubiquitin system. Nat Cell Biol 14:117–123

Natsume T, Kiyomitsu T, Saga Y, Kanemaki MT (2016) Rapid protein depletion in human cells by auxin-inducible degron tagging with short homology donors. Cell Rep 15:210–218

Penchev I, Gumbin S, Scavone F, Berninghausen O, Becker T, Kopito R, Beckmann R (2025) UFMylation orchestrates spatiotemporal coordination of RQC at the ER. Sci Adv 11:eadv0435

Perez-Riverol Y, Bai J, Bandla C, García-Seisdedos D, Hewapathirana S, Kamatchinathan S, Kundu DJ, Prakash A, Frericks-Zipper A, Eisenacher M et al (2022) The PRIDE database resources in 2022: a hub for mass spectrometry-based proteomics evidences. Nucleic Acids Res 50:D543–D552

Phillips BP, Miller EA (2020) Ribosome-associated quality control of membrane proteins at the endoplasmic reticulum. J Cell Sci 133:jcs251983

Ran FA, Hsu PD, Wright J, Agarwala V, Scott DA, Zhang F (2013) Genome engineering using the CRISPR-Cas9 system. Nat Protoc 8:2281–2308

Scavone F, Gumbin SC, Da Rosa PA, Kopito RR (2023) RPL26/uL24 UFMylation is essential for ribosome-associated quality control at the endoplasmic reticulum. Proc Natl Acad Sci USA 120:e2220340120

Schwanhäusser B, Busse D, Li N, Dittmar G, Schuchhardt J, Wolf J, Chen W, Selbach M (2011) Global quantification of mammalian gene expression control. Nature 473:337–342

Shao S, Brown A, Santhanam B, Hegde RS (2015) Structure and assembly pathway of the ribosome quality control complex. Mol Cell 57:433–444

Shao S, Hegde RS (2014) Reconstitution of a minimal ribosome-associated ubiquitination pathway with purified factors. Mol Cell 55:880–890

Shen PS, Park J, Qin Y, Li X, Parsawar K, Larson MH, Cox J, Cheng Y, Lambowitz AM, Weissman JS et al (2015) Protein synthesis. Rqc2p and 60S ribosomal subunits mediate mRNA-independent elongation of nascent chains. Science 347:75–78

Shoemaker CJ, Green R (2012) Translation drives mRNA quality control. Nat Struct Mol Biol 19:594–601

Smyth GK (2004) Linear models and empirical bayes methods for assessing differential expression in microarray experiments. Stat Appl Genet Mol Biol 3:Article3

Stephani M, Picchianti L, Gajic A, Beveridge R, Skarwan E, Hernandez VS, de M, Mohseni A, Clavel M, Zeng Y, Naumann C et al (2020) A cross-kingdom conserved er-phagy receptor maintains endoplasmic reticulum homeostasis during stress. eLife 9:1–105

Sundaramoorthy E, Leonard M, Mak R, Liao J, Fulzele A, Bennett EJ (2017) ZNF598 and RACK1 regulate mammalian ribosome-associated quality control function by mediating regulatory 40S ribosomal ubiquitylation. Mol Cell 65:751–760.e4

Tanaka M, Sotta N, Duncan S, Chiba Y, Onouchi H, Marée AFM, Naito S, Grieneisen VA, Fujiwara T (2025) Ribosome stalling-induced NIP5;1 mRNA decay triggers ARGONAUTE1-dependent transcription downregulation. Nucleic Acids Res 53:gkaf159

Tatsumi K, Sou Y, Tada N, Nakamura E, Iemura S, Natsume T, Kang SH, Chung CH, Kasahara M, Kominami E et al (2010) A novel type of E3 ligase for the Ufm1 conjugation system*. J Biol Chem 285:5417–5427

Taus T, Köcher T, Pichler P, Paschke C, Schmidt A, Henrich C, Mechtler K (2011) Universal and confident phosphorylation site localization using phosphoRS. J Proteome Res 10:5354–5362

Tesina P, Lessen LN, Buschauer R, Cheng J, Wu CC-C, Berninghausen O, Buskirk AR, Becker T, Beckmann R, Green R (2020) Molecular mechanism of translational stalling by inhibitory codon combinations and poly(A) tracts. EMBO J 39:EMBJ2019103365

 © The Author(s)

von der Malsburg K, Shao S, Hegde RS (2015) The ribosome quality control pathway can access nascent polypeptides stalled at the Sec61 translocon. Mol Biol Cell 26:2168–2180

Voorhees RM, Fernández IS, Scheres SHW, Hegde RS (2014) Structure of the mammalian ribosome-Sec61 complex to 3.4 Å resolution. Cell 157:1632–1643

Walczak CP, Leto DE, Zhang L, Riepe C, Muller RY, DaRosa PA, Ingolia NT, Elias JE, Kopito RR (2019) Ribosomal protein RPL26 is the principal target of UFMylation. Proc Natl Acad Sci USA 116:1299–1308

Wang L, Xu Y, Rogers H, Saidi L, Noguchi CT, Li H, Yewdell JW, Guydosh NR, Ye Y (2020) UFMylation of RPL26 links translocation-associated quality control to endoplasmic reticulum protein homeostasis. Cell Res 30:5–20

Wang L, Xu Y, Yun S, Yuan Q, Satpute-Krishnan P, Ye Y (2023) SAYSD1 senses UFMylated ribosome to safeguard co-translational protein translocation at the endoplasmic reticulum. Cell Rep 42:112028

Yu X, Willmann MR, Anderson SJ, Gregory BD (2016) Genome-wide mapping of uncapped and cleaved transcripts reveals a role for the nuclear mRNA Cap-binding complex in cotranslational RNA decay in Arabidopsis. Plant Cell 28:2385–2397

## Acknowledgements

We thank Kitti Csalyi and Thomas Sauer at the Max Perutz Labs Biooptics FACS facility, and Elisabeth Roitinger at the Vienna BioCenter Proteomics Core Facility, for their help. We thank Gijs Versteeg (Max Perutz Labs, Vienna) and Johannes Zuber (IMP, Vienna) for assistance with the iCas9 RKO cell lines and lentiviral transduction, and Yihong Ye (NIH, Bethesda) for the CytoK0, CytoK20, ERK0, and ERK20 plasmids. This research was funded in whole or in part by the Austrian Science Fund (FWF) [FWF-W1261, FWF-DOC 177B] to GEK, the [FWF-SFB F79] and Vienna Science and Technology Fund, WWTF-LS21 to GEK and YD, and European Research Council Grant (Project number: 101043370) to YD. ASA and MM are supported by the DOC fellowship of the Austrian Academy of Sciences. For open access purposes, the author has applied a CC BY public copyright license to any author-accepted manuscript version arising from this submission.

## Author contributions

**Milica Mihailovic**: Conceptualization; Formal analysis; Validation; Investigation; Visualization; Methodology; Writing—original draft; Writing—review and editing. **Aleksandra S Anisimova**: Conceptualization; Formal analysis; Validation; Investigation; Visualization; Methodology; Writing—review and editing. **Bu Erte**: Conceptualization; Formal analysis; Validation; Investigation; Visualization; Methodology; Writing—review and editing. **Ni Zhan**: Conceptualization; Formal analysis; Validation; Investigation; Visualization; Methodology; Writing—review and editing. **Ioanna Styliara**: Formal analysis; Investigation; Methodology. **Yasin Dagdas**: Conceptualization; Supervision; Funding acquisition; Investigation; Methodology; Project administration; Writing—review and editing. **Gülsün Elif Karagöz**: Conceptualization; Supervision; Funding acquisition; Investigation; Writing—original draft; Project administration; Writing—review and editing.

Source data underlying figure panels in this paper may have individual authorship assigned. Where available, figure panel/source data authorship is listed in the following database record: biostudies:S-SCDT-10_1038-S44318-026-00753-9.

## Disclosure and competing interests statement

The authors declare no competing interests.

**Open Access** This article is licensed under a Creative Commons Attribution 4.0 International License, which permits use, sharing, adaptation, distribution and reproduction in any medium or format, as long as you give appropriate credit to the original author(s) and the source, provide a link to the Creative Commons licence, and indicate if changes were made. The images or other third party material in this article are included in the article's Creative Commons licence, unless indicated otherwise in a credit line to the material. If material is not included in the article's Creative Commons licence and your intended use is not permitted by statutory regulation or exceeds the permitted use, you will need to obtain permission directly from the copyright holder. To view a copy of this licence, visit http://creativecommons.org/licenses/by/4.0/. Creative Commons Public Domain Dedication waiver http://creativecommons.org/publicdomain/zero/1.0/ applies to the data associated with this article, unless otherwise stated in a credit line to the data, but does not extend to the graphical or creative elements of illustrations, charts, or figures. This waiver removes legal barriers to the re-use and mining of research data. According to standard scholarly practice, it is recommended to provide appropriate citation and attribution whenever technically possible.

© The Author(s) 2026

# Expanded View Figures

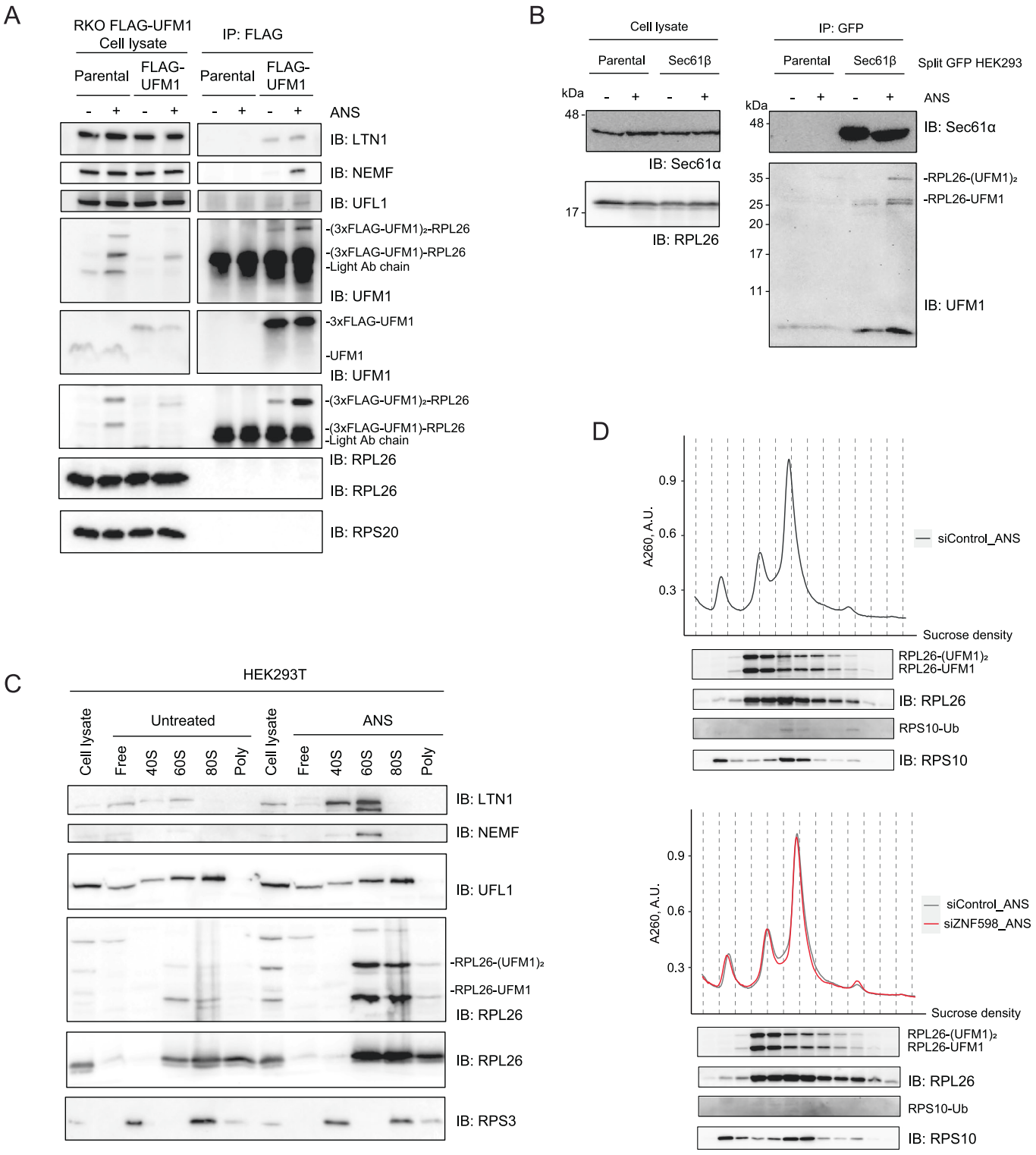



**Figure EV1. The RQC and UFM1 E3 ligase machinery associate with stalled ribosomes.**

(**A**) Immunoblot analysis of FLAG IP eluates upon 200 nM 1 h ANS treatment or from untreated RKO parental or RKO FLAG-UFM1 cells. (**B**) Immunoblot analysis of GFP IP eluates upon 4 μM 3 h ANS treatment or from untreated HEK293 split GFP parental or HEK293 Sec61β-split GFP cell lines. (**C**) Immunoblots of selected sucrose fractions of HEK293T cell lysates upon 200 nM 1 h ANS treatment or from untreated control condition. (**D**) Polysome profiles from HCT116 cells upon 72 h knockdown of control siRNA (top panel) or ZNF598 (bottom panel), accompanied by immunoblots showing RPL26 and RPS10 protein levels from corresponding fractions.

 © The Author(s)

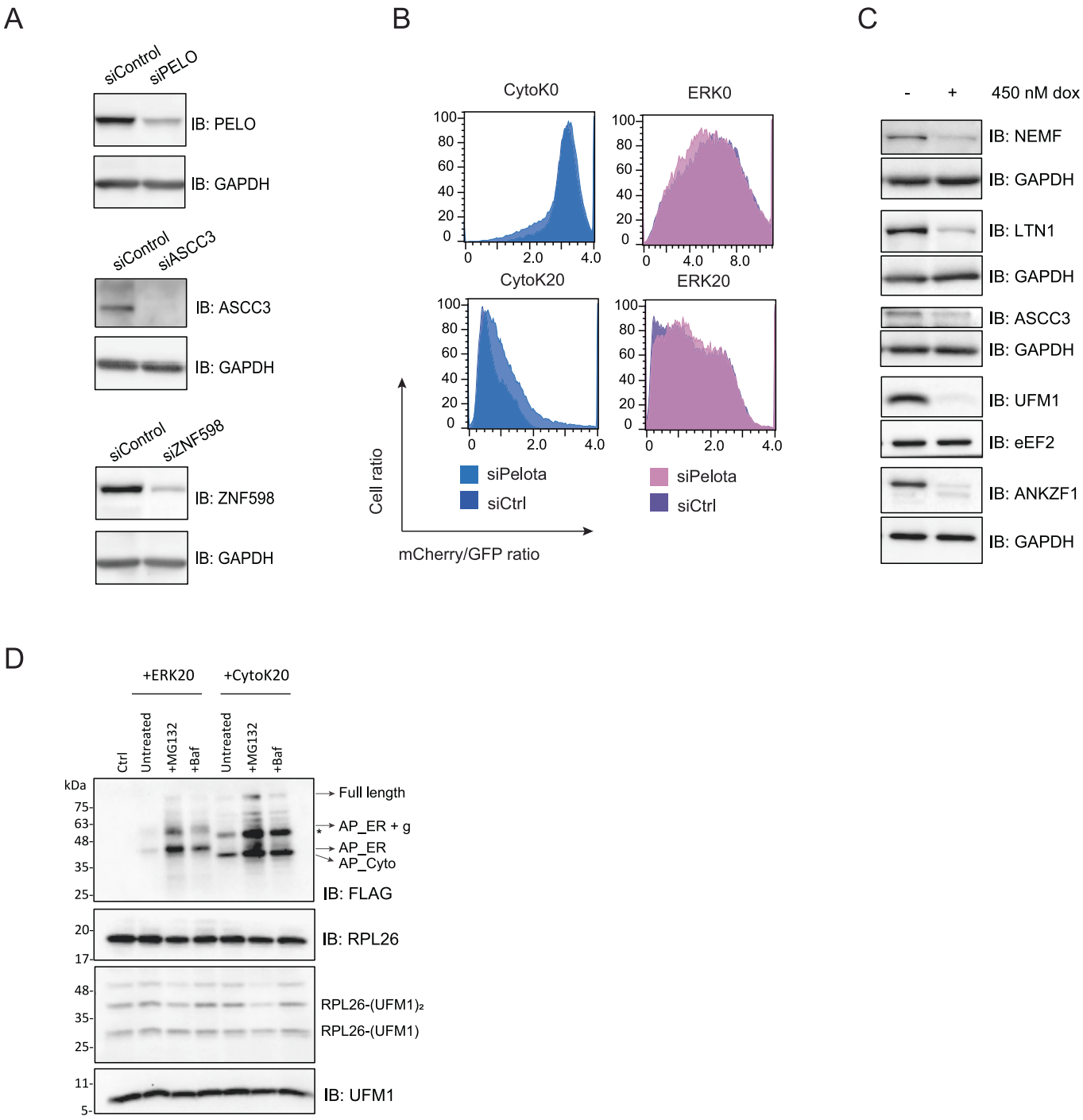



**Figure EV2. The ER stalling reporter is primarily stabilized by a proteasomal inhibitor.**

(**A**) Immunoblots showing knockdowns of RQC proteins Pelota, ASCC3, or ZNF598 upon 72 h siRNA treatment in HCT116 cells. GAPDH is used as a loading control. (**B**) Readthrough of reporters from Fig. 2A shown by mCherry/GFP ratio measured by FACS after 24 h expression in HCT116 cells upon siRNA-mediated knockdown of Pelota compared to non-targeting control siRNA. (**C**) Immunoblots showing knockouts of RQC proteins NEMF, LTN1, ASCC3, ANKZF1, or UFM1 knockout upon 48 h dox treatment in RKO cells. GAPDH or eEF2 are used as a loading control. (**D**) Immunoblots showing reporter accumulation upon 24 h expression of CytoK20 or ERK20 in HCT116 cells after treatment with either 20 nM MG132 for 3 h, 10 nM Baf for 16 h, or untreated as a control. AP arrested peptide, * degradation products.

© The Author(s)

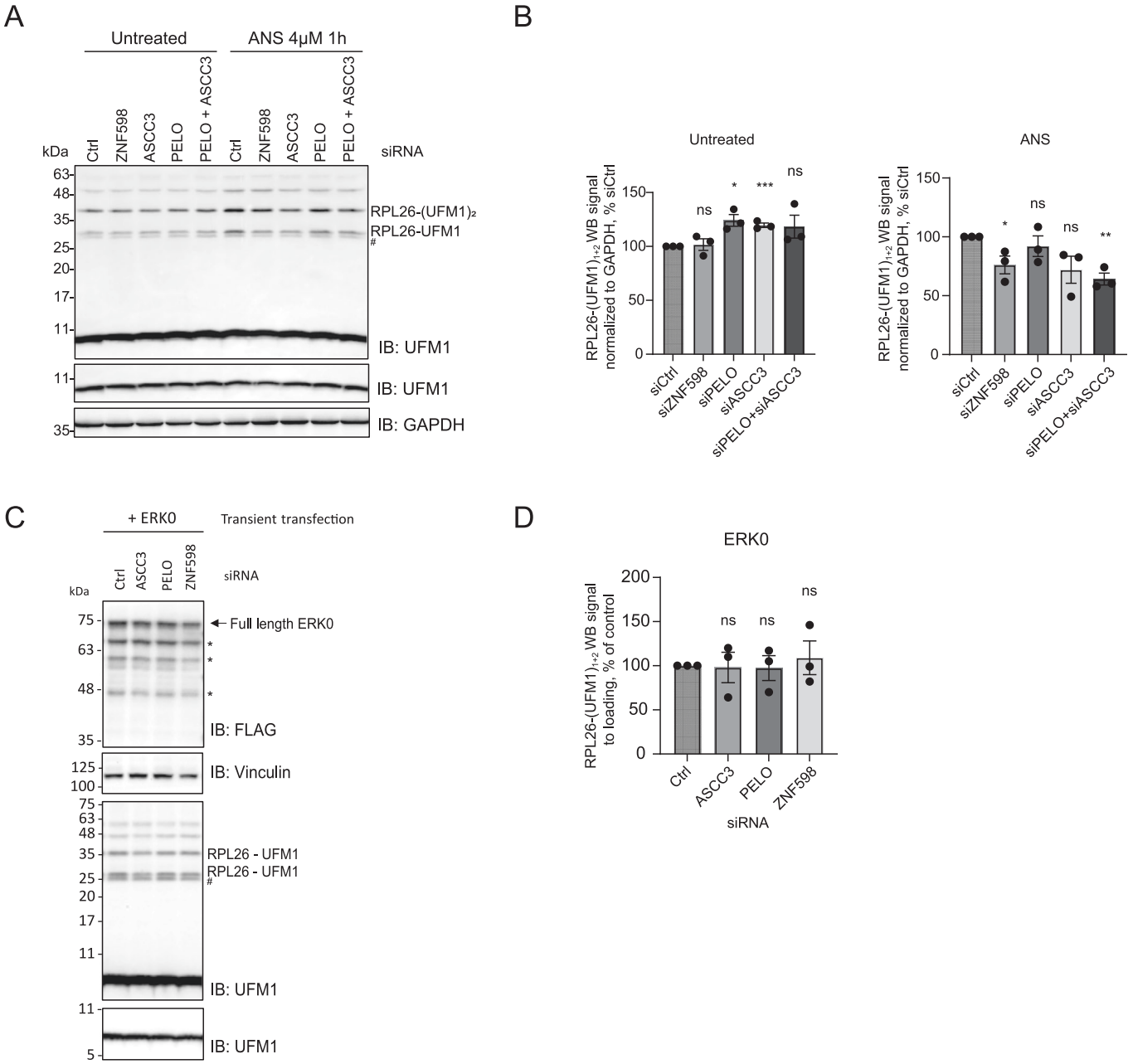



**Figure EV3. Ribosomal splitting precedes UFMylation of RPL26.**

(**A**) UFMylation levels visualized by UFM1 immunoblot in untreated or 1 h 4 μM ANS treated HCT116 cells upon 72 h siRNA-mediated knockdown of RQC components or non-targeting control. (**B**) Quantification of (**A**) with unpaired two-sided Student *t*-test, $n = 3$. Error bars represent SEM. (**C**) UFMylation levels visualized by UFM1 immunoblot in HCT116 cells upon 72 h siRNA-mediated knockdown of RQC components or non-targeting control, and 24 h expression of ERK0. (**D**) Quantification of (**C**) with unpaired two-sided Student *t*-test, $n = 3$. Error bars represent SEM. ****$P \le 0.0001$, ***$P \le 0.001$, **$P \le 0.01$, *$P \le 0.05$. List of complete *P* values available in Dataset EV2. # - UFC1-UFM1 complex, * degradation products.

 © The Author(s)

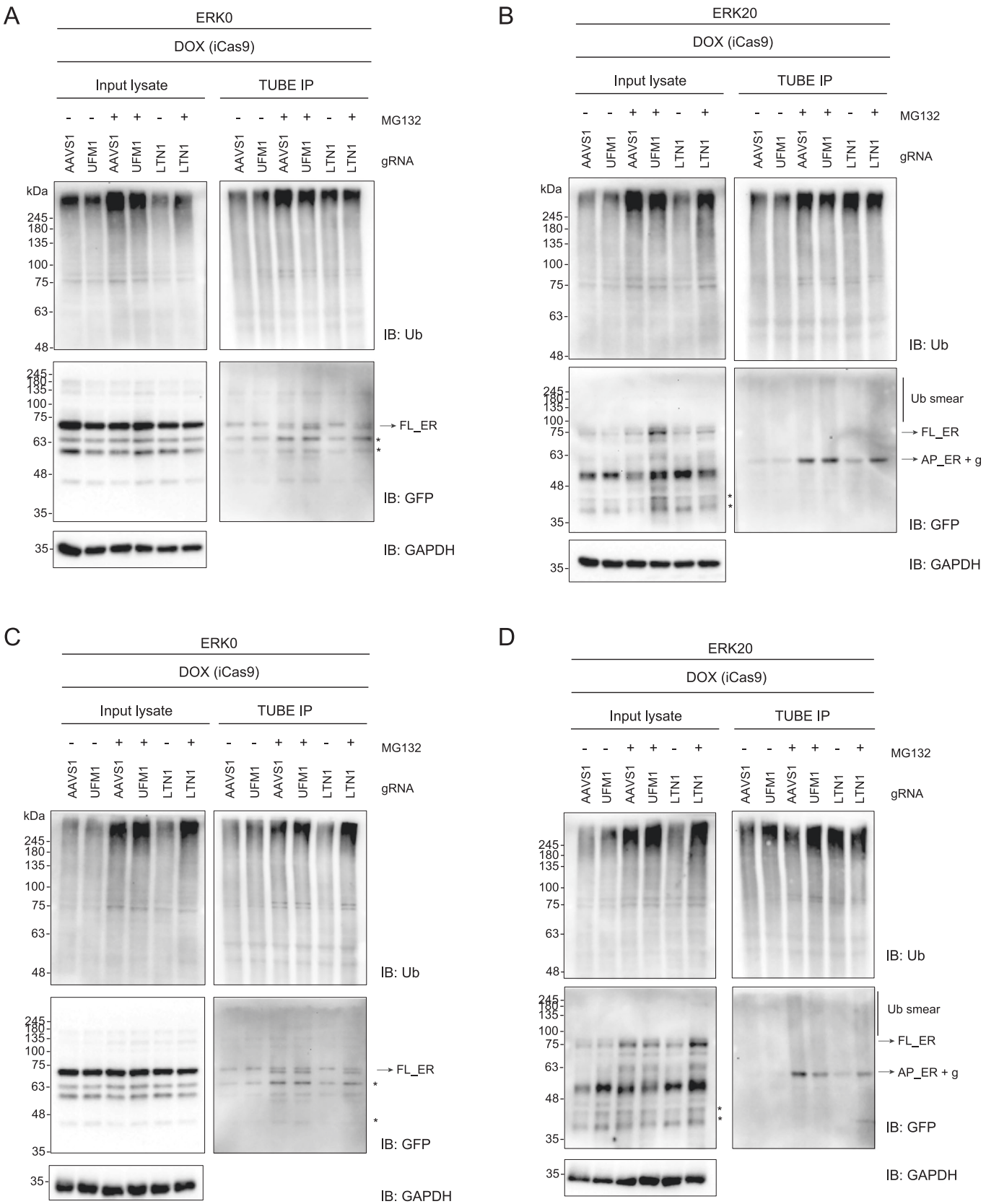

A
ERK0
DOX (iCas9)
Input lysate
TUBE IP
MG132
gRNA
AAVS1
UFM1
LTN1
kDa
IB: Ub
FL_ER
IB: GFP
IB: GAPDH
B
ERK20
Ub smear
AP_ER + g
C
D

**Figure EV4. The loss of LTN1 or UFM1 does not impair the ubiquitination of ERK20.**

TUBE assays were performed from RKO iCas9 AAVS1 (non-targeting control), LTN1 or UFM1 KO cell line upon 24 h expression of ERK0 (**A**, **C**) or ERK20 reporter (**B**, **D**) and 3 h treatment with 20 μM proteasome inhibitor MG132 or DMSO as control. Protein levels are analyzed by immunoblotting. Representative duplicates. FL full length, AP arrested peptide, g glycosylation, * degradation products.


© The Author(s)

## 2.2. Dual regulation of the unfolded protein response by IGF2BP3 during ER stress

*2.2.1. Preamble*

This manuscript addresses the regulation of the unfolded protein response (UPR), a conserved set of signaling cascades that maintain ER homeostasis, by an RNA-binding protein IGF2BP3. During ER stress, marked by an increase in misfolded proteins in the ER, the UPR is activated, leading to transcriptional upregulation of ER chaperones, ER degradative machineries (ER-associated degradation and ER-phagy), and lipid synthesis enzymes to increase ER size and, consequently, its folding capacity. In addition to the transcriptional regulation, many UPR effector mRNAs are also post-translationally regulated, however, the mechanism of this regulation has not been understood.

This paper shows that the conserved RNA-binding protein IGF2BP3 binds UPR target transcripts during ER stress, leading to their destabilization. This is achieved by increased IGF2BP3 interaction with the mRNA decapping complex and the UPR sensor RNAse IRE1 during ER stress. The destabilization of IGF2BP3's target mRNAs reduces ER translational burden and helps alleviate stress. Additionally, IGF2BP3 induces transcriptional reprogramming by stabilizing the transcription factor HMGA2, which, in turn, upregulates the transcription of UPR target genes. This dual regulation relieves the translational burden under ER stress conditions while ensuring a potent UPR response and maintaining ER proteostasis.

The work presented in this manuscript addresses the overarching question of this thesis: the regulation of ER quality control and ER translational proteostasis.

This paper has been accepted for publication in *Genes & Development* on March 19th, 2026 under the doi: 10.1101/gad.353291.125.

2.*2.2. Contribution statement*

For the following manuscript, I have established and optimized the aggresome assays, performed puromycin incorporation assays, analyzed the data, and edited the manuscript before submission.

# Dual regulation of the unfolded protein response by IGF2BP3 during ER stress

Aleksandra S Anisimova[1,2], Sabina Omerbegovic [1,5], Milica Mihailovic [1,2], Sascha Gratzl [1,2], Harald Hornegger[1,2], Irmgard Fischer[1], Gijs A Versteeg[1,3], Stefan L Ameres[1,4], G Elif Karagöz[1,5,#]

1. Max Perutz Labs, Vienna BioCenter Campus, Dr.-Bohr-Gasse 9, 1030, Vienna, Austria.
2. Vienna BioCenter PhD Program, a Doctoral School of the University of Vienna and the Medical University of Vienna, A-1030 Vienna, Austria.
3. University of Vienna, Center for Molecular Biology, Department of Microbiology, Immunobiology, and Genetics, Dr.-Bohr-Gasse 9, 1030, Vienna, Austria.
4. University of Vienna, Center for Molecular Biology, Department of Biochemistry and Cell Biology, Dr.-Bohr-Gasse 9, 1030, Vienna, Austria.
5. Medical University of Vienna, Center for Medical Biochemistry, Dr.-Bohr-Gasse 9, 1030, Vienna, Austria.

# Correspondence: guelsuen.karagoez@meduniwien.ac.at

## Abstract

Misfolded protein accumulation in the endoplasmic reticulum (ER) perturbs cellular homeostasis, causing pathological ER stress. While a transcriptional response is paramount for the Unfolded Protein Response (UPR), which counters ER protein-folding overload, multiple UPR-linked mRNAs are post-transcriptionally regulated. However, the mechanisms mediating this regulation remain unclear. Here, we reveal specific interactions between the conserved RNA-binding protein IGF2BP3 and transcripts encoding UPR effectors. During ER stress, IGF2BP3 destabilizes many of its target transcripts, including UPR effectors. Mechanistically, ER stress enhances IGF2BP3's association with the mRNA decapping complex and the ER stress sensor RNase IRE1, which correlates with a shift toward mRNA destabilization. Unexpectedly, prolonged depletion of IGF2BP3 inhibits the UPR via decreased transcription of UPR target genes. Together, our findings suggest that IGF2BP3 contributes to proteostasis during ER stress through a dual mechanism: directly promoting mRNA degradation to reduce translation and folding burden and indirectly supporting transcriptional activation of the UPR.

## Introduction

Protein-folding homeostasis is paramount for robust cell function. Underlining the importance of this homeostasis, various stress-response pathways surveil and react to protein-folding perturbations. In the endoplasmic reticulum (ER), a critical site for the folding of secreted and transmembrane proteins, protein-folding homeostasis is maintained by a conserved signaling cascade known as the “Unfolded Protein Response” (UPR). In metazoans, the UPR is driven by three parallel ER-tethered sensor/transducers: IRE1, PERK, and ATF6. Each sensor monitors the accumulation of misfolded proteins in the ER and takes corrective actions to restore homeostasis.

The UPR increases protein folding and degradation capacity in the ER through transcriptional upregulation of chaperones, foldases, ER-associated degradation (ERAD), and ER-phagy components (Travers, Patil et al. 2000, Lee, Iwakoshi et al. 2003, Sriburi, Jackowski et al. 2004, Bernales, McDonald et al. 2006, Acosta-Alvear, Zhou et al. 2007, Bommiasamy, Back et al. 2009, Schuck, Prinz et al. 2009, Schuck, Gallagher et al. 2014, Khaminets, Heinrich et al. 2015, Fumagalli, Noack et al. 2016, Grumati, Morozzi et al. 2017). However, if homeostasis is not achieved in a timely manner, the UPR initiates cell death programs that eliminate defective cells for the benefit of the organism (Lin, Li et al. 2007, Lu, Liang et al. 2014). Together with the magnitude and duration of the ER stress, the interplay between the UPR branches sets molecular timers that govern the decision to either repair the damaged cell or eliminate it as a potential threat. These factors heavily depend on cell identity as well as metabolic and cellular state (Lin, Li et al. 2007, Lu, Liang et al. 2014).

While the UPR-driven transcriptional response is essential for maintaining ER homeostasis, cells also utilize a variety of post-transcriptional mechanisms to adapt to ER stress (Harding, Zhang et al. 1999, Harding, Zhang et al. 2000, Holcik and Sonenberg 2005, Walter P. and D. 2011). The early response to ER stress converges on the shutdown of global translation by the ER-tethered kinase PERK, which reduces global protein synthesis (Harding, Zhang et al. 1999, Harding, Zhang et al. 2000, Holcik and Sonenberg 2005, Walter P. and D. 2011). During translational shutdown, some translationally silenced mRNAs are protected from turnover, whereas others are degraded (Buchan and Parker 2009, Buchan, Nissan et al. 2010, Protter and Parker 2016). In parallel, the UPR sensor IRE1 cleaves ER-localized mRNAs via the regulated IRE1-dependent decay of messenger RNAs (RIDD), proposed to decrease the protein folding load in the ER (Hollien and Weissman 2006, Le Thomas, Ferri et al. 2021). Apart from its role in tuning protein synthesis into the ER, RIDD protects cells from apoptosis via opposing the transcriptional upregulation of the death receptor 5 (DR5) mRNA expression induced by the PERK-ATF4 branch (Lu, Lawrence et al. 2014). While it is clear that posttranscriptional mechanisms contribute to life-and-death decisions during ER stress, the mechanistic details of how this is achieved have been poorly understood.

RNA-binding proteins (RBPs) mediate post-transcriptional mechanisms that facilitate the adaptation to developmental and metabolic changes or cellular perturbations (Hentze, Castello et al. 2018, Gebauer, Schwarzl et al. 2021). Using immunoprecipitation coupled to mass

spectrometry analyses (IP-MS/MS) of the UPR sensor IRE1, we previously revealed that it is associated with a highly conserved RBP, IGF2BP3 (insulin-like growth factor 2 mRNA-binding protein 3), in a stress-dependent manner (Acosta-Alvear, Karagoz et al. 2018). IGF2BPs are a conserved family of RBPs that regulate mRNA fate by controlling target mRNA stability, localization, and translation (reviewed in (Degrauwe, Suva et al. 2016)). IGF2BPs were proposed to protect mRNAs from degradation by competing with microRNA binding (Jønson, Christiansen et al. 2014, Muller, Bley et al. 2018). More recently, IGF2BP family members have been shown to function as readers of m6A and m7G mRNA modifications. While all IGF2BPs guard m6A-modified mRNAs from decay, IGF2BP1 and IGF2BP3 facilitate the degradation of mRNAs harboring m7G modifications (Huang, Weng et al. 2018, Liu, Dou et al. 2024). Among the three IGF2BP paralogs in mammalian cells, IGF2BP1 and IGF2BP3 are expressed at high levels during early development (Leeds, Kren et al. 1997, Mueller-Pillasch, Pohl et al. 1999, Mori, Sakakibara et al. 2001), regulate mRNAs involved in cell growth and migration (Yaniv and Yisraeli 2002, Huttelmaier, Zenklusen et al. 2005, Noubissi, Elcheva et al. 2006, Bell, Wächter et al. 2013, Jønson, Christiansen et al. 2014, Conway, Van Nostrand et al. 2016), and are therefore necessary for healthy embryo development. Notably, expression of all IGF2BP paralogs is upregulated in various cancers, and this strongly correlates with poor patient outcomes, enhanced tumor growth, drug resistance, and metastasis (Hansen, Hammer et al. 2004, Bell, Wächter et al. 2013, Lederer, Bley et al. 2014).

Several studies show that during proteotoxic stress induced by heat shock or arsenite treatment, IGF2BPs promote mRNA stability by preventing mRNA degradation. Moreover, they facilitate target mRNA translation once the stress is relieved (Stöhr, Lederer et al. 2006, Weidensdorfer, Stohr et al. 2009, Huang, Weng et al. 2018). Given these data, IGF2BPs may mediate post-transcriptional regulation in response to organelle-specific stress. However, whether IGF2BP3 responds to ER stress and contributes to restoring ER homeostasis remains unclear.

In this study, we assessed the role of IGF2BP3 in regulating UPR-associated transcripts. Our data show that the stress-dependent association of IGF2BP3 with IRE1 is conserved across cell lines, revealing that IGF2BP3 binds to prominent UPR-effector transcripts. Using genome-wide transcriptome and mRNA stability analyses, we demonstrate that IGF2BP3 regulates the UPR at both the post-transcriptional and transcriptional levels, thereby forming a unique gene regulatory network that modulates the UPR.

## Results

### IGF2BP3 associates with IRE1 during ER stress

To decipher post-transcriptional mechanisms regulating mRNA fate during ER stress, we focused on the primary post-transcriptional regulator, the ER-tethered RNase IRE1, which binds to and cleaves the ER-bound mRNAs during ER stress. To this end, we characterized the interactome of the ER-tethered RNase IRE1, a key post-transcriptional regulator that binds and cleaves ER-localized mRNAs during ER stress. In a previous work, we mapped the IRE1 interactome by IP-MS/MS in HEK293T and multiple myeloma cells and identified select RBPs

associated with IRE1 (Acosta-Alvear, Karagoz et al. 2018). We hypothesized that RBPs that interact with IRE1 during ER stress regulate the stability of UPR-relevant mRNAs associated with IRE1. Among those RBPs, IGF2BP3 stood out, as it was also recovered in IRE1 IP-MS/MS under denaturing conditions after RNA-protein cross-linking, suggesting a robust association with IRE1 and RNA-containing complexes (**Supplemental Fig. S1A**).

To test whether the ER stress-induced increase in IGF2BP3 association with IRE1 extended across different cell types, we performed IPs of endogenous IRE1 followed by Western blot analysis in HCT116 cells. IGF3BP3's interaction with IRE1 increased 1.6-fold after 4 h of ER stress compared to unstressed controls. To address whether IGF2BP3 and IRE1 are bridged by RNAs, we performed IRE1 IPs in the presence of RNase. We found that the interaction between IRE1 and IGF2BP3 was partially sensitive to RNase treatment, indicating that both RNA-protein and protein-protein interactions contribute to their association (**Fig. 1A**). Consistent with this result, we also recovered IRE1 using reciprocal IGF2BP3 pull-downs in HEK293T cells in an ER stress-dependent manner (**Supplemental Fig. S1B**). From these results, we concluded that during ER stress IRE1 and IGF2BP3 exist in RNA-protein complexes. The fact that these complexes were identified across multiple cell types suggests their potential importance for general cellular biology.

**IGF2BP3 interacts with UPR target mRNAs**

The mRNAs interacting with IGF2BP3 under steady-state conditions have been well established (Hafner, Landthaler et al. 2010, Conway, Van Nostrand et al. 2016, Anisimova and Karagöz 2023), but it is unclear whether proteotoxic stress alters the binding landscape of IGF2BP3. To address this, we defined IGF2BP3-bound mRNAs during ER stress in HCT116 cells using Infra-Red Photoactivatable Ribonucleoside-enhanced Crosslinking and Immunoprecipitation (IR-PAR-CLIP) (Anisimova and Karagöz 2023). Due to extensive RNase cleavage and presence of T to C (T-C) transitions, which mark the crosslink position, this approach allows nucleotide-resolution detection of RBP-interaction sites in target RNAs (Hafner, Landthaler et al. 2010). IGF2BP3 IR-PAR-CLIP was performed under homeostatic conditions, during early response (1 h), and at peak response (4 h) time points after UPR induction by TM. As UPR target genes are transcriptionally upregulated under these conditions, we performed total transcriptome sequencing in parallel to account for changes in transcript levels.

On average IGF2BP3 IR-PAR-CLIP produced 45-times more unique deduplicated reads relative to the IgG controls with ~50% of the reads containing T-C transitions (**Supplemental Fig. S1C**). To identify IGF2BP3-bound transcripts we performed T-C aware peak calling using PARalyzer (Corcoran, Georgiev et al. 2011). Transcripts containing at least one cluster of IGF2BP3-crosslinked reads with more than 25 gene counts per million (CPM) and over 50% T-C conversions per read were considered IGF2BP3-bound. After correcting for transcript levels (IR-PAR-CLIP CPM > transcriptome CPM), IR-PAR-CLIP identified 2313 IGF3BP3-bound transcripts under homeostatic conditions (**Supplemental Fig. S1D, Supplemental Table S1**). A short ER stress induction (1 hour) did not significantly alter neither the levels of the hallmark UPR-target transcripts nor IGF2BP3 binding; however, a 4-hour treatment led to strong UPR

induction (**Fig. 1B**). Under these conditions, IGF2BP3 interacted with a transcript set largely overlapping that observed under control conditions, with 157 additional transcripts interacting exclusively during ER stress (**Supplemental Fig. S1D**). These transcripts were enriched in those involved in ER stress response and proteasomal degradation (**Supplemental Fig. S1E**). We further defined a list of 2470 IGF2BP3-bound transcripts present in either control or ER stress (4 h) conditions (**Supplemental Table S1**). Gene ontology analyses of those mRNAs revealed that regulation of transcription, protein degradation, differentiation, intracellular communication, and response to ER stress were the top-enriched biological processes (**Supplemental Fig. S1F**).

In agreement with the published data, our IGF2BP3 IR-PAR-CLIP analyses showed that under homeostatic conditions, IGF2BP3 binds to most of its target mRNAs through their 3' UTRs (**Supplemental Fig. S1G**) (Hafner, Landthaler et al. 2010, Anisimova and Karagöz 2023). While IGF2BP3's binding preference for 3' UTRs was not affected by ER stress, the IGF2BP3-binding motifs showed distinct differences (**Supplemental Fig. S2A**). The top five 5 nt-long motifs enriched in IGF2BP3-bound IR-PAR-CLIP reads included those with CA-rich sequences common among IGF2BP3 binding motifs (Conway, Van Nostrand et al. 2016, Schneider, Hung et al. 2019). Three motifs (UCCAG, AGCCU, and UGCCA) were common for both conditions. In contrast, upon stress, novel ACUGU and ACCUG motifs were highly enriched in comparison to a canonical CAUU-containing motif (Hafner, Landthaler et al. 2010). Fluorescence anisotropy experiments demonstrated that purified IGF2BP3 binds RNAs containing the ACUGU motif, which is enriched under ER stress, with an affinity comparable to that observed for the canonical UCCAG and CAUUU motifs (Kd $\approx$ 400 nM). In contrast, we only detected low-affinity binding to a negative control RNA (**Supplemental Fig. S2B**, **Supplemental Table S1**). These results indicated that IGF2BP3 associates with novel sequences during ER stress.

Next, we tested whether ER stress alters the pool of transcripts associated with IGF2BP3. Upon ER stress induction, the number of IGF2BP3-bound reads derived from UPR-induced genes increased. These UPR targets included genes encoding for the master transcription factors XBP1, ATF4, CHOP (*DDIT3*), and the major chaperones BiP (*HSPA5*) and DNAJB9 (**Fig. 1C**). At the same time, some canonical targets of IGF2BP3, such as *HMGA2* mRNA (Jønson, Christiansen et al. 2014), were depleted from the IGF2BP3-bound transcript pool (**Fig. 1C**). To assess the binding of IGF2BP3 to the UPR target transcripts we defined 228 genes that were upregulated at least 2-fold upon ER stress induction as "UPR-induced". To account for changes in mRNA levels, we next compared ER stress-induced changes in transcript levels with changes in IGF2BP3-bound transcripts (**Fig. 1D**) and calculated an "IGF2BP3 binding" score by normalizing the IR-PAR-CLIP reads to transcript levels (**Fig. 1E, F**). These analyses revealed that IGF2BP3 binds UPR-induced transcripts to a similar extent in both homeostatic and ER stress conditions, suggesting that for most genes the observed increase in IGF2BP3-bound reads results from increased transcription of UPR target genes during ER stress. However, while for multiple UPR targets IGF2BP3-bound reads increased linearly with increased expression, some transcripts such as *HSPA5* and *HSP90B1,* showed preferential IGF2BP3 binding during ER stress (**Fig. 1F, G, Supplemental Fig. S2C**). Additionally, we identified

several novel IGF2BP3 targets, such as *DDIT3,* which were only expressed during ER stress (**Fig. 1B, G**).

IGF2BP3 is a reader of $m^6A$ and internal $m^7G$-modified RNAs (Huang, Weng et al. 2018, Liu, Dou et al. 2024). As mRNA methylation is regulated under proteotoxic stress (Zhou, Wan et al. 2015, Wei, Harada et al. 2021), stress-induced changes in methylation could alter IGF2BP3 target association. We therefore tested whether these motifs are more frequent in IGF2BP3-bound reads under ER stress than under unstressed conditions. $m^6A$ modifications predominantly occur on consensus sequence motifs and are enriched in 5′-DRA*CH-3′ sequences (**DRACH**, D=A, G or U; H=A, C or U) (Linder, Grozhik et al. 2015). Analysis of the consensus DRACH motif in IGF2BP3-binding sites showed a stress-dependent increase in the enrichment of this motif (**Supplemental Fig. S2D**). Similarly, the consensus motifs for internal $m^7G$ deposition derived from recent transcriptome-wide mapping approaches (Malbec, Zhang et al. 2019, Zhao, Qing et al. 2023) showed a stress-dependent increase in the occurrence of these motifs (GANGAN) in IGF2BP3-bound RNAs, indicating that the deposition of these modifications might contribute to IGF2BP3's RNA selectivity during ER stress (**Supplemental Fig. S2D**). In line with these findings, the strongest IGF2BP3 binding peaks at the *HSPA5* 3′ UTR correspond to experimentally confirmed $m^6A$ ((Liang, Ye et al. 2024), see Materials and Methods) and $m^7G$ (Malbec, Zhang et al. 2019) deposition sites (**Supplemental Fig. S2E**).

Supporting our IP-MS/MS data, IGF2BP3 was bound to one-third of the transcripts interacting with IRE1 during ER stress (**Supplemental Fig. S2F**). The IGF2BP3-binding sites did not overlap with IRE1 RIDD cleavage sites on most of the common IRE1 and IGF2BP3-bound mRNAs. Those analyses suggested that IGF2BP3 binding does not compete with IRE1 (**Supplemental Fig. S2G**). To sum up, we found that IGF2BP3 interacts with transcripts encoding UPR target genes during ER stress, identifying IGF2BP3 as a potential post-transcriptional regulator of the UPR.

**IGF2BP3 depletion dampens UPR signaling**

Based on our findings above, we hypothesized that IGF2BP3 might post-transcriptionally regulate UPR-induced mRNAs. We, therefore, set out to identify transcripts that are functionally regulated by IGF2BP3. To this end, IGF2BP3 was depleted in colon carcinoma HCT116 cells by CRISPR/Cas9-mediated knockout (**Supplemental Fig. S3A**) and transcriptome analyses were performed under homeostatic and ER-stress conditions (**Supplemental Table S2**). IGF2BP3 knockout resulted in moderate changes in the total transcriptome (**Fig. 2A**). Specifically, it led to the downregulation of genes involved in regulation of transcription, cell proliferation and migration, development, and response to growth factors, consistent with previous reports (Lederer, Bley et al. 2014, Ennajdaoui, Howard et al. 2016, Mizutani, Imamachi et al. 2016, Anisimova and Karagöz 2023) (**Supplemental Fig. S3B**). To address the effect of IGF2BP3 depletion on the cellular response to ER stress, we defined 288 UPR target transcripts as those upregulated by more than two-fold upon ER stress including those bound by IGF2BP3 (58 transcripts) (**Fig. 2B, left panel**) and followed their levels upon IGF2BP3 depletion (**Fig. 2B, right panel**). Transcriptome analysis showed that the levels of the UPR target transcripts were

lower in IGF2BP3 knockouts compared to the parental cells under ER stress (**Fig. 2B, C**). While IGF2BP3 depletion had only a moderate impact on individual UPR effector transcripts (**Fig. 2B**), changes were evident when analyzed for the whole group (**Fig. 2C**). In contrast, the levels of other IGF2BP3-bound transcripts were less affected by IGF2BP3 CRISPR/Cas9-mediated knockout (**Fig. 2A, C**). Thus, IGF2BP3 specifically impacts UPR target transcripts during ER stress (**Fig. 2B, C**).

To account for the adaptation of cells to long-term depletion of IGF2BP3 and to bypass the clonal selection, we used siRNA-based depletion as an orthogonal approach to validate our findings (**Supplemental Table S2**). Using an siRNA pool against IGF2BP3, we obtained 75 percent depletion in 48 hours in HCT116 cells (**Supplemental Fig. S3C, D**). The siRNA knockdown experiments confirmed the data obtained by the CRISPR/Cas9-based IGF2BP3 knockouts, indicating that depletion of IGF2BP3 dampens UPR signaling (**Fig. 2D**). Reverse transcription quantitative PCR (RT-qPCR) analyses of IGF2BP3-interacting transcripts confirmed these results at milder, closer to physiological ER stress conditions, showing that IGF2BP3 knockout leads to a decrease in the levels of major UPR targets downstream of PERK (*ATF4*, *DDIT4*), IRE1 (*XBP1* total and spliced), and ATF6 (*HSPA5*) (**Fig. 2E**). Intriguingly, our analyses showed that during ER stress, depletion of IGF2BP3 not only reduced the levels of IGF2BP3-bound UPR targets but also affected those that are not its direct interactors (**Fig. 2B, C, D**). The data suggested that IGF2BP3 depletion leads to the downregulation of the entire pathway, possibly through secondary, indirect mechanisms. We confirmed these findings using global proteomic analysis of wild-type cells and IGF2BP3 knockouts, demonstrating that IGF2BP3 depletion decreased the protein abundance of UPR targets during ER stress (**Fig. 2F, Supplemental Fig. S3E, Supplemental Table S3**). Altogether, our data showed that IGF2BP3 depletion tunes down UPR.

**IGF2BP3 shapes the UPR through transcriptional feedback loops**

As mentioned above, our genome-wide approaches revealed that, in addition to IGF2BP3-bound transcripts, the levels of UPR targets not directly bound to IGF2BP3 also decreased upon IGF2BP3 depletion, suggesting a secondary, indirect effect (**Fig. 2B, C, D, F**). Because IGF2BP3 controls the stability of several mRNAs involved in transcriptional regulation, we hypothesized that the indirect effects observed upon IGF2BP3 depletion result from transcriptional reprogramming.

To uncover the primary mechanism of IGF2BP3-mediated regulation during ER stress, we aimed to uncouple transcriptional reprogramming from post-transcriptional regulation. To test whether transcriptional reprogramming contributes to the changes in the transcript levels upon IGF2BP3 depletion, we used thiol (SH)-linked alkylation for the metabolic sequencing of RNA (SLAMseq) method (**Fig. 3A**). In SLAMseq, nascent transcripts are metabolically labelled, allowing assessment of *de novo* RNA synthesis (Herzog, Reichholf et al. 2017). We performed two hours of pulse labeling in HCT116 cells with $s^4U$, followed by total RNA extraction, alkylation, and mRNA 3′-end library preparation under homeostatic conditions and after 5 hours of ER stress (with $s^4U$ added for the last two hours) (**Supplemental Table S4**). First, we followed

changes in transcript levels synthesized during the 2 hours of the $s^4U$ pulse (*de novo* transcriptome, T-C reads). SLAMseq analyses showed that siRNA-mediated depletion of IGF2BP3 decreased transcription of the UPR target genes (**Fig. 3B, C**) indicating that IGF2BP3 indirectly contributes to transcriptional reprogramming, potentially by affecting the expression of one or more transcriptional regulators. Indeed, several mRNAs encoding for transcription factors were downregulated upon IGF2BP3 depletion (**Supplemental Fig. S4A**).

To dissect this transcriptional circuitry, we focused on two of the top candidate regulators, whose mRNA levels decreased strongly upon IGF2BP3 depletion. The canonical IGF2BP3 target HMGA2 (Jønson, Christiansen et al. 2014) (**Supplemental Fig. S4B**), which encodes a nonhistone chromatin factor (Pfannkuche, Summer et al. 2009), and a *forkhead* box transcription factor FOXD1 (Hatini, Huh et al. 1996, Quintero-Ronderos and Laissue 2018), (**Supplemental Fig. S4C**). siRNA-mediated knockdown of either HMGA2 or FOXD1 significantly reduced levels of the UPR target transcripts specifically under ER stress, indicating a functional contribution to the UPR (**Fig. 3D, Supplemental Fig. S4D, E**). In contrast, depleting these factors did not affect the control transcripts *UBC* and *EEF1A1,* which are transcribed at high rates but not ER stress-regulated, supporting the selective role of HMGA2 and FOXD1 in UPR regulation (**Supplemental Fig. S4F, G**). Notably, HMGA2 knockdown also reduced *FOXD1* mRNA levels (**Supplemental Fig. S4H**), suggesting that HMGA2 acts upstream in this transcriptional program. In line with this model, IR-PAR-CLIP did not detect IGF2BP3 binding to *FOXD1* mRNA (**Supplemental Table S1**). Moreover, depletion of either IGF2BP3 or HMGA2 produced similar effects on the UPR target transcripts, and co-depletion did not show an additive effect (**Supplemental Fig. S4I**). These data suggest that HMGA2 is the primary driver of the transcriptional programming downstream of IGF2BP3.

To systematically assess the contribution of post-transcriptional regulation to the levels of UPR target transcripts, we calculated changes in mRNA stability by comparing per-gene average T-C conversion rates following IGF2BP3 depletion. In SLAM-seq, T-C conversions mark newly synthesized ($s^4U$-labeled) RNA. The T-C conversion rate represents the ratio of T-C conversions to the total T coverage per gene (see Materials and Methods) and therefore reflects the relative contribution of newly synthesized versus pre-existing mRNA. A decrease in the T-C conversion rate indicates stabilization, whereas an increase indicates destabilization. Surprisingly, our analyses showed that IGF2BP3 depletion increased the stability of IGF2BP3-bound transcripts, including those encoding for the UPR target genes, particularly during ER stress (**Fig. 3E, Supplemental Fig. S4J**). These data indicated that IGF2BP3-driven post-transcriptional and transcriptional mechanisms control UPR transcript levels in opposing directions.

Consistent with IGF2BP3 adopting a more destabilizing function under stress, when transcription was inhibited by actinomycin D (ActD) treatment, IGF2BP3 depletion increased the levels of *XBP1* (spliced and total) mRNAs during ER stress (**Fig. 3F, G, Supplemental Fig. S4K**). A similar trend was observed for *DDIT3* (CHOP) (**Fig. 3F, G**). Notably, this destabilization effect was specific to ER stress and was not observed for a non-target control transcript, *UBC* (**Supplemental Fig. S4L**). These data suggested that IGF2BP3 regulates the UPR in two ways: 1. It binds to and destabilizes its target mRNAs during ER stress. 2. It indirectly upregulates the

transcription of the UPR target genes. This transcriptional regulatory mechanism supports differential regulation of UPR target transcripts by IGF2BP3 during ER stress. The transcriptional response is more potent, and this way, IGF2BP3 facilitates the UPR. This model explains how IGF2BP3 depletion leads to decreased levels of the UPR target transcripts, while its depletion increases the stability of its post-transcriptional targets. The IGF2BP3-driven dual regulatory mechanism might allow cells to reduce the protein-folding burden while ensuring they elicit a potent UPR during ER stress.

**IGF2BP3 facilitates mRNA degradation during ER stress**

Our transcriptomics and SLAMseq analyses showed that siRNA-mediated IGF2BP3 depletion resulted in both stabilization and destabilization of IGF2BP3-bound transcripts under homeostatic conditions. Most top-regulated transcripts encoded proteins involved in cell proliferation and motility (e.g., *HMGA2*, *CARM1, TRIB1*, *NACC2*) (An, Kim et al. 2004, Frietze, Lupien et al. 2008, Xuan, Wang et al. 2013, Singh, Han et al. 2023). Notably, several of these target mRNAs encoded transcription factors (*ZNF385A*), regulators of gene expression (*HMGA2*, *CARM1, NACC2*), or RNA metabolism (*AGO2, ZFP36L1*), underlining that IGF2BP3-mediated post-transcriptional regulation impinges on potent gene regulatory networks to remodel the transcriptome.

The SLAM-seq analyses also revealed that, in contrast to homeostatic conditions, IGF2BP3 binding is associated with destabilization of its target mRNAs during ER stress (**Fig. 3E**)**.** The observed increase in IGF2BP3-mediated destabilization upon ER stress was specific for IGF2BP3-bound transcripts (**Fig. 3E**) and was also evident at the level of total mRNA abundance (**Fig. 4A**). In line with these analyses, IGF2BP3 destabilized a higher number of transcripts during ER stress compared to homeostatic conditions (**Fig. 4B, C**)**.** Together, these findings suggest that ER stress shifts IGF2BP3 function toward destabilizing its target transcripts.

Our data confirmed that IGF2BP3 stabilizes *HMGA2* mRNA (Jønson, Christiansen et al. 2014), whereas it destabilizes *ZFP36L1* mRNA (Ennajdaoui, Howard et al. 2016), as reported in earlier studies (**Fig. 4B, D, E**). In line with the published work, depletion of IGF2BP3 resulted in lower levels of *HMGA2* mRNA under homeostatic conditions, supporting the notion that IGF2BP3 binding protects this transcript from decay (**Fig. 4B, C, D**). The SLAMseq analyses further showed that the regulation is achieved at the posttranscriptional level, as IGF2BP3 depletion did not result in decrease of *HMGA2* transcription (**Supplemental Fig. S5A**). Using RT-qPCR analyses, we confirmed that IGF2BP3 did not stabilize *HMGA2* mRNA as efficiently during ER stress as under homeostatic conditions (**Fig. 4E**). These results were corroborated by actinomycin D chase experiments, which showed that IGF2BP3 depletion decreased the half-life of *HMGA2* mRNA under homeostatic conditions while not impacting it during ER stress (**Fig. 4F**).

Consistent with our data suggesting that IGF2BP3 switches to a degradative function during ER stress, we observed more pronounced destabilization of a subset of transcripts that IGF2BP3

also destabilizes under homeostatic conditions (**Fig. 4B, C, Supplemental Fig. S5A**). Both the transcriptomics (**Fig. 4B, C, D, Supplemental Fig. S5A**) and RT-qPCR data (**Fig. 4E**) showed that IGF2BP3 depletion increased the levels of a well-described target, *ZFP36L1* mRNA under homeostatic conditions supporting earlier work (Ennajdaoui, Howard et al. 2016) that proposed IGF2BP3 facilitates *ZFP36L1* mRNA degradation. This effect was more pronounced during ER stress (**Fig. 4C, D, E**), with *ZFP36L1* mRNA showing an increased half-life upon IGF2BP3 depletion under stress conditions in actinomycin D chase experiments (**Fig. 4F**). These analyses indicated that ER stress modulates IGF2BP3 function, shifting the functional consequences of IGF2BP3 binding towards mRNA degradation.

We next asked whether IGF2BP3-mediated mRNA degradation reduces translational burden during ER stress. To measure global translational output, we performed puromycin incorporation assays in wild-type and IGF2BP3-depleted cells under ER stress. IGF2BP3 knockdown resulted in increased puromycin incorporation, indicating elevated translation (**Fig. 4G, H**). Importantly, we found that depletion of IGF2BP3 under those conditions led to increased protein aggregation (**Fig. 4I**). These results reveal the importance of IGF2BP3-mediated posttranscriptional regulation in maintaining a balance between translation and protein folding during the ER stress. To summarize, these findings suggest that IGF2BP3-dependent mRNA degradation helps limit translational burden during ER stress.

**ER stress promotes the association of IGF2BP3 with the mRNA decapping complex**

The association of IGF2BP3 with the mRNA degradation machinery was previously proposed to regulate a subset of its target mRNAs (Ennajdaoui, Howard et al. 2016, Mizutani, Imamachi et al. 2016, Latifkar, Wang et al. 2022). Therefore, we employed proteomics to investigate whether changes in the IGF2BP3 interactome explain the increase in IGF2BP3-mediated degradation during ER stress. To this end, we immunoprecipitated IGF2BP3 from HCT116 cells (**Supplemental Table S5**). The proteomics analyses showed that IGF2BP3 co-IP recovered proteins involved in almost all distinct steps of mRNA metabolism including transcription (RNA Pol II subunits, transcription factors), mRNA splicing (spliceosome components, SR proteins), export (THO complex subunits, MAGOH, RBM8A) and translation (ribosomal proteins) (**Supplemental Table S5, Supplemental Fig. S6A, B**), supporting the model that IGF2BPs are loaded onto nascent transcripts in the nucleus and shuttle to the cytoplasm (Pan, Huttelmaier et al. 2007). IGF2BP3 also interacted with signal recognition particle (SRP) components, showing that IGF2BP3 binds to mRNAs during active translation en route to the ER, which aligns with our data. Apart from these factors, our analyses identified an association of IGF2BP3 with the RNA degradation machinery (RNA deadenylation and decapping complex, exosome, XRN1) under both homeostatic and ER stress conditions (**Supplemental Table S5, Supplemental Fig. S6A**). These data supported the notion that IGF2BP3 accompanies its mRNA targets from synthesis to degradation.

To reduce complexity in our experiments, we aimed to eliminate long-distance RNA-bridged interactors and treated the samples with RNase. RNase treatment reduced the abundance of many interactors, suggesting that they associate with IGF2BP3 through RNA-bridged interactions. Nonetheless, most of its interactors were still detected in the co-IP likely because a

large portion of IGF2BP3s is embedded within mRNP complexes that are inaccessible to RNases (**Supplemental Fig. S6C**). The highly RNase-sensitive interactors were enriched for proteins involved in mRNA splicing, maturation and export (**Supplemental Fig. S6D**). RBPs and components of the mRNA degradation machinery showed variable RNase sensitivity. For instance, YBX1, HuR (ELAVL1), G3BP1/2, PABPC1, AGO2, and LSM complex were highly RNase sensitive. The RBPs FXR1/2, RNases IRE1 and XRN1, and the components of the decapping machinery (EDC3, EDC4, DCP1A, DCP2) were comparatively RNase-resistant, indicating that they are part of more compact assemblies with IGF2BP3 mediated by both protein and RNA interactions (**Supplemental Fig. S6C**).

While ER stress caused only modest changes in IGF2BP3 binding to the majority of interacting proteins, its association with a subset of proteins, including RNase IRE1, increased (**Fig. 5A**), supporting our initial findings (**Fig. 1A, Supplemental Fig. S1A, B**). Notably, during ER stress, IGF2BP3 bound more strongly to all components of the mRNA decapping machinery (EDC3, EDC4, DCP1A, DCP2) (**Fig. 5A, B, Supplemental Fig. S6E**), which is in line with the increase of its pro-degradatory function during ER stress. We validated this finding by performing co-IP of split-GFP–tagged IGF2BP3 from HEK293T cells. EDC4 was recovered in the IGF2BP3 IP, and its interaction increased upon ER stress, supporting the endogenous co-IP–MS results (**Fig. 5C, D**). We further corroborated our findings by performing a reciprocal co-IP of another decapping complex component, EDC3, tagged with split-mNeonGreen (mNG), which recovered IGF2BP3 and confirmed its increased association with the decapping complex upon ER stress (**Fig. 5E, F**). These data suggested that increased interaction of IGF2BP3 with the mRNA decapping machinery might enable more efficient degradation of its target mRNAs during ER stress.

To identify proteins mediating the specific interaction of IGF2BP3 with the mRNA decapping complex, we performed an AlphaFold2-Multimer *in silico* screen of pairwise protein-protein interactions between IGF2BP3 and confident interactors identified by proteomics analyses (Jumper, Evans et al. 2021, Evans, O'Neill et al. 2022, Mirdita, Schutze et al. 2022). In AlphaFold, a high interface-predicted template modeling score (ipTM score > 0.6) indicates high confidence interfaces. Since our dataset contained many RBPs with disordered segments, we used the average PEAK score. The average PEAK score quantifies the predicted error in the relative position of two residues and is more sensitive in identifying regions of high confidence for proteins with smaller interaction surfaces and interactions involving disordered regions (Jumper, Evans et al. 2021, Evans, O'Neill et al. 2022, Mirdita, Schutze et al. 2022). The AlphaFold2-Multimer screen identified 14 highly confident IGF2BP3 protein interactors with an average PEAK score larger than 0.75. EDC3 was the second top interactor of IGF2BP3 with an average PEAK score of 0.87 (**Fig. 5G**). To validate those findings, we performed AlphaFold3 (Abramson, Adler et al. 2024) prediction with subdomains of IGF2BP3 and EDC3. IGF2BP3 comprises two N-terminal RNA-recognition motif (RRM) domains and four K Homology (KH) domains connected with two disordered linkers (Schneider, Hung et al. 2019). EDC3 comprises an N-terminal SM domain connected to the YjeF domain by a long disordered segment (Tritschler, Eulalio et al. 2007) (**Fig. 5H, I**). The AlphaFold3 prediction of the complexes formed between the proteins' subdomains revealed that the RRM2 domain of IGF2BP3 interacts with the YjeF domain of EDC3 with high confidence (ipTM = 0.72) (**Fig. 5H,**

**I, Supplemental Fig. S7A**). Importantly, our high-throughput AlphaFold2-Multimer predictions identified the same interaction surface between IGF2BP3 and EDC3 using the full-length proteins, increasing our confidence. In contrast, AlphaFold3 did not predict a confident interaction between other subdomains of both proteins (**Supplemental Fig. S7A**).

To experimentally validate the binding interface predicted by the structural models, we engineered a quadruple IGF2BP3 mutant (I88A, P90A, H91A, W94A) to impair its binding to EDC3 and called it IGF2BP3-4A mutant (**Fig. 5I**). We confirmed that IGF2BP3-4A mutant behaves as wild-type IGF2BP3 during purification (**Supplemental Fig. S7B**). Moreover, we found that purified IGF2BP3-4A displays secondary structure features comparable to those of the wild-type protein (**Supplemental Fig. S7C**), indicating mutations do not impact IGF2BP3 stability. We next co-expressed GFP-tagged wild-type EDC3 with FLAG-tagged wild-type IGF2BP3 or IGF2BP3-4A in HCT116 IGF2BP3 knockout cells and performed pulldown experiments to assess the interaction. Our data revealed that the IGF2BP3-4A mutant is largely impaired in binding to EDC3 (**Fig. 5J, K**), indicating that the interaction surface identified by the Alphafold predictions is essential for IGF2BP3 binding to EDC3. Altogether, we identified a novel interaction between IGF2BP3 and the mRNA decapping complex.

IGF2BP3's KH domains are responsible for RNA recognition, whereas its RRM domains bind RNA with relatively low affinity and specificity (Jia, Gut et al. 2018, Schneider, Hung et al. 2019). In other RNA-binding proteins, the RRM domains also participate in protein–protein interactions (Maris, Dominguez et al. 2005); we now show that RRM2 mediates IGF2BP3's binding to EDC3 and does not overlap with RNA-binding by the RRM1 domain (Jia, Gut et al. 2018) (**Fig. 5I**). Similarly, EDC3 dimerization is mediated by its YjeF domain, and the IGF2BP3 binding does not interfere with its self-association (Ling, Decker et al. 2008).

To determine the functional relevance of this interaction, we reintroduced wild-type IGF2BP3 or the IGF2BP3-4A mutant into IGF2BP3 knockout cells via lentiviral transduction. After confirming expression levels comparable to endogenous IGF2BP3 (**Supplemental Fig. S7D, E**), we evaluated the impact of disrupting the IGF2BP3–EDC3 interaction on target transcripts by RT-qPCR. Expression of the IGF2BP3-4A mutant resulted in higher levels of IGF2BP3 target mRNAs (**Fig. 5L**). In contrast, it did not affect control mRNAs, which were not destabilized by IGF2BP3 (**Supplemental Fig. S7F**), supporting our model. Interestingly, *ZFP36L1* levels were unchanged upon disruption of the IGF2BP3–decapping complex interaction, consistent with a proposed miRNA-dependent mechanism for its degradation (Ennajdaoui, Howard et al. 2016). To summarize, our findings converge on the model that the increased association of IGF2BP3 with the mRNA decapping complex shifts its function towards promoting target transcript degradation during ER stress.

## Discussion

Among its many essential functions, the ER is the site of folding and maturation of secreted and transmembrane proteins, which together comprise approximately one-third of the proteome. Cells need to rapidly adapt to changes in ER protein-folding demands, as separating protein synthesis and folding into distinct compartments poses a challenge. To overcome this, cells use

diverse post-transcriptional and translational mechanisms to adjust the ER protein-folding load. Here, we discovered that IGF2BP3-driven post-transcriptional mechanisms facilitate mRNA degradation, as well as indirectly tune transcription to generate gene regulatory networks that promote UPR signaling while relieving protein-folding load on the ER.

Based on our published proteomics data on the interaction of the ER stress sensor RNase IRE1 with IGF2BP3 (Acosta-Alvear, Karagoz et al. 2018), here we explored the role of IGF2BP3 in post-transcriptional regulation of mRNA fate during ER stress. Our IR-PAR-CLIP analyses revealed that IGF2BP3 binds to UPR target transcripts during ER stress, including those encoding the major ER chaperones (BiP, calreticulin) and the master UPR transcription factors, XBP1, ATF4, and CHOP. Using complementary approaches to probe for post-transcriptional and transcriptional (RNA-Seq and SLAMseq) changes upon IGF2BP3 depletion, we discovered a dual regulatory role mediated by IGF2BP3-driven post-transcriptional control that maintains cellular homeostasis during ER stress. The SLAMseq analyses revealed that upon ER stress IGF2BP3 indirectly promotes transcriptional branches of the UPR, while simultaneously facilitates degradation of its broad mRNA target pool. This IGF2BP3-driven dual regulation helps cells to decrease cellular protein folding burden while enabling them to efficiently express UPR target mRNAs (**Fig. 6**).

Mechanistically, IGF2BP3 activates the UPR by stabilizing its canonical direct target, *HMGA2*. HMGA2 is a non-histone chromatin factor that controls gene expression by altering chromatin architecture (Pfannkuche, Summer et al. 2009) and supports transcriptional programs linked to embryonic development (Zhou, Benson et al. 1995) and oncogenesis (Fedele, Berlingieri et al. 1998, Mansoori, Mohammadi et al. 2021). Our experiments identify HMGA2 as a key mediator of IGF2BP3-driven transcriptional regulation of UPR genes. Notably, we identified FOXD1, a *forkhead* box transcription factor ;(Hatini, Huh et al. 1996, Quintero-Ronderos and Laissue 2018), as a downstream target of HMGA2 that contributes to UPR activation. The transcriptional branches of the UPR are controlled by a complex network of transcription factors (Jimenez-Beltran, Valle-Bautista et al. 2026). In line with this, our data show that HMGA2 promotes transcriptional feedback loops and upregulates multiple UPR genes across all three branches. Supporting our findings, HMGA2 was shown to promote ATF4 transcription (Luo, Zhang et al. 2023).

In addition to IGF2BP3-mediated regulation of UPR effector RNAs, our data revealed that ER stress leads to a functional switch in IGF2BP3, increasing its destabilizing function. In line with these observations, we discovered that ER stress modulates IGF2BP3 interaction with its canonical targets. IGF2BP3 stabilizes *HMGA2* mRNA by protecting it from miRNA-driven degradation (Jønson, Christiansen et al. 2014). Notably, under mild ER stress, IGF2BP3 protects HMGA2, but under harsher ER stress conditions, IGF2BP3 binding to HMGA2 mRNA decreases, leading to less efficient stabilization and reduced HMGA2 transcript levels. This mechanism may contribute as a negative regulator of the UPR, helping to prevent excessive activation. Beyond the UPR, HMGA2 regulates key programs in embryonic development, stem cell maintenance, and tumorigenesis (Pfannkuche, Summer et al. 2009, Ashar, Chouinard et al. 2010, Vignali and Marracci 2020). Therefore, the decrease in HMGA2 levels during ER stress

might also affect these processes, suggesting a broader impact of IGF2BP3-mediated regulation under stress.

IGF2BP3 stabilizes its target mRNAs during heat shock stress (Huang, Weng et al. 2018), suggesting that IGF2BP3 can drive opposing outcomes for its target transcripts depending on the cellular input. This dynamic and plastic response aligns with the cellular need to adjust transcript levels rapidly during proteotoxic stress. Importantly, IGF2BP3 depletion increased global translational output and protein aggregation under ER stress conditions, highlighting the physiological relevance of IGF2BP3-mediated mRNA destabilization.

Our IP-MS/MS analyses of IGF2BP3 revealed that IGF2BP3 strongly associates with all the components of the mRNA decapping complex, an interaction that increases around 50% during ER stress. Moreover, a high-throughput AlphaFold2-multimer screen identified a novel interaction surface between EDC3 and IGF2BP3 with high confidence, and an IGF2BP3 mutant engineered to disrupt this interaction was impaired in its binding to EDC3, supporting these findings. Supporting our findings, we further show that disrupting IGF2BP3–EDC3 interaction increases the levels of mRNAs destabilized by IGF2BP3. Altogether, we conclude that the increased association of IGF2BP3 with the mRNA decapping complex and RNase IRE1 enhances the degradation of its targets during ER stress. Future work will provide insights into the mechanisms that mediate the preferred association of the mRNA decapping complex with IGF2BP3 during ER stress.

IGF2BP3 is an essential regulator of early development, and its overexpression in various tumors correlates with poor prognosis and cancer aggressiveness (Lederer, Bley et al. 2014, Mizutani, Imamachi et al. 2016, Xu, Sheng et al. 2019). Similarly, physiological UPR contributes to development and differentiation, while cancer cells hijack this process to promote their growth (Salvagno, Mandula et al. 2022). We hypothesize that the dual-layered regulation we have uncovered allows cells to shift between opposing IGF2BP3 regulatory effects on UPR targets implying a cell state-specific regulation. While this regulatory plasticity may contribute to exquisite regulation during development, the balance may be tipped in cancer and impact UPR-driven cell fate decisions, presenting a novel avenue for therapeutic targeting. To sum up, we discovered a novel IGF2BP3-mediated dual regulatory mechanism that ensures an adaptive response to ER stress.

## Competing interest statement

S.L.A. declare competing interests based on a granted patent related to SLAMseq. S.L.A. is co-founder, advisor, and member of the board of QUANTRO Therapeutics GmbH.

## Acknowledgments

We are grateful to Niko Popitsch for support with the transcriptomics experiments and analyses of sequencing data. We are thankful to the Vienna BioCenter Next-Generation Sequencing Facility for deep sequencing services, Max Perutz Labs Proteomics Facility for mass

spectrometry analyses, Max Perutz Labs BioOptics FACS Facility for assistance with cell sorting and analytical experiments, and Protein Technologies Facility at Vienna BioCenter Core Facilities (VBCF) for assistance with circular dicroism experiments. We thank Roland Foisner and Nana Naetar-Kerenyi for their input on CRISPR/Cas9 editing. We thank Erinc Hallacli for valuable assistance with co-immunoprecipitation experiments. RKO cells were a kind gift of the Johannes Zuber lab. G.E.K. acknowledges funding from the Austrian Science Fund (FWF-SFB F79, FWF-DOC 177B). For open access purposes, the author has applied a CC-BY public copyright license to any author-accepted manuscript version arising from this submission. A.S.A. and M.M. are supported by the DOC Fellowship Programme of the Austrian Academy of Sciences.

## Author Contributions

ASA and GEK conceived the project. ASA designed and performed most of the experiments, and analyzed the data. SO performed selected immunoprecipitation and RT-qPCR experiments. MM performed puromycin incorporation and aggresome detection experiments. HH and SG performed biochemical characterization of the IGF2BP3 protein and fluorescent anisotropy assays. IF performed imaging experiments. SLA, GV, and GEK supervised experimental procedures. ASA and GEK wrote the first draft, and all the authors edited the manuscript. GEK acquired funding.

## Materials and methods

### Mammalian cell culture

HCT116 WT cells were a kind gift from the Manuela Baccarini Lab (Max Perutz Labs). HCT116 cells conditionally expressing doxycycline-inducible (tetON) OsTIR1 were obtained from the Masato Kanemaki lab (Natsume, Kiyomitsu et al. 2016). RKO cells expressing doxycycline-inducible Cas9 were a kind gift from Johannes Zuber (IMP, Vienna, Austria) (de Almeida, Hinterndorfer et al. 2021). HEK293T cells expressing splitGFP-IGF2BP3 were a kind gift of Manuel Leonetti established using published protocols (Leonetti, Sekine et al. 2016). HEK293T cells expressing split mNeonGreen-EDC3 were a kind gift of Manuel Leonetti (Chen-Zuckerberg Biohub, USA (Cho, Cheveralls et al. 2022)).

HCT116 cells were cultured in McCoy's 5A (modified) medium (Sigma, M9309) supplemented with 10% fetal bovine serum (Gibco, 10437028), 2 mM L-Glutamine (Sigma, G7513), 1% Pen/Step (Sigma, P0781). HEK293T cells were cultured in high-glucose DMEM media (Sigma, D5796) supplemented as above. RKO cells were cultured in RPMI-1640 media (Sigma, R8758) supplemented with 10% fetal bovine serum (Gibco, 10437028), 2 mM L-Glutamine (Sigma, G7513), 1% Pen/Step (Sigma, P0781), 1x non-essential amino acids (Thermo Scientific, 11140050), and 2 mM sodium pyruvate (Gibco, 11360070). All cell lines were cultured in a humidified incubator at 37°C and 5% CO2 and regularly tested for Mycoplasma infection with the EZ-PCR™ Mycoplasma Detection Kit (Biological Industries).

### Western blotting

80% confluent cells were lysed with RIPA buffer (150 mM NaCl, 1% NP-40, 0.5% Sodium deoxycholate, 0.1% SDS, and 25 mM TRIS pH 7.4) with 1x EDTA-free protease inhibitor cocktail (Roche). Lysates were clarified using a table-top centrifuge at maximum speed (20,000 g) for 20 min at 4°C. Western blot samples were denatured at 95 °C for 5 min in 1x SDS sample buffer (50 mM Tris-HCl pH 6.8, 2% SDS, 0.1% Bromophenol blue, 10% glycerol, 20 mM DTT). Following denaturing, the samples were loaded onto a 10%, 12% or 15% sodium dodecyl sulfate (SDS) gel. Proteins were transferred onto a 0.2 µm nitrocellulose membrane (Amersham) using BioRad Trans-Blot Turbo Transfer System or with wet transfer in transfer buffer (25 mM TRIS, 190 mM glycine, 20% ethanol) for 110 min at 120 V. Membranes were stained with Ponceau S and blocked in 5% milk for 1 hour. The primary antibody (**Supplemental Table S6**) was diluted in 2.5% milk and incubated overnight at 4 °C. The membrane was washed 5 times with TBST (20 mM TRIS, 150 mM NaCl, 0.1% Tween 20), and the membranes were incubated for 1 h with the secondary antibody (**Supplemental Table S6**) diluted in 2.5% milk. After the incubation the membranes were washed 5 times with TBST. Membranes were developed with enhanced chemiluminescent (ECL) horse radish peroxidase substrate (WESTAR ETA C ULTRA 2.0, Cyanagen), imaged using BioRad ChemiDoc, and analyzed using ImageLab software (6.1.0). Near-infrared Western blotting was performed as described above with the following modifications. Membranes were blocked in Intercept (TBS) Blocking Buffer (LICORbio). Primary antibodies were diluted in Intercept (TBS) Blocking Buffer (LICORbio) supplemented with 0.15% Tween 20, and secondary antibodies (IRDye 800CW Goat anti-rabbit, LICORbio) in Intercept T20 (TBS) Antibody Diluent (LICORbio). Before imaging, membranes were an additional three times in TBS (5 min each) and imaged on LICOR Odyssey CLx fluorescence imager.

**IR-PAR-CLIP of IGF2BP3 – sequencing library preparation and data processing**

The detailed protocol for the infrared (IR) PAR-CLIP of IGF2BP3 is described in (Anisimova, Karagöz, 2023). 125 million (5x ø15 cm dishes) HCT116 inducible tetON OsTIR1 cells were used per condition. 100 µM 4sU (Sigma) was added to the cell culture media 15 h prior to collection. ER stress was induced with 5 µg/mL TM for 4 hours prior to collection. DMSO in 1:1000 dilution was used a control. IGF2BP3 was immunoprecipitated with anti-IGF2BP3 Proteintech antibody (14642-1-AP, lot 00088732). anti-IgG Proteintech antibody (30000-0-AP) was used as a control. RNase I (Ambion) was used for the in-lysate RNase digestion at 0.1 U/µL and for the on-bead digestion in 1 mL of the lysis buffer at 0.025 U/µL. IR-PAR-CLIP libraries were sequenced on a NovaSeq 6000 S1 on SR100 (Illumina) at the Vienna BioCenter NGS facility with 55 million reads per sample on average. UMIs were extracted and adapter sequences were trimmed using UMI-tools v1.1.1 (Smith et al. 2017). The reads were size- and quality-trimmed using Trimmomatic v0.30 (Bolger et al. 2014) to have a length between 18 and 45 nt. The reads were then mapped to human genome hg38 using GENCODE annotation (release 36) with bowtie v0.12.7 (Langmead et al. 2009), allowing up to three mismatches and deduplicated using UMI-tools v1.1.1. Gene counts were obtained using the FeatureCounts function of the Subread package v2.0.1(Liao, Smyth et al. 2014). Gene counts for protein coding genes were RLE normalized to calculate the counts per million values (CPM), filtered to only include genes with CPM higher than 5 in at least one third of the libraries, and the differential expression analysis was performed with edgeR glmQLFTest (Generalized Linear Model Quasi-Likelihood F-test) (Robinson, McCarthy et al. 2010). GO term analysis was performed with

Enrichr webserver (Chen, Tan et al. 2013, Kuleshov, Jones et al. 2016). Redundancy in GO terms was reduced using GOSemSim (Yu, Li et al. 2010) and rrvgo (Sayols 2023). Full GO term enrichment lists are shown in supplementary materials.

**IR-PAR-CLIP of IGF2BP3 – matching transcriptome library preparation and data processing**

An aliquot of the lysate was taken before the in-lysate RNase digest for total RNA isolation and sequencing. Total RNA was isolated using peqGOLD TriFast (Peqlab, VWR) and transcriptome libraries were prepared with QuantSeq 3' mRNA-Seq Library Prep Kit (Lexogen). Libraries were sequenced on a NextSeq2000 P2 at SR100 mode (Illumina) at the Vienna BioCenter NGS facility with 30 million reads per sample on average. The quality-, adapter-, and polyA-trimmed reads were aligned to human genome hg38 using GENCODE annotation (release 36) with STAR v2.7.5c. As the reads originate from cross-linked PAR-CLIP samples and have T to C transitions, mismatches were allowed. Gene counts for protein coding genes were RLE normalized to calculate the counts per million values (CPM), filtered to only include genes with a CPM higher than 1 in at least half of the libraries. Differential expression analysis was performed with edgeR glmQLFTest (Robinson and Oshlack 2010).

**IR-PAR-CLIP of IGF2BP3 – computational analysis**

To estimate relative binding of IGF2BP3, IR-PAR-CLIP CPMs were divided to the matching total transcriptome QuantSeq CPMs. A pseudocount of 1 CPM was added to all samples and only genes with mean CPM for QuantSeq samples greater than 5 CPM were taken for the analysis. To identify IGF2BP3 target genes, IGF2BP3-binding clusters were called with PARalyzer v1.5 (Corcoran, Georgiev et al. 2011) (ini file is available in **Supplemental Table S6**). Genes that had at least one cluster containing more than 25 CPM and more than 50% of T to C conversions per read in two replicates (number 2 and 3) per condition were selected as IGF2BP3 targets. Samples from replicate 1 were excluded from target identification due to lower final read number and therefore lower number of identified clusters and targets. The target lists were filtered to only include targets with PAR-CLIP CPMs higher than total transcriptome QuantSeq CPMs. PAR-CLIP genomic tracks were visualized using svist4get v1.2.20 (Egorov, Sakharova et al. 2019). The enrichment of 5-nt motifs in IGF2BP3 PAR-CLIP reads was analyzed with HOMER v4.11 (Heinz, Benner et al. 2010), findMotifs.pl command using shuffled background. m6A and m7G motif enrichment analysis was done for IR-PAR-CLIP reads (replicates were pooled per condition) using MEME suite SEA (simple enrichment analysis) (Grant 2021). Motif enrichment was calculated either over shuffled sequences or pooled IR-PAR-CLIP reads for particular condition (indicated in figure legends). Positions of methylation sites for *HSPA5* were mapped based on miCLIP-seq data from m6A Atlas 2.0 (Liang, Ye et al. 2024) (datasets GSE152633 (Cho, Lee et al. 2021), GSE161304 (Cotter, Gallon et al. 2021), GSE137675 (Jia, Chai et al. 2019), GSE98623 (Vu, Pickering et al. 2017) from m6A and m7G miCLIP-seq (Malbec, Zhang et al. 2019). Sequencing data processing was done using the HPC of the Center for Integrative Bioinformatics Vienna (CIBIV) and Life Science Compute Cluster (LiSC) of the University of Vienna, Austria.

**Establishment of IGF2BP3 knockout cell lines and siRNA knockdown**

For IGF2BP3 knockout cell line generation, gRNA sequences (clones E4 and A3: 5′TGGCACCGACTGATAGAGCT 3′; clone D12: 5′ACGCGTAGCCAGTCTTCACC 3′) were cloned into the pSpCas9 (BB)-2A-GFP (PX458) (plasmid #48138; Addgene) (Ran, Hsu et al. 2013). HCT116 tetON OsTIR1 cells were transiently transfected using jetOPTIMUS reagent (Tamar, 101000051), and GFP-positive single-cell clones were FACS sorted at BD FACSAria IIIu at Max Perutz Labs BioOptics FACS Facility. HCT116 cells do not express IGF2BP1 (Mongroo, Noubissi et al. 2011). For siRNA knockdown, HCT116 cells (WT or tetON OsTIR1) or RKO iCas9 were transfected with IGF2BP3 (Dharmacon, L-003976-00-0005) SMARTpool siRNAs using DharmaFECT 2 (Dharmacon, T-2002-01) at 75 nM for 48 hours. For depletion of HMGA2 and FOXD1, cells were transfected with SMARTpool siRNAs (Dharmacon) targeting HMGA2 (L-013495-00-0005) and FOXD1 (J-011862-00-0005) at 50 nM for 48 h. ON-TARGETplus nontargeting siRNA pool (Dharmacon, D-001810-10-05) was used as a control.

**Establishment of doxycycline-inducible IGF2BP3 knockout RKO cell lines**

RKO-Dox-Cas9 (iCas9) cell lines for doxycycline-inducible knockout IGF2BP3 were established using lentiviral transduction with lentiviral particles (produced as described in (Hornegger, Anisimova et al. 2024) containing Dual-sgRNA_hU6-mU6 vectors described in (de Almeida, Hinterndorfer et al. 2021) expressing two sgRNAs against IGF2BP3 (5′ TGGCACCGACTGATAGAGCT 3′ and 5′ GAAGATACTTTCTAGGTCCG 3′) or against non-coding locus AAVS1 (5’ CGCTGTGCCCCGATGCACAC 3’ and 5′ GGCGCGTCGCTCGCTCGCTC 3′) from human and mouse U6 promoters and eBFP2 from a PGK promoter. The eBFP2-positive cells were FACS sorted at BD FACSMelody™ Cell Sorter at Max Perutz Labs BioOptics FACS Facility.

**Establishment of HCT116 cell lines expressing IGF2BP3 4A mutant**

For establishment of HCT116 cell lines expressing IGF2BP3 WT and 4A mutant at endogenous levels, HCT116 tetON OsTIR1 IGF2BP3 KO (clone A3) cells were transduced with lentiviral particles (produced and transduced as described in (Hornegger, Anisimova et al. 2024) containing the plenti-CAG-IRES-GFP vector (Lu, Middleton et al. 2014) (Addgene #69047) with full-length IGF2BP3 WT and 4A mutant (I88A, P90A, H91A, W94A). IGF2BP3 sequences were cloned into the plenti-CAG-IRES-GFP vector using EcoRI and XhoI restriction sites. To achieve expression levels comparable to endogenous IGF2BP3, GFP-positive cell populations were gated for high, middle, and low GFP expression levels and sorted in two consecutive rounds on Cytek Aurora CS™ Cell Sorter at Max Perutz Labs BioOptics FACS Facility. The expression levels of IGF2BP3 WT and 4A mutant were compared to those in the HCT116 tetON OsTIR1 cell line using near-infrared western blotting, and populations with endogenous IGF2BP3 WT and 4A mutant levels were selected.

**Total transcriptome sequencing (RNA-Seq) of IGF2BP3 knockout HCT116 cells**

HCT116 tetON OsTIR1 IGF2BP3 knockout clones E4, A3, and D12 (in duplicates) and parental cells (four replicates) were treated with 5 µg/mL TM for 4 hours (1:1000 DMSO was used as a control). Total RNA was isolated using peqGOLD TriFast (Peqlab, VWR), treated with RNase-free DNase I (NEB), and re-purified with peqGOLD TriFast (Peqlab, VWR). RNA precipitation was done using the isopropanol method. Total RNA sequencing libraries were prepared with

NEBNext Poly(A) mRNA Magnetic Isolation Module (NEB, E7490L) and NEBNext Ultra II Directional RNA Library Prep Kit (NEB, E7765L) by Vienna BioCenter NGS facility sequenced on a NovaSeq S4 on PE100 (Illumina) with 55 million reads per sample on average. The quality- and adapter-trimmed reads were aligned to human genome hg38 using GENCODE annotation (release 36) with STAR v2.7.5c allowing up to two mismatches per read. Gene counts for protein coding genes were RLE normalized to calculate the counts per million values (CPM), filtered to only include genes with CPM higher than 5 in at least half of the libraries, and differential expression analysis was performed with edgeR glmQLFTest (Robinson and Oshlack 2010).

**RNA-Seq of HCT116 cells upon siRNA-mediated depletion of IGF2BP3**

HCT116 WT cells were depleted of IGF2BP3 using siRNA pools as described in "Establishment of IGF2BP3 knockout cell lines and siRNA knockdown" section. ER stress was induced with 5 µg/mL TM for 4 hours prior to collection. One ~80% confluent well of a 6-well plate per condition (three biological replicates per condition) was washed with ice-cold PBS (Sigma) supplemented with 100 mg/mL cycloheximide, lysed on a plate on ice with 350 µL of ice-cold lysis buffer (20 mM HEPES pH 7.3, 150 mM KCl, 5 mM MgCl2, 1% Triton X-100, 100 mg/mL cycloheximide, 1 mM DTT, 1x EDTA-free protease inhibitor cocktail), scraped, and transferred to 1.5 mL RNase-free tube. Cell lysates were passed three times through the 27G needle, incubated on ice for 10 min with intermittent vortexing, and clarified on a table-top centrifuge at maximum speed (20,000 g) for 20 min at 4°C. Total RNA was extracted from 15 µL of the lysate using KingFisher Flex Purification System (Thermo) with the High-Performance RNA Isolation kit (Molecular Tools Shop, Vienna BioCenter). RNA-Seq libraries were prepared with NEBNext Poly(A) mRNA Magnetic Isolation Module (NEB, E7490L) and NEBNext Ultra II Directional RNA Library Prep Kit (NEB, E7765L) and sequenced on a NovaSeq SP on SR100 (Illumina) with 30 million reads per sample on average. The quality- and adapter-trimmed reads were aligned to human genome hg38 using GENCODE annotation (release 36) with STAR v2.7.5c allowing up to two mismatches per read. Gene counts for protein coding genes were filtered to include genes with coding sequence length-normalized CPM values higher than 5 in at least one third of the libraries. Differential expression analysis was performed with edgeR glmQLFTest (Robinson and Oshlack 2010).

**Comparison of the RKO transcriptome upon doxycycline-inducible Cas9- and siRNA-mediated depletion of IGF2BP3**

IGF2BP3 depletion was induced in RKO iCas9 cells with 250 ng/mL doxycycline for 72 hours. siRNA-mediated depletion was performed in RKO iCas9 as described in the "Establishment of IGF2BP3 knockout cell lines and siRNA knockdown" section. RKO transcriptome was obtained using SLAMseq protocol (Herzog, Reichholf et al. 2017). 4-thiouridine ($s^4U$) was added to cell culture media at 250 µM 2 hours prior collection. Total RNA was extracted using the KingFisher Flex Purification System (Thermo) with the High-Performance RNA Isolation kit (Molecular Tools Shop, Vienna BioCenter). During the isolation RNA was treated with RNase-free DNase I (NEB). Samples were prepared according to the standard SLAMseq protocol described in (Herzog, Reichholf et al. 2017). Briefly, total RNA was alkylated with 10 mM iodoacetamide in alkylation buffer (50 mM sodium phosphate buffer pH 8.0, 50% DMSO) at 50°C for 15 min and purified

using the KingFisher Flex Purification System. Sequencing libraries were prepared with NEBNext Poly(A) mRNA Magnetic Isolation Module (NEB, E7490L) and NEBNext Ultra II Directional RNA Library Prep Kit (NEB, E7765L) and sequenced on a NovaSeq SP on SR100 (Illumina) at the Vienna BioCenter NGS facility with 30 million reads per sample on average. The quality- and adapter-trimmed reads were aligned to human genome hg38 using GENCODE annotation (release 36) with STAR v2.7.5c allowing up to five mismatches per read. Total gene counts for protein coding genes were analyzed and genes were filtered to include those with coding sequence length-normalized CPM > 5 in at least half of the libraries. Differential expression analysis was performed with edgeR glmQLFTest (Robinson and Oshlack 2010). The data were processed using the HPC of the Center for Integrative Bioinformatics Vienna (CIBIV).

**Identification of siRNA pool off-targets from siRNA knockdown experiments**

To exclude possible siRNA off-target genes we compared changes in gene expression upon doxycycline-inducible knockout and siRNA-mediated depletion of IGF2BP3 in RKO iCas9 cells. Genes were considered off-targets if changes in their levels were more than 20% upon siRNA-mediated depletion, but less than 10% upon doxycycline-inducible knockout. Significance was not considered for this analysis due to overall small amplitude of changes. The identified off-targets are listed in **Supplemental Table S2**. These genes were excluded from analyses of experiments where IGF2BP3 was depleted with siRNA pools.

**SLAMseq of HCT116 upon siRNA-mediated depletion of IGF2BP3**

HCT116 WT cells were depleted of IGF2BP3 using siRNA pools as described in “Establishment of IGF2BP3 knockout cell lines and siRNA knockdown” section. ER stress was induced in using a 5 hour-long treatment with 5 µg/mL TM (1:1000 DMSO was used as a control). 4-thiouridine ($s^4U$) was added to cell culture media at 250 µM 2 hours prior collection. Total RNA was extracted using the KingFisher Flex Purification System (Thermo) with the High-Performance RNA Isolation kit (Molecular Tools Shop, Vienna BioCenter). During the isolation RNA was treated with RNase-free DNase I (NEB). SLAMseq samples were prepared according to the standard SLAMseq protocol described in (Herzog, Reichholf et al. 2017). Briefly, total RNA was alkylated with 10 mM iodoacetamide in alkylation buffer (50 mM sodium phosphate buffer pH 8.0, 50% DMSO) at 50°C for 15 min and purified using the KingFisher Flex Purification System. Sequencing libraries were prepared with NEBNext Poly(A) mRNA Magnetic Isolation Module (NEB, E7490L) and NEBNext Ultra II Directional RNA Library Prep Kit (NEB, E7765L) and sequenced on a NovaSeq SP on SR100 (Illumina) at the Vienna BioCenter NGS facility with 30 million reads per sample on average. The SLAMseq fastq files were trimmed and aligned to human genome hg38 using the conversion-aware nf-core/slamseq analysis pipeline v1.0.0 (Neumann, Herzog et al. 2019, Ewels, Peltzer et al. 2020) with default parameters. T-C conversion rates were calculated using the *slamdunk* pipeline (Neumann, Herzog et al. 2019). The T-C conversion rate values are ratios of T-C conversions to the total T coverage at each T-position within annotated 3’ UTR. Position-wise conversion rates were averaged across all T positions per gene to obtain a gene-level T-C conversion rate. T-C conversion rates reflect the fraction of newly synthesized RNA and inversely correlate with mRNA stability estimates. Genes were filtered to only include those with both total and T-C CPM > 5 for at least half of the samples. The differential expression analysis was performed with edgeR glmQLFTest (Robinson

and Oshlack 2010)). Sample siControl ER stress replicate 3 was a clear outlier on a PCA plot and was excluded from analysis. The data were processed using the Life Science Compute Cluster (LiSC) of the University of Vienna.

**RNA isolation and RT-qPCR**

Total RNA was isolated using the KingFisher Flex Purification System (Thermo) with the High-Performance RNA Isolation kit (Molecular Tools Shop, Vienna BioCenter). During the isolation RNA was treated with DNase I (M0303S, NEB). cDNA was prepared with LunaScript RT SuperMix (NEB) and amplified in a qPCR reaction with 2x Hot Start qPCR master mix (Molecular Tools Shop, Vienna BioCenter) using BioRad CFX 384 Touch machine. The qPCR primers are listed in **Supplemental Table S6**. mRNA levels were calculated relative to *RPL6* levels. mRNA decay rate constants and half-lives were calculated from ordinary least-squares linear regression of ln-transformed mRNA levels over time following actinomycin D treatment, as described previously (Chen, Ezzeddine et al. 2008).

**Puromycin incorporation assay**

HCT116 WT cells were depleted of IGF2BP3 using siRNA pools as described in “Establishment of IGF2BP3 knockout cell lines and siRNA knockdown” section, or transfected with control non-targeting siRNA. One well from a 24-well plate was used per condition. ER stress was induced by a 4-hour treatment with 5 µg/mL TM (1:1000 DMSO was used as a control). Cells were treated with 20 µg/mL puromycin 30 min before collection. Cells were collected in 100 µL of RIPA buffer (150 mM NaCl, 1% NP-40, 0.5% Sodium deoxycholate, 0.1% SDS, and 25 mM TRIS pH 7.4) with 1x EDTA-free protease inhibitor cocktail (Roche). Lysates were clarified using a table-top centrifuge at maximum speed (20,000 g) for 20 min at 4°C. Samples for Western Blot were prepared as described in “Western blotting” section.

**Aggresome detection assay**

Aggresome detection was performed using Enzo PROTEOSTAT® Aggresome Detection Kit (ENZ-51035-0025). HCT116 WT cells were depleted of IGF2BP3 using siRNA pools as described in “Establishment of IGF2BP3 knockout cell lines and siRNA knockdown” section, or transfected with control non-targeting siRNA. One well from a 6-well plate was used per condition. ER stress was induced by a 4-hour treatment with 5 µg/mL TM (1:1000 DMSO was used as a control). Cells were washed in cold PBS and collected by trypsinization. Cells were pelleted by centrifugation at 400 g for 5 min, and the pellet was washed twice with PBS. At the last wash, cells were resuspended in ~200 µL of remaining PBS and fixed by adding the cell suspension dropwise into 1 mL of 4% formaldehyde solution in PBS and incubated on room temperature for 30 min. Fixed cells were collected by centrifugation at 800 g for 15 min and washed once with 1 mL of PBS. After centrifugation at 800 g for 15 min, supernatant was discarded, cells were permeabilized by adding the cell suspension into 1 mL of cell permeabilization buffer (0,5% Triton X-100, 3 mM EDTA pH 8, in 1x commercial assay buffer from Enzo PROTEOSTAT® Aggresome Detection Kit) and incubated for 30 min on ice. Cells were collected by centrifugation at 800 g for 15 min at 4°C, supernatant was discarded and cells were washed with 1 mL of PBS. The resulting cell suspension was filtered through the strainer cap of a Fluorescence-activated cell sorting (FACS)-compatible BD tube and the suspension

was centrifuged at 800 g for 15 min at 4°C. After removing supernatant, remaining cell pellet was stained by resuspending it in 500 uL of freshly diluted 1:200 PROTEOSTAT® Aggresome Detection Reagent in 1x assay buffer from the kit. After 30 min incubation at room temperature protected from light, the samples were analysed by FACS on Bio-Rad ZE5 Cell Analyzer in 488 nm excitation and 583/52 nm emission filter.

**Total proteome of IGF2BP3 KO HCT116 cells – sample preparation**

Parental HCT116 tetON OsTIR1 cells and IGF2BP3 full knockout (clone A3) cells were grown to ~70% confluency and treated with 100 ng/mL TM for 8 hours (1:50,000 DMSO was used as a control). Cells were washed twice with 10 mL of ice-cold PBS, collected by scraping and pelleting at 500 g at 4°C for 5 min, flash frozen in N2l, and stored at -80°C. Four replicates per condition were collected. The cell pellets were lysed in heated 2% sodium deoxycholate 0.1 M Tris/HCl pH 8.8 at 95°C for 10 min. Then it was sonicated in Bioruptor for 5 cycles 30/30 second with level H in a cold room. When it was cooled down, 1 µL benzonase was added and incubated on ice for 30 min followed by another sonication in Bioruptor for 5 cycles 30/30 second with level H in a cold room. It was kept on ice for another 10 min before centrifuged at 10°C 15000 g for 10 min to pellet cell debris. The supernatant was transferred to a new tube and the protein concentration was measured with a microBCA assay (Thermofisher). About 50 µg protein in 25 µL was reduced with 1 µL of 250 mM dithiothreitol (DTT) for 30 min at 50°C before adding 1 µL of 500 mM iodoacetamide and incubating for 30 min at room temperature in the dark. Remaining iodoacetamide was quenched with 0.5 µL of 250 mM DTT for 10 min. The solution was diluted to 1% sodium deoxycholate using 25 µL 50 mM ammonium bicarbonate. Proteins were digested with 0.5 µg LysC (mass spectrometry grade, FUJIFILM Wako chemicals) in 0.5 µL 50 mM ammonium bicarbonate at room temperature for 3 h, then digested further with 1 µg trypsin (Trypsin Gold, Promega) in 1 µL 50 mM ammonium bicarbonate at 37°C overnight. The digest was stopped by the addition of 10% trifluoroacetic acid (TFA) to a final concentration of 2%. Then the samples were centrifugated at 14000rpm for 10min and the supernatant was transferred to a new tube and the supernatant was desalted using a 96-well OASIS MCX µElution plate (Waters, 30 µm particle size, 186001830BA) following the manufacturer's protocol. and the supernatant was desalted using a 96-well OASIS MCX µElution plate (Waters, 30 µm particle size, 186001830BA) following the manufacturer's protocol.

**Total proteome of IGF2BP3 KO HCT116 cells – liquid chromatography-mass spectrometry**

LC-MS analysis was performed on a Vanquish Neo UHPLC system (Thermo Scientific) coupled to an Orbitrap Astral mass spectrometer (Thermo Scientific). The system was equipped with a Nanospray Flex ion source (Thermo Scientific), and a Column Heater (IonOpticks) connected to a Heater Controller (IonOpticks). Peptides were loaded onto a trap column (PepMap Neo C18 5mm × 300 µm, 5 µm particle size, Thermo Scientific) using 0.1% TFA as mobile phase, and separated on an analytical column (Aurora Ultimate XT C18, 25 cm × 75 µm, 1.7 µm particle size, IonOpticks), applying a linear gradient starting with a mobile phase of 98% solvent A (0.1% FA) and 2% solvent B (80% acetonitrile, 0.08% FA), increasing to 35% solvent B over 60 min at a flow rate of 300 nl/min. The analytical column was heated to 50°C. The mass spectrometer was operated in data-independent acquisition (DIA) mode. Survey scans were acquired from 380-980 m/z, normalized AGC target of 300%, resolution of 240,000 in the orbitrap with a

maximum 5ms injection time. In total, 149 MS2 spectra were acquired across a mass range of 380.4-980.7 m/z using an isolation window of 4 m/z with 0 m/z overlap between windows. Window placement optimization is on. Selected ions were analyzed using a maximum injection time of 5ms, normalized AGC target of 500% after HCD fragmentation with normalized collision energy of 25% in the Astral detector. MS2 scan range is 150-2000. The loop control is time with a 0.6 s cycle.

**Total proteome of IGF2BP3 KO HCT116 cells – Mass spectrometry data analysis**

MS raw data were processed with Spectronaut (20.4, Biognosys). The library-free DirectDIA+ workflow was employed for analysis of the raw files, the *H. sapiens* 1 protein per gene reference proteome from Uniprot (Proteome ID: UP000005640, release 2025_01), concatenated with a database of 379 common laboratory contaminants (release 2025_01, https://github.com/maxperutzlabs-ms/perutz-ms-contaminants), and an entry for P17861-2. The cleavage specificity was set to full trypsin specificity (Trypsin/P), with two missed cleavages allowed. Carbamidomethyl was used as fixed cysteine modification; methionine oxidation and protein N-terminal acetylation were specified as variable modifications. Cross-run normalization was disabled, and all other settings were used at their default values.
fied as variable modifications. Cross-run normalization was disabled, and all other settings were used at their default values.
riable modifications. Cross-run normalization was disabled, and all other settings were used at their default values.
Computational analysis was performed using Python and the in-house developed Python library MsReport (0.0.32) (Hollenstein, Maurer-Granofszky et al. 2023). Only non-contaminant proteins identified with a minimum of two peptides and being quantified in at least two replicates of one condition were considered for further analysis. LFQ protein intensities were log2-transformed and normalized across samples using the ModeNormalizer from MsReport. The ModeNormalizer method involves calculating log2 protein ratios for all pairs of samples and determining normalization factors based on the modes of all ratio distributions. Missing values were imputed by drawing random values from a normal distribution. Sigma and mu of this distribution were calculated per sample from the standard deviation and median of the observed log2 protein intensities (μ = median sample LFQ intensity – 1.8 standard deviations of the sample LFQ intensities, σ = 0.3 × standard deviation of the sample LFQ intensities). iBAQ intensities were calculated by dividing protein intensities by the number of theoretically observable tryptic peptides between 6 and 30 amino acids. To estimate the relative protein abundances within each sample, the iBAQ intensities were normalized by dividing them by the total sum of iBAQ intensities for all proteins in the sample. Statistical analysis was performed using the linear models for microarray analysis (limma) v.3.54.2 (Ritchie, Phipson et al. 2015) package in R. Moderated t-statistics were calculated using the limma-trend method, and multiple testing correction was applied using the Benjamini–Hochberg method. The Python library XlsxReport (0.1.1) was used to create formatted Excel files summarizing the results of the proteomics experiments (**Supplemental Table S3**).

**Co-Immunoprecipitation of endogenous IGF2BP3 followed by mass spectrometry – sample preparation**

One ø15 cm dish of 80% confluent HCT116 WT cells was used per condition. To induce ER stress, cells were treated with 5 µg/mL TM for 4 hours, and DMSO at 1:1000 dilution was used as a control. Cells were washed with ice-cold PBS and collected by scraping and pelleting at 500 g at 4°C for 5 min. Cells were lysed in 250 µL of lysis buffer (25 mM HEPES pH 7.3, 150 mM NaCl, 0.5% NP-40, 0.5 mM EDTA, 10% Glycerol, 1x EDTA-free protease inhibitor cocktail, 1x PhosSTOP) per condition by incubation on ice 15 min with intermittent vortexing. The lysate was clarified by centrifugation at 20,000 g for 20 min at 4°C. 10 µg of Proteintech anti-IGF2BP3 antibody (14642-1-AP, lot 00088732) or Proteintech IgG control (30000-0-AP) was coupled to the 40 µL of protein G Dynabeads (Invitrogen) in 1 mL of lysis buffer for 20 min, rotating at room temperature, washed three times with 1 mL of the lysis buffer, resuspended in the original bead volume (40 µL) and added to 200 µL of the clarified lysate. Beads were washed five times with 1 mL of wash buffer (25 mM HEPES pH 7.3, 150 mM NaCl, 0.5 mM EDTA, 10% Glycerol). Each wash was incubated on ice for 3 min. For RNase digestion 0.1 U/µL of RNase I (Ambion) and 1 U/µL of RNase T1 (EN0541) were added to the second wash. Samples were incubated at room temperature for 10 min on a rotator. The control (undigested) samples were kept on ice. The proteins were eluted from the beads with 20 µL 100 mM glycine pH 2.0 three times and the pooled supernatant was adjusted to alkaline using about 20 µL 1M Tris pH 8.0. Disulfide bonds were reduced with 3.2 µL of 250 mM dithiothreitol (DTT) for 30 min at room temperature before adding 3.2 µL of 500 mM iodoacetamide and incubating for 30 min at room temperature in the dark. Remaining iodoacetamide was quenched with 1.6 µL of 250 mM DTT for 10 min. Proteins were digested with 300 ng trypsin (Trypsin Gold, Promega) in 3 µL 50 mM ammonium bicarbonate at 37°C overnight. The digest was stopped by the addition of 10% trifluoroacetic acid (TFA) to a final concentration of 0.5%. The peptides were desalted using C18 Stagetips (Rappsilber, Mann et al. 2007).

**Co-Immunoprecipitation of endogenous IGF2BP3 followed by mass spectrometry – Liquid chromatography-mass spectrometry analysis**

Peptides were separated on a Vanquish Neo nano-flow chromatography system (Thermo-Fisher), using a trap-elute method for sample loading (Acclaim PepMap C18, 2 cm × 0.1 mm, 5 µm, Thermo-Fisher), and a C18 analytical column (Acclaim PepMap C18, 50 cm × 0.075 mm, 2 µm, Thermo-Fisher), applying a segmented linear gradient from 2% to 35% and finally 80% solvent B (80 % acetonitrile, 0.1 % formic acid; solvent A 0.1 % formic acid) at a flow rate of 230 nL/min over 120min. Eluting peptides were analyzed on an Exploris 480 Orbitrap mass spectrometer (Thermo-Fisher Scientific) coupled to the column with a FAIMS pro ion-source (Thermo-Fisher Scientific) using coated emitter tips (PepSep, MSWil) with the following settings: The mass spectrometer was operated in DDA mode with two FAIMS compensation voltages (CV) set to -45 or -60 and 1.5 s cycle time per CV. The survey scans were obtained in a mass range of 350-1500 m/z, at a resolution of 60k at 200 m/z, and a normalized AGC target at 100%. The most intense ions were selected with an isolation width of 1.4 m/z, fragmented in the HCD cell at 30% collision energy, and the spectra recorded for max. 50 ms at a normalized AGC target of 100% and a resolution of 15k. Peptides with a charge of +2 to +6 were included for fragmentation, the peptide match feature was set to preferred, the exclude isotope feature was enabled, and selected precursors were dynamically excluded from repeated sampling for 45 seconds.

**Co-Immunoprecipitation of endogenous IGF2BP3 followed by mass spectrometry – Proteomics data analysis**

The RAW MS data were analyzed with FragPipe (20.0), using MSFragger (4.1) (Kong, Leprevost et al. 2017). IonQuant (1.10.27) (Yu, Haynes et al. 2021) and Philosopher (5.0.0) (da Veiga Leprevost, Haynes et al. 2020) . The default FragPipe workflow for label free quantification (LFQ-MBR) was used, except “Normalize intensity across runs” was turned off. Cleavage specificity was set to Trypsin/P, with two missed cleavages allowed. The protein FDR was set to 1%. A mass of 57.02146 (carbamidomethyl) was used as fixed cysteine modification; methionine oxidation and protein N-terminal acetylation were specified as variable modifications. MS2 spectra were searched against the human 1 protein per gene reference proteome from Uniprot (Proteome ID: UP000005640, release 2024_01), concatenated with a database of 382 common laboratory contaminants (release 2023.03, https://github.com/maxperutzlabs-ms/perutz-ms-contaminants).

Computational analysis was performed using Python and the in-house developed Python library MsReport (version 0.0.24, (Hollenstein, Maurer-Granofszky et al. 2023)). LFQ protein intensities reported by FragPipe were log2-transformed and normalized across samples using the ModeNormalizer from MsReport. The missing normalized LFQ intensity values were imputed by drawing random values from a normal distribution after filtering out contaminants, proteins with less than 2 peptides and less than 2 quantified values in at least one group. Differences between groups were statistically evaluated using the LIMMA 3.52.1 (Ritchie, Phipson et al. 2015) at 5% FDR (Benjamini-Hochberg). The in-house Python library XlsxReport (0.1.0) was used to create a formatted Excel file summarizing the results of protein quantification. Proteins were filtered to only include those that have at least 6 identified peptides and 24 spectral count events, both summed across all samples. Proteins were considered IGF2BP3 interactors if their normalized LFQ values were enriched more than 4 times over IgG control, *P* value adj. < 0.05 at least in one treatment condition. GO term analysis was performed with Enrichr webserver (Chen, Tan et al. 2013). Redundancy in GO terms was reduced using GOSemSim (Yu, Li et al. 2010, Kuleshov, Jones et al. 2016) and rrvgo (Sayols 2023). Full GO term enrichment lists are shown in supplementary materials.

**Co-Immunoprecipitation of endogenous IRE1**

One ø15 cm dish of 80% confluent HCT116 WT cells was used per condition. To induce ER stress, cells were treated with 5 µg/mL TM for 4 hours, DMSO in 1:1000 dilution was used a control. Cells were washed with ice-cold PBS and collected by scraping and pelleting at 500 g at 4°C for 5 min. Cells were lysed in 250 µL of lysis buffer (25 mM HEPES pH 7.3, 150 mM NaCl, 0.5% NP-40, 0.5 mM EDTA, 10% Glycerol, 1x EDTA-free protease inhibitor cocktail, 1x PhosSTOP) per condition by incubation on ice 15 min with intermittent vortexing. The lysate was clarified by centrifugation at 20,000 g for 20 min at 4°C. 10 µg of anti-IRE1 antibody (SantaCruz, clone B-12, sc-390960, lot# J2521) were coupled to 40 µL of protein G Dynabeads (Invitrogen) in 1 mL of the lysis buffer for 20 min rotating at room temperature, washed three times with 1 mL of the lysis buffer, washed twice in 0.3 mL of the conjugation buffer (20 mM sodium phosphate, 150 mM NaCl, pH 7.5) and crosslinked to the Dynabeads with 5 mM bissulfosuccinimidyl suberate (BS3) in 1 mL of the conjugation buffer for 30 min rotating at room temperature. The

reaction was quenched by addition of 25 µL 1 M Tris-HCl (pH 7.5) followed by 15 min incubation rotating at room temperature. The Dynabeads with the crosslinked antibody were washed three times with 0.5 mL of the lysis buffer, resuspended in the original bead volume (40 µL) and added to 200 µL of the clarified lysate. The lysate was incubated with the beads for 3 hours at 4°C. Beads were washed three times with 1 mL of the wash buffer (25 mM HEPES pH 7.3, 150 mM NaCl, 0.5 mM EDTA, 10% Glycerol). Each wash was incubated on ice for 3 min. For RNase digestion 0.1 U/µL of RNase I (Ambion) and 1 U/µL of RNase T1 (EN0541) were added to the second wash. Samples were incubated at room temperature for 10 min on a rotator. Proteins were eluted in 25 µL of 1x SDS sample buffer at +95 °C for 5 min, loaded on SDS-PAGE and analyzed by western blotting as described above (**Supplemental Table S6**).

**Co-Immunoprecipitation of GFP-IGF2BP3 and mNeonGreen-EDC3**

One ø15 cm dish of 80% confluent HEK293T split GFP-IGF2BP3 or split mNeonGreen-EDC3 cells was used per condition. Parental HEK293T split GFP cells were used as a background control. To induce ER stress, cells were treated with 5 µg/mL TM for 4 hours (if other time is not indicated), DMSO in 1:1000 dilution was used a control. Cells were washed with ice-cold PBS and collected by scraping and pelleting at 500 g at 4°C for 5 min. Cells were lysed in 250 µL of lysis buffer (25 mM TrisHCl pH 7.4, 100 mM KCl, 0.5% NP-40, 10% Glycerol, 1x EDTA-free protease inhibitor cocktail, 1 U/µL Murine RNase inhibitor (NEB)) per condition by incubation on ice for 10 min. The lysate was clarified by centrifugation at 4°C 20,000 g for 20 min. The GFP-IGF2BP3 IP was performed using 40 µL of GFP-trap magnetic beads (ChromoTek) per condition. 20 µL of mNeonGree-trap magnetic beads (ChromoTek) per condition were used for mNeonGreen-EDC3. The lysate was incubated with the beads beads for 1 hour at 4°C with addition of 2 U/µL of RNase I (Ambion) and the beads were washed 5 times with 0.2 mL of ice-cold lysis buffer. Proteins were eluted in 25 µL of 1x SDS sample buffer at +95 °C for 5 min, loaded on SDS-PAGE and analyzed by western blotting as described above with anti-IGF2BP3, anti-EDC4, and anti-EDC3 antibodies (**Supplemental Table S6**).

**Co-Immunoprecipitation of GFP-EDC3 and 3xFLAG-IGF2BP3 WT and 4A mutant**

One well of 6-well plate was used per condition. ~70% confluent HCT116 tetON OsTIR1 IGF2BP3 KO cells clone A3 were transfected with transient expression plasmids expressing free eGFP (pEGFP-C1) or eGFP-EDC3 (pT7-EGFP-C1-HsEDC3) and 3xFLAG-hsIGF2BP3 WT or 4A mutant (this study). pT7-EGFP-C1-HsEDC3 was a gift from Elisa Izaurralde (Addgene plasmid # 25032). Cells were transfected with a total of 1 µg of DNA with jetOptimus reagent (Polyplus) according to the manufacturer's instructions. Cells were washed with ice-cold PBS and lysed in 200 µL of lysis buffer (25 mM TrisHCl pH 7.4, 100 mM KCl, 0.5% NP-40, 10% Glycerol, 1x EDTA-free protease inhibitor cocktail, 1 U/µL Murine RNase inhibitor (NEB)) per condition by incubation on ice for 10 min. The lysate was clarified by centrifugation at 4°C 20,000 g for 20 min. The lysate was incubated with the 20 µL GFP-trap beads for 1 hour at 4°C with addition of 2 U/µL of RNase I (Ambion) and the beads were washed 5 times with 0.2 mL of ice-cold lysis buffer. Proteins were eluted in 25 µL of 1x SDS sample buffer at +95 °C for 5 min, loaded on SDS-PAGE and analyzed by western blotting as described above with anti-GFP and anti-FLAG antibodies (**Supplemental Table S6**).

### *In silico* screening of IGF2BP3 protein-protein interactions

Protein-protein interaction screening of IGF2BP3 was performed using the AlphaFold2 Multimer (Jumper, Evans et al. 2021, Evans, O'Neill et al. 2022, Mirdita, Schutze et al. 2022) via the HT-ColabFold pipeline (Hohmann, Graf et al. 2024) . To this end pairwise interactions were analyzed for full length IGF2BP3 (O00425, IF2B3_HUMAN) versus IGF2BP3 interactors identified using co-IP-MS. In total 1213 predictions were made. PEAKscore was used to evaluate the prediction of the interaction. It represents the inverse, scaled (0-1) minimum Precision Alignment Error (PAE) between analyzed chains. HT-ColabFold screening was done using the HPC of the Center for Integrative Bioinformatics Vienna (CIBIV) and Life Science Compute Cluster (LiSC) of the University of Vienna, Austria.

The interactions between the separate domains of IGF2BP3 and EDC3 were analyzed using AlphaFold 3 (Abramson, Adler et al. 2024). The domain separation was defined using the following boundaries: IGF2BP3 (O00425, IF2B3_HUMAN) RRM1/2 – aa 1-195, linker1-KH1/2 – aa 160-350, KH1/2-linker2 – aa 196-405, linker2-KH3/4 - aa 343-579; EDC3 (Q96F86, EDC3_HUMAN) SM – aa 1-68, YjeF - aa 283-487.

### IGF2BP3 protein expression and purification

Full-length IGF2BP3 WT and 4A constructs were cloned into a pGEX-6P-2 vector containing an N-terminal GST-tag and a 3 C cleavage site. Protein purification was performed as described in (Hornegger, Anisimova et al. 2024). Specifically, the proteins were expressed in Rosetta (DE3) cells grown to an OD of ~0.7 and induced with 400 µM IPTG. Cells were grown over night at 20 °C, pelleted and frozen in liquid nitrogen. Proteins were purified by resuspending the pellet in GST lysis buffer (25 mM HEPES pH 7.2, 1 M NaCl, 5% glycerol, 2 mM DTT, 0.5 mM PMSF, 2 mM EDTA) and lysing the cells in a EmulsiFlex C3 homogenizer. After pelleting non-soluble cell debris was removed by centrifugating the lysate at 40,000 g for 30 min at 4 °C. Proteins were loaded onto a GST HiTrap HP 5 mL column, washed with GST wash buffer (25 mM HEPES pH 7.2, 500 mM NaCl, 5% glycerol, 2 mM DTT, 0.5 mM PMSF, 2 mM EDTA) and eluted with a gradient of 20 mM reduced glutathione in GST wash buffer. Bound nucleotides were removed by loading the proteins onto a Heparin HiTrap HP 5 mL column after diluting the NaCl concentration to 100 mM (with wash buffer without NaCl), washing them with wash buffer (25 mM HEPES pH 7.2, 100 mM NaCl, 5 % glycerol, 2 mM DTT, 0.5 mM PMSF, 2 mM EDTA) and eluting them with a gradient of 1 M NaCl in wash buffer. The GST-tag was cleaved off by incubating the eluted protein with GST-3C overnight at 4 °C. The tag and the 3 C protease were separated by running the cleaved protein over a GST HiTrap 5 mL column using the same buffers as during the affinity purification. The flow through was pooled and further purified via size exclusion chromatography (SEC). Proteins were eluted with SEC buffer (25 mM HEPES, 150 mM NaCl, 2 mM DTT). Protein concentration was measured using a Nanodrop.

### Analytical Size Exclusion Chromatography

Purified IGF2BP3 WT and IGF2BP3 4A proteins were diluted to 20 µM in SEC buffer (25mM HEPES 7.2, 150mM NaCl, 2mM DTT) and centrifuged at 14,000 × g for 10 min at 4 °C to remove insoluble aggregates. 20 µl of each sample was injected onto a Superdex 200 Increase 5/150 GL column (Cytiva) equilibrated in Size Exclusion Chromatography (SEC) buffer and connected to an ÄKTA pure micro chromatography system (Cytiva) at 4 °C. Proteins were

separated at a flow rate of 0.1 ml/min. Elution was monitored by UV absorbance at 280 nm. Fractions were collected in 50 µl increments. Fractions corresponding to elution volumes between 1.4 ml and 1.8 ml, spanning the main absorbance peak at 280 nm, were analyzed by SDS-PAGE using self-cast 12% acrylamide gels under denaturing and reducing conditions. Electrophoresis was performed at 200 V for 45 min. Proteins were visualized by Coomassie staining.

**Circular Dichroism**

Purified IGF2BP3 WT and IGF2BP3 4A were thawed, centrifuged at 4 °C for 15 min at 20,000 g and dialyzed into 1 L circular dichroism buffer (25 mM Potassium Phosphate, 150 mM $(NH_4)_2SO_4$ pH 7.3) overnight at 4 °C using 3.5 kDa MWCO dialysis tubing (Thermofisher, LOT: X352983). Next day, proteins were centrifuged at 4 °C for 15 min at 20,000 g and diluted to 0.2 mg/ml with circular dichroism buffer. The CD spectral measurement was performed at 20 °C in a 1 mm pathlength quartz cuvette using a Chirascan Plus CD Spectrometer (Applied Photophysics) in triplicates. The spectrometer was purged with nitrogen overnight. The purge check and the absolute lower wavelength and high voltage signal quality checks were performed preceding the sample measurement (1 nm bandwidth, 0.5 step size, 0.5 s integration time). The circular dichroism buffer background spectrum was acquired and subtracted prior to spectral analysis in GraphPad Prism (192 nm to 260 nm). For each spectrum, normalization was performed using the minimum and maximum intensity values measured within the 192–260 nm wavelength range as reference points. The circular dichroism spectroscopy measurement was performed at the Protein Technologies Facility at Vienna BioCenter Core Facilities (VBCF), member of the Vienna BioCenter (VBC), Austria.

**Fluorescence Anisotropy**

Fluorescence polarization assays were performed between IGF2BP3 WT and 5'-fluorescein-labeled RNA probes (5'FluorT-AAUCCAGAA, 5'FluorT-AACAUUUAA, 5'FluorT-AAACUGUAA, 5'FluorT-AAAAAAAAA; synthesized and RNase-Free HPLC purified by Integrated DNA Technologies Germany GmbH, Germany) as follows. IGF2BP3 WT was thawed and centrifuged for 15 min at 20,000 g and 4 °C. The sample with the highest protein concentration was prepared in anisotropy buffer (25 mM HEPES 7.2; 150 mM NaCl) in a 384 well plate (Corning). A concentration series was created by diluting the sample 1:1 with anisotropy buffer. Final protein concentrations ranged from 3.9 nM to 4 µM. 1µl of 10 x RNA containing buffer (250 nM RNA, 25 mM HEPES, 150 mM NaCl, pH 7.2) was added per well to reach a final concertation of 25 nM of fluoresceine-labelled RNA in 10 µL reaction volume. Subsequently, samples were incubated for 30 min on ice. The fluorescence anisotropy was measured in triplicates using a TECAN Sparc spectrofluorometer at 525 nm with a band width of 20 nm at 20 °C and an excitation wavelength of 485 nm, a band width of 10 nm, 30 flashes with gain 75, automatic mirror setting, 0 s settling time and Z-position at 19300 µm. The G-factor was determined once for every experiment and used to calculate the anisotropy by measuring 25 nM RNA in anisotropy buffer in the beginning of the experiment. The fluorescence anisotropy value was calculated by the manufacturer's software. KD's were calculated in GraphPad Prism by using a dose response curve to fit the data using following model Y = bottom + (top-bottom)/(1+10^((log10(Kd)-log10(x))*n)).

## Data deposition

Next-generation sequencing data have been deposited in GEO with the following identifiers:
GSE289214 – RNA-Seq of HCT116 cells upon IGF2BP3 CRISPR/Cas9 knockout in control and ER stress conditions
GSE289023 – IR-PAR-CLIP of IGF2BP3 in HCT116 cells in control and ER stress conditions
GSE289024 – transcriptome (QuantSeq) of HCT116 cells in control and ER stress conditions matching IR-PAR-CLIP samples
GSE289424 – transcriptome (RNA-Seq) of HCT116 cells upon IGF2BP3 siRNA knockdown knockout in control and ER stress conditions
GSE289482 – SLAMseq of HCT116 cells upon IGF2BP3 knockdown in control and endoplasmic reticulum (ER) stress conditions
GSE289480 – SLAMseq of doxycycline-inducible knockout and siRNA-mediated depletion of IGF2BP3 in RKO iCas9 cells.

Mass spectrometry proteomics data have been deposited at the ProteomeXchange Consortium via the PRIDE partner repository (Perez-Riverol, Bai et al. 2022) with the dataset identifiers:
PXD073640 – Total proteome of IGF2BP3 CRISPR/Cas9 knockout cells in control and ER stress conditions
PXD060548 – Co-Immunoprecipitation of endogenous IGF2BP3 followed by mass spectrometry in control and ER stress conditions

## Figures

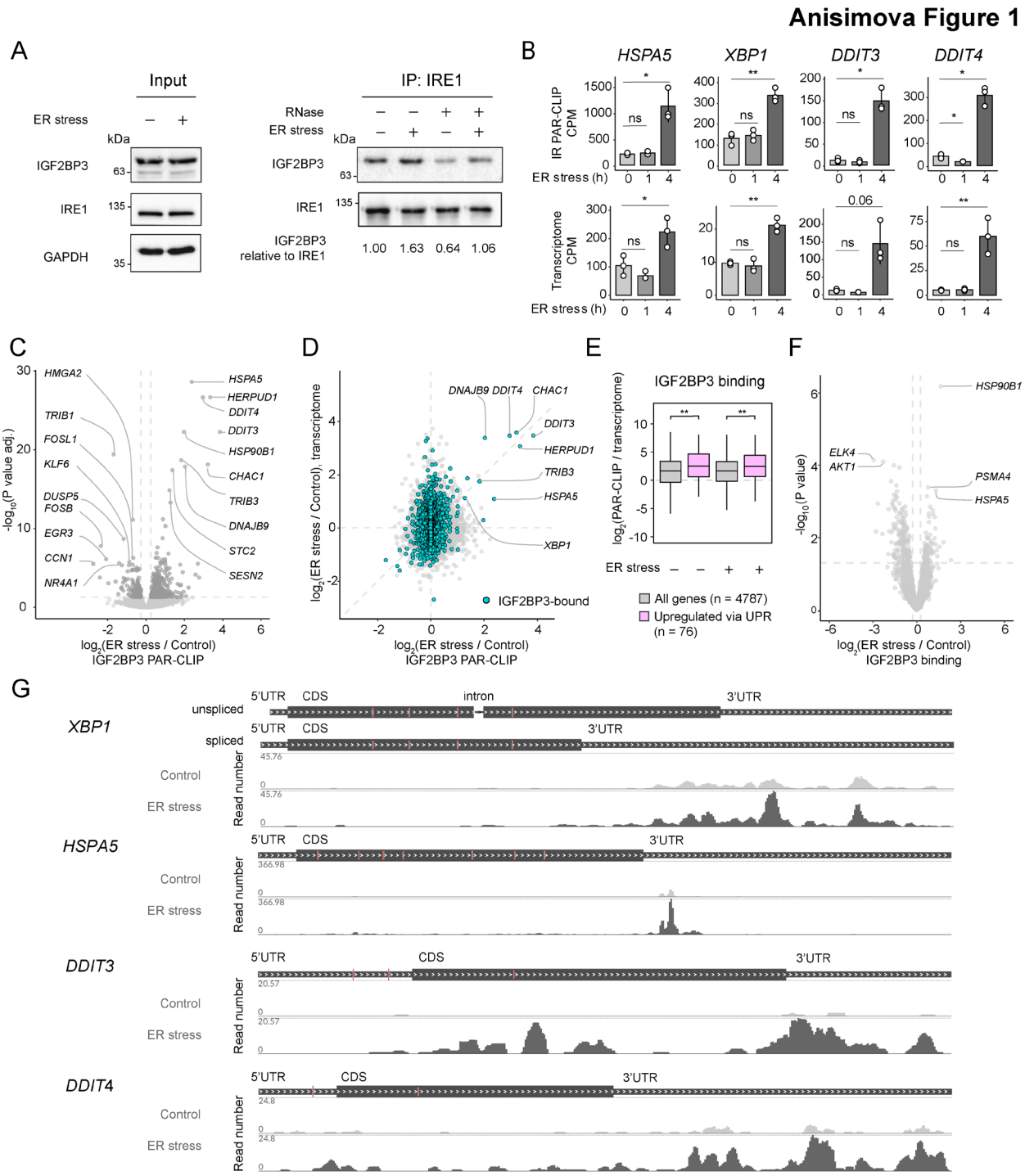



**Figure 1. IGF2BP3 interacts with the UPR target mRNAs.**

**A.** Western blot of IGF2BP3 showing its association with IRE1 after immunoprecipitation of endogenous IRE1 from HCT116 WT cells treated with ER stress-inducing drug TM at 5 µg/mL for 4 hours with or without RNase in the washes. **B.** Normalized read count numbers (CPM) for IGF2BP3-bound reads (IR-PAR-CLIP) and total transcript levels (QuantSeq) of selected UPR

target genes upon ER stress induction with TM at 5 µg/mL for 1 and 4 hours. Data are the mean ± s.d of n=3 biological replicates. *P* values were calculated by unpaired two-sided Student's t-test. **C.** Volcano plot showing changes in IGF2BP3 IR-PAR-CLIP CPM upon ER stress treatment. *P* values were calculated by edgeR glmQLFTest. **D.** Scatter plot comparing changes in IGF2BP3 IR-PAR-CLIP read counts with the total transcriptome changes (QuantSeq) upon ER stress treatment. **E.** Boxplot showing changes in IGF2BP3 binding (IR-PAR-CLIP CPM / QuantSeq CPM) to all genes and UPR upregulated genes (upregulated more than two-fold in ER stress than in control, *P* value adj. < 0.05, total RNA-Seq) upon ER stress and control conditions. *P* values were calculated by two-sided Wilcoxon test. **F.** Volcano plot showing changes in IGF2BP3 binding (IR-PAR-CLIP CPM / QuantSeq CPM) upon ER stress and control conditions. IGF2BP3-bound transcripts are shown. n=3 biological replicates. *P* values were calculated by edgeR glmQLFTest. **G.** Representative IGF2BP3 IR-PAR-CLIP coverage examples. Where not indicated otherwise, ER stress was induced with TM at 5 µg/mL for 4 hours. For IR-PAR-CLIP and transcriptome experiments n=3 biological replicates. *$P < 0.05$; **$P < 0.01$; ***$P < 0.001$; ****$P < 0.0001$.

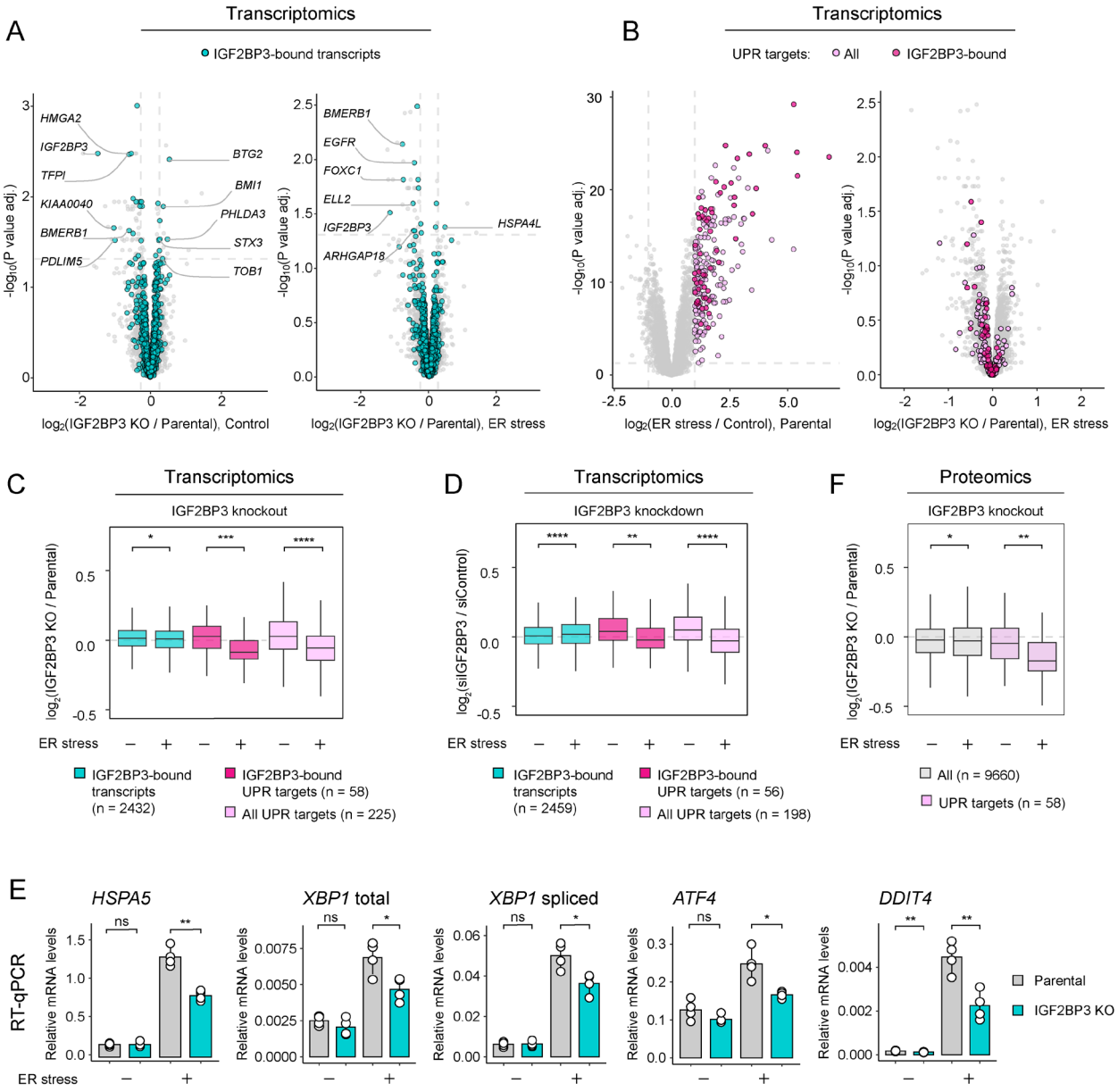



**Figure 2. IGF2BP3 depletion dampens the unfolded protein response.**
**A.** Volcano plot of transcriptome (RNA-seq) changes upon IGF2BP3 KO in control (left panel) and ER stress conditions (right panel). *P* values were calculated by edgeR glmQLFTest. **B.** Volcano plot of transcriptome (RNA-seq) changes upon ER stress treatment showing the selection of UPR targets (left panel), and volcano plot upon IGF2BP3 KO in ER stress conditions with highlighted UPR targets (upregulated more than two-fold in ER stress than in control, *P* value adj. < 0.05, total RNA-Seq) and IGF2BP3-bound UPR targets (right panel). *P* values were calculated by edgeR glmQLFTest. **C.** Boxplot showing changes in transcript levels upon IGF2BP3 KO for IGF2BP3-bound transcripts, UPR targets, and IGF2BP3-bound UPR targets. *P* values were calculated by two-sided Wilcoxon test. **D.** Boxplot showing changes in

transcript levels upon siRNA-mediated IGF2BP3 for IGF2BP3-bound transcripts, UPR targets, and IGF2BP3-bound UPR targets. n=3 biological replicates. *P* values were calculated by two-sided Wilcoxon test. **E.** RT-qPCR analyses of relative mRNA levels for UPR targets (*HSPA5*, *XBP1* spliced and total, *ATF4*, *DDIT4*) in IGF2BP3 KO and parental cells treated with 100 ng/mL TM for 7 hours. n=4 biological replicates. *P* values were calculated by unpaired two-sided Student's t-test. **F.** Boxplot showing changes in protein levels (total proteome mass spectrometry) upon IGF2BP3 KO for all identified proteins and UPR targets (upregulated more than 25% in ER stress than in control, *P* value adj. < 0.05, total proteome). ER stress was induced with 100 ng/mL TM for 7 hours. *P* values were calculated by two-sided Wilcoxon test. n=4 biological replicates.

If not indicated otherwise, ER stress was induced with TM at 5 µg/mL for 4 hours. For the transcriptome analysis IGF2BP3 KO cell three clones (in duplicates) and parental cells in quadruplicate were used. In RT-qPCR analyses, mRNA levels were normalized to *RPL6*. **P* < 0.05; ***P* < 0.01; ****P* < 0.001; *****P* < 0.0001.

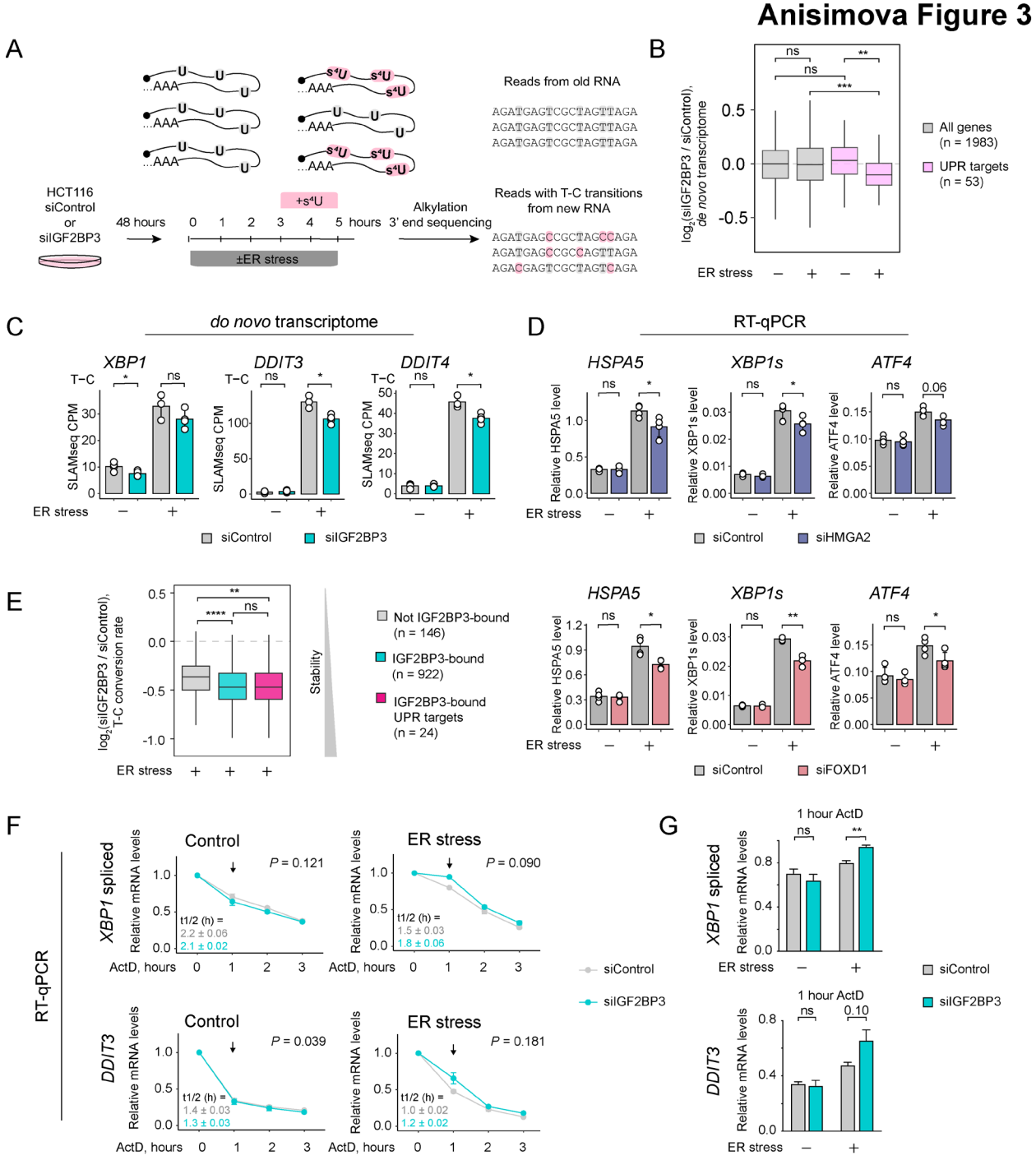



**Figure 3. IGF2BP3 shapes the UPR through transcriptional feedback loops.**

**A.** Design of the thiol (SH)-linked alkylation for the metabolic sequencing of RNA (SLAMseq) experiment. IGF2BP3 is depleted for 48 hours using siRNA. Prior to collection cells were treated with TM at 5 µg/mL or with DMSO as a control for 5 h. In the last 2 hours 100 µM 4-thiouridine ($s^4U$) was added to the cells to label the newly synthesized mRNA. **B.** Boxplot showing changes in *de novo* transcripts levels of UPR targets (transcribed during 2-hour $s^4U$ pulse) T-C (SLAMseq T-C CPM) upon siRNA-mediated depletion of IGF2BP3. *P* values were calculated by

two-sided Wilcoxon test. **C.** SLAMseq *de novo* (T-C) CPM values for selected UPR target genes (*XBP1*, *DDIT4*, and *DDIT3*). Data are the mean ± s.d of n=4 biological replicates. *P* values were calculated by unpaired two-sided Student's t-test. **D.** RT-qPCR of *HSPA5*, *XBP1* spliced, and *ATF4* in unstressed cells and cells treated with TM at 100 ng/mL for 8 hours upon siRNA-mediated depletion of HMGA2 (upper panel) and FOXD1 (lower panel). Data are the mean ± s.d. of n=4 biological replicates. *P* values were calculated by unpaired two-sided Student's t-test. **E.** Boxplot showing changes in estimated transcript stability upon ER stress following siRNA-mediated IGF2BP3 depletion for IGF2BP3-bound transcripts, IGF2BP3-bound UPR targets, and non-IGF2BP3 bound transcripts (IR-PAR-CLIP CPM / QuantSeq CPM < 0.1). The changes in transcript stability were assessed by analyzing the differences in average T-C conversion rates per gene following IGF2BP3 depletion. T-C conversion rate values indicate the relative abundance of both pre-existing and newly synthesized mRNA for a given gene, with a decrease in these values suggesting increased stabilization. *P* values were calculated by two-sided Wilcoxon test. **F.** RT-qPCR analyses of degradation rates of the UPR targets *XBP1* (spliced) and *DDIT3* upon siRNA-mediated depletion of IGF2BP3. HCT116 cells were treated with TM at 250 ng/mL for 4 hours and the transcription was blocked with 5 µg/mL ActD for indicated time points. Data are the mean ± s.e. of n=4 biological replicates. *P* values were calculated by paired two-sided Student's t-test. **G.** Barplots showing results of RT-qPCR analyses of *XBP1* (spliced) and *DDIT3* total mRNA levels in unstressed cells and cells treated with TM at 250 ng/mL for 4 hours. Arrows indicate the 1-hour ActD treatment time point selected for boxplot representation in E**.** *P* values were calculated by unpaired two-sided Student's t-test.

For the SLAMseq experiments n=4 biological replicates. In RT-qPCR analyses, mRNA levels were normalized to *RPL6*. **P* < 0.05; ***P* < 0.01; ****P* < 0.001; *****P* < 0.0001.

**Anisimova Figure 4**

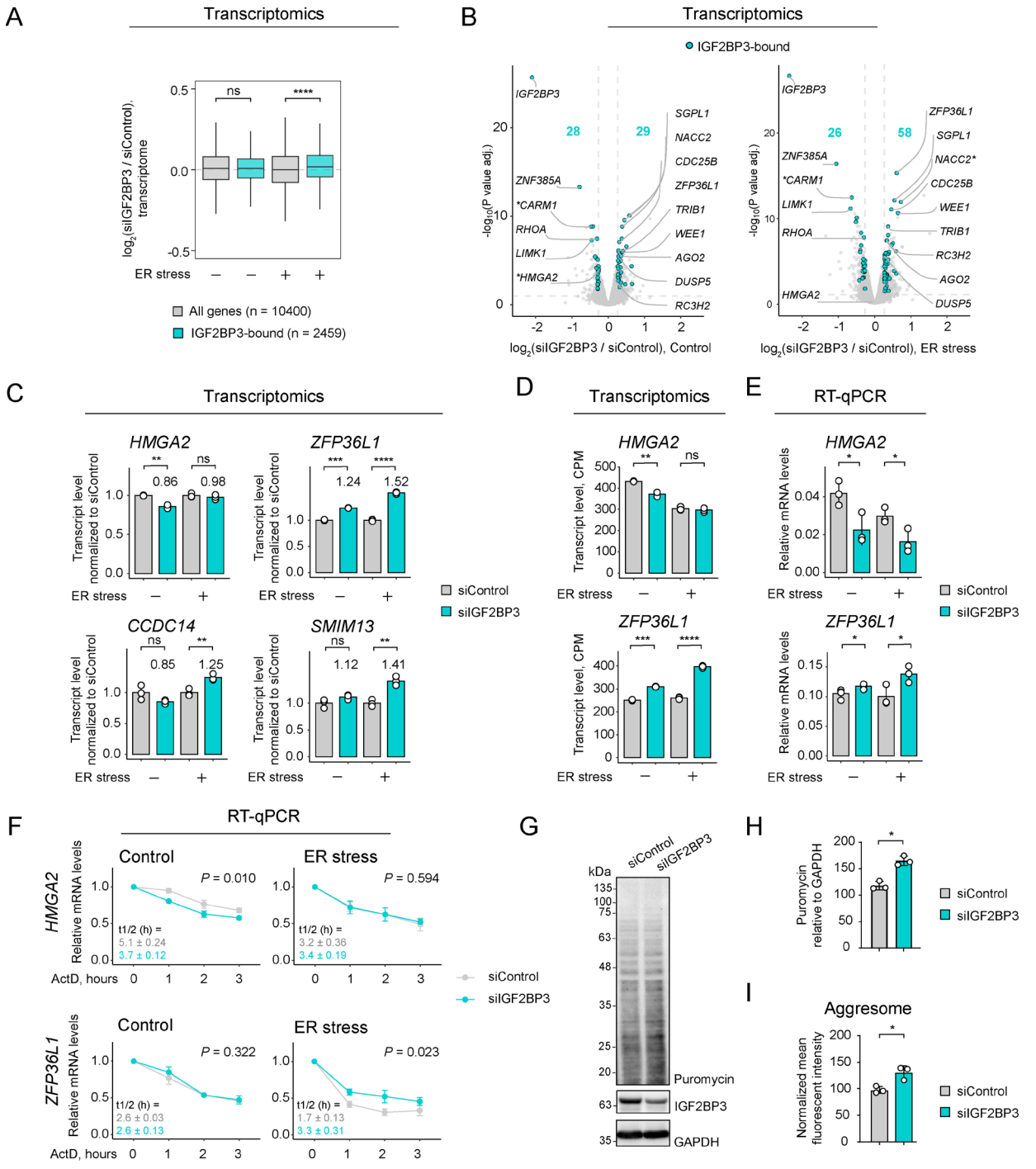



**Figure 4. IGF2BP3 facilitates the degradation of its target mRNAs during ER stress.**
**A.** Boxplot showing changes in total transcript levels (RNA-seq) upon siRNA-mediated depletion of IGF2BP3 for all genes and IGF2BP3-bound transcripts in control and ER stress conditions. **B.** Volcano plots of total transcriptome changes (RNA-seq) upon siRNA-mediated IGF2BP3 depletion with regulated genes highlighted (ΔRNA-seq > 20% and *P* value adj. < 0.05). * marks the genes encoding transcriptional regulators. **C.** Barplots showing total RNA-seq CPM values

normalized to siControl conditions for selected genes regulated by IGF2BP3. Data are the mean ± s.d of n=3 biological replicates. *P* values were calculated by unpaired two-sided Student's t-test. Numbers indicate normalized mean data. **D.** Barplots showing total RNA-seq CPM values for *HMGA2* and *ZFP36L1*. Data are the mean ± s.d of n=3 biological replicates. *P* values were calculated by unpaired two-sided Student's t-test. **E.** Barplots showing results of RT-qPCR analyses of *HMGA2* and *ZFP36L1* in unstressed cells and cells treated with TM at 5 µg/mL for 6 hours upon siRNA-mediated depletion of IGF2BP3. Data are the mean ± s.d. of n=3 biological replicates. *P* values were calculated by unpaired two-sided Student's t-test. **F**. RT-qPCR analyses of degradation rates for *HMGA2* and *ZFP36L1* upon siRNA-mediated depletion of IGF2BP3. HCT116 cells were treated with TM at 5 µg/mL for 3 hours and the transcription was blocked with ActD for indicated time points. Data are the mean ± s.e. of n=3 biological replicates. *P* values were calculated by paired two-sided Student's t-test. **G.** Western blot showing global protein synthesis (30 min puromycin pulse) upon siRNA-mediated depletion of IGF2BP3 in ER stress conditions. **H.** Quantification of G. Data are the mean ± s.d. of n=3 biological replicates. *P* values were calculated by unpaired two-sided Student's t-test. **I.** Flow cytometry analysis of aggresome formation using the ProteoStat dye upon siRNA-mediated depletion of IGF2BP3 in ER stress conditions. Data are the mean ± s.d. of n=3 biological replicates. *P* values were calculated by unpaired two-sided Student's t-test.

For the transcriptome analyses n=3 biological replicates. In RT-qPCR analyses, mRNA levels were normalized to *RPL6*. ER stress was induced with 5 µg/mL TM for 4 hours. **P* < 0.05; ***P* < 0.01; ****P* < 0.001; *****P* < 0.0001.

**Anisimova Figure 5**

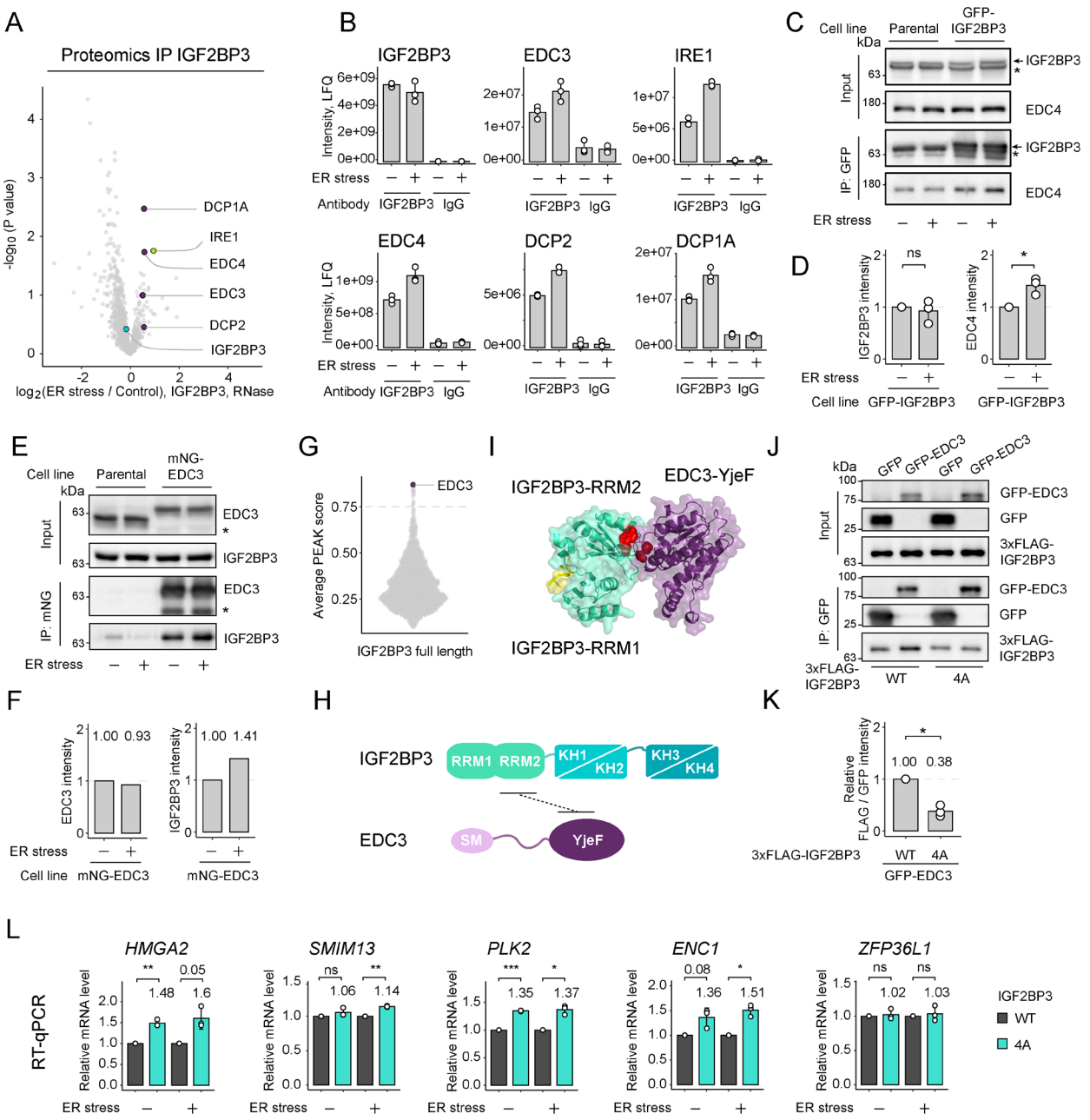



**Figure 5. ER stress promotes the association of IGF2BP3 with mRNA decapping complex.** **A.** Volcano plot comparing interactome of endogenous IGF2BP3 (co-IP–MS analysis) in control and ER stress conditions. Proteins whose interaction with IGF2BP3 is largely resistant to RNase treatment (≤50% reduction) are shown. **B.** Normalized LFQ values for selected examples of IGF2BP3 interacting proteins that increase interaction with IGF2BP3 upon ER stress. Data are the mean ± s.d. of n=3 biological replicates. **C.** Western blot showing association of EDC4 with IGF2BP3 upon ER stress after immunoprecipitation of GFP-IGF2BP3 from HEK293T cells. * IGF2BP2 isoforms recognized by the polyclonal anti-IGF2BP3 antibody. **D.** Quantification of C.

Data are the mean ± s.d. of n=3 biological replicates. *P* values were calculated by unpaired two-sided Student's t-test. **E**. Western blot showing association of IGF2BP3 with EDC3 upon ER stress after immunoprecipitation of mNeonGreen-EDC3 from HEK293T cells. * split-mNeonGreen-EDC3 degradation product. **F.** Quantification of E. **G.** Violin plot of AlphaFold2-Multimer (Jumper, Evans et al. 2021, Evans, O'Neill et al. 2022, Mirdita, Schutze et al. 2022) PEAK scores predicting putative protein-protein interactions between full-length IGF2BP3 and IGF2BP3 interaction partners identified using co-IP-MS. **H.** Domain architecture of IGF2BP3 and EDC3. **I.** Predicted structural model (AlphaFold3) (Abramson, Adler et al. 2024) of IGF2BP3 RRM1/2 domains (cyan) interacting with EDC3 YjeF domain (violet) through RRM2. RNA interacting with RRM1 is shown in yellow to highlight the RNA interaction interface (Jia, Gut et al. 2018). IGF2BP3 residues I88, P90, H91, W94 are shown in red. **J.** Western blot showing association of IGF2BP3 with EDC3 after immunoprecipitation of GFP-EDC3 from HCT116 IGF2BP3 KO cells expressing 3xFLAG-IGF2BP3 WT or 4A (I88A, P90A, H91A, W94A) mutant. **K.** Quantification of J. Data are the mean ± s.d. of n=3 biological replicates. *P* values were calculated by unpaired two-sided Student's t-test. **L.** RT-qPCR of IGF2BP3 target mRNAs in HCT116 cells expressing IGF2BP3 WT or the IGF2BP3 4A mutant. mRNA levels were normalized to *RPL6* and shown relative to IGF2BP3 WT. Data are the mean ± s.d. of n=3 biological replicates. *P* values were calculated by unpaired two-sided Student's t-test.
For IGF2BP3 co-IP–MS analysis n=3 biological replicates. ER stress was induced with 5 µg/mL TM for 4 hours. *$P < 0.05$.

**Anisimova Figure 6**

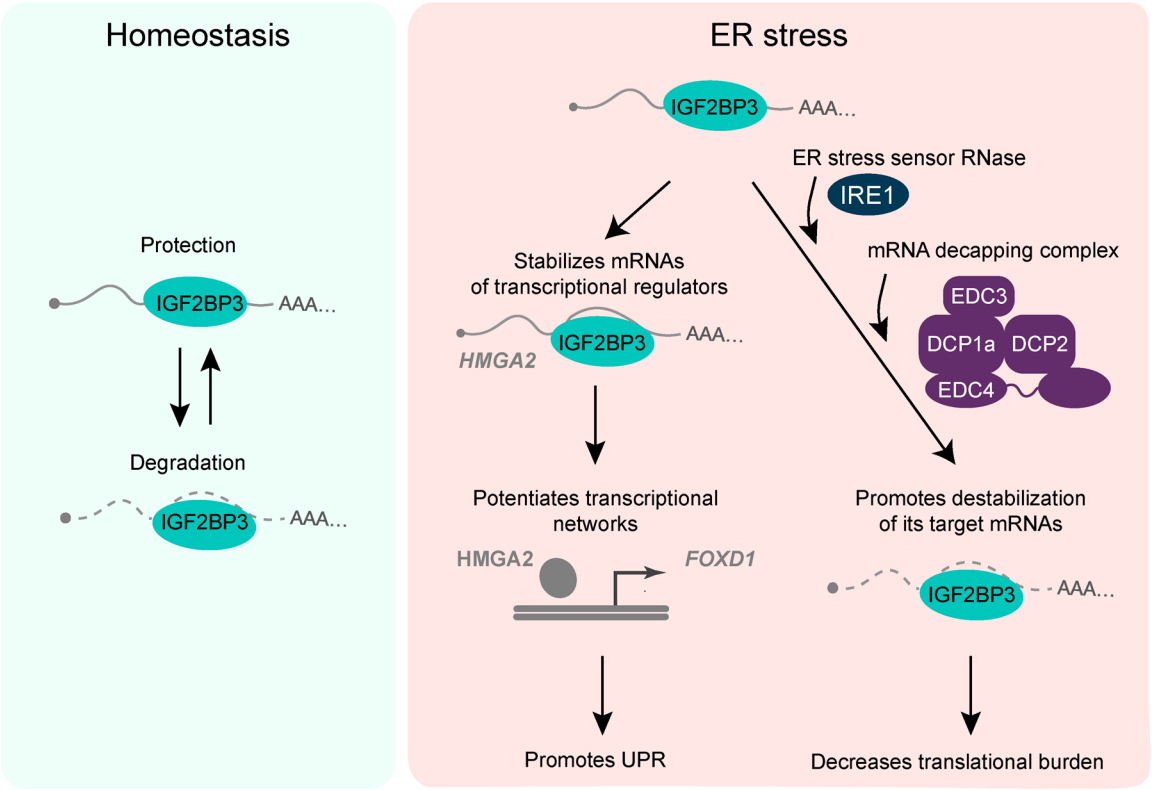



**Figure 6. Model of IGF2BP3 function and regulation in ER stress conditions.**
Depending on the transcript identity, IGF2BP3 binding to its target mRNAs can either promote their degradation or increase stability. Under homeostatic conditions, there is a balance between stabilization and degradation by IGF2BP3. ER stress increases the pro-degradation function of IGF2BP3 and degradation of its target transcripts, including the UPR effector mRNAs, through increased interaction of IGF2BP3 with mRNA decapping complexes and, potentially, with the ER stress sensor RNase IRE1. Upon ER stress, IGF2BP3 indirectly elicits potent UPR by stabilizing mRNA encoding a secondary transcriptional regulator of the UPR, HMGA2. This dual-layered regulation allows IGF2BP3 to specifically upregulate UPR targets while broadly driving degradation of other transcripts to decrease ER folding load until stress is relieved.

## References


Abramson, J., J. Adler, J. Dunger, R. Evans, T. Green, A. Pritzel, O. Ronneberger, L. Willmore, A. J. Ballard, J. Bambrick, S. W. Bodenstein, D. A. Evans, C. C. Hung, M. O'Neill, D. Reiman, K. Tunyasuvunakool, Z. Wu, A. Zemgulyte, E. Arvaniti, C. Beattie, O. Bertolli, A. Bridgland, A. Cherepanov, M. Congreve, A. I. Cowen-Rivers, A. Cowie, M. Figurnov, F. B. Fuchs, H. Gladman, R. Jain, Y. A. Khan, C. M. R. Low, K. Perlin, A. Potapenko, P. Savy, S. Singh, A. Stecula, A. Thillaisundaram, C. Tong, S. Yakneen, E. D. Zhong, M. Zielinski, A. Zidek, V. Bapst, P. Kohli, M. Jaderberg, D. Hassabis and J. M. Jumper (2024). "Accurate structure prediction of biomolecular interactions with AlphaFold 3." Nature **630**(8016): 493-500.

Acosta-Alvear, D., G. E. Karagoz, F. Frohlich, H. Li, T. C. Walther and P. Walter (2018). "The unfolded protein response and endoplasmic reticulum protein targeting machineries converge on the stress sensor IRE1." Elife **7**.

Acosta-Alvear, D., Y. Zhou, A. Blais, M. Tsikitis, N. H. Lents, C. Arias, C. J. Lennon, Y. Kluger and B. D. Dynlacht (2007). "XBP1 controls diverse cell type- and condition-specific transcriptional regulatory networks." Mol Cell **27**(1): 53-66.

An, W., J. Kim and R. G. Roeder (2004). "Ordered cooperative functions of PRMT1, p300, and CARM1 in transcriptional activation by p53." Cell **117**(6): 735-748.

Anisimova, A. S. and G. E. Karagöz (2023). "Optimized infrared photoactivatable ribonucleoside-enhanced crosslinking and immunoprecipitation (IR-PAR-CLIP) protocol identifies novel IGF2BP3-interacting RNAs in colon cancer cells." RNA (New York, N.Y.) **29**(11): 1818-1836.

Ashar, H. R., R. A. Chouinard, Jr., M. Dokur and K. Chada (2010). "In vivo modulation of HMGA2 expression." Biochim Biophys Acta **1799**(1-2): 55-61.

Bell, J. L., K. Wächter, B. Mühleck, N. Pazaitis, M. Köhn, M. Lederer and S. Hüttelmaier (2013). "Insulin-like growth factor 2 mRNA-binding proteins (IGF2BPs): post-transcriptional drivers of cancer progression?" Cellular and Molecular Life Sciences **70**(15): 2657-2675.

Bernales, S., K. L. McDonald and P. Walter (2006). "Autophagy counterbalances endoplasmic reticulum expansion during the unfolded protein response." PLoS Biol **4**(12): e423.

Bommiasamy, H., S. H. Back, P. Fagone, K. Lee, S. Meshinchi, E. Vink, R. Sriburi, M. Frank, S. Jackowski, R. J. Kaufman and J. W. Brewer (2009). "ATF6alpha induces XBP1-independent expansion of the endoplasmic reticulum." J Cell Sci **122**(Pt 10): 1626-1636.

Buchan, J. R., T. Nissan and R. Parker (2010). "Analyzing P-bodies and stress granules in Saccharomyces cerevisiae." Methods in enzymology **470**: 619-640.

Buchan, J. R. and R. Parker (2009). "Eukaryotic stress granules: the ins and outs of translation." Mol Cell **36**(6): 932-941.

Chen, C. Y., N. Ezzeddine and A. B. Shyu (2008). "Messenger RNA half-life measurements in mammalian cells." Methods Enzymol **448**: 335-357.

Chen, E. Y., C. M. Tan, Y. Kou, Q. Duan, Z. Wang, G. V. Meirelles, N. R. Clark and A. Ma'ayan (2013). "Enrichr: interactive and collaborative HTML5 gene list enrichment analysis tool." BMC Bioinformatics **14**: 128.

Cho, N. H., K. C. Cheveralls, A. D. Brunner, K. Kim, A. C. Michaelis, P. Raghavan, H. Kobayashi, L. Savy, J. Y. Li, H. Canaj, J. Y. S. Kim, E. M. Stewart, C. Gnann, F. McCarthy, J. P. Cabrera, R. M. Brunetti, B. B. Chhun, G. Dingle, M. Y. Hein, B. Huang, S. B. Mehta, J. S. Weissman, R. Gomez-Sjoberg, D. N. Itzhak, L. A. Royer, M. Mann and M. D. Leonetti (2022). "OpenCell: Endogenous tagging for the cartography of human cellular organization." Science **375**(6585): eabi6983.

Cho, S., G. Lee, B. F. Pickering, C. Jang, J. H. Park, L. He, L. Mathur, S. S. Kim, S. Jung, H. W. Tang, S. Monette, J. D. Rabinowitz, N. Perrimon, S. R. Jaffrey and J. Blenis (2021). "mTORC1

promotes cell growth via m(6)A-dependent mRNA degradation." Mol Cell **81**(10): 2064-2075 e2068.
Conway, A. E. E., E. L. Van Nostrand, G. A. A. Pratt, S. Aigner, M. L. L. Wilbert, B. Sundararaman, P. Freese, N. J. J. Lambert, S. Sathe, T. Y. Y. Liang, A. Essex, S. Landais, C. B. B. Burge, D. L. L. Jones, G. W. W. Yeo, G. A. A. Pratt, B. Sundararaman, A. Essex, G. W. W. Yeo, D. L. L. Jones, C. B. B. Burge, P. Freese, M. L. L. Wilbert, S. Sathe, E. L. Van Nostrand, S. Landais, A. E. E. Conway, T. Y. Y. Liang, S. Aigner, E. L. Van Nostrand, G. A. A. Pratt, S. Aigner, M. L. L. Wilbert, B. Sundararaman, P. Freese, N. J. J. Lambert, S. Sathe, T. Y. Y. Liang, A. Essex, S. Landais, C. B. B. Burge, D. L. L. Jones, G. W. W. Yeo, G. A. A. Pratt, B. Sundararaman, A. Essex, G. W. W. Yeo, D. L. L. Jones, C. B. B. Burge, P. Freese, M. L. L. Wilbert, S. Sathe, E. L. Van Nostrand, S. Landais, A. E. E. Conway, T. Y. Y. Liang and S. Aigner (2016). "Enhanced CLIP Uncovers IMP Protein-RNA Targets in Human Pluripotent Stem Cells Important for Cell Adhesion and Survival." Cell Reports **15**(3): 666-679.
Corcoran, D. L., S. Georgiev, N. Mukherjee, E. Gottwein, R. L. Skalsky, J. D. Keene and U. Ohler (2011). "PARalyzer: definition of RNA binding sites from PAR-CLIP short-read sequence data." Genome Biol **12**(8): R79.
Cotter, K. A., J. Gallon, N. Uebersax, P. Rubin, K. D. Meyer, S. Piscuoglio, S. R. Jaffrey and M. A. Rubin (2021). "Mapping of m(6)A and Its Regulatory Targets in Prostate Cancer Reveals a METTL3-Low Induction of Therapy Resistance." Mol Cancer Res **19**(8): 1398-1411.
da Veiga Leprevost, F., S. E. Haynes, D. M. Avtonomov, H. Y. Chang, A. K. Shanmugam, D. Mellacheruvu, A. T. Kong and A. I. Nesvizhskii (2020). "Philosopher: a versatile toolkit for shotgun proteomics data analysis." Nat Methods **17**(9): 869-870.
de Almeida, M., M. Hinterndorfer, H. Brunner, I. Grishkovskaya, K. Singh, A. Schleiffer, J. Jude, S. Deswal, R. Kalis, M. Vunjak, T. Lendl, R. Imre, E. Roitinger, T. Neumann, S. Kandolf, M. Schutzbier, K. Mechtler, G. A. Versteeg, D. Haselbach and J. Zuber (2021). "AKIRIN2 controls the nuclear import of proteasomes in vertebrates." Nature **599**(7885): 491-496.
Degrauwe, N., M. L. Suva, M. Janiszewska, N. Riggi and I. Stamenkovic (2016). "IMPs: an RNA-binding protein family that provides a link between stem cell maintenance in normal development and cancer." Genes Dev **30**(22): 2459-2474.
Egorov, A. A., E. A. Sakharova, A. S. Anisimova, S. E. Dmitriev, V. N. Gladyshev and I. V. Kulakovskiy (2019). "svist4get: a simple visualization tool for genomic tracks from sequencing experiments." BMC Bioinformatics **20**(1): 113.
Ennajdaoui, H., J. M. Howard, T. Sterne-Weiler, F. Jahanbani, D. J. Coyne, P. J. Uren, M. Dargyte, S. Katzman, J. M. Draper, A. Wallace, O. Cazarez, S. C. Burns, M. Qiao, L. Hinck, A. D. Smith, M. M. Toloue, B. J. Blencowe, L. O. Penalva and J. R. Sanford (2016). "IGF2BP3 Modulates the Interaction of Invasion-Associated Transcripts with RISC." Cell Rep **15**(9): 1876-1883.
Evans, R., M. O'Neill, A. Pritzel, N. Antropova, A. Senior, T. Green, A. Žídek, R. Bates, S. Blackwell, J. Yim, O. Ronneberger, S. Bodenstein, M. Zielinski, A. Bridgland, A. Potapenko, A. Cowie, K. Tunyasuvunakool, R. Jain, E. Clancy, P. Kohli, J. Jumper and D. Hassabis (2022). "Protein complex prediction with AlphaFold-Multimer." bioRxiv: 2021.2010.2004.463034.
Ewels, P. A., A. Peltzer, S. Fillinger, H. Patel, J. Alneberg, A. Wilm, M. U. Garcia, P. Di Tommaso and S. Nahnsen (2020). "The nf-core framework for community-curated bioinformatics pipelines." Nat Biotechnol **38**(3): 276-278.
Fedele, M., M. T. Berlingieri, S. Scala, L. Chiariotti, G. Viglietto, V. Rippel, J. Bullerdiek, M. Santoro and A. Fusco (1998). "Truncated and chimeric HMGI-C genes induce neoplastic transformation of NIH3T3 murine fibroblasts." Oncogene **17**(4): 413-418.
Frietze, S., M. Lupien, P. A. Silver and M. Brown (2008). "CARM1 regulates estrogen-stimulated breast cancer growth through up-regulation of E2F1." Cancer Res **68**(1): 301-306.
Fumagalli, F., J. Noack, T. J. Bergmann, E. Cebollero, G. B. Pisoni, E. Fasana, I. Fregno, C. Galli, M. Loi, T. Solda, R. D'Antuono, A. Raimondi, M. Jung, A. Melnyk, S. Schorr, A. Schreiber,

L. Simonelli, L. Varani, C. Wilson-Zbinden, O. Zerbe, K. Hofmann, M. Peter, M. Quadroni, R. Zimmermann and M. Molinari (2016). "Translocon component Sec62 acts in endoplasmic reticulum turnover during stress recovery." Nat Cell Biol **18**(11): 1173-1184.
Gebauer, F., T. Schwarzl, J. Valcarcel and M. W. Hentze (2021). "RNA-binding proteins in human genetic disease." Nat Rev Genet **22**(3): 185-198.
Grant, T. L. B. a. C. E. (2021). SEA: Simple Enrichment Analysis of motifs. Biorxiv.
Grumati, P., G. Morozzi, S. Holper, M. Mari, M. I. Harwardt, R. Yan, S. Muller, F. Reggiori, M. Heilemann and I. Dikic (2017). "Full length RTN3 regulates turnover of tubular endoplasmic reticulum via selective autophagy." Elife **6**.
Hafner, M., M. Landthaler, L. Burger, M. Khorshid, J. Hausser, P. Berninger, A. Rothballer, M. Ascano, Jr., A. C. Jungkamp, M. Munschauer, A. Ulrich, G. S. Wardle, S. Dewell, M. Zavolan and T. Tuschl (2010). "Transcriptome-wide identification of RNA-binding protein and microRNA target sites by PAR-CLIP." Cell **141**(1): 129-141.
Hansen, T. V., N. A. Hammer, J. Nielsen, M. Madsen, C. Dalbaeck, U. M. Wewer, J. Christiansen and F. C. Nielsen (2004). "Dwarfism and impaired gut development in insulin-like growth factor II mRNA-binding protein 1-deficient mice." Mol Cell Biol **24**(10): 4448-4464.
Harding, H. P., Y. Zhang, A. Bertolotti, H. Zeng and D. Ron (2000). "Perk is essential for translational regulation and cell survival during the unfolded protein response." Molecular cell **5**(5): 897-904.
Harding, H. P., Y. Zhang and D. Ron (1999). "Protein translation and folding are coupled by an endoplasmic-reticulum-resident kinase." Nature **397**(6716): 271-274.
Hatini, V., S. O. Huh, D. Herzlinger, V. C. Soares and E. Lai (1996). "Essential role of stromal mesenchyme in kidney morphogenesis revealed by targeted disruption of Winged Helix transcription factor BF-2." Genes Dev **10**(12): 1467-1478.
Heinz, S., C. Benner, N. Spann, E. Bertolino, Y. C. Lin, P. Laslo, J. X. Cheng, C. Murre, H. Singh and C. K. Glass (2010). "Simple combinations of lineage-determining transcription factors prime cis-regulatory elements required for macrophage and B cell identities." Mol Cell **38**(4): 576-589.
Hentze, M. W., A. Castello, T. Schwarzl and T. Preiss (2018). "A brave new world of RNA-binding proteins." Nat Rev Mol Cell Biol **19**(5): 327-341.
Herzog, V. A., B. Reichholf, T. Neumann, P. Rescheneder, P. Bhat, T. R. Burkard, W. Wlotzka, A. von Haeseler, J. Zuber and S. L. Ameres (2017). "Thiol-linked alkylation of RNA to assess expression dynamics." Nature Methods **14**(12): 1198-1204.
Hohmann, U., M. Graf, U. Schellhaas, B. Pacheco-Fiallos, L. Fin, D. Riabov-Bassat, T. Pühringer, M.-F. Szalay, L. Tirián, D. Handler, J. Brennecke and C. Plaschka (2024). "A molecular switch orchestrates the nuclear export of human messenger RNA." bioRxiv: 2024.2003.2024.586400.
Holcik, M. and N. Sonenberg (2005). "Translational control in stress and apoptosis." Nat Rev Mol Cell Biol **6**(4): 318-327.
Hollenstein, D. M., M. Maurer-Granofszky, W. Reiter, D. Anrather, T. Gossenreiter, R. Babic, N. Hartl, C. Kraft and M. Hartl (2023). "Chemical Acetylation of Ligands and Two-Step Digestion Protocol for Reducing Codigestion in Affinity Purification-Mass Spectrometry." J Proteome Res **22**(10): 3383-3391.
Hollien, J. and J. S. Weissman (2006). "Decay of endoplasmic reticulum-localized mRNAs during the unfolded protein response." Science **313**(5783): 104-107.
Hornegger, H., A. S. Anisimova, A. Muratovic, B. Bourgeois, E. Spinetti, I. Niedermoser, R. Covino, T. Madl and G. E. Karagoz (2024). "IGF2BP1 phosphorylation in the disordered linkers regulates ribonucleoprotein condensate formation and RNA metabolism." Nat Commun **15**(1): 9054.
Huang, H., H. Weng, W. Sun, X. Qin, H. Shi, H. Wu, B. S. Zhao, A. Mesquita, C. Liu, C. L. Yuan, Y.-C. C. Hu, S. Hüttelmaier, J. R. Skibbe, R. Su, X. Deng, L. Dong, M. Sun, C. Li, S. Nachtergaele, Y. Wang, C. Hu, K. Ferchen, K. D. Greis, X. Jiang, M. Wei, L. Qu, J.-L. L. Guan,

C. He, J. Yang and J. Chen (2018). "Recognition of RNA N 6-methyladenosine by IGF2BP proteins enhances mRNA stability and translation." Nature Cell Biology **20**(3): 285-295.
Huttelmaier, S., D. Zenklusen, M. Lederer, J. Dictenberg, M. Lorenz, X. Meng, G. J. Bassell, J. Condeelis and R. H. Singer (2005). "Spatial regulation of beta-actin translation by Src-dependent phosphorylation of ZBP1." Nature **438**(7067): 512-515.
Jia, M., H. Gut and J. A. Chao (2018). "Structural basis of IMP3 RRM12 recognition of RNA." RNA **24**(12): 1659-1666.
Jia, R., P. Chai, S. Wang, B. Sun, Y. Xu, Y. Yang, S. Ge, R. Jia, Y. G. Yang and X. Fan (2019). "m(6)A modification suppresses ocular melanoma through modulating HINT2 mRNA translation." Mol Cancer **18**(1): 161.
Jimenez-Beltran, M. A., R. Valle-Bautista and E. R. Vazquez-Martinez (2026). "Expanding the landscape of the unfolded protein response: The roles of secondary transcription factors in development and disease." Cell Stress Chaperones **31**(1): 100141.
Jønson, L., J. Christiansen, T. V. O. Hansen, J. Vikeså, Y. Yamamoto and F. C. Nielsen (2014). "IMP3 RNP safe houses prevent miRNA-directed HMGA2 mRNA decay in cancer and development." Cell reports **7**(2): 539-551.
Jumper, J., R. Evans, A. Pritzel, T. Green, M. Figurnov, O. Ronneberger, K. Tunyasuvunakool, R. Bates, A. Zidek, A. Potapenko, A. Bridgland, C. Meyer, S. A. A. Kohl, A. J. Ballard, A. Cowie, B. Romera-Paredes, S. Nikolov, R. Jain, J. Adler, T. Back, S. Petersen, D. Reiman, E. Clancy, M. Zielinski, M. Steinegger, M. Pacholska, T. Berghammer, S. Bodenstein, D. Silver, O. Vinyals, A. W. Senior, K. Kavukcuoglu, P. Kohli and D. Hassabis (2021). "Highly accurate protein structure prediction with AlphaFold." Nature **596**(7873): 583-589.
Khaminets, A., T. Heinrich, M. Mari, P. Grumati, A. K. Huebner, M. Akutsu, L. Liebmann, A. Stolz, S. Nietzsche, N. Koch, M. Mauthe, I. Katona, B. Qualmann, J. Weis, F. Reggiori, I. Kurth, C. A. Hubner and I. Dikic (2015). "Regulation of endoplasmic reticulum turnover by selective autophagy." Nature **522**(7556): 354-358.
Kong, A. T., F. V. Leprevost, D. M. Avtonomov, D. Mellacheruvu and A. I. Nesvizhskii (2017). "MSFragger: ultrafast and comprehensive peptide identification in mass spectrometry-based proteomics." Nat Methods **14**(5): 513-520.
Kuleshov, M. V., M. R. Jones, A. D. Rouillard, N. F. Fernandez, Q. Duan, Z. Wang, S. Koplev, S. L. Jenkins, K. M. Jagodnik, A. Lachmann, M. G. McDermott, C. D. Monteiro, G. W. Gundersen and A. Ma'ayan (2016). "Enrichr: a comprehensive gene set enrichment analysis web server 2016 update." Nucleic Acids Res **44**(W1): W90-97.
Latifkar, A., F. Wang, J. J. Mullmann, E. Panizza, I. R. Fernandez, L. Ling, A. D. Miller, C. Fischbach, R. S. Weiss, H. Lin, R. A. Cerione and M. A. Antonyak (2022). "IGF2BP2 promotes cancer progression by degrading the RNA transcript encoding a v-ATPase subunit." Proc Natl Acad Sci U S A **119**(45): e2200477119.
Le Thomas, A., E. Ferri, S. Marsters, J. M. Harnoss, D. A. Lawrence, I. Zuazo-Gaztelu, Z. Modrusan, S. Chan, M. Solon, C. Chalouni, W. Li, H. Koeppen, J. Rudolph, W. Wang, T. D. Wu, P. Walter and A. Ashkenazi (2021). "Decoding non-canonical mRNA decay by the endoplasmic-reticulum stress sensor IRE1α." Nature Communications **12**(1): 1-15.
Lederer, M., N. Bley, C. Schleifer and S. Huttelmaier (2014). "The role of the oncofetal IGF2 mRNA-binding protein 3 (IGF2BP3) in cancer." Semin Cancer Biol **29**: 3-12.
Lee, A. H., N. N. Iwakoshi and L. H. Glimcher (2003). "XBP-1 regulates a subset of endoplasmic reticulum resident chaperone genes in the unfolded protein response." Molecular and cellular biology **23**(21): 7448-7459.
Leeds, P., B. T. Kren, J. M. Boylan, N. A. Betz, C. J. Steer, P. A. Gruppuso and J. Ross (1997). "Developmental regulation of CRD-BP, an RNA-binding protein that stabilizes c-myc mRNA in vitro." Oncogene **14**(11): 1279-1286.

Leonetti, M. D., S. Sekine, D. Kamiyama, J. S. Weissman and B. Huang (2016). "A scalable strategy for high-throughput GFP tagging of endogenous human proteins." Proc Natl Acad Sci U S A **113**(25): E3501-3508.
Liang, Z., H. Ye, J. Ma, Z. Wei, Y. Wang, Y. Zhang, D. Huang, B. Song, J. Meng, D. J. Rigden and K. Chen (2024). "m6A-Atlas v2.0: updated resources for unraveling the N6-methyladenosine (m6A) epitranscriptome among multiple species." Nucleic Acids Res **52**(D1): D194-D202.
Liao, Y., G. K. Smyth and W. Shi (2014). "featureCounts: an efficient general purpose program for assigning sequence reads to genomic features." Bioinformatics **30**(7): 923-930.
Lin, J. H., H. Li, D. Yasumura, H. R. Cohen, C. Zhang, B. Panning, K. M. Shokat, M. M. Lavail and P. Walter (2007). "IRE1 signaling affects cell fate during the unfolded protein response." Science (New York, N.Y.) **318**(5852): 944-949.
Linder, B., A. V. Grozhik, A. O. Olarerin-George, C. Meydan, C. E. Mason and S. R. Jaffrey (2015). "Single-nucleotide-resolution mapping of m6A and m6Am throughout the transcriptome." Nat Methods **12**(8): 767-772.
Ling, S. H., C. J. Decker, M. A. Walsh, M. She, R. Parker and H. Song (2008). "Crystal structure of human Edc3 and its functional implications." Mol Cell Biol **28**(19): 5965-5976.
Liu, C., X. Dou, Y. Zhao, L. Zhang, L. Zhang, Q. Dai, J. Liu, T. Wu, Y. Xiao and C. He (2024). "IGF2BP3 promotes mRNA degradation through internal m(7)G modification." Nat Commun **15**(1): 7421.
Lu, G., R. E. Middleton, H. Sun, M. Naniong, C. J. Ott, C. S. Mitsiades, K. K. Wong, J. E. Bradner and W. G. Kaelin, Jr. (2014). "The myeloma drug lenalidomide promotes the cereblon-dependent destruction of Ikaros proteins." Science **343**(6168): 305-309.
Lu, M., D. A. Lawrence, S. Marsters, D. Acosta-Alvear, P. Kimmig, A. S. Mendez, A. W. Paton, J. C. Paton, P. Walter and A. Ashkenazi (2014). "Opposing unfolded-protein-response signals converge on death receptor 5 to control apoptosis." Science **345**(6192): 98-101.
Lu, Y., F. X. Liang and X. Wang (2014). "A synthetic biology approach identifies the mammalian UPR RNA ligase RtcB." Mol Cell **55**(5): 758-770.
Luo, S., C. Zhang, Z. Gao, L. Jiang, Q. Li, X. Shi, Y. Kong and J. Cao (2023). "ER stress-enhanced HMGA2 plays an important role in Cr (VI)-induced glycolysis and inhibited oxidative phosphorylation by targeting the transcription of ATF4." Chem Biol Interact **369**: 110293.
Malbec, L., T. Zhang, Y. S. Chen, Y. Zhang, B. F. Sun, B. Y. Shi, Y. L. Zhao, Y. Yang and Y. G. Yang (2019). "Dynamic methylome of internal mRNA N(7)-methylguanosine and its regulatory role in translation." Cell Res **29**(11): 927-941.
Mansoori, B., A. Mohammadi, H. J. Ditzel, P. H. G. Duijf, V. Khaze, M. F. Gjerstorff and B. Baradaran (2021). "HMGA2 as a Critical Regulator in Cancer Development." Genes (Basel) **12**(2).
Maris, C., C. Dominguez and F. H. Allain (2005). "The RNA recognition motif, a plastic RNA-binding platform to regulate post-transcriptional gene expression." FEBS J **272**(9): 2118-2131.
Mirdita, M., K. Schutze, Y. Moriwaki, L. Heo, S. Ovchinnikov and M. Steinegger (2022). "ColabFold: making protein folding accessible to all." Nat Methods **19**(6): 679-682.
Mizutani, R., N. Imamachi, Y. Suzuki, H. Yoshida, N. Tochigi, T. Oonishi, Y. Suzuki and N. Akimitsu (2016). "Oncofetal protein IGF2BP3 facilitates the activity of proto-oncogene protein eIF4E through the destabilization of EIF4E-BP2 mRNA." Oncogene **35**(27): 3495-3502.
Mongroo, P. S., F. K. Noubissi, M. Cuatrecasas, J. Kalabis, C. E. King, C. N. Johnstone, M. J. Bowser, A. Castells, V. S. Spiegelman and A. K. Rustgi (2011). "IMP-1 displays cross-talk with K-Ras and modulates colon cancer cell survival through the novel proapoptotic protein CYFIP2." Cancer Res **71**(6): 2172-2182.
Mori, H., S. Sakakibara, T. Imai, Y. Nakamura, T. Iijima, A. Suzuki, Y. Yuasa, M. Takeda and H. Okano (2001). "Expression of mouse igf2 mRNA-binding protein 3 and its implications for the developing central nervous system." J Neurosci Res **64**(2): 132-143.

Mueller-Pillasch, F., B. Pohl, M. Wilda, U. Lacher, M. Beil, C. Wallrapp, H. Hameister, W. Knochel, G. Adler and T. M. Gress (1999). "Expression of the highly conserved RNA binding protein KOC in embryogenesis." Mech Dev **88**(1): 95-99.
Muller, S., N. Bley, M. Glass, B. Busch, V. Rousseau, D. Misiak, T. Fuchs, M. Lederer and S. Huttelmaier (2018). "IGF2BP1 enhances an aggressive tumor cell phenotype by impairing miRNA-directed downregulation of oncogenic factors." Nucleic Acids Res **46**(12): 6285-6303.
Natsume, T., T. Kiyomitsu, Y. Saga and M. T. Kanemaki (2016). "Rapid Protein Depletion in Human Cells by Auxin-Inducible Degron Tagging with Short Homology Donors." Cell Reports **15**(1): 210-218.
Neumann, T., V. A. Herzog, M. Muhar, A. von Haeseler, J. Zuber, S. L. Ameres and P. Rescheneder (2019). "Quantification of experimentally induced nucleotide conversions in high-throughput sequencing datasets." BMC Bioinformatics **20**(1): 258.
Noubissi, F. K., I. Elcheva, N. Bhatia, A. Shakoori, A. Ougolkov, J. Liu, T. Minamoto, J. Ross, S. Y. Fuchs and V. S. Spiegelman (2006). "CRD-BP mediates stabilization of betaTrCP1 and c-myc mRNA in response to beta-catenin signalling." Nature **441**(7095): 898-901.
Pan, F., S. Huttelmaier, R. H. Singer and W. Gu (2007). "ZBP2 facilitates binding of ZBP1 to beta-actin mRNA during transcription." Mol Cell Biol **27**(23): 8340-8351.
Perez-Riverol, Y., J. Bai, C. Bandla, D. Garcia-Seisdedos, S. Hewapathirana, S. Kamatchinathan, D. J. Kundu, A. Prakash, A. Frericks-Zipper, M. Eisenacher, M. Walzer, S. Wang, A. Brazma and J. A. Vizcaino (2022). "The PRIDE database resources in 2022: a hub for mass spectrometry-based proteomics evidences." Nucleic Acids Res **50**(D1): D543-D552.
Pfannkuche, K., H. Summer, O. Li, J. Hescheler and P. Droge (2009). "The high mobility group protein HMGA2: a co-regulator of chromatin structure and pluripotency in stem cells?" Stem Cell Rev Rep **5**(3): 224-230.
Protter, D. S. and R. Parker (2016). "Principles and Properties of Stress Granules." Trends Cell Biol **26**(9): 668-679.
Quintero-Ronderos, P. and P. Laissue (2018). "The multisystemic functions of FOXD1 in development and disease." J Mol Med (Berl) **96**(8): 725-739.
Ran, F. A., P. D. Hsu, J. Wright, V. Agarwala, D. A. Scott and F. Zhang (2013). "Genome engineering using the CRISPR-Cas9 system." Nature Protocols **8**(11): 2281-2308.
Rappsilber, J., M. Mann and Y. Ishihama (2007). "Protocol for micro-purification, enrichment, pre-fractionation and storage of peptides for proteomics using StageTips." Nat Protoc **2**(8): 1896-1906.
Ritchie, M. E., B. Phipson, D. Wu, Y. Hu, C. W. Law, W. Shi and G. K. Smyth (2015). "limma powers differential expression analyses for RNA-sequencing and microarray studies." Nucleic Acids Research **43**(7): e47-e47.
Robinson, M. D., D. J. McCarthy and G. K. Smyth (2010). "edgeR: a Bioconductor package for differential expression analysis of digital gene expression data." Bioinformatics (Oxford, England) **26**(1): 139-140.
Robinson, M. D. and A. Oshlack (2010). "A scaling normalization method for differential expression analysis of RNA-seq data." Genome Biol **11**(3): R25.
Salvagno, C., J. K. Mandula, P. C. Rodriguez and J. R. Cubillos-Ruiz (2022). "Decoding endoplasmic reticulum stress signals in cancer cells and antitumor immunity." Trends Cancer **8**(11): 930-943.
Sayols, S. (2023). "rrvgo: a Bioconductor package for interpreting lists of Gene Ontology terms." MicroPubl Biol **2023**.
Schneider, T., L. H. Hung, M. Aziz, A. Wilmen, S. Thaum, J. Wagner, R. Janowski, S. Muller, S. Schreiner, P. Friedhoff, S. Huttelmaier, D. Niessing, M. Sattler, A. Schlundt and A. Bindereif (2019). "Combinatorial recognition of clustered RNA elements by the multidomain RNA-binding protein IMP3." Nat Commun **10**(1): 2266.

Schuck, S., C. M. Gallagher and P. Walter (2014). "ER-phagy mediates selective degradation of endoplasmic reticulum independently of the core autophagy machinery." J Cell Sci **127**(Pt 18): 4078-4088.
Schuck, S., W. A. Prinz, K. S. Thorn, C. Voss and P. Walter (2009). "Membrane expansion alleviates endoplasmic reticulum stress independently of the unfolded protein response." The Journal of cell biology **187**(4): 525-536.
Singh, K., C. Han, J. L. Fleming, A. P. Becker, J. McElroy, T. Cui, B. Johnson, A. Kumar, E. Sebastian, C. A. Showalter, M. S. Schrock, M. K. Summers, V. Becker, Z. Y. Tong, X. Meng, H. R. Manring, M. Venere, E. H. Bell, P. A. Robe, A. L. Grosu, S. J. Haque and A. Chakravarti (2023). "TRIB1 confers therapeutic resistance in GBM cells by activating the ERK and Akt pathways." Sci Rep **13**(1): 12424.
Sriburi, R., S. Jackowski, K. Mori and J. W. Brewer (2004). "XBP1: a link between the unfolded protein response, lipid biosynthesis, and biogenesis of the endoplasmic reticulum." J Cell Biol **167**(1): 35-41.
Stöhr, N., M. Lederer, C. Reinke, S. Meyer, M. Hatzfeld, R. H. Singer and S. Hüttelmaier (2006). "ZBP1 regulates mRNA stability during cellular stress." The Journal of Cell Biology **175**(4): 527-534.
Travers, K. J., C. K. Patil, L. Wodicka, D. J. Lockhart, J. S. Weissman and P. Walter (2000). "Functional and genomic analyses reveal an essential coordination between the unfolded protein response and ER-associated degradation." Cell **101**(3): 249-258.
Tritschler, F., A. Eulalio, V. Truffault, M. D. Hartmann, S. Helms, S. Schmidt, M. Coles, E. Izaurralde and O. Weichenrieder (2007). "A divergent Sm fold in EDC3 proteins mediates DCP1 binding and P-body targeting." Mol Cell Biol **27**(24): 8600-8611.
Vignali, R. and S. Marracci (2020). "HMGA Genes and Proteins in Development and Evolution." Int J Mol Sci **21**(2).
Vu, L. P., B. F. Pickering, Y. Cheng, S. Zaccara, D. Nguyen, G. Minuesa, T. Chou, A. Chow, Y. Saletore, M. MacKay, J. Schulman, C. Famulare, M. Patel, V. M. Klimek, F. E. Garrett-Bakelman, A. Melnick, M. Carroll, C. E. Mason, S. R. Jaffrey and M. G. Kharas (2017). "The N(6)-methyladenosine (m(6)A)-forming enzyme METTL3 controls myeloid differentiation of normal hematopoietic and leukemia cells." Nat Med **23**(11): 1369-1376.
Walter P. and R. D. (2011). "The unfolded protein response: from stress pathway to homeostatic regulation." Science **334**(6059): 1081-1086.
Wei, J., B. T. Harada, D. Lu, R. Ma, B. Gao, Y. Xu, E. Montauti, N. Mani, S. M. Chaudhuri, S. Gregory, S. E. Weinberg, D. D. Zhang, R. Green, C. He and D. Fang (2021). "HRD1-mediated METTL14 degradation regulates m(6)A mRNA modification to suppress ER proteotoxic liver disease." Mol Cell **81**(24): 5052-5065 e5056.
Weidensdorfer, D., N. Stohr, A. Baude, M. Lederer, M. Kohn, A. Schierhorn, S. Buchmeier, E. Wahle and S. Huttelmaier (2009). "Control of c-myc mRNA stability by IGF2BP1-associated cytoplasmic RNPs." RNA **15**(1): 104-115.
Xu, W., Y. Sheng, Y. Guo, Z. Huang, Y. Huang, D. Wen, C. Y. Liu, L. Cui, Y. Yang and P. Du (2019). "Increased IGF2BP3 expression promotes the aggressive phenotypes of colorectal cancer cells in vitro and vivo." Journal of Cellular Physiology **234**(10): 18466-18479.
Xuan, C., Q. Wang, X. Han, Y. Duan, L. Li, L. Shi, Y. Wang, L. Shan, Z. Yao and Y. Shang (2013). "RBB, a novel transcription repressor, represses the transcription of HDM2 oncogene." Oncogene **32**(32): 3711-3721.
Yaniv, K. and J. K. Yisraeli (2002). "The involvement of a conserved family of RNA binding proteins in embryonic development and carcinogenesis." Gene **287**(1-2): 49-54.
Yu, F., S. E. Haynes and A. I. Nesvizhskii (2021). "IonQuant Enables Accurate and Sensitive Label-Free Quantification With FDR-Controlled Match-Between-Runs." Mol Cell Proteomics **20**: 100077.

Yu, G., F. Li, Y. Qin, X. Bo, Y. Wu and S. Wang (2010). "GOSemSim: an R package for measuring semantic similarity among GO terms and gene products." Bioinformatics **26**(7): 976-978.
Zhao, Z., Y. Qing, L. Dong, L. Han, D. Wu, Y. Li, W. Li, J. Xue, K. Zhou, M. Sun, B. Tan, Z. Chen, C. Shen, L. Gao, A. Small, K. Wang, K. Leung, Z. Zhang, X. Qin, X. Deng, Q. Xia, R. Su and J. Chen (2023). "QKI shuttles internal m(7)G-modified transcripts into stress granules and modulates mRNA metabolism." Cell **186**(15): 3208-3226 e3227.
Zhou, J., J. Wan, X. Gao, X. Zhang, S. R. Jaffrey and S. B. Qian (2015). "Dynamic m(6)A mRNA methylation directs translational control of heat shock response." Nature **526**(7574): 591-594.
Zhou, X., K. F. Benson, H. R. Ashar and K. Chada (1995). "Mutation responsible for the mouse pygmy phenotype in the developmentally regulated factor HMGI-C." Nature **376**(6543): 771-774.

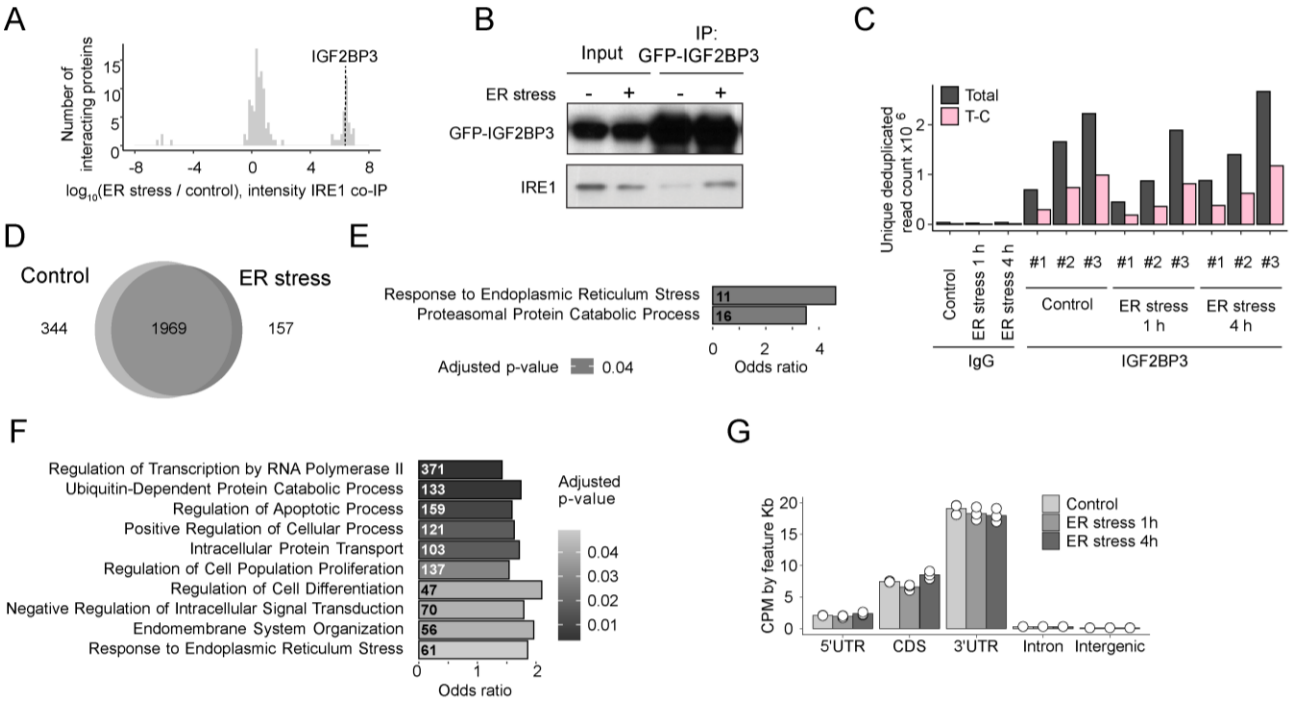
**Supplemental Data**

# Dual regulation of the unfolded protein response by IGF2BP3 during ER stress

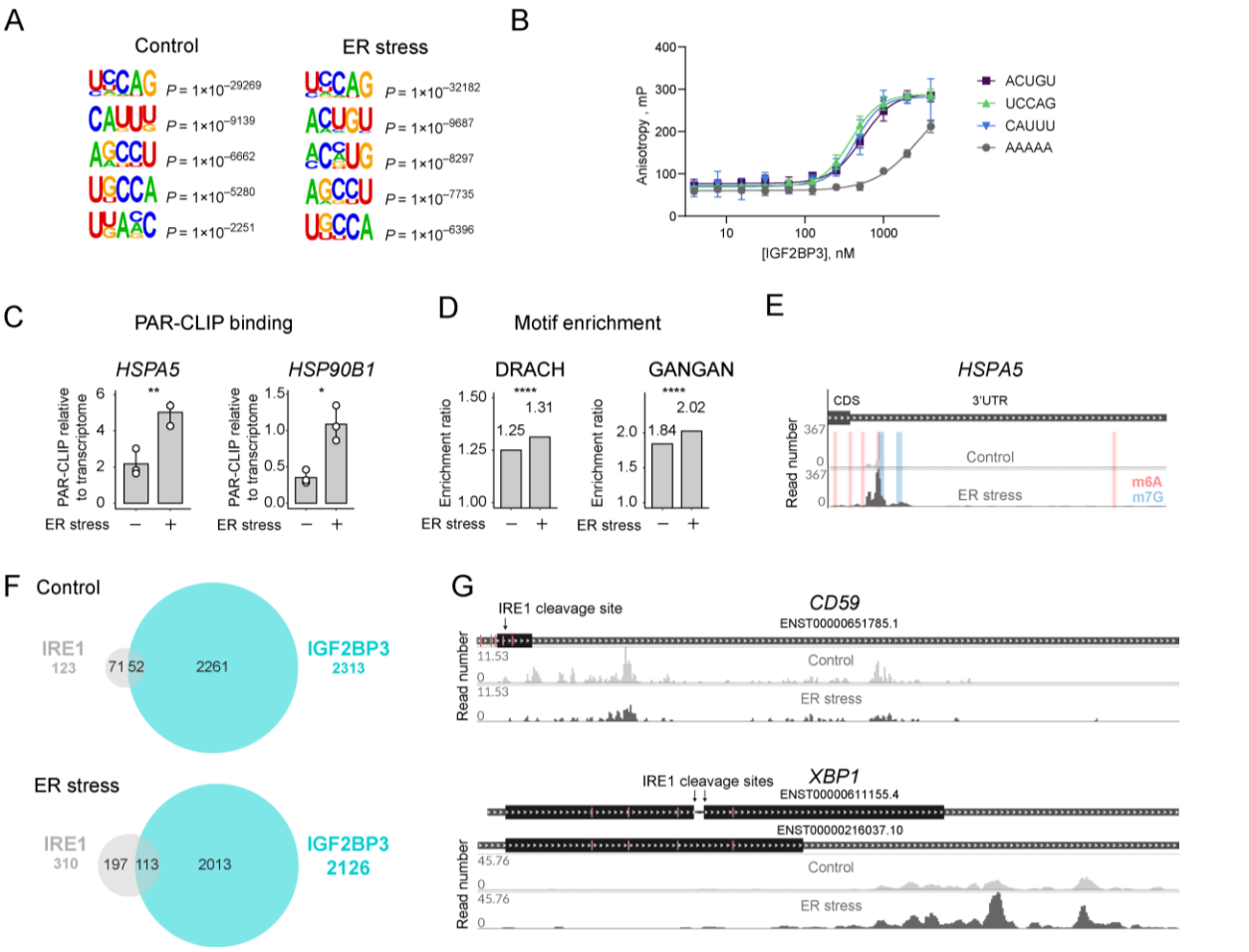
Aleksandra S Anisimova[1,2], Sabina Omerbegovic [1,5], Milica Mihailovic [1,2], Sascha Gratzl [1,2], Harald Hornegger[1,2], Irmgard Fischer[1], Gijs A Versteeg[1,3], Stefan L Ameres[1,4], G Elif Karagöz[1,5,#]

1. Max Perutz Labs, Vienna BioCenter Campus, Dr.-Bohr-Gasse 9, 1030, Vienna, Austria.
2. Vienna BioCenter PhD Program, a Doctoral School of the University of Vienna and the Medical University of Vienna, A-1030 Vienna, Austria.
3. University of Vienna, Center for Molecular Biology, Department of Microbiology, Immunobiology, and Genetics, Dr.-Bohr-Gasse 9, 1030, Vienna, Austria.
4. University of Vienna, Center for Molecular Biology, Department of Biochemistry and Cell Biology, Dr.-Bohr-Gasse 9, 1030, Vienna, Austria.
5. Medical University of Vienna, Center for Medical Biochemistry, Dr.-Bohr-Gasse 9, 1030, Vienna, Austria.

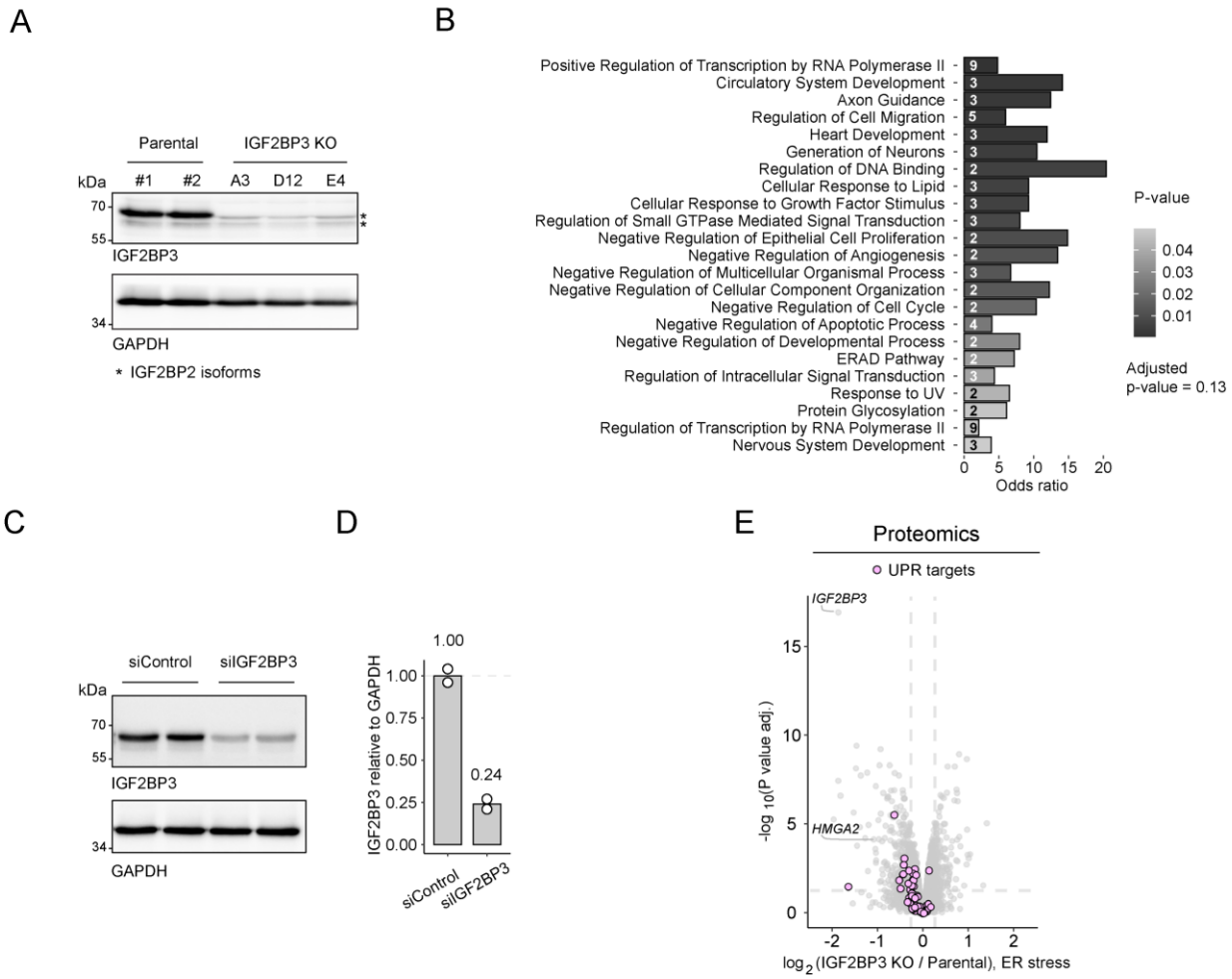
This file contains **Supplemental Figures S1 – S7**, **Supplemental References**.



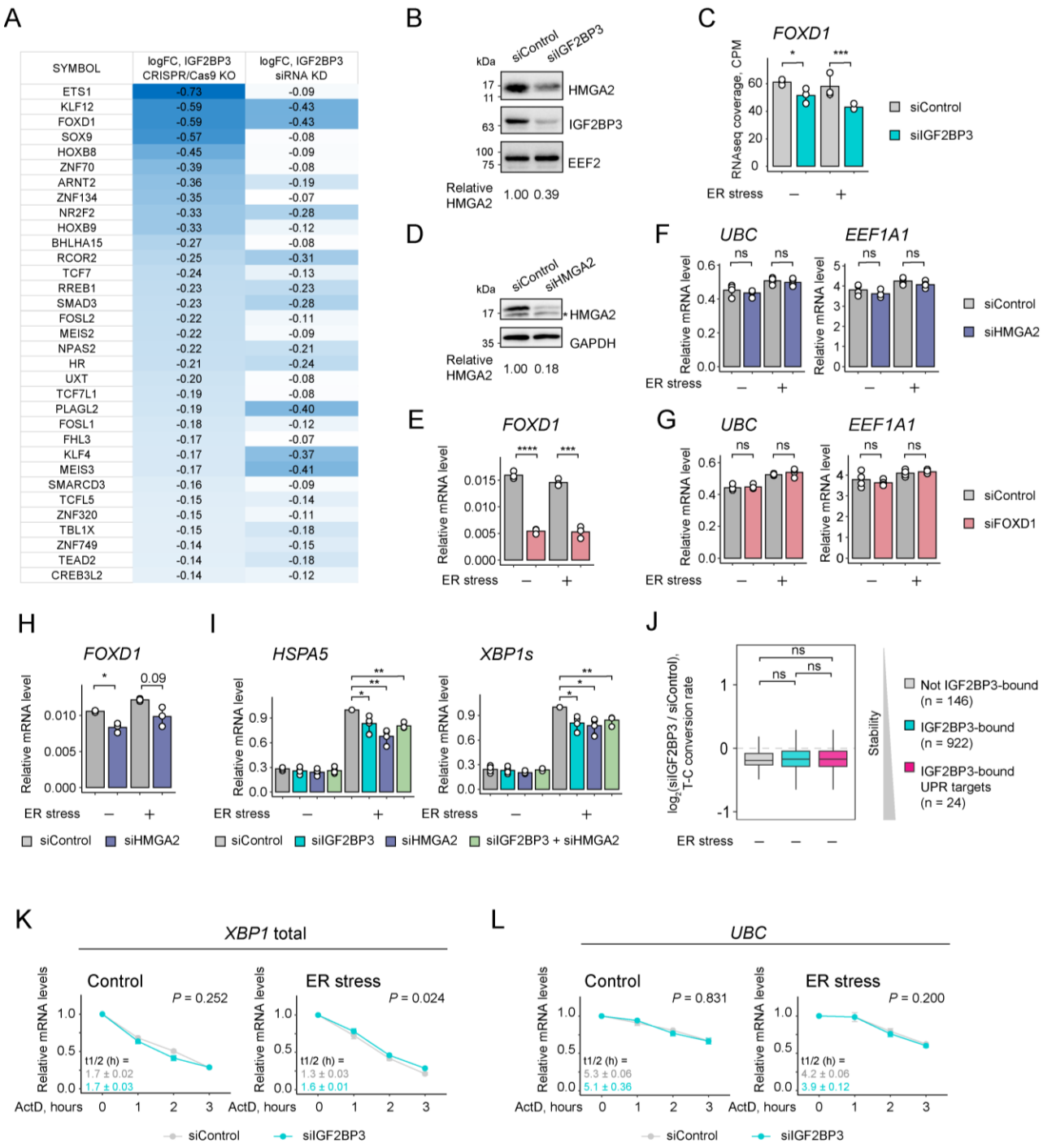

**Supplemental Figure S1. A.** Histogram showing the distribution of fold changes in normalized peptide intensity values of IRE1 interaction partners upon ER stress (crosslinking mass spectrometry data from Acosta-Alvear, Karagöz et al., 2018 (Acosta-Alvear, Karagoz et al. 2018)). Proteins identified in IgG or non-crosslinking controls were excluded from the analysis (n = 126). **B.** Western blot of IRE1 showing its association with IGF2BP3 after immunoprecipitation of GFP-IGF2BP3 from HEK293T cells treated with ER stress-inducing drug TM at 5 µg/mL for 4 hours. **C.** Barplots showing numbers of total and T-C containing unique deduplicated IR-PAR-CLIP read counts per library before normalization. **D.** Venn diagram showing the intersection of IGF2BP3 IR-PAR-CLIP targets in DMSO control and ER stress conditions (4-hour treatment with 5 µg/mL tunicamycin). **E.** GO term analysis of 157 IGF2BP3-bound transcripts identified in only in ER stress conditions **F.** GO term analysis of 2470 IGF2BP3-bound transcripts identified in either control or ER stress conditions. **G.** Feature length-normalized aggregated IGF2BP3 IR-PAR-CLIP coverage of genomic features. For IR-PAR-CLIP and transcriptome experiments n=3 biological replicates.




**Supplemental Figure S2. A.** 5nt-long consensus motifs enriched in IGF2BP3 IR-PAR-CLIP reads over scrambled control in control and ER stress conditions (4 hr). Motif enrichment analysis was performed using HOMER software on pooled replicates. **B.** Fluorescence anisotropy experiments of full-length IGF2BP3 WT and 5′-fluorescein-labeled RNA probes containing the indicated motif. Data are the mean ± s.d of n=3 technical replicates. The curves represent the fit of the Hill equation (see Materials and Methods). **C.** IGF2BP3 binding values (IR-PAR-CLIP CPM / QuantSeq CPM) for selected genes. Data are the mean ± s.d of n=3 biological replicates. *P* values were calculated by unpaired two-sided Student's t-test. **D.** Motif enrichment analysis of IGF2BP3 IR-PAR-CLIP reads for m6A consensus motif DRACH and m7G consensus motif GANGAN. First, the motif enrichment was calculated for the DMSO control samples over scrambled background. Next, the motif enrichment was calculated for the samples treated with TM for 4 hours using DMSO control sample as a background. Analysis was performed using MEME suite SEA software on pooled replicates. **E.** Representative IGF2BP3 IR-PAR-CLIP coverage example for 3' UTR of *HSPA5.* m6A ((Liang, Ye et al. 2024), see Materials and Methods) and m7G (Malbec, Zhang et al. 2019) methylation sites are highlighted. **F.** Venn diagram showing the intersection between IGF2BP3 and IRE1 PAR-CLIP targets (Acosta-Alvear, Karagoz et al. 2018) in control and ER stress conditions. **G.** Representative IGF2BP3 IR-PAR-CLIP coverage of IRE1 targets *XBP1* and *CD59*. **P* < 0.05; ***P* < 0.01; ****P* < 0.001; *****P* < 0.0001.



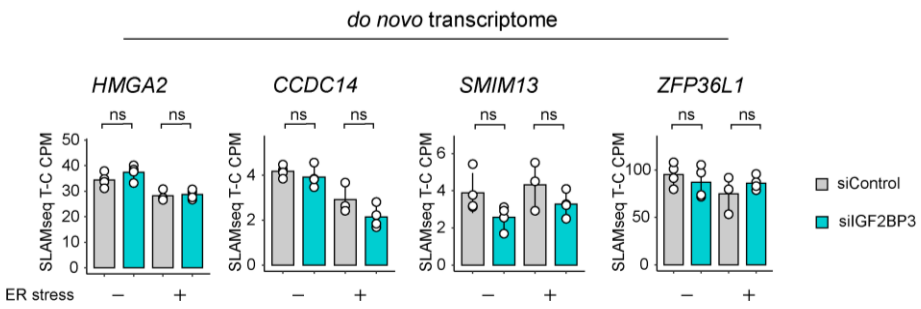

**Supplemental Figure S3. A.** Western blot of parental and IGF2BP3 KO HCT116 cell lines (clones A3, D12 and E4). * IGF2BP2 isoforms recognized by polyclonal anti-IGF2BP3 antibody. **B.** GO term analysis of genes downregulated in IGF2BP3 KO comparing to parental cells during ER stress. edgeR glmQLFTest *P* value adj. < 0.05. **C.** Western blot showing depletion of IGF2BP3 after 48-hour treatment with siRNA against IGF2BP3 compared to control siRNA. **D.** Quantification of C. n=2 technical replicates. **E.** Volcano plot of total proteome changes upon IGF2BP3 KO in ER stress conditions. n=4 biological replicates. *P* values were calculated using limma-trend moderated t-test.



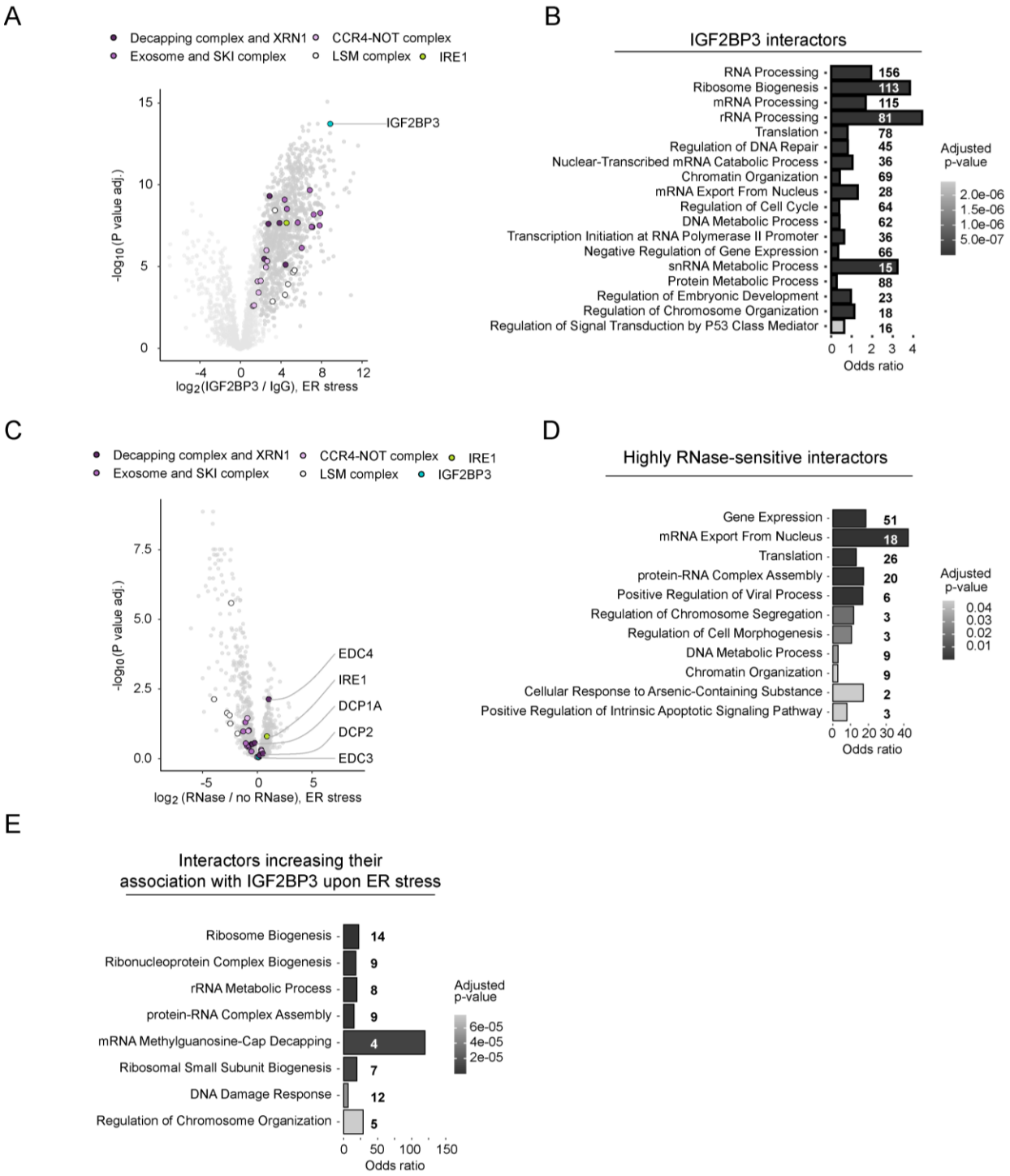

**Supplemental Figure S4.** **A.** Table showing $\log_2$(IGF2BP3 depletion / control) values for transcriptional regulators (GO:0140110) that were downregulated more than 10% or 5% upon IGF2BP3 CRISPR/Cas9- or siRNA-mediated depletion, respectively, under ER stress conditions. **B.** Western blot showing HMGA2 levels upon siRNA-mediated depletion of IGF2BP3. **C.** FOXD1 transcript levels (RNA-Seq, CPM) upon siRNA-mediated depletion of IGF2BP3. Data are the mean ± s.d. of n=3 biological replicates. *P* values were calculated by edgeR glmQLFTest. **D.** Western blot confirming siRNA-mediated depletion of HMGA2 * unspecific band. **E.** RT-qPCR

confirming siRNA-mediated depletion of *FOXD1*. **F** and **G.** RT-qPCR of control transcripts *UBC* and *EEF1A* upon siRNA-mediated depletion of HMGA2 and FOXD1, respectively. **H.** RT-qPCR of *FOXD1* upon siRNA-mediated depletion of HMGA2. **I.** RT-qPCR comparing levels of *HSPA5*, *XBP1* spliced, and *ATF4* upon siRNA-mediated depletion of IGF2BP3, HMGA2, or combined depletion of both. **J**. Boxplot showing changes in estimated transcript stability (T-C conversion rates) in unstressed conditions following siRNA-mediated IGF2BP3 depletion for IGF2BP3-bound transcripts, IGF2BP3-bound UPR targets, and non-IGF2BP3 bound transcripts (IR-PAR-CLIP CPM / QuantSeq CPM < 0.1). *P* values were calculated by two-sided Wilcoxon test. **K** and **L.** RT-qPCR analyses of degradation rates of the UPR target *XBP1* (total) and the control transcript *UBC* upon siRNA-mediated depletion of IGF2BP3. HCT116 cells were treated with TM at 250 ng/mL for 4 hours and the transcription was blocked with 5 µg/mL ActD for indicated time points. Data are the mean ± s.e. of n=4 biological replicates. *P* values were calculated by paired two-sided Student's t-test. For the SLAMseq experiments n=4 biological replicates. In RT-qPCR analyses, mRNA levels were normalized to *RPL6*. ER stress was induced with 100 ng/mL TM for 8 hours. **P* < 0.05; ***P* < 0.01; ****P* < 0.001; *****P* < 0.0001.

A

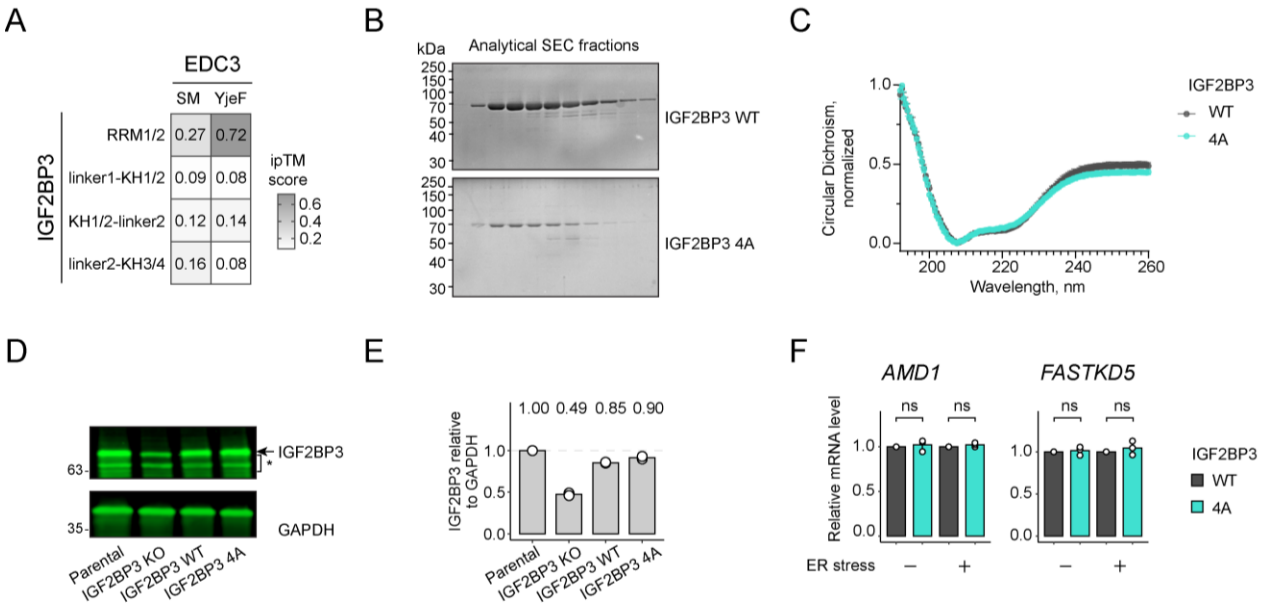



**Supplemental Figure S5. A**.Barplots showing SLAMseq *de novo* (T-C CPM) transcript levels for selected transcripts regulated by IGF2BP3. Data are the mean ± s.d of n=4 biological replicates. *P* values were calculated by unpaired two-sided Student's t-test.




**Supplemental Figure S6**. **A.** Volcano plot of co-IP–MS analysis of endogenous IGF2BP3 upon ER stress (TM, 5 µg/mL, 4 h) using IGF2BP3 antibody versus IgG control. IGF2BP3 interaction partners (4 times enriched over IgG control, *P* value adj. < 0.05) are shown in dark gray. **B.** GO term enrichment analysis of IGF2BP3 interaction partners (4 times enriched over IgG control at least in one treatment condition, *P* value adj. < 0.05). **C.** Volcano plots comparing IGF2BP3 interactome with and without RNase treatment. **D.** GO term enrichment analysis of IGF2BP3-

interacting proteins that decreased their association with IGF2BP3 upon RNase treatment (*P* value adj. < 0.05). **E.** GO term enrichment analysis of IGF2BP3-interacting proteins that increased their association with IGF2BP3 upon ER stress for more than 20%. For IGF2BP3 co-IP–MS analysis n=3 biological replicates.




**Supplemental Figure S7. A.** Matrix showing AlphaFold3 ipTM scores between separate domains of IGF2BP3 and EDC3. **B.** Coomassie-stained SDS-PAGE of fractions from analytical size-exclusion chromatography (SEC) of IGF2BP3 WT and the IGF2BP3 4A mutant. **C.** Circular dichroism spectra of IGF2BP3 WT and the IGF2BP3 4A mutant. Data are the mean ± s.d. of n=3 technical replicates. **D.** Near-infrared Western blot showing expression levels of IGF2BP3 WT and the IGF2BP3 4A mutant introduced into IGF2BP3 KO HCT116 cell line. * IGF2BP2 isoforms recognized by the polyclonal anti-IGF2BP3 antibody. **E.** Quantification of D. Data are the mean ± s.d. of n=2 technical replicates. **F.** RT-qPCR of control mRNAs in HCT116 cells expressing IGF2BP3 WT or IGF2BP3-4A mutant. mRNA levels were normalized to *RPL6* and shown relative to IGF2BP3 WT. Data are the mean ± s.d. of n=3 biological replicates. *P* values were calculated by unpaired two-sided Student's t-test. ER stress was induced with 5 µg/mL TM for 4 hours.

**Supplemental references**

Acosta-Alvear, D., G. E. Karagoz, F. Frohlich, H. Li, T. C. Walther and P. Walter (2018). "The unfolded protein response and endoplasmic reticulum protein targeting machineries converge on the stress sensor IRE1." Elife **7**.

Liang, Z., H. Ye, J. Ma, Z. Wei, Y. Wang, Y. Zhang, D. Huang, B. Song, J. Meng, D. J. Rigden and K. Chen (2024). "m6A-Atlas v2.0: updated resources for unraveling the N6-methyladenosine (m6A) epitranscriptome among multiple species." Nucleic Acids Res **52**(D1): D194-D202.

Malbec, L., T. Zhang, Y. S. Chen, Y. Zhang, B. F. Sun, B. Y. Shi, Y. L. Zhao, Y. Yang and Y. G. Yang (2019). "Dynamic methylome of internal mRNA N(7)-methylguanosine and its regulatory role in translation." Cell Res **29**(11): 927-941.

# 3. Discussion

UFMylation was shown to be important for ER homeostasis. However, the precise function of this modification and its role have remained elusive. The work of this thesis provided a mechanistic insight into the precise role of UFMylation in ER protein quality control by dissecting the course of events upon ribosome stalling at the ER, and the interdependence of RQC and UFMylation machineries.

## 3.1. Ribosome rescue and RQC are implicated in ER protein quality control

RPL26 is UFMylated upon ribosomal stalling during co-translational protein translocation into the ER lumen[79,97], and this modification is required for the clearance of the stalled ribosomes at the ER[80,97]. However, factors that recognize and clear UFMylated ribosomes, as well as the precise timing and role of UFMylation in the ER quality control, were incompletely understood. In order to discover pathways contributing to the clearance of UFMylated ribosomes at the ER, we performed proteomics on FLAG immunoprecipitates of ribosomal fractions from FLAG-UFM1 cell lines upon ribosome stalling. We identified the RQC component NEMF as specifically associated with UFMylated ribosomes in a stalling-dependent manner. Additionally, using IP-WB experiments, we confirmed stalling-specific association of NEMF and LTN1 with the UFMylated ribosomes at RPL26. These data showed that the RQC components directly interact with UFMylated ribosomes and are directly involved in their clearance. In addition, the Sec61β IPs upon ANS-induced stalling show specific enrichment of UFMylated RPL26 with the translocon, indicating that UFMylated ribosomes are ER-bound.

Since the RQC machinery was recruited to UFMylated ribosomes at the ER in a stalling-dependent manner, I wanted to test whether the ribosome rescue steps are also facilitated by the same machinery on the ER as upon cytosolic stalled ribosomes. Unlike the mechanism of cytosolic stalling, the events following ribosome stalling during co-translational protein targeting into the ER have been scarcely studied. Given the topological constraints of the translocon-docked ribosome at the ER membrane and the physical separation of the cytosolic ribosome rescue factors and the RQC, a question arises as to which factors are needed to properly clear the stalled ribosomes at the ER. Using biochemical and cellular assays, I have shown that the cytosolic ribosome recognition and rescue factors ZNF598 and ASC-1 complex can access the stalled ribosomes at the ER. The previously shown phenotype of increased read-through upon the loss of these two components in cells expressing cytosolic stalling reporters[60,63] was recapitulated in our system with the ER-targeted stalling reporter ERK20 (initially described here[97]). Another study showed that the loss of these factors led to increased read-through of ER-stalling reporters with alternative topologies, and only a short folded domain before the stalling-inducing poly(A) stretch[80]. These data show that the initial recognition and ribosome splitting steps upon ribosome stalling are functioning in the same way for ribosomes stalled at the ER as the cytosolic stalled ribosomes.

## 3.2. Both the RQC and UFMylation are needed for the clearance of RNCs at the ER

There is some evidence that the RQC components NEMF and LTN1 can access stalled peptides in the ER[132]. Apart from the RQC, the inability to UFMylate RPL26 in cells without the C-terminal tail of RPL26 also causes the accumulation of the peptides stalled at the ER[80].

However, it was unclear whether these two machineries act on the same pathway and what the precise course of events after ribosome stalling at the ER is.

To answer these questions, I depleted cells of components of the RQC or the UFMylation system and assessed accumulation of the ERK20 stalling reporter. Given the redundancy of quality control pathways and the cellular adaptation to individual component loss, we used an inducible knockout system that allows a precise time control of the depletion during the drug treatment only. Similar experiments were also performed using siRNA-mediated depletion, allowing temporary, controlled depletion of proteins of interest as an independent validation. The level of the ERK20 reporter increased upon depletion of RQC and UFM1, indicating that ERK20 is cleared by those pathways. Importantly, this increase was comparable in the absence of RQC components and the UFMylation machinery, therefore, both of the pathways are necessary for the clearance of stalled peptides at the ER and they likely act on pathway. This phenotype is in contrast to the clearance mechanism of the ribosomes stalled in the cytosol, which needs only the RQC machinery for degradation[64,66], underlying the specific role of UFMylation in ER-bound ribosome clearance.

### 3.3. Ribosome recognition and splitting upon stalling at the ER are prerequisites for UFMylation

After establishing that both RQC and UFMylation are needed for clearance of stalled ribosomes at the ER, I addressed the order of signaling events upon stalling induction at the ER is. To understand this cross-talk, I implemented the same strategies of temporary protein depletion as described in Chapter 3.2. and assessed the effects of loss of ribosome recognition and rescue factors, as well as of RQC components, on UFMylation. Upon ribosomal stalling induced by ANS, I observed a decrease in UFMylation of RPL26 when ribosome recognition and splitting factors, namely ZNF598, the ASC-1 complex, and Pelota, were depleted. This effect was specific to stalling, as I did not observe a change in UFMylation levels under steady-state conditions. This showed us that ribosome recognition and splitting are necessary steps before UFMylation. RPL26 UFMylation levels were not completely abolished without ribosome rescue factors, but instead went down to the steady-state UFMylation levels. As UFMylation is also required for 60S-translocon interaction release upon translation termination at the ER[77,78], the residual levels should correspond to the background level of UFMylation responsible for empty 60S subunit release.

In contrast, under the same steady-state conditions, the loss of RQC factors increased UFMylation. This result showed that the RQC plays a constant background surveillance role, detecting emerging RQC substrates and catalyzing their degradation. The impact of LTN1 depletion on RPL26 UFMylation was previously reported in neurons, showing the same phenotype: increased UFMylation[134]. The inability to degrade UFMylated post-split 60S-peptidyl-tRNA complexes in cells depleted of NEMF or LTN1 leads to their accumulation, thereby increasing UFMylation. However, upon ribosome stalling, loss of NEMF and LTN1 did not cause further increase in RPL26 UFMylation levels. This phenotype can be explained by a strong increase in UFMylation upon ANS-mediated stalling induction, exhausting the UFMylation pool and hindering further increases in UFMylation levels.

To specifically test the impact of loss of ribosome rescue and RQC components on UFMylation upon ER stalling, I repeated these experiments in cells expressing cytosolic or ER-targeted stalling reporters, CytoK20 or ERK20, respectively. Upon loss of ribosome recognition factor ZNF598 and the ribosome-splitting factor ASC-1 complex, UFMylation levels decreased in cells expressing ERK20. Loss of Pelota did not affect UFMylation levels, as expected, since Pelota acts on 3'-end truncated mRNAs, whereas ERK20 serves as a reporter that causes internal ribosome stalling. In contrast to ERK20, neither the cytosolic stalling reporter nor the ER-targeted control reporter ERK0 showed an impact on UFMylation upon loss of ribosome rescue components. Interestingly, we observed an increase in UFMylation in cells expressing ERK20 and depleted of NEMF, indicating that UFMylation is independent of NEMF binding, confirming our earlier findings that NEMF associates with UFMylated 60S subunits. Also, the loss of tRNA release RQC factor ANKZF1 did not significantly increase UFMylation, showing that UFMylation is independent of ANKZF1's activity and, therefore, independent of the nascent chain release. Altogether, this data shows that UFMylation happens on the 60S-peptidyl-tRNA complexes upon ribosomal stalling at the ER.

### 3.4. UFM1 E3 ligase binds 60S-peptidyl-tRNA complexes

The large gap in understanding the role of UFMylation in ER homeostasis stems from a conundrum: the reported UFM1 E3 ligase binds to empty 60S subunits upon translation termination at the ER[77,78], while the proposed role of UFMylation is to clear arrested polypeptides at the ER. The structural data show that the UFM1 E3 ligase binds empty 60S subunits in a manner incompatible with the simultaneous binding of the 40S subunit, the translocon, or the tRNA[77,78]. However, based on structural models, we hypothesized that the UFM1 E3 ligase can adopt conformations that enable its binding to the post-split 60S-peptidyl-tRNA complexes upon ribosomal stalling at the ER. To investigate this, I used the ER stalling reporter ERK20 and immunoprecipitated nascent chains from bulk ribosomal fractions, thereby enriching for ribosome-nascent chain complexes (RNC) and their interactors. I showed that UFL1, the catalytic component of the UFM1 E3 complex, coprecipitates with RNCs upon induction of ribosome stalling at the ER. Therefore, UFM1 E3 ligase can adopt an alternative conformation that allows its binding while the nascent chain, along with the tRNA, remains attached to the 60S subunit. This alternative mode of binding can be achieved due to a flexibility of C-terminal domain of UFL1 which is connected to the tandem WH domains through a disordered hinge region[77,78], which allows for the displacement of the C-terminal region to accommodate the bound tRNA, while ensuring extensive contacts with the 60S ribosomal subunit through the rest of UFL1's WH domains, CDK5RAP3, and DDRGK1 (see Chapter 2.1. Figure 4).

I also tested the impact of the loss of RQC components on UFL1 binding to 60S-peptidyl-tRNA complexes. I show that UFL1 binding is not impacted by NEMF loss, meaning that NEMF binding is not a necessary prerequisite for the binding of UFM1 E3 ligase. In the pulldowns from NEMF-deficient cells, I observed UFMylated RPL26, indicating that the function of the UFM1 E3 ligase is not dependent on NEMF, and probably precedes it. The confirmation of our experimental approach is presented through the specificity of NEMF pulldowns only from cell lysates expressing the stalling-inducing reporter, as well as the dependence of LTN1 interaction on NEMF, which was previously shown for cytosolic stalled ribosomes[64]. These

results also show that the same 60S-peptidyl-tRNA complex can be recognized by both the RQC and the UFMylation machineries, as evidenced by the binding of UFL1 and NEMF/LTN1 in the same pulldowns. This finding was confirmed in a recent structural paper showing that UFL1's C-terminal domain rotates back on itself, allowing the simultaneous binding with NEMF, with which it directly interacts, forming an augmented β-sheet[81]. Therefore, UFM1 E3 ligase can recognize post-split 60S-peptidyl-tRNA complexes as its canonical substrates.

### 3.5. The effects of UFMylation in ER protein quality control

After dissecting the precise course of events upon ribosomal stalling at the ER, I wanted to assess the functional implications of RPL26 UFMylation in ER protein quality control. Due to the fact that UFMylation is necessary only for the ER-stalled ribosomes, and its previously established role in the release of empty 60S subunits upon translation termination at the ER[77,78], I assumed that the role of UFMylation is to facilitate the disengagement of the 60S-translocon close interaction, in order to allow the access of RQC components to the nascent chain. The decrease in LTN1 binding to RNCs in cells depleted of UFM1 shows that UFMylation indeed facilitates LTN1 access to the nascent chain. Further mechanistic details of LTN1's role in this process are discussed in the following section.

### 3.6. The role of LTN1 in ER protein quality control

The dependence of LTN1 on UFMylation suggests that UFMylation is required for LTN1's access to the nascent chain, facilitating subsequent ubiquitination. To test this, I used the Tandem Ubiquitin-Binding Entity (TUBE) assays in cells lacking UFM1 to assess LTN1's ubiquitination activity. I observed that, although nascent chain clearance was LTN1-dependent, nascent chain ubiquitination was largely unaffected in cells lacking LTN1.

The explanation for this unusual phenotype lies in the close proximity of a wide variety of cellular E3 ligases, which could ubiquitinate incomplete peptides in the absence of LTN1. The binding of LTN1 to the 60S-peptidyl-tRNA complex is a crucial step due to LTN1's specificity for ribosome-bound nascent chain substrates. LTN1 binding stabilizes the 60S-peptidyl-tRNA complex long enough to possibly avoid premature nascent chain extraction and consequent aggregation, whereas other E3 ligases could ubiquitinate the nascent chain substrates, ultimately leading to downstream degradation. Interestingly, a recent preprint also showed that LTN1's ubiquitination was dispensable for the degradation of nascent chains of RQC cytosolic substrate[135]. Instead, their proposed mechanism is that LTN1's ubiquitination helps the release of nascent chains from the 60S subunit, followed by cytosolic deubiquitination and another round of ubiquitination by the other cytosolic E3 ligases, now a signal for degradation by the proteasome[135]. Even though this mechanism is convoluted and remains to be further tested, the model suggesting that ubiquitination by LTN1 is not necessary for nascent chain degradation is intriguing. To further experimentally address this, separation-of-function mutants should be developed, allowing precise separation of LTN1's enzymatic and binding functions. That way, this proposed mechanism can be tested by assessing the impact of the binding mutant rescue in the LTN1 knockout genetic background on the stabilization of the ER-staling reporter.

Structural data showed that deUFMylation of RPL26 is necessary for the dissociation of the UFM1 E3 ligase from the post-termination 60S subunit[77,81]. Given UFM1 E3 ligase's alternative role in releasing the tightly bound 60S-peptidyl-tRNA complexes from the translocon, and the data showing an increase in UFMylation in LTN1 KO cells, both from us and others[134], it is plausible that deUFMylation should precede LTN1's access to the nascent chain in its quality control role. I tested this hypothesis by assessing the co-immunoprecipitation of LTN1 with the 60S-peptidyl-tRNA complexes from cells lacking deUFMylase UFSP2. However, I did not observe a decrease in LTN1 binding in UFSP2-depleted cells. Therefore, deUFMylation is not necessary for LTN1's access to the 60S-peptidyl-tRNA. It is plausible that recognition of the deUFMylation substrate happens only once the nascent chain is extracted from the 60S subunit for degradation, which would structurally be the same deUFMylation substrate as the post-termination empty 60S subunits. This way, UFSP2 can recognize a unique substrate to release UFM1 from RPL26, followed by the release of the UFM1 E3 ligase complex from the 60S subunit as well.

## 3.7. The phylogenetic conservation of UFMylation's role in ER quality control

The UFMylation system is highly conserved in metazoans. To assess the conservation of its role in ER quality control in other species, we tested the dependence of RPL26 UFMylation on ribosome rescue and RQC components in the plant species *Arabidopsis thaliana*. We show that the ribosome-splitting factors mutants *ascc3* and *Pelota* exhibit decreased UFMylation upon ANS-induced ribosome stalling in *A. thaliana*, confirming the necessity of ribosomal splitting for UFMylation of RPL26 across species.

Since UFMylation is not present in fungi, the question arises as to how the 60S subunit post-termination release, as well as 60S-peptidyl-tRNA release during quality control, is mediated in fungi. In yeast, unlike mammalian mechanism, most secretory proteins are translocated into the ER post-translationally[136]. In this mechanism, Sec62 and Sec63 bind the Sec61 translocon, assisting the translocation together with Hsp70 chaperone BiP (Kar2 in yeast)[137]. Sec63's FN3 domain (fibronectin type-III) binds to the loop between transmembrane region 6 and 7 (L6/7) of Sec61 in the cytosolic side[138]. During co-translational translocation in yeast, the Ssh1 (Sec sixty-one homolog 1 from *S. cerevisiae*) complex forms interactions with the ribosomes through the same loop 6, and loop 8 in close proximity[139]. Since the majority of secretory proteins in yeast are post-translationally inserted into the ER, there is a readily available pool of Sec62 and Sec63 proteins at the membrane[136]. Given that the binding of the 60S subunit is mutually exclusive with binding of the Sec62-Sec63 complex to Sec61 translocon, it is plausible that 60S is readily displaced by the Sec62-Sec63 complex, in a mechanism that does not require UFMylation, resulting in the translocon configuration that allows subsequent post-translational insertion into the ER.

In yeast, ribosome splitting and recycling are mediated by release factors eRF1 and eRF3 in the canonical translation termination, or Dom34 and Hbs1 in the case of ribosome stalling[140]. For RQC substrate degradation, the homologous RQC components are necessary in yeast: LTN1 homolog Rkr1/Ltn1 and NEMF homolog Rqc2[54,133]. Rkr1 was also shown to ubiquitinate the arrested polypeptide during the ER targeting[133], on a 60S-peptidyl-tRNA substrate remaining after ribosome splitting by the Dom34:Hbs1 complex. Although the UFMylation

machinery is absent in yeast, Rkr1/Ltn1 can nevertheless ubiquitinate peptide substrates and target them for degradation. Whether the translocon-60S engagement is more flexible in yeast and therefore facilitates the access of Rkr1/Ltn1 to the nascent chain, or if there is an alternative accessory factor that grants Rkr1/Ltn1's access to its substrate is yet to be uncovered.

## 4. Limitations and future perspectives

The mechanisms following ribosome stalling at the ER presented in this thesis were tested using the ERK20 reporter, which has a rather bulky EGFP domain before the stalling sequence and mimics aberrant stalling into the poly(A) tail. The next step in proving the universality of this mechanism across different substrates would be to systematically test their different topologies, including the presence of folded domains or disordered regions, the reporter length, different stretches of transmembrane domains, truncated reporters, and extensive secondary structures. It would be interesting to test whether the process kinetics also depend on these factors through stability experiments. Beyond the exogenously expressed stalling reporters, future research is needed to understand the roles of RQC and UFMylation in endogenous stalling-inducing mRNAs.

Additionally, I have discovered through proteomics that certain 40S ribosomal proteins are also UFMylated, in addition to the main 60S target RPL26. More research is needed to understand whether the UFMylation of these targets also has a role in the arrested peptide clearance or takes an orthogonal regulatory role.

The precise timing and regulation of RPL26 deUFMylation is not well understood. More experimental evidence is needed to understand the kinetics of deUFMylation, and its potential role in closing the ribosome rescue cycle and resetting the system for next translation initiation. Also, whether UFM1 has to be cleaved from RPL26 before next round of translation is unclear and yet to be studied in detail.

## 5. References


1. Karagöz, G. E., Acosta-Alvear, D. & Walter, P. The unfolded protein response: Detecting and responding to fluctuations in the protein-folding capacity of the endoplasmic reticulum. *Cold Spring Harbor Perspectives in Biology* **11**, a033886 (2019).
2. Radanović, T. & Ernst, R. The Unfolded Protein Response as a Guardian of the Secretory Pathway. *Cells* **10**, 2965 (2021).
3. McKenna, M. J. & Shao, S. The Endoplasmic Reticulum and the Fidelity of Nascent Protein Localization. *Cold Spring Harb Perspect Biol* **15**, a041249 (2023).
4. Kettel, P. & Karagöz, G. E. Endoplasmic reticulum: Monitoring and maintaining protein and membrane homeostasis in the endoplasmic reticulum by the unfolded protein response. *Int J Biochem Cell Biol* **172**, 106598 (2024).
5. Jacquemyn, J., Cascalho, A. & Goodchild, R. E. The ins and outs of endoplasmic reticulum-controlled lipid biosynthesis. *EMBO Rep* **18**, 1905–1921 (2017).
6. Phillips, M. J. & Voeltz, G. K. Structure and function of ER membrane contact sites with other organelles. *Nat Rev Mol Cell Biol* **17**, 69–82 (2016).
7. Chen, S., Novick, P. & Ferro-Novick, S. ER structure and function. *Current Opinion in Cell Biology* **25**, 428–433 (2013).
8. Westrate, L. M., Lee, J. E., Prinz, W. A. & Voeltz, G. K. Form Follows Function: The Importance of Endoplasmic Reticulum Shape. *Annual Review of Biochemistry* **84**, 791–811 (2015).
9. Wu, H., Carvalho, P. & Voeltz, G. K. Here, there, and everywhere: The importance of ER membrane contact sites. *Science* **361**, eaan5835 (2018).
10. Terasaki, M. *et al.* Stacked endoplasmic reticulum sheets are connected by helicoidal membrane motifs. *Cell* **154**, 285–296 (2013).
11. Kirk, S. J., Cliff, J. M., Thomas, J. A. & Ward, T. H. Biogenesis of secretory organelles during B cell differentiation. *J Leukoc Biol.* **87**, 245–255 (2010).
12. Shibata, Y., Voeltz, G. K. & Rapoport, T. A. Rough Sheets and Smooth Tubules. *Cell* **126**, 435–439 (2006).
13. Hu, J., Prinz, W. A. & Rapoport, T. A. Weaving the Web of ER Tubules. *Cell* **147**, 1226–1231 (2011).
14. Voeltz, G. K., Prinz, W. A., Shibata, Y., Rist, J. M. & Rapoport, T. A. A Class of Membrane Proteins Shaping the Tubular Endoplasmic Reticulum. *Cell* **124**, 573–586 (2006).
15. De Craene, J.-O. *et al.* Rtn1p Is Involved in Structuring the Cortical Endoplasmic Reticulum. *MBoC* **17**, 3009–3020 (2006).
16. Shibata, Y. *et al.* The reticulon and DP1/Yop1p proteins form immobile oligomers in the tubular endoplasmic reticulum. *J Biol Chem* **283**, 18892–18904 (2008).
17. Sawyer, E. M. *et al.* SigmaR1 shapes rough endoplasmic reticulum membrane sheets. *Developmental Cell* **59**, 2566-2577.e7 (2024).
18. Schmidt, H. R. *et al.* Crystal structure of the human σ1 receptor. *Nature* **532**, 527–530 (2016).
19. Loewen, C. J. R., Roy, A. & Levine, T. P. A conserved ER targeting motif in three families of lipid binding proteins and in Opi1p binds VAP. *EMBO J* **22**, 2025–2035 (2003).
20. Clapham, D. E. Calcium Signaling. *Cell* **131**, 1047–1058 (2007).
21. Fan, G. *et al.* Gating machinery of InsP3R channels revealed by electron cryomicroscopy. *Nature* **527**, 336–341 (2015).
22. Elvekrog, M. M. & Walter, P. Dynamics of co-translational protein targeting. *Curr Opin Chem Biol* **29**, 79–86 (2015).
23. Kobayashi, K. *et al.* Structure of a prehandover mammalian ribosomal SRP·SRP receptor targeting complex. *Science* **360**, 323–327 (2018).
24. Rapoport, T. A., Li, L. & Park, E. Structural and Mechanistic Insights into Protein Translocation. *Annual Review of Cell and Developmental Biology* **33**, 369–390 (2017).
25. Egea, P. F. *et al.* Substrate twinning activates the signal recognition particle and its receptor. *Nature* **427**, 215–221 (2004).

26. Kutay, U., Ahnert-Hilger, G., Hartmann, E., Wiedenmann, B. & Rapoport, T. A. Transport route for synaptobrevin via a novel pathway of insertion into the endoplasmic reticulum membrane. *EMBO J* **14**, 217–223 (1995).
27. McDowell, M. A. *et al.* Structural Basis of Tail-Anchored Membrane Protein Biogenesis by the GET Insertase Complex. *Molecular Cell* **80**, 72-86.e7 (2020).
28. Stefanovic, S. & Hegde, R. S. Identification of a Targeting Factor for Posttranslational Membrane Protein Insertion into the ER. *Cell* **128**, 1147–1159 (2007).
29. Guna, A., Volkmar, N., Christianson, J. C. & Hegde, R. S. The ER membrane protein complex is a transmembrane domain insertase. *Science* **359**, 470–473 (2018).
30. Jonikas, M. C. *et al.* Comprehensive characterization of genes required for protein folding in the endoplasmic reticulum. *Science* **323**, 1693–1697 (2009).
31. Hetz, C. The unfolded protein response: controlling cell fate decisions under ER stress and beyond. *Nat Rev Mol Cell Biol* **13**, 89–102 (2012).
32. Chen, X., Shi, C., He, M., Xiong, S. & Xia, X. Endoplasmic reticulum stress: molecular mechanism and therapeutic targets. *Sig Transduct Target Ther* **8**, 352 (2023).
33. Bartoszewski, R. *et al.* Activation of the unfolded protein response by deltaF508 CFTR. *Am J Respir Cell Mol Biol* **39**, 448–457 (2008).
34. Yadav, R. K., Chae, S.-W., Kim, H.-R. & Chae, H. J. Endoplasmic reticulum stress and cancer. *J Cancer Prev* **19**, 75–88 (2014).
35. Cox, J. S. & Walter, P. A Novel Mechanism for Regulating Activity of a Transcription Factor That Controls the Unfolded Protein Response. *Cell* **87**, 391–404 (1996).
36. Cox, J. S., Shamu, C. E. & Walter, P. Transcriptional induction of genes encoding endoplasmic reticulum resident proteins requires a transmembrane protein kinase. *Cell* **73**, 1197–1206 (1993).
37. Sidrauski, C. & Walter, P. The Transmembrane Kinase Ire1p Is a Site-Specific Endonuclease That Initiates mRNA Splicing in the Unfolded Protein Response. *Cell* **90**, 1031–1039 (1997).
38. Moncan, M., Rakhsh-Khorshid, H., Eriksson, L. A., Samali, A. & Gorman, A. M. Insights into the structure and function of the RNA ligase RtcB. *Cell. Mol. Life Sci.* **80**, 352 (2023).
39. Tirasophon, W., Lee, K., Callaghan, B., Welihinda, A. & Kaufman, R. J. The endoribonuclease activity of mammalian IRE1 autoregulates its mRNA and is required for the unfolded protein response. *Genes Dev* **14**, 2725–2736 (2000).
40. Kopp, M. C., Larburu, N., Durairaj, V., Adams, C. J. & Ali, M. M. UPR proteins IRE1 and PERK switch BiP from chaperone to ER stress sensor. *Nat Struct Mol Biol* **26**, 1053–1062 (2019).
41. Harding, H. P., Calfon, M., Urano, F., Novoa, I. & Ron, D. Transcriptional and Translational Control in the Mammalian Unfolded Protein Response. *Annual Review of Cell and Developmental Biology* **18**, 575–599 (2002).
42. Ebert, S. M. *et al.* Biology of Activating Transcription Factor 4 (ATF4) and Its Role in Skeletal Muscle Atrophy. *The Journal of Nutrition* **152**, 926–938 (2022).
43. Oka, O. B. V. *et al.* Activation of the UPR sensor ATF6α is regulated by its redox-dependent dimerization and ER retention by ERp18. *Proc. Natl. Acad. Sci. U.S.A.* **119**, e2122657119 (2022).
44. Koba, H. *et al.* Reinvestigation of Disulfide-bonded Oligomeric Forms of the Unfolded Protein Response Transducer ATF6. *Cell Struct. Funct.* **45**, 9–21 (2020).
45. Tam, A. B. *et al.* The UPR Activator ATF6 Responds to Proteotoxic and Lipotoxic Stress by Distinct Mechanisms. *Developmental Cell* **46**, 327-343.e7 (2018).
46. Doma, M. K. & Parker, R. Endonucleolytic cleavage of eukaryotic mRNAs with stalls in translation elongation. *Nature* **440**, 561–564 (2006).
47. Letzring, D. P., Wolf, A. S., Brule, C. E. & Grayhack, E. J. Translation of CGA codon repeats in yeast involves quality control components and ribosomal protein L1. *RNA* **19**, 1208–1217 (2013).
48. Shao, S., von der Malsburg, K. & Hegde, R. S. Listerin-Dependent Nascent Protein Ubiquitination Relies on Ribosome Subunit Dissociation. *Molecular Cell* **50**, 637–648 (2013).
49. Tsuboi, T. *et al.* Dom34:hbs1 plays a general role in quality-control systems by dissociation of a stalled ribosome at the 3' end of aberrant mRNA. *Mol Cell* **46**, 518–529 (2012).

50. Worpenberg, L., Gobet, C. & Naef, F. Codon-specific ribosome stalling reshapes translational dynamics during branched-chain amino acid starvation. *Genome Biol* **26**, 315 (2025).
51. Juszkiewicz, S. & Hegde, R. S. Initiation of Quality Control during Poly(A) Translation Requires Site-Specific Ribosome Ubiquitination. *Molecular Cell* **65**, 743-750.e4 (2017).
52. Arthur, L. *et al.* Translational control by lysine-encoding A-rich sequences. *Sci Adv* **1**, e1500154 (2015).
53. Yan, L. L., Simms, C. L., McLoughlin, F., Vierstra, R. D. & Zaher, H. S. Oxidation and alkylation stresses activate ribosome-quality control. *Nat Commun* **10**, 5611 (2019).
54. Yonashiro, R. *et al.* The Rqc2/Tae2 subunit of the ribosome-associated quality control (RQC) complex marks ribosome-stalled nascent polypeptide chains for aggregation. *Elife* **5**, e11794 (2016).
55. Aleksandrova, E. V. *et al.* Mechanism of release factor–mediated peptidyl-tRNA hydrolysis on the ribosome. *Science* **388**, eads9030 (2025).
56. Alkalaeva, E. Z., Pisarev, A. V., Frolova, L. Y., Kisselev, L. L. & Pestova, T. V. In vitro reconstitution of eukaryotic translation reveals cooperativity between release factors eRF1 and eRF3. *Cell* **125**, 1125–1136 (2006).
57. Pisareva, V. P., Skabkin, M. A., Hellen, C. U. T., Pestova, T. V. & Pisarev, A. V. Dissociation by Pelota, Hbs1 and ABCE1 of mammalian vacant 80S ribosomes and stalled elongation complexes. *EMBO J* **30**, 1804–1817 (2011).
58. Becker, T. *et al.* Structure of the no-go mRNA decay complex Dom34-Hbs1 bound to a stalled 80S ribosome. *Nat Struct Mol Biol* **18**, 715–720 (2011).
59. Ikeuchi, K. *et al.* Collided ribosomes form a unique structural interface to induce Hel2-driven quality control pathways. *EMBO J* **38**, e100276 (2019).
60. Juszkiewicz, S. *et al.* ZNF598 Is a Quality Control Sensor of Collided Ribosomes. *Mol Cell* **72**, 469-481.e7 (2018).
61. Sundaramoorthy, E. *et al.* ZNF598 and RACK1 Regulate Mammalian Ribosome-Associated Quality Control Function by Mediating Regulatory 40S Ribosomal Ubiquitylation. *Mol Cell* **65**, 751-760.e4 (2017).
62. Matsuo, Y. *et al.* Ubiquitination of stalled ribosome triggers ribosome-associated quality control. *Nat Commun* **8**, 159 (2017).
63. Juszkiewicz, S., Speldewinde, S. H., Wan, L., Svejstrup, J. Q. & Hegde, R. S. The ASC-1 Complex Disassembles Collided Ribosomes. *Mol Cell* **79**, 603-614.e8 (2020).
64. Shao, S., Brown, A., Santhanam, B. & Hegde, R. S. Structure and Assembly Pathway of the Ribosome Quality Control Complex. *Molecular Cell* **57**, 433–444 (2015).
65. Kostova, K. K. *et al.* CAT-tailing as a fail-safe mechanism for efficient degradation of stalled nascent polypeptides. *Science* **357**, 414–417 (2017).
66. Shao, S., von der Malsburg, K. & Hegde, R. S. Listerin-dependent nascent protein ubiquitination relies on ribosome subunit dissociation. *Mol Cell* **50**, 637–648 (2013).
67. Abaeva, I. S., Bulakhov, A. G., Hellen, C. U. T. & Pestova, T. V. The ribosome-associated quality control factor TCF25 imposes K48 specificity on Listerin-mediated ubiquitination of nascent chains by binding and specifically orienting the acceptor ubiquitin. *bioRxiv* 2024.10.17.618946 (2024).
68. Kuroha, K., Zinoviev, A., Hellen, C. U. T. & Pestova, T. V. Release of Ubiquitinated and Non-ubiquitinated Nascent Chains from Stalled Mammalian Ribosomal Complexes by ANKZF1 and Ptrh1. *Molecular Cell* **72**, 286-302.e8 (2018).
69. Verma, R. *et al.* Vms1 and ANKZF1 peptidyl-tRNA hydrolases release nascent chains from stalled ribosomes. *Nature* **557**, 446–451 (2018).
70. Meyer, H., Bug, M. & Bremer, S. Emerging functions of the VCP/p97 AAA-ATPase in the ubiquitin system. *Nat Cell Biol* **14**, 117–123 (2012).
71. Verma, R., Oania, R. S., Kolawa, N. J. & Deshaies, R. J. Cdc48/p97 promotes degradation of aberrant nascent polypeptides bound to the ribosome. *Elife* **2**, e00308 (2013).
72. Cappadocia, L. & Lima, C. D. Ubiquitin-like Protein Conjugation: Structures, Chemistry, and Mechanism. *Chem Rev* **118**, 889–918 (2018).

73. Komatsu, M. *et al.* A novel protein-conjugating system for Ufm1, a ubiquitin-fold modifier. *EMBO J* **23**, 1977–1986 (2004).
74. Morreale, F. E. & Walden, H. Types of Ubiquitin Ligases. *Cell* **165**, 248-248.e1 (2016).
75. Schapira, M., Calabrese, M. F., Bullock, A. N. & Crews, C. M. Targeted protein degradation: expanding the toolbox. *Nat Rev Drug Discov* **18**, 949–963 (2019).
76. Komatsu, M., Inada, T. & Noda, N. N. The UFM1 system: Working principles, cellular functions, and pathophysiology. *Molecular Cell* **84**, 156–169 (2024).
77. DaRosa, P. A. *et al.* UFM1 E3 ligase promotes recycling of 60S ribosomal subunits from the ER. *Nature* **627**, 445–452 (2024).
78. Makhlouf, L. *et al.* The UFM1 E3 ligase recognizes and releases 60S ribosomes from ER translocons. *Nature* **627**, 437–444 (2024).
79. Walczak, C. P. *et al.* Ribosomal protein RPL26 is the principal target of UFMylation. *Proceedings of the National Academy of Sciences of the United States of America* **116**, 1299–1308 (2019).
80. Scavone, F., Gumbin, S. C., Da Rosa, P. A. & Kopito, R. R. RPL26/uL24 UFMylation is essential for ribosome-associated quality control at the endoplasmic reticulum. *Proceedings of the National Academy of Sciences* **120**, e2220340120 (2023).
81. Penchev, I. *et al.* UFMylation orchestrates spatiotemporal coordination of RQC at the ER. *Science Advances* **11**, eadv0435 (2025).
82. Gak, I. A. *et al.* UFMylation regulates translational homeostasis and cell cycle progression. 2020.02.03.931196 Preprint at https://doi.org/10.1101/2020.02.03.931196 (2020).
83. Wang, Z. *et al.* MRE11 UFMylation promotes ATM activation. *Nucleic Acids Res* **47**, 4124–4135 (2019).
84. Qin, B. *et al.* UFL1 promotes histone H4 ufmylation and ATM activation. *Nat Commun* **10**, 1242 (2019).
85. Zhang, M. *et al.* RCAD/Ufl1, a Ufm1 E3 ligase, is essential for hematopoietic stem cell function and murine hematopoiesis. *Cell Death Differ* **22**, 1922–1934 (2015).
86. Yang, R. *et al.* CDK5RAP3, a UFL1 substrate adaptor, is crucial for liver development. *Development* **146**, dev169235 (2019).
87. Tatsumi, K. *et al.* The Ufm1-activating enzyme Uba5 is indispensable for erythroid differentiation in mice. *Nat Commun* **2**, 181 (2011).
88. Cai, Y. *et al.* UFBP1, a Key Component of the Ufm1 Conjugation System, Is Essential for Ufmylation-Mediated Regulation of Erythroid Development. *PLOS Genetics* **11**, e1005643 (2015).
89. Muona, M. *et al.* Biallelic Variants in UBA5 Link Dysfunctional UFM1 Ubiquitin-like Modifier Pathway to Severe Infantile-Onset Encephalopathy. *Am J Hum Genet* **99**, 683–694 (2016).
90. Colin, E. *et al.* Biallelic Variants in UBA5 Reveal that Disruption of the UFM1 Cascade Can Result in Early-Onset Encephalopathy. *Am J Hum Genet* **99**, 695–703 (2016).
91. Briere, L. C. *et al.* A description of novel variants and review of phenotypic spectrum in UBA5-related early epileptic encephalopathy. *Cold Spring Harb Mol Case Stud* **7**, a005827 (2021).
92. Ivanov, I. *et al.* Hypomyelination with Atrophy of Basal Ganglia and Cerebellum (HABC) Due to UFM1 Mutation in Roma Patients - Severe Early Encephalopathy with Stridor and Severe Hearing and Visual Impairment. A Single Center Experience. *CNS Neurol Disord Drug Targets* **22**, 207–214 (2023).
93. Di Rocco, M. *et al.* Novel spondyloepimetaphyseal dysplasia due to UFSP2 gene mutation. *Clin Genet* **93**, 671–674 (2018).
94. Mattern, L. *et al.* Variant of the catalytic cysteine of UFSP2 leads to spondyloepimetaphyseal dysplasia type Di Rocco. *Bone Rep* **18**, 101683 (2023).
95. Yoo, H. M. *et al.* Modification of ASC1 by UFM1 is crucial for ERα transactivation and breast cancer development. *Mol Cell* **56**, 261–274 (2014).
96. Yoo, H. M., Park, J. H., Kim, J. Y. & Chung, C. H. Modification of ERα by UFM1 Increases Its Stability and Transactivity for Breast Cancer Development. *Molecules and Cells* **45**, 425–434 (2022).
97. Wang, L. *et al.* UFMylation of RPL26 links translocation-associated quality control to endoplasmic reticulum protein homeostasis. *Cell Research* **30**, 5–20 (2020).

98. Millrine, D. *et al.* Human UFSP1 is an active protease that regulates UFM1 maturation and UFMylation. *Cell Reports* **40**, 111168 (2022).
99. Kang, S. H. *et al.* Two novel ubiquitin-fold modifier 1 (Ufm1)-specific proteases, UfSP1 and UfSP2. *J Biol Chem* **282**, 5256–5262 (2007).
100. Millrine, D., Peter, J. J. & Kulathu, Y. A guide to UFMylation, an emerging posttranslational modification. *FEBS J* **290**, 5040-5056 (2023).
101. Kumar, M. *et al.* Structural basis for UFM1 transfer from UBA5 to UFC1. *Nat Commun* **12**, 5708 (2021).
102. Gavin, J. M. *et al.* Mechanistic study of Uba5 enzyme and the Ufm1 conjugation pathway. *J Biol Chem* **289**, 22648–22658 (2014).
103. Oweis, W. *et al.* Trans-Binding Mechanism of Ubiquitin-like Protein Activation Revealed by a UBA5-UFM1 Complex. *Cell Rep* **16**, 3113–3120 (2016).
104. Peter, J. J. *et al.* A non-canonical scaffold-type E3 ligase complex mediates protein UFMylation. *EMBO J* **41**, EMBJ2022111015 (2022).
105. Zhang, J. *et al.* Deficiency of Murine UFM1-Specific E3 Ligase Causes Microcephaly and Inflammation. *Mol Neurobiol* **59**, 6363–6372 (2022).
106. Chen, F. *et al.* Neuronal CDK5RAP3 deficiency leads to encephalo-dysplasia via upregulation of N-glycosylases and glycogen deposition. *Cell Death Discov* **11**, 146 (2025).
107. Chen, F. *et al.* Loss of Ufl1/Ufbp1 in hepatocytes promotes liver pathological damage and carcinogenesis through activating mTOR signaling. *Journal of Experimental & Clinical Cancer Research* **42**, 110 (2023).
108. Weisz-Hubshman, M. *et al.* DDRGK1 is required for the proper development and maintenance of the growth plate cartilage. *Hum Mol Genet* **31**, 2820–2830 (2022).
109. Lu, M. *et al.* DDRGK1 preserves intervertebral disc development through ufmylation. *Cell. Mol. Life Sci.* **83**, 47 (2025).
110. Li, J. *et al.* Ufm1-Specific Ligase Ufl1 Regulates Endoplasmic Reticulum Homeostasis and Protects Against Heart Failure. *Circ: Heart Failure* **11**, e004917 (2018).
111. Simsek, D. *et al.* The Mammalian Ribo-interactome Reveals Ribosome Functional Diversity and Heterogeneity. *Cell* **169**, 1051-1065.e18 (2017).
112. Liang, J. R. *et al.* A Genome-wide ER-phagy Screen Highlights Key Roles of Mitochondrial Metabolism and ER-Resident UFMylation. *Cell* **180**, 1160-1177.e20 (2020).
113. Stephani, M. *et al.* A cross-kingdom conserved er-phagy receptor maintains endoplasmic reticulum homeostasis during stress. *eLife* **9**, 1–105 (2020).
114. Naumann, C. *et al.* The Local Phosphate Deficiency Response Activates Endoplasmic Reticulum Stress-Dependent Autophagy. *Plant Physiol* **179**, 460–476 (2019).
115. Mihailovic, M. *et al.* The coordinated action of UFMylation and the RQC pathways clears arrested polypeptides at the ER. *EMBO J* **45**, 3252–3275 (2026).
116. Wang, L. *et al.* SAYSD1 senses UFMylated ribosome to safeguard co-translational protein translocation at the endoplasmic reticulum. *Cell Reports* **42**, 112028. (2023).
117. Jiang, H., Luo, S. & Li, H. Cdk5 activator-binding protein C53 regulates apoptosis induced by genotoxic stress via modulating the G2/M DNA damage checkpoint. *J Biol Chem* **280**, 20651–20659 (2005).
118. Liu, J. *et al.* UFMylation maintains tumour suppressor p53 stability by antagonizing its ubiquitination. *Nat Cell Biol* **22**, 1056–1063 (2020).
119. Hafner, A., Bulyk, M. L., Jambhekar, A. & Lahav, G. The multiple mechanisms that regulate p53 activity and cell fate. *Nat Rev Mol Cell Biol* **20**, 199–210 (2019).
120. Yates, L. A., Zhang, X. & Burgers, P. M. DNA Damage and Replication Stress Checkpoints. *Annu Rev Biochem* **94**, 195–221 (2025).
121. Qin, B. *et al.* UFL1 promotes histone H4 ufmylation and ATM activation. *Nat Commun* **10**, 1242 (2019).
122. Abuetabh, Y. *et al.* DNA damage response revisited: the p53 family and its regulators provide endless cancer therapy opportunities. *Exp Mol Med* **54**, 1658–1669 (2022).

123. Yiu, S. P. T. *et al.* An Epstein-Barr virus protein interaction map reveals NLRP3 inflammasome evasion via MAVS UFMylation. *Molecular Cell* **83**, 2367-2386.e15 (2023).
124. Kulsuptrakul, J., Wang, R., Meyers, N. L., Ott, M. & Puschnik, A. S. A genome-wide CRISPR screen identifies UFMylation and TRAMP-like complexes as host factors required for hepatitis A virus infection. *Cell Reports* **34**, 108859 (2021).
125. Snider, D. L., Park, M., Murphy, K. A., Beachboard, D. C. & Horner, S. M. Signaling from the RNA sensor RIG-I is regulated by ufmylation. *Proceedings of the National Academy of Sciences* **119**, e2119531119 (2022).
126. Cai, Y. *et al.* Indispensable role of the Ubiquitin-fold modifier 1-specific E3 ligase in maintaining intestinal homeostasis and controlling gut inflammation. *Cell Discov* **5**, 7 (2019).
127. Peterková, L., Kmoníčková, E., Ruml, T. & Rimpelová, S. Sarco/Endoplasmic Reticulum Calcium ATPase Inhibitors: Beyond Anticancer Perspective. *J Med Chem* **63**, 1937–1963 (2020).
128. Zhang, Y., Zhang, M., Wu, J., Lei, G. & Li, H. Transcriptional Regulation of the Ufm1 Conjugation System in Response to Disturbance of the Endoplasmic Reticulum Homeostasis and Inhibition of Vesicle Trafficking. *PLOS ONE* **7**, e48587 (2012).
129. Lemaire, K. *et al.* Ubiquitin Fold Modifier 1 (UFM1) and Its Target UFBP1 Protect Pancreatic Beta Cells from ER Stress-Induced Apoptosis. *PLOS ONE* **6**, e18517 (2011).
130. Huang, H. *et al.* WBP11 inhibits UFL1-mediated UFMylation of NONO to drive hepatocellular carcinoma progression. *Oncogene* **44**, 4673–4685 (2025).
131. Zhou, J. *et al.* Dysregulation of PD-L1 by UFMylation imparts tumor immune evasion and identified as a potential therapeutic target. *Proc. Natl. Acad. Sci. U.S.A.* **120**, e2215732120 (2023).
132. von der Malsburg, K., Shao, S. & Hegde, R. S. The ribosome quality control pathway can access nascent polypeptides stalled at the Sec61 translocon. *Mol Biol Cell* **26**, 2168–2180 (2015).
133. Crowder, J. J. *et al.* Rkr1/Ltn1 Ubiquitin Ligase-mediated Degradation of Translationally Stalled Endoplasmic Reticulum Proteins. *J Biol Chem* **290**, 18454–18466 (2015).
134. Endo, R. *et al.* Dysregulation of ribosome-associated quality control elicits cognitive disorders via overaccumulation of TTC3. *Proc Natl Acad Sci U S A* **120**, e2211522120 (2023).
135. Li, X. & Mariappan, M. Nascent Chain Ubiquitination is Uncoupled from Degradation to Enable Protein Maturation. 2023.10.09.561585 Preprint at https://doi.org/10.1101/2023.10.09.561585 (2023).
136. Kizmaz, B. & Herrmann, J. M. Membrane insertases at a glance. *J Cell Sci* **136**, jcs261219 (2023).
137. Brodsky, J. L., Hamamoto, S., Feldheim, D. & Schekman, R. Reconstitution of protein translocation from solubilized yeast membranes reveals topologically distinct roles for BiP and cytosolic Hsc70. *J Cell Biol* **120**, 95–102 (1993).
138. Itskanov, S. & Park, E. Structure of the posttranslational Sec protein-translocation channel complex from yeast. *Science* **363**, 84–87 (2019).
139. Becker, T. *et al.* Structure of Monomeric Yeast and Mammalian Sec61 Complexes Interacting with the Translating Ribosome. *Science* **326**, 1369–1373 (2009).
140. Shoemaker, C. J. & Green, R. Kinetic analysis reveals the ordered coupling of translation termination and ribosome recycling in yeast. *Proc Natl Acad Sci U S A* **108**, E1392–E1398 (2011).

## 6. Abbreviations

| | |
|---|---|
| ABCE1 | ATP-binding cassette sub-family E member 1 |
| ANKZF1 | Ankyrin repeat and zinc finger domain-containing protein 1 |
| ANS | Anisomycin |
| ASC-1 complex | Activating signal cointegrator 1 complex |
| ATF4 | Activating transcription factor 4 |
| ATF6 | Activating transcription factor 6 |
| ATM | Ataxia-telangiectasia mutated kinase |
| ATP | Adenosine triphosphate |
| CAT-tails | C-terminal alanine and threonine extensions |
| CC domain | Coiled-coil domain |
| CDK5RAP3 | Cyclin-dependent kinase 5 regulatory subunit-associated protein 3 |
| CRISPR | Clustered regularly interspaced short palindromic repeats |
| CRISPRi | CRISPR interference |
| DDRGK1 (UFBP1) | DDRGK domain-containing protein 1 (UFM1-binding protein 1) |
| E1 enzyme | Ubiquitin-activating enzyme |
| E2 enzyme | Ubiquitin-conjugating enzyme |
| E3 ligase | Ubiquitin-ligating enzyme |
| EBV | Epstein-Barr virus |
| eIF2α | Eukaryotic initiation factor 2 alpha |
| EMC | Endoplasmic reticulum membrane protein complex |
| ER | Endoplasmic reticulum |
| eRF1 | Eukaryotic release factor 1 |
| eRF3 | Eukaryotic release factor 3 |
| FFAT motif | Two phenylalanines in an acidic tract |
| FN3 | Fibronectin type-III |
| G1 | Gap 1 cell cycle phase |
| G2 | Gap 2 cell cycle phase |
| GET pathway | Guided entry of tail-anchored proteins pathway |
| GGQ motif | Glycine-glycine-glutamine motif |
| GTP | Guanosine triphosphate |
| Hbs1 | Elongation factor 1 alpha-like protein |
| Hbs1L | HBS1-like protein |
| iCas9 | Inducible CRISPR-associated protein 9 |
| IP | Immunoprecipitation |
| IP-MS | Immunoprecipitation–mass spectrometry |

| | |
|---|---|
| IP-WB | Immunoprecipitation–Western blot |
| $IP_3R$ | Inositol 1,4,5-trisphosphate receptor |
| IRE1 | Inositol-requiring enzyme 1 |
| LTN1 | Listerin E3 ubiquitin ligase 1 |
| M | Mitotic cell cycle phase |
| µM | Micromolar concentration |
| MAVS | Mitochondrial antiviral-signaling protein |
| MRN | MRE11-RAD50-NBS1 protein complex |
| mRNA | Messenger RNA |
| MRE11 | Meiotic recombination 11 homolog |
| NEMF | Nuclear export mediator factor |
| nM | Nanomolar concentration |
| NONO | Non-POU domain-containing octamer-binding protein |
| PD-L1 | Programmed cell death 1 ligand 1 |
| PERK | Eukaryotic translation initiation factor 2-alpha kinase 3 |
| PIC | Pre-initiation complex |
| PTC | Peptidyl transferase center |
| RIG-I | Retinoic acid-inducible gene I |
| RING domain | Really interesting new gene domain |
| RNC | Ribosome–nascent chain complex |
| RPL26 | Large ribosomal subunit protein uL24 |
| RPS10 | Small ribosomal subunit protein eS10 |
| RPS20 | Small ribosomal subunit protein uS10 |
| RQC | Ribosome-associated quality control |
| RtcB | RNA 2′,3′-cyclic phosphate and 5′-OH ligase |
| pWH domain | Partial winged-helix domain |
| SEC61 | Protein translocation channel (Sec61 complex) |
| SGTA | Small glutamine-rich tetratricopeptide repeat-containing protein α |
| siRNA | Small interfering RNA |
| SRα | Signal recognition particle receptor alpha subunit |
| SRP | Signal recognition particle |
| TA proteins | Tail-anchored proteins |
| TCF25 | Transcription factor 25 |
| TG | Thapsigargin |
| TMD | Transmembrane domain |
| tRNA | Transfer RNA |
| TUBE | Tandem ubiquitin-binding entities |
| UBA5 | UFM1-activating enzyme 5 |
| UBC domain | Ubiquitin-conjugating domain |

| | |
|---|---|
| UFC1 | UFM1-conjugating enzyme 1 |
| UFL1 | UFM1-specific ligase 1 |
| UFM1 | Ubiquitin-fold modifier 1 |
| UFMylation | Conjugation of UFM1 to substrate proteins |
| UFIM | UFM1-interacting motif |
| UFSP1 | UFM1-specific protease 1 |
| UFSP2 | UFM1-specific protease 2 |
| UPR | Unfolded protein response |
| uS3 | Small ribosomal subunit protein uS3 |
| uS10 | Small ribosomal subunit protein uS10 |
| VAPs | Vesicle-associated membrane protein-associated proteins |
| VCP | Valosin-containing protein |
| WH domain | Winged-helix domain |
| XBP1 | X-box binding protein 1 |
| ZNF598 | Zinc finger protein 598 |

# 7. Appendix

## 7.1. UFMylation anchors splicing factors at the ER to reprogram nuclear splicing

### *7.1.1. Preamble*

This paper uncovers a new regulatory mechanism and role of UFMylation in retaining splicing factors at the ER, therefore establishing inter-organellar communication from the ER to the nucleus, resulting in changed nuclear splicing. UFMylation is a highly conserved post-translational modification among eukaryotes, and the loss or mutations in UFMylation cascade causes phenotypes of ER homeostasis perturbations across organisms, heavy developmental impacts and lethality in mice, as well as various human pathologies. These data hint towards an alternative conserved mechanism of broader homeostatic regulation apart from UFMylation's role in resolving stalled ribosomes at the ER, which is the research question of this manuscript.

This research uncovers a novel regulatory mechanism linking UFMylation to the nuclear splicing. Upon ribosome stalling at the ER, serine/arginine-rich (SR) splicing factors are retained at the ER, and therefore depleted from their functional nuclear localization, resulting in increased intron retention. The transcripts that are spliced by the SR splicing factors include important ER homeostasis regulators, such as lipid metabolic enzymes, and proteins involved in endomembrane-associated processes. These findings point to UFMylation as a regulator of retrograde ER-to-nucleus signaling and broad membrane homeostasis across species.

The work presented in this manuscript relates to the overarching question of this thesis, which is the regulation of ER quality control and ER translational proteostasis, and directly answers the first question of my thesis by uncovering a process regulated by UFMylation of RPL26 at the ER-stalled ribosomes.

This paper has been accepted for revision in *Nature* on April 24$^{th}$, 2026. The manuscript is also published on biorxv under the following doi: https://doi.org/10.64898/2026.03.30.715226.

### *7.1.2. Contribution statement*

For the following manuscript, I have optimized the fractionation experiments from the human cell lines, was involved in the hypothesis formation, and edited the manuscript before submission.

# UFMylation anchors splicing factors at the ER to reprogram nuclear splicing

**Ni Zhan[1,#,*], Ranjith K. Papareddy[2,#], Bu Erte[2], Aleksandra S. Anisimova[3,4], Catarina Perdigao[5], Marilyn Tirard-Thevenoud[5], Milica Mihailovic[3,4], Hasan Akyol[1], G. Elif Karagöz[3], Nils Brose[5], Nicholas A.T. Irwin[1], Yasin Dagdas[1,2,6,*]**

[1]Gregor Mendel Institute (GMI), Austrian Academy of Sciences, Vienna BioCenter (VBC), Vienna, Austria
[2]Heidelberg University, Centre for Organismal Studies (COS), 69120 Heidelberg, Germany
[3]Max Perutz Labs, Medical University of Vienna, Vienna BioCenter (VBC), Vienna, Austria
[4]Vienna BioCenter PhD Program, Doctoral School of the University of Vienna and Medical University of Vienna, Vienna, Austria
[5]Department of Molecular Neurobiology, Max Planck Institute for Multidisciplinary Sciences, Göttingen, Germany
[6]Cluster of Excellence GreenRobust, Heidelberg University, 69120 Heidelberg, Germany

[#]Contributed equally
[*]Correspondence: ni.zhan@gmi.oeaw.ac.at, yasin.dagdas@cos.uni-heidelberg.de

## Abstract

How organelles communicate stress to the nucleus to coordinate adaptive responses remains a fundamental question in cell biology. Here, we identify a non-canonical retrograde signaling pathway in which stalling-induced UFMylation of ER-associated ribosomes anchors splicing regulators at the ER, directly coupling translational stress to nuclear RNA processing. Phylogenetic profiling linked the UFMylation machinery to a network of nuclear mRNA processing factors. Fractionation-based quantitative proteomics further supported this link and revealed that translational stress triggers UFM1-dependent retention of serine/arginine-rich (SR) splicing factors at the ER, depleting their nuclear pools. Mechanistically, UFMylated ribosomes physically tether SR proteins at the ER surface, driving widespread intron retention that preferentially targets transcripts encoding membrane lipid metabolism and endomembrane-associated processes—a response conserved from plants to mammals. These findings reframe UFMylation from a local ribosome repair signal to a systems-level coordinator of ER-nucleus communication that reprograms nuclear splicing and reshapes membrane-associated gene expression with implications for diverse human diseases linked to UFMylation defects.

## Introduction

The endoplasmic reticulum (ER) is responsible for the synthesis of nearly one-third of the cellular proteome and is the primary site for membrane-bound and secretory protein biogenesis[1–3]. Disruption of ER function perturbs proteostasis; when ribosomes stall or misfolded proteins accumulate, cells activate multiple quality control mechanisms, including the unfolded protein response (UPR), ER-associated degradation (ERAD), selective autophagy of ER fragments (ER-phagy), and ribosome-associated quality control (ER-RQC)[3–7]. Unlike cytosolic RQC[3,8–10], ribosome stalling at the ER occurs at the SEC61 translocon, where stalled 60S subunits obstruct both the translocon and the ribosomal exit tunnel, creating a unique surveillance challenge. A defining feature of ER-RQC is UFMylation, a ubiquitin-like post-translational modification[11,12]. At the ER, the transmembrane protein DDRGK1 and CDK5RAP3 (C53) serve as adaptors for UFMylation[13]. Upon ribosome stalling, UFL1–C53–DDRGK1 forms an E3 ligase complex that conjugates UFM1 to ribosomal protein RPL26[14–16], facilitating release of the 60S subunit and enabling LTN1-mediated degrdation of the arrested nascent chain[17–20]. Beyond this core role, UFMylation promotes lysosomal clearance of translocon-arrested proteins via translocation-associated quality control (TAQC) and activates C53-mediated ER-phagy[4,21,22].

Physiologically, our previous studies demonstrated that the UFMylation pathway is essential for maintaining ER homeostasis in plants, with knockout mutants exhibiting hypersensitivity to ER and salt stress[4,21,23]. In animal cells UFMylation has been implicated in diverse processes, including lipid metabolism[24], ER–Golgi trafficking[25], ER expansion[26], and development[27], while its disruption leads to embryonic lethality in mice and various human pathologies[11,27,28]. These established roles of suggested that UFMylation coordinate broader cellular adaptations to ER translational stress, beyond the local resolution of ribosome stalling. Indeed, two recent genome-wide CRISPR screens in human iPSC-derived neurons independently identified UFMylation as major modifiers of tau aggregation

and propagation [29,30]. While paradoxical at first glance, given that tau is a cytosolic protein, these studies also suggest UFMylation plays a role beyond ER-RQC.

Here, we uncover a mechanism that resolves this paradox. Phylogenetic profiling revealed an unexpected coevolutionary link between UFMylation machinery and nuclear mRNA processing factors. Further mechanistic analyses show that ribosome stalling triggers retention of SR splicing factors at UFMylated ER-bound ribosomes, depleting their nuclear pools. This spatial redistribution rewires the splicing landscape, with intron retention emerging as the predominant outcome across plants, human cells, and mouse neurons. The affected transcripts are enriched for genes encoding membrane lipid metabolism and endomembrane processes, suggesting a feedback circuit for membrane remodeling under stress. Our findings define a retrograde signaling pathway coupling translational surveillance to mRNA splicing.

# Results

## Phylogenetic profiling and nuclear proteomics link UFMylation with nuclear mRNA processing

Previous studies have identified co-evolutionary relationships among the canonical components of the UFMylation cascade[21,31]. To examine UFMylation function more broadly, we used phylogenetic profiling to identify additional UFM1-associated proteins. Correlating the presence-absence patterns of UFM1 with eukaryotic protein families across diverse taxa revealed 103 putatively co-evolving protein families (Fig. 1a, b). As expected, these included the core UFMylation machinery (UFL1, UFC1, DDRGK1, C53, UBA5, and UFSP2) and known associated factors such as ODR4[32] (Fig. 1c). Gene ontology analysis of the co-evolved proteins revealed functional enrichments beyond ER homeostasis, including actin related Scar-WAVE complex, double strand break repair (the Fanconi anemia complex), cytokinesis, and RNA processing (Fig. 1c and Fig. S1a, Table S1). The link to DNA damage response is consistent with recent studies linking UFMylation to genome stability and DNA repair[11].

To assess whether this evolutionary link reflects physical interactions, we used AlphaFold2-Multimer to screen for potential contacts between UFMylation machinery and co-evolving proteins. High-confidence models predicted an interaction between the E3 ligase component DDRGK1 and the transcription-export (THO/TREX) subunit THO6 (Fig. 1d, Table S2). Co-immunoprecipitation in *Arabidopsis* further confirmed that THO6 physically associates with both DDRGK1 and C53 (Fig. S1c, d).

Since our phylogenetic profiling and AlphaFold multimer analyses indicated a link between UFMylation and the nucleus, we next tested whether UFMylation remodels the nuclear proteome during translational stress. We performed quantitative proteomics on nuclear fractions from wild-type (Col-0) and *ufm1* mutant *Arabidopsis* seedlings subjected to translational stress (anisomycin, ANS) (Fig. 1e, Table S3). Fractionation purity was validated by Histone H3 enrichment and the absence of the cytosolic marker UGPase (Fig. S1e, f). Gene Ontology analysis revealed that spliceosome-related proteins were significantly reduced in the nuclear fraction in a UFM1-dependent manner (Fig. 1f). Consistent with phylogenetic predictions, proteomic profiling confirmed the reduced nuclear abundance of multiple mRNA processing factors, including spliceosomal components and splicing factors (e.g., RSZ22, RSZ22a), THO/TREX subunits (THO1), and nucleoporins (Fig. 1g, h). The known UFMylation-associated autophagy protein ATG6 was also depleted from the nuclear fraction[23]. Importantly, integrated proteomic and RNA-seq analysis indicated that these changes were independent of transcriptional regulation (Fig. S1g–l; Table S4). Since UFMylation is induced at the ER, we reasoned that nucleocytoplasmic shuttling proteins among the nuclear-depleted factors could represent candidates for UFM1-dependent spatial regulation. We focused on RSZ22 for further investigation, as it is a well-characterized member of the serine/arginine-rich (SR) protein family with established nucleocytoplasmic shuttling activity[33]. Immunoblotting validated the UFM1-dependent reduction of nuclear RSZ22 following stress, while total cellular levels in whole-cell lysates remained unchanged (Fig. 1i–j; Fig. S1m). Together, these data indicate that UFMylation regulates the stress-induced redistribution of mRNA processing factors between the nucleus and cytoplasm.

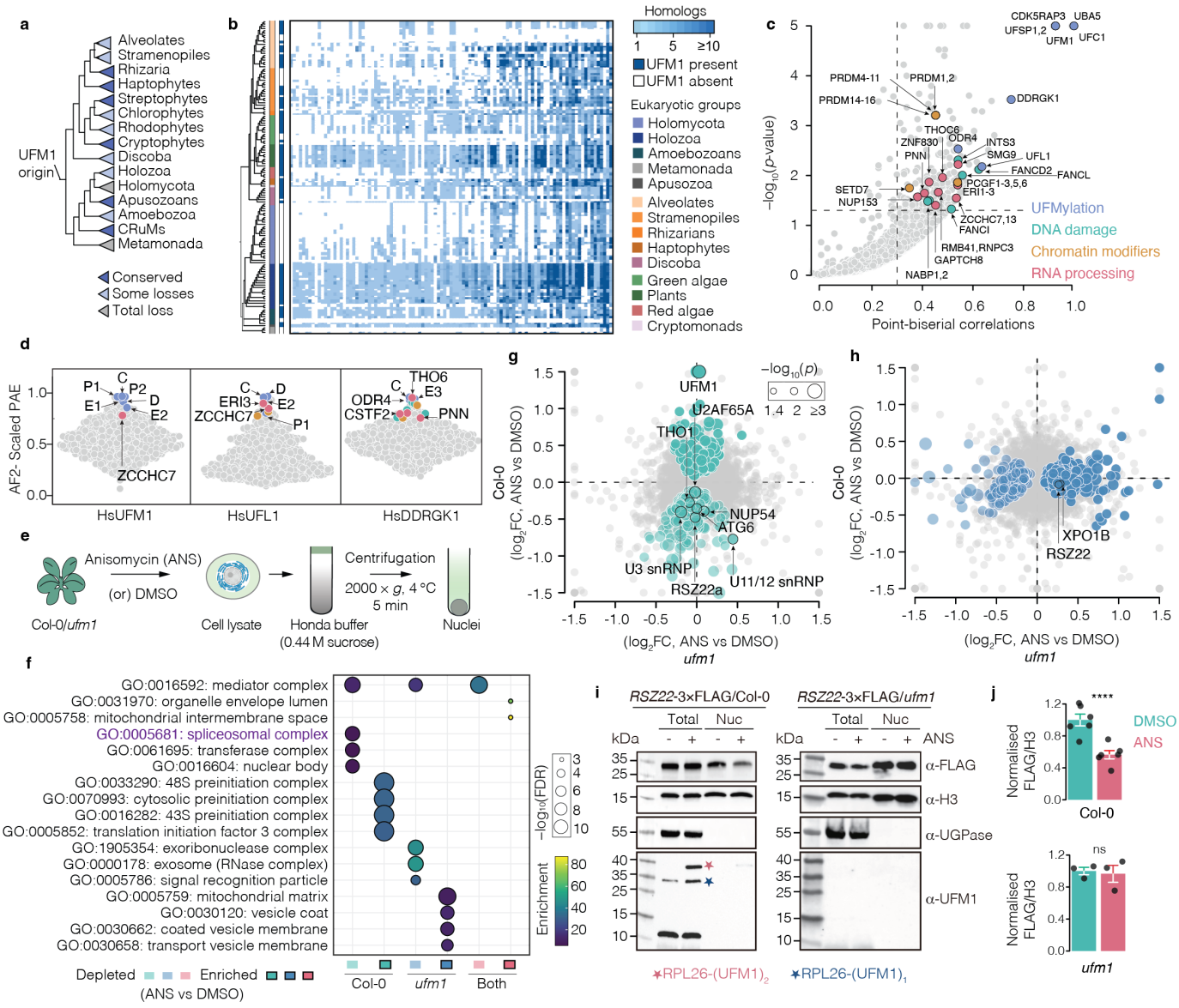



**Figure 1** | **Integrated evolutionary and proteomic profiling links UFMylation to nuclear mRNA processing.** **a**, Phylogenetic distribution of UFM1 across major eukaryotic lineages. Conservation status is color-coded as conserved (blue), partial loss (light blue) or total loss (grey). The inferred evolutionary origin is indicated. **b**, Co-evolutionary heatmap of core UFMylation machinery and co-evolved genes across representative eukaryotes. Color intensity indicates copy number; supergroups shown on the right. **c**, Association plot of nuclear genes co-evolving with UFMylation components (point-biserial correlation $\geq 0.3$, $P < 0.05$). Candidates are colored by functional category, highlighting enrichment in DNA damage, chromatin, and RNA processing pathways. **d**, Dot plot illustrating AlphaFold2 (AF2) Multimer interaction predictions of coevolved genes against UFMylation machinery. The Y-axis represents the average protein interaction score across the top three ranked models, calculated from domain-specific Predicted Aligned Error (PAE) values rescaled from 0 to 1. Abbreviations: P1, P2: UFSP1 and 2; E1, E2, E3: UBA5, UFC1, and UFL1; C: CDK5RAP3; D: DDRGK1. Coevolved genes with Scaled PAE $\geq 0.75$ are colored according to key in **Fig. 1c**. **e**, Experimental workflow for nuclear fractionation of 10-day-old *Arabidopsis* Col-0 and *ufm1* seedlings treated with DMSO or anisomycin (ANS, 4 h). **f**, GO enrichment of proteins altered by ANS. Top four terms per condition ($\leq$ 300 genes, adjusted $P \leq 0.01$, fold enrichment $\geq 5$) are shown. Dot size and color indicate $-\log_{10}$(FDR) and fold enrichment, respectively. **g, h**, Scatter plots of $\log_2$ fold-changes (ANS versus DMSO) in *ufm1* (x-axis) versus Col-0 (y-axis). Proteins significantly altered in Col-0 (green, **g**) or *ufm1* (blue, **h**) are highlighted, dot size reflects $-\log_{10}$(FDR). **i**, Immunoblotting analysis of RSZ22 abundance in total (whole cell lysates) and nuclear fractions from 10-day-old *RSZ22*-3×FLAG seedlings (Col-0 and *ufm1* backgrounds) treated with DMSO or ANS (4 h). H3 and UGPase are nuclear and cytosolic markers. Mono- (1) and di- (2) UFMylated RPL26 are indicated. See (Fig. S1m) and source data for replicates. **j**, Quantification of RSZ22 nuclear abundance normalized to H3. Dots represent independent biological replicates; bars indicate mean ± standard error of the mean (s.e.m.). Statistical significance: Wilcoxon rank sum test, **** $P < 0.0001$; $ns$, not significant. **Fig. S1 on page 27**

## UFMylation retains nucleocytoplasmic shuttling factors at the ER upon ribosome stalling

Given that SR proteins are evolutionarily conserved nucleocytoplasmic shuttling factors[34,35], we hypothesized that

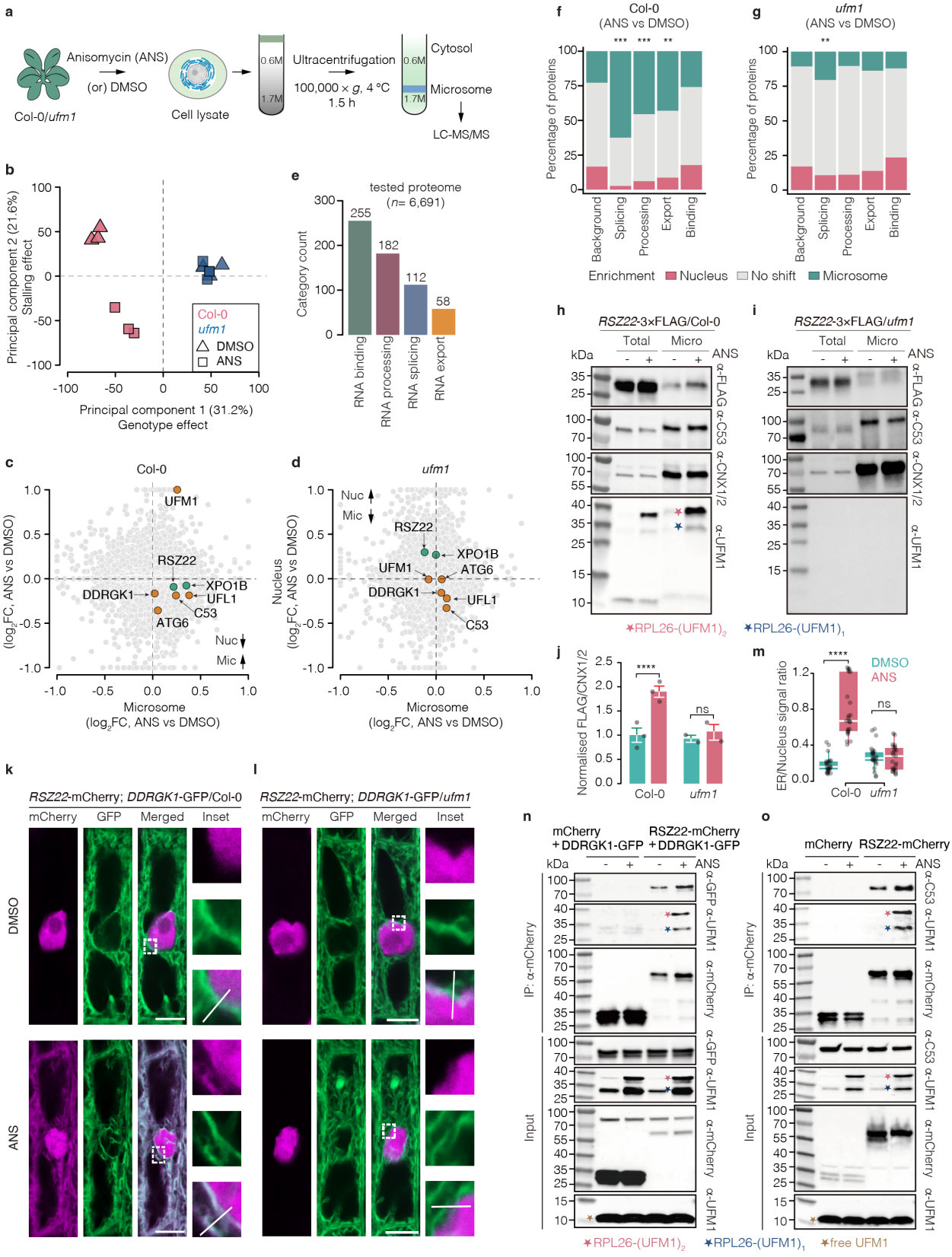


**Figure 2 | UFMylation retains nucleocytoplasmic shuttling factors at the ER upon ribosome stalling.** **a**, Experimental workflow for microsomal proteome analysis of 10-day-old seedlings treated with DMSO or ANS (4 h). **b**, Principal component analysis (PCA) of microsomal proteome ($n = 3$ biological replicates). PC1 and PC2 reflect proteomic separation by genotype and treatment. **c, d**, Scatter plots comparing ANS-induced $\log_2$ fold-changes in microsomal (x-axis) versus nuclear (y-axis) fractions in Col-0 (**c**) and *ufm1* (**d**). RNA-associated factors (e.g., RSZ22, XPO1B) and UFMylation machinery components are highlighted, illustrating UFM1-dependent redistribution. **e**, Functional annotation of quantified microsomal proteome (total quantified proteins $n = 6,691$), showing number of RNA-related proteins by categories. **f, g**, Stacked bar charts show the distribution of proteins across subcellular enrichment classes following ANS treatment. Proteins were classified based on $\Delta$ enrichment, defined as $\log_2$FC(microsome) $-$ $\log_2$FC(nucleus): $\Delta > +0.25$ indicates microsome enrichment, $\Delta < -0.25$ indicates nuclear enrichment, and intermediate values indicate no detectable shift. Statistical significance denotes enrichment of microsome-shifted proteins relative to all quantified proteins (background), assessed using Fisher's exact test with Benjamini-Hochberg FDR correction ( ** $P < 0.01$, *** $P < 0.001$). **h, i**, Immunoblot analysis of *RSZ22*-3×FLAG and endogenous C53 in total lysates and microsomal fractions ($n = 3$ for *RSZ22*-3×FLAG in Col-0; $n = 2$ for *RSZ22*-3×FLAG in *ufm1*). CNX1/2 serves as an ER marker. Mono- (1) and di- (2) UFMylated RPL26 are indicated. See (Fig. S2f–h) and source data for replicates. **j**, Quantification of RSZ22 microsomal enrichment (FLAG/CNX1/2 ratio) from (**h**), (**i**); Bars indicate mean ± s.e.m. Statistical significance: Wilcoxon rank sum test, **** $P < 0.0001$; $ns$, not significant. **k, l**, Representative confocal images of RSZ22-mCherry and DDRGK1-GFP (ER marker) in root cells from Col-0 (**k**) and *ufm1* (**l**) backgrounds. ANS (1–2 h) induces RSZ22-ER signal overlap in Col-0 (**k**), and the signal overlap was absent in *ufm1* (**l**). Enlarged views and white lines indicate line-scan regions. Scale bars, 10 $\mu$m. See (Fig. S3a–b) for line-scan profiles. **m**, Quantification of ER-to-nucleus RSZ22 signal ratios from (**k**), (**l**). Data are mean ± SD from 3 biological replicates. Each dot represents an individual cell ($n = 15$ cells from 3 biological replicates). Bars indicate mean ± SD. Statistical significance was determined by two-tailed unpaired t-test **** $P \leq 0.0001$; $ns$, not significant. **n, o**, In vivo Co-IP of RSZ22 interactions with DDRGK1 and UFMylated RPL26 (**n**) or interaction of RSZ22 with endogenous C53 and UFMylated RPL26 (**o**) under DMSO or ANS (4 h) treatment ($n = 2$). Proteins were extracted from *Arabidopsis* lines co-expressing DDRGK1-GFP with either mCherry (control) or RSZ22-mCherry in Col-0 background seedlings (**n**), or from mCherry (control) and RSZ22-mCherry seedlings (**o**). Input samples were normalized by Bradford assay prior to loading. The consistent level of endogenous free UFM1 (unconjugated) in input fractions serves as an internal loading control to show equal protein loading across all lanes. RSZ22-mCherry was immunoprecipitated using RFP-Trap beads. Mono- (1), di- (2) UFMylated RPL26 and free UFM1 are indicated. See (Fig. S3c–d) for replicates.
**Fig. S2 and S3 on page 29 and 30**

UFMylated ribosomes at the ER could serve as platforms for spatially retaining these factors, thereby depleting them from the nucleus under stress. To test this, we isolated ER-derived microsomal fractions from wild-type (Col-0) and *ufm1* mutant *Arabidopsis* seedlings treated with DMSO or ANS (Fig. 2a). Microsomal purity was confirmed by enrichment of the ER marker CNX1/2 and the absence of the cytosolic protein NIT1 (Fig. S2a). Principal component analysis revealed that the microsomal proteome displayed clear segregation by genotype and stress treatment, whereas the nuclear proteome showed limited separation (Fig. 2b and Fig. S2b). This disparity likely reflects the fact that sequestration of shuttling factors at the ER, a compartment where they are normally sparse, generates a high-contrast signal, whereas their depletion from the nucleus represents a subtle shift against a large nuclear background.

Quantitative analysis of the microsomal proteome revealed significant UFM1-dependent enrichment of several nucleocytoplasmic shuttling factors following stress, including RSZ22 and the export factor XPO1B (Fig. 2c, d). RSZ22 is the *Arabidopsis* homolog of human SRSF7 and undergoes active shuttling between the nucleus and cytoplasm, a process partially mediated by the XPO1 export pathway[33,36,37]. Integrating the nuclear and microsomal datasets revealed a reciprocal redistribution pattern: multiple mRNA processing factors exhibited decreased nuclear abundance coupled with increased ER retention, and this redistribution was UFM1-dependent (Fig. 2e–g and Fig. S2d, e, Table S5). Immunoblotting confirmed this spatial shift for RSZ22, showing increased ER association with a corresponding reduction in nuclear levels following ANS treatment (Fig. 1i, j; Fig. 2h–j; Fig. S1m; S2f–h). Confocal imaging of RSZ22-mCherry with the ER marker DDRGK1-GFP confirmed a shift from nucleus to cytoplasm, partially localizing to the ER upon stress, which was absent in *ufm1* mutants (Fig. 2k–m and Fig. S3a, b).

We next tested whether this mechanism extends to other co-evolved factors. THO6, which physically associates with the UFMylation machinery (Fig. 1c and Fig. S1c, d), similarly accumulated at the ER in a UFM1-dependent manner upon stress (Fig. S3e–i). To determine whether the microsomal retention of RSZ22 is mediated by physical association with the UFMylation machinery, we performed co-immunoprecipitation experiments. RSZ22 associated

with UFMylation components C53 and DDRGK1, as well as with UFMylated RPL26 (Fig. 2n, o and Fig. S3c, d), consistent with its ER recruitment. Together, these findings demonstrate that ribosome stalling induces UFM1-dependent retention of nucleocytoplasmic shuttling factors at the ER, providing a mechanism for their nuclear depletion.

## UFM1-dependent anchoring of splicing factors to stalled ER-associated ribosomes

To determine whether ER retention occurs directly at ribosomes, we performed proteomics of ribosomes isolated from *Arabidopsis* seedlings treated with ANS at various times (4 h, pooled time-course, and 16 h). Ribosomal fractions (60S, monosomes, and disomes) were isolated via sucrose-gradient fractionation and analyzed by LC-MS/MS (Fig. 3a). As an internal benchmark, the UFMylation E3 ligase complex (C53, UFL1, and DDRGK1) was enriched on stalled ribosomes in a UFM1-dependent manner (Fig. 3b and Fig. S4a–f, Table S6).

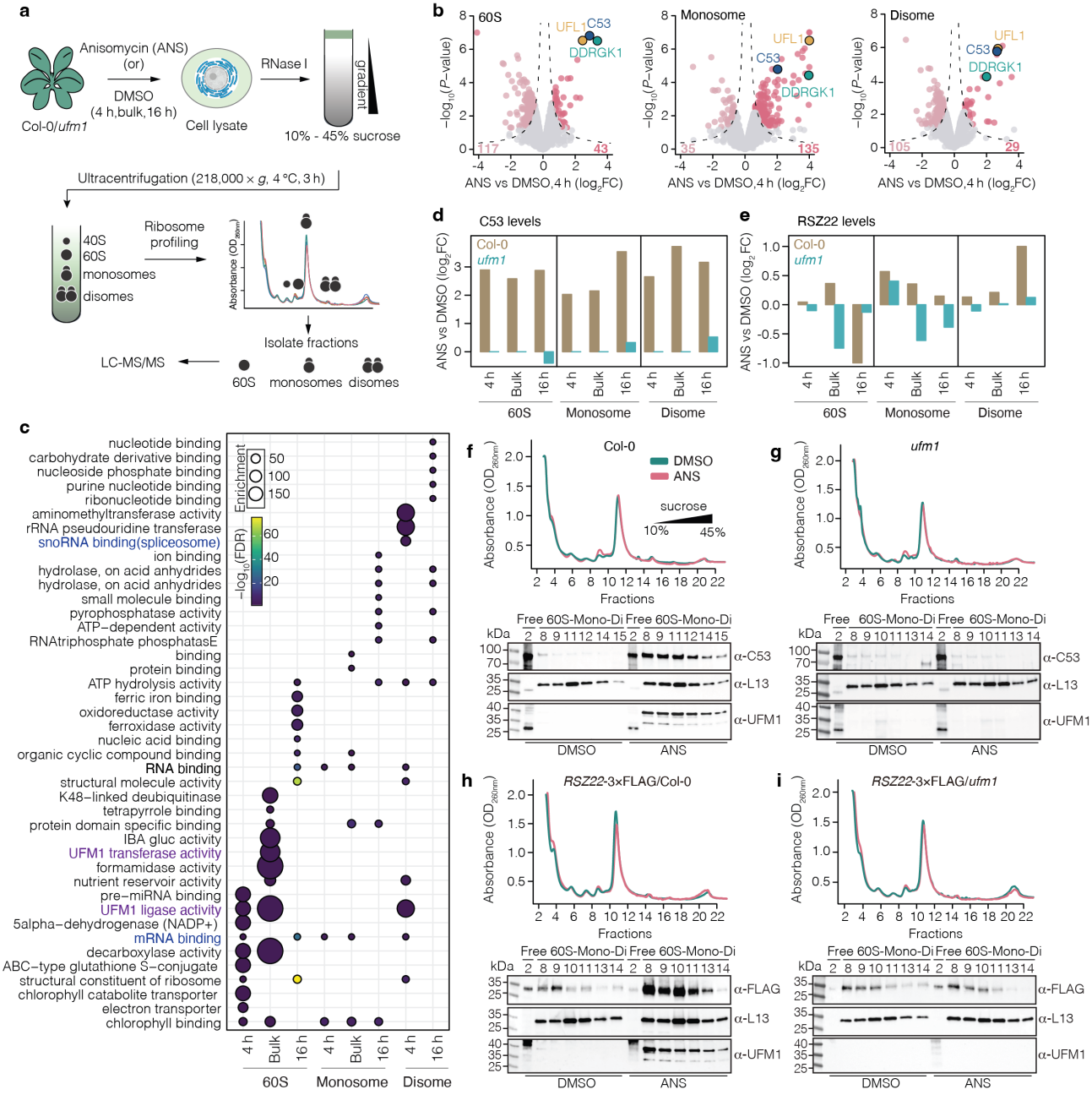


**Figure 3** | **UFM1-dependent anchoring of splicing factors to stalled ER-associated ribosomes. a**, Schematic workflow for ribosome proteomics using 10-day-old Col-0 and *ufm1* seedlings treated with DMSO or ANS. Ribosomal fractions (60S, monosome and disome) were isolated by RNase I digestion and sucrose gradient sedimentation for LC-MS/MS. Three datasets were analyzed: 4 h, a bulk sample (pooled from 1, 4, 8, 16 h treatments), and 16 h. **b**, Volcano plots (4-h dataset) showing ANS-induced recruitment of UFMylation components (UFL1, C53 and DDRGK1) to 60S, monosomes and disomes in Col-0. x-axis, $\log_2$FC (ANS versus DMSO); y-axis, $-\log_{10}(P$ value). **c**, GO enrichment analysis of stalling induced ribosome-enriched proteins in Col-0 plants. Dot color and size indicate $-\log_{10}$(FDR) and fold enrichment, respectively. Representative functional categories are highlighted. **d, e**, MS-based abundance profiles of C53 (**d**) and RSZ22 (**e**) across ribosomal fractions. Bars represent $\log_2$ fold change (ANS versus DMSO) in Col-0 (olive) and *ufm1* (cyan) from three datasets (4 h, bulk and 16 h). **f, g**, Sucrose gradient sedimentation and immunoblot analysis of endogenous C53 from Col-0 (**f**) and *ufm1* (**g**) seedlings treated with DMSO or ANS (4 h). UV absorbance ($A_{260}$) profiles (top) indicate ribosome distribution across 10%–45% gradients. Fractions were immunoblotted for C53, L13 (60S marker), and UFM1 ($n = 3$). Free: ribosome-free fractions. See (Fig. S5d–g) for replicates. **h, i**, Sucrose gradient sedimentation and immunoblot analysis of *RSZ22*-3×FLAG in Col-0 (**h**) and *ufm1* (**i**) backgrounds. Fractions were immunoblotted for FLAG, L13, and UFM1 ($n = 3$). See (Fig. S5h–k) for additional replicates. **Fig. S4 and S5 on page 31 and 32**

Gene Ontology analysis of the stalling-induced ribosome-enriched proteins revealed the significant enrichment for mRNA binding and spliceosome proteins (Fig. 3c). Intersection analysis revealed a complex, translation-state-specific response to ANS stress (Fig. S4g). Heatmap clustering showed a largely intact global response in the *ufm1* mutant. But distinct subsets of candidate proteins showed UFM1-dependent association (Fig. S4h). For example, both C53 and the splicing factor RSZ22 are recruited to ribosomes in a stress and UFM1-dependent manner, while total cellular levels remained unchanged (Fig. 3d–i and Fig. S5a–c). Independent biological replicates confirmed the robustness of this association (Fig. S5d–k).

Importantly, the UFM1-dependent retention of mRNA processing factors represents a functionally distinct layer from known stalled ribosome sensing and splitting process. The conserved factors PEL1 and MBF1b (plant homologs of mammalian PELO and EDF1, respectively)[10,38,39] were similarly enriched on stalled ribosomes in both wild-type and *ufm1* mutants (Fig. S4i, j). These results demonstrate that while the foundational ribosome rescue machinery remains intact in the *ufm1* mutant and operates independently of UFMylation, the UFM1 cascade supports an additional signaling function: capturing nucleocytoplasmic shuttling factors at ER-associated ribosomes. Together, these results establish that translational stress triggers UFM1-dependent recruitment of mRNA processing proteins to stalled ribosomes, where they are physically retained.

## UFM1-dependent intron retention selectively targets ER-related transcripts across species

To test the functional consequences of UFM1-dependent splicing factor retention, we analyzed stalling-induced alternative splicing across three systems: *Arabidopsis* seedlings, human colorectal carcinoma cell line (RKO), and mouse primary neurons. We fractionated the *Arabidopsis* and human samples into cytosolic and nuclear components, while total RNA was used for the mouse primary neurons. Ribosome stalling triggered widespread alternative splicing in all three models, with intron retention (IR) as the conserved outcome (Fig. 4a–c, Table S7). Strikingly, the magnitude of this response, measured by the mean absolute error (MAE) of aggregate splicing changes was significantly reduced in *ufm1* mutants, indicating that a substantial fraction of IR events depends on UFM1 (Fig. 4a–f and Fig. S6a–e, h–k). This establishes UFMylation as a key conserved regulator of stress-induced splicing via the spatial retention of splicing factors at ER-associated ribosomes.

We next characterized the features of stalling-responsive introns. While approximately half of IR events were strictly UFM1-dependent (Fig. 4a–c, Table S7), the overall IR landscape exhibited conserved positional biases: retained introns were specifically located within 3′UTRs that are longer than the genomic average, a feature typical for nonsense-mediated decay (NMD) substrates[40,41] (Fig. 4g–i). Specifically, these introns are followed by downstream splice junctions beyond the 55-nt boundary that triggers NMD, a pattern conserved across species (Fig. 4j, k and Fig. S7a–d). In both *Arabidopsis* and human cells, stress-induced IR events detected in the nuclear fraction were depleted from the cytosolic fraction, suggesting potential NMD targeting (Fig. S6f, g). Both UFM1-dependent and -independent

introns exhibited weak splice site signatures, including lower entropy (maximum entropy score) at the 3′ splice site and reduced polypyrimidine tracts (Fig. 4l, m and Fig. S7e–i).

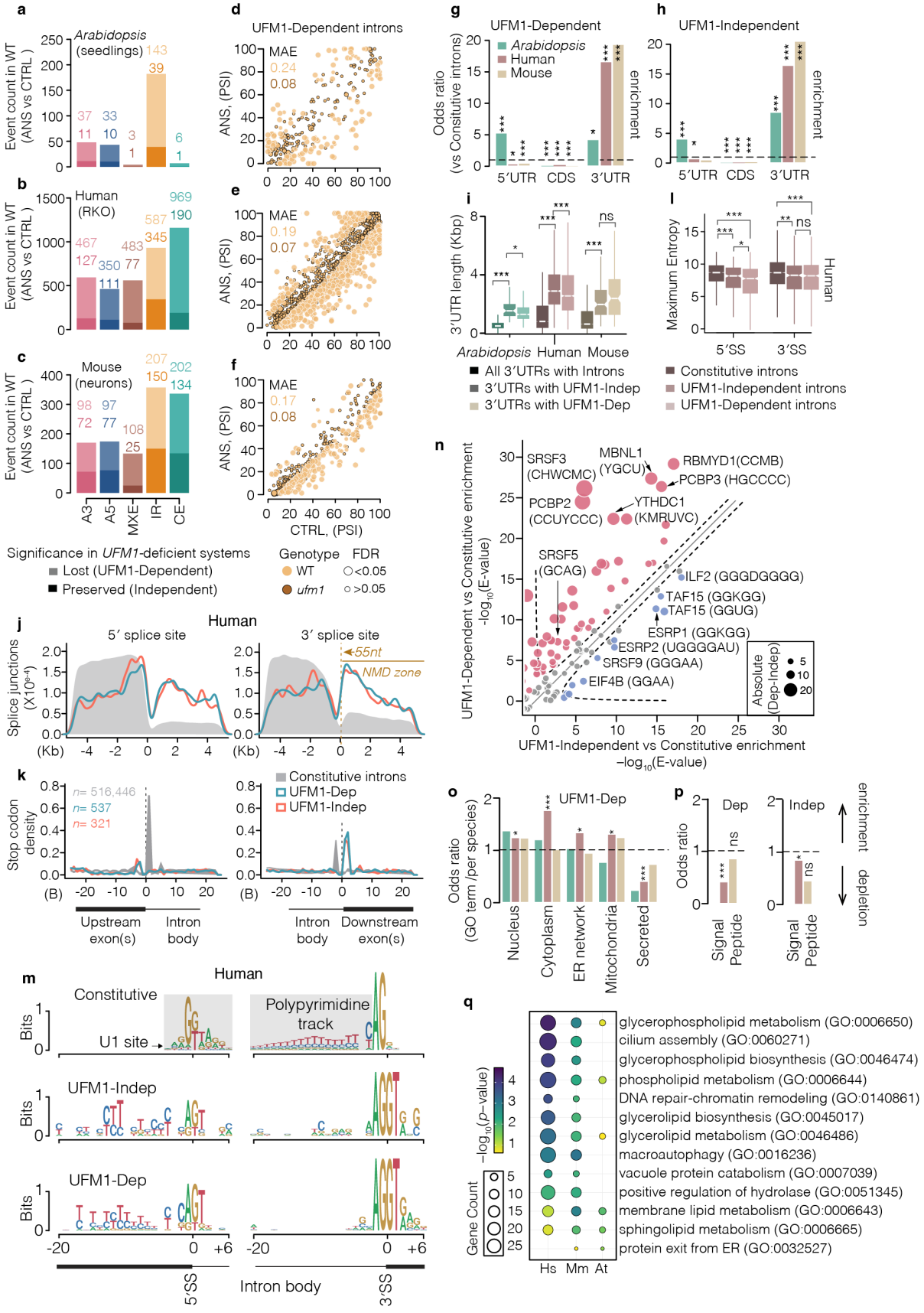


**Figure 4 | A conserved UFM1-dependent program of intron retention targets a distinct RNA landscape. a–c**, Quantification of alternative splicing changes induced by anisomycin (ANS)-mediated ribosome stalling in nuclear RNA from *Arabidopsis thaliana* seedlings (**a**) and human RKO cells (**b**), and total RNA from mouse neurons (**c**). Significant events were identified in wild-type (WT) samples using rMATS (FDR $< 0.05$) with an absolute change in percent spliced-in ($|\Delta\text{PSI}| > 0.1$), for all event types except cassette exons ($|\Delta\text{PSI}| > 0.2$). Events detected in WT but absent in *UFM1*-deficient systems (human *UFM1* knockout, mouse *Ufm1* knockout, and *Arabidopsis ufm1* knockout) were classified as UFM1-dependent (light shading); events in both WT and *UFM1*-deficient backgrounds were classified as UFM1-independent (dark shading). Event type: A3, alternative $3'$ splice site; A5, alternative $5'$ splice site; MXE, mutually exclusive exons; IR, retained intron; CE, cassette exon. **d–f**, Scatter plots comparing percent spliced-in (PSI) value under control and ANS conditions for UFM1 dependent intron retention events. WT events are shown in yellow, and events in *UFM1*-deficient systems are shown in dark yellow with black outlines; dot size reflects the False Discovery Rate (FDR). Mean Absolute Error (MAE) values summarize global splicing shifts per genotype. **g, h**, Genomic distribution of UFM1-dependent (**g**) and independent (**h**) retained introns across $5'$ untranslated regions (UTRs), coding sequences (CDS), and $3'$UTRs. Odds ratios calculated relative to constitutive introns. Ribosome stalling-dependent intron removal is significantly enriched in $3'$ untranslated regions ($3'$UTRs) (Fisher's exact test; $^{*}P < 0.05$, $^{**}P < 0.001$, $^{***}P < 0.0001$). **i**, Length distribution of $3'$UTRs colored by species and shaded by type: all $3'$UTRs with introns (dark shade), $3'$UTRs with UFM1-independent IRs (medium shade), and $3'$UTRs with UFM1-dependent IRs (light shade). The $3'$UTRs undergoing stalling-induced intron retention are significantly longer than all $3'$UTRs with constitutive introns in the genome (Wilcoxon rank-sum test; $^{*}P < 0.05$, $^{**}P < 0.001$, $^{***}P < 0.0001$). **j, k**, Metagene profiles of splice junction coverage (**j**) and stop codon density (**k**) relative to intron position. Compared with constitutive introns (grey), which are efficiently spliced and typically reside downstream of stop codons (canonical $3'$UTR introns), UFM1-dependent (green) and independent (orange) introns retain junction coverage and are enriched for premature termination codons near the $3'$ splice site. Persistence junction signal downstream of the 55-nucleotide nonsense-mediated decay (NMD) boundary (yellow line) indicates these introns are potentially sensitive to NMD. Kb: Kilobases; B: Bases. **l**, Splice site strength quantified by maximum entropy (MaxEnt) scores. Both UFM1-dependent and independent introns display weaker $5'$ and $3'$ splice sites compared with constitutive introns (Wilcoxon rank-sum test; $^{***}P < 0.0001$), with UFM1-dependent introns exhibiting significantly weaker $5'$ splice sites. **m**, Sequence logos of nucleotide composition surrounding the $5'$ and $3'$ splice sites. UFM1-dependent introns characterized by a conserved $5'$ exonic CAG motif and C-rich sequences (see (Fig. S7e–g) for nucleotide probability). **n**, Comparison of RNA-binding protein (RBP) motif enrichment in UFM1-dependent versus UFM1-independent introns relative to constitutive introns from human. The diagonal indicates equal enrichment ($y = x$). Dashed curves denote hyperbolic significance thresholds ($y = x + c + k/x$, where $c = 1.0$ and $k = 1.5$). Dot size represents the absolute difference in $-\log_{10}$(E-value) between UFM1-dependent and UFM1-independent enrichments. UFM1-dependent introns are preferentially enriched for CAG and C-rich motif-binding RBPs (e.g., SRSF3, YTHDC1, SRSF5); UFM1-independent introns enriched for G-rich binding factors (e.g., ILF2, TAF15). **o, p**, Subcellular localization (**o**) and signal peptide (**p**) analyses of transcripts containing stalling-induced introns. Colored according to key in **Fig. 4g**. Both UFM1-dependent and independent targets are depleted for secretory pathway annotations and signal peptides (Fisher's exact test; $^{*}P < 0.05$, $^{***}P < 0.0001$). **q**, GO enrichment analysis of UFM1-dependent transcripts shows overrepresentations of biological processes related to membrane lipid metabolism and endomembrane-associated processes rather than protein secretion. **Fig. S6 and S7 on page 33 and 35**

What distinguishes UFM1-dependent introns? Focusing on introns whose retention was reduced in *ufm1* mutants, we identified a distinct RNA signature: even weaker 3′ splice sites, a conserved 5′ exonic CAG motif, and CT-rich sequences (Fig. 4m and Fig. S7e–i). Motif analysis in human cells predicted that these features facilitate recognition by SR proteins including SRSF3 and SRSF5, as well as the m$^6$A reader YTHDC1 (Fig. 4n), suggesting selective regulation of mRNA splicing in UFM1-dependent manner.

Functional annotation revealed that genes affected by UFM1-dependent IR events were enriched for membrane lipid metabolism and endomembrane-associated processes but depleted for secreted proteins (Fig. 4o–q). In contrast, UFM1-independent events were enriched for spliceosome and RNA-processing components (Fig. S7j, k). This functional divergence suggests that UFMylation imposes a selective layer of regulation on transcripts encoding ER-remodeling machinery.

Together, these results demonstrate that ribosome stalling induces a conserved, UFM1-dependent splicing program defined by a unique RNA signature and enriched for membrane-associated cellular processes. By sequestering splicing factors at the ER, UFMylation couples translational stress to nuclear mRNA processing, selectively reshaping the expression of membrane-associated genes, likely leading to membrane remodeling.

## Discussion

Our findings establish UFMylation as a retrograde signaling system that couples ER translational stress to nuclear gene expression. By anchoring SR splicing factors at stalled ribosomes, UFMylation creates a spatial regulatory axis between the ER and nucleus that reprograms the splicing landscape (Fig. 5). The conservation of this pathway from plants to mammals suggests it represents a fundamental adaptation for coordinating membrane homeostasis with translational surveillance. This mechanism operates in parallel to the canonical Unfolded Protein Response but acts post-transcriptionally rather than through transcriptional reprogramming. The conservation of this pathway from plants to mammals suggests it represents a fundamental adaptation for coordinating membrane homeostasis with translational surveillance. While the three UPR branches (IRE1, PERK, and ATF6) restore ER homeostasis primarily through transcriptional reprogramming or translational attenuation[42,43], the UFMylation-SR axis enables post-transcriptional adjustment of gene expression. This distinction has important implications: whereas UPR activation requires sustained stress to trigger transcriptional programs, UFMylation-mediated splicing changes can occur rapidly upon ribosome stalling, potentially providing a faster adaptive response. The bidirectional intron retention we observe is consistent with altered nuclear availability of SR factors. SR proteins regulate alternative splicing in a concentration-dependent manner[34], and UFM1-dependent ER retention of RSZ22 (Fig. 2–3) reduces its nuclear abundance, potentially shifting the stoichiometric balance among nuclear SR family members[44–46]. Consistent with this hypothesis, the enrichment of SR-binding motifs among UFM1-dependent targets supports a direct mechanistic link between SR protein sequestration and splicing outcomes (Fig. 4n).

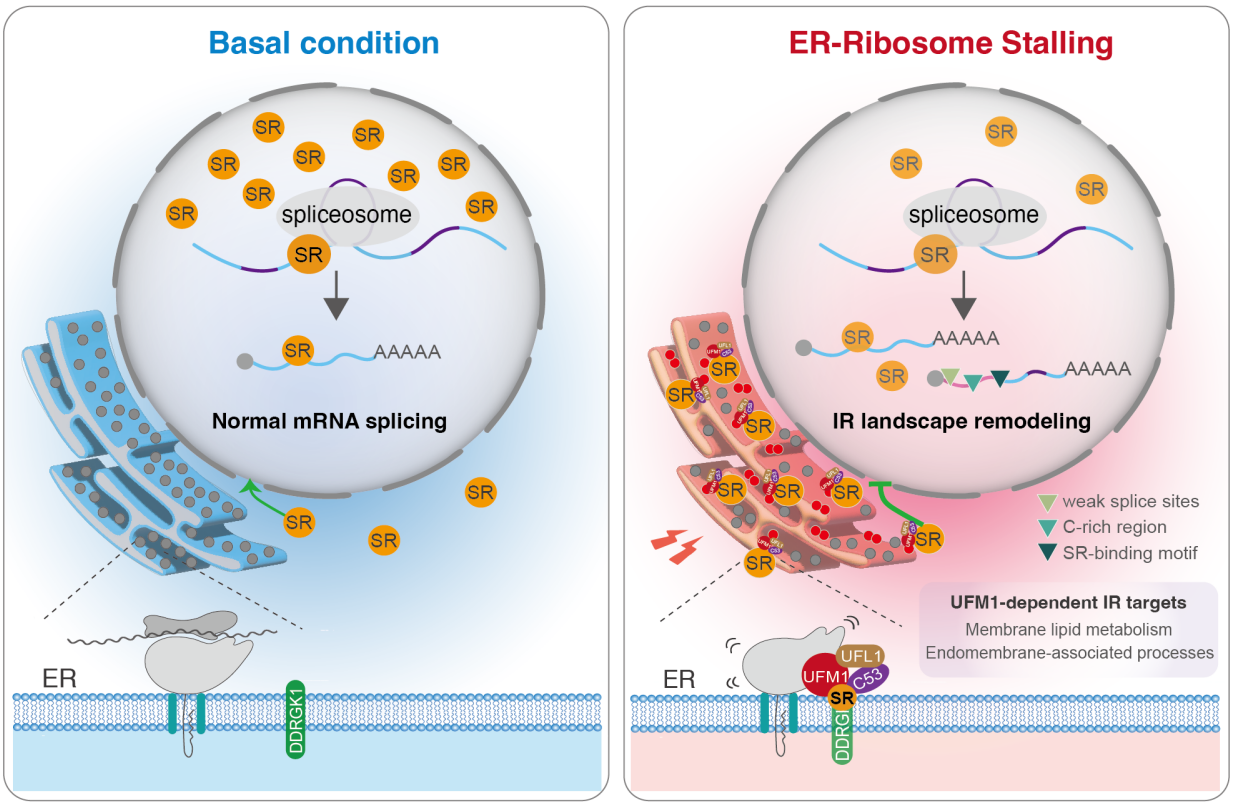



**Figure 5 | Working model of UFM1-dependent spatial retention coupling ER-translational stress to nuclear splicing.** Under basal conditions, SR shuttling proteins circulate between the ER and nucleus, supporting normal constitutive splicing. Under translational stress, activation of UFMylation at the translocon converts the ER-bound ribosomes into a docking platform, resulting in spatial retention of specific SR splicing factors (e.g., RSZ22) at the ER membrane, depleting their nuclear pool and remodeling the intron retention landscape of transcripts enriched for ER-related functions (e.g., membrane lipid metabolism and endomembrane-associated processes). UFM1-dependent introns are defined by a conserved RNA signature (weak splice sites, C-rich region, SR-binding motif). ER, endoplasmic reticulum; SR, serine/arginine-rich.

The functional significance of UFM1-dependent splicing changes is underscored by convergent evidence across independent datasets. Cross-species analysis reveals that UFM1-responsive intron retention events are consistently enriched in pathways governing membrane lipid metabolism and endomembrane-associated processes (Fig. 4q). This functional bias is mirrored at the evolutionary level, where UFM1 co-evolves with a broad network of membrane-remodeling genes (Fig. S1a, Table S8), and at the proteomic level, where the stress-responsive microsome proteome is enriched for membrane remodeling factors (Fig. 2b, Fig. S2c, Table S9). These observations suggest that UFMylation does not primarily reduce protein load entering the ER, as might be expected from a quality control pathway, but rather reshapes ER membrane composition to adapt to translational stress. This reframing positions UFMylation as a coordinator of membrane homeostasis rather than simply a ribosome rescue mechanism.

Our findings also provide a mechanistic framework for understanding the unexpected connections between UFMylation and neurological diseases. The identification of UFMylation components as modifiers of tau aggregation in iPSC-derived neurons initially seemed paradoxical[29,30], given tau's cytosolic localization. Our discovery that UFMylation controls nuclear splicing through SR protein sequestration resolves this paradox: disruption of UFMylation would alter the splicing landscape of numerous transcripts, potentially including those encoding factors that influence tau proteostasis (Table S7). More broadly, the diverse pathologies associated with UFMylation defects[27,28,47,48], including developmental abnormalities, metabolic dysfunction, and neurodegeneration, may reflect tissue-specific consequences of dysregulated splicing rather than solely defects in ribosome quality control. Our work reveals that ER-bound ribosomes serve not only as sites of protein synthesis and quality control but also as signaling platforms that communicate with the nucleus. The UFMylation-SR axis illustrates that organellar stress responses extend beyond local repair mechanisms to coordinate genome-wide changes in gene expression. While RSZ22 serves as a representative candidate, the extensive interactions within the SR family suggest it likely acts as part of a broader network subject to UFM1-dependent retention[33,49,50]. Whether other SR factors undergo similar retention and what molecular determinants govern their recognition remain key questions for future investigation. Given the essential role of UFMylation in development and its links to human disease, therapeutic modulation of this pathway, whether through targeting UFMylation itself or downstream splicing events, may offer new avenues for intervention in conditions characterized by ER stress.

## Materials and methods

### Plant materials and growth conditions

All *Arabidopsis thaliana* transgenic lines used in this study originate from the Columbia (Col-0) ecotype background and are listed in the materials section. Mutant lines used in this study are listed in the materials section.

Seeds were sterilized in 70% (v/v) ethanol with 0.5% (v/v) Tween-20 for 10 min, washed with absolute ethanol and sterile distilled water. After stratification at 4 °C for 2 days in the dark, seeds were germinated in liquid half-strength Murashige and Skoog (1/2 MS) medium containing Murashige and Skoog salt + Gamborg B5 vitamin mixture, 1% (w/v) sucrose, and 0.5 g $L^{-1}$ MES (pH 5.7). Seedlings were grown under a 16-h light/8-h dark photoperiod with a light intensity of 50 $\mu$mol $m^{-2}$ $s^{-1}$ with constant shaking at 90 rpm.

For chemical treatments, 7- to 10-day-old *Arabidopsis* seedlings grown in liquid 1/2 MS medium were treated with 100 $\mu$M anisomycin (ANS, Santa Cruz Biotechnology) or an equal volume of DMSO (control) for 4 h under continuous light with shaking at 90 rpm.

### Cloning and transgene construction

Coding sequences of *RSZ22* (At4g31580) and *THO6* (At2g19430) were amplified from Col-0 cDNA. PCR fragments were digested with *Bsa*I restriction enzyme and cloned into pMiniT 2.0 vectors with the same *Bsa*I site to generate intermediate constructs pMiniT-*RSZ22* and pMiniT-*THO6*. *Arabidopsis thaliana* transformation constructs were assembled using the GreenGate (GG) cloning system in the pGGSun backbone[51]. *E. coli* DH5$\alpha$ was used for plasmid propagation (Vienna BioCenter, in-house). All plasmids and primers used in this study are listed in the Materials section. Constructs were introduced into *Agrobacterium tumefaciens* strain GV3101 (C58 [RifR] Ti pMP90 [pTiC58DT-DNA] [gentR] Nopaline [pSoup-tetR]), all transgenic plants were generated using the floral dipping method[52].

The *ufm1* mutant and the transgenic lines include pUbi::DDRGK1-GFP/Col-0 and pUbi::mCherry were described

previously[4,53]. Double transgenic lines were generated by introducing constructs into existing transgenic backgrounds. Specifically, the pGGSun_Ubi10::*RSZ22*-mCherry and pGGSun_Ubi10::*THO6*-mCherry constructs were separately transformed into pUbi::DDRGK1-GFP/Col-0 plants to generate the pUbi::*RSZ22*-mCherry; pUbi::DDRGK1-GFP/Col-0 and pUbi::*THO6*-mCherry; pUbi::DDRGK1-GFP/Col-0 lines, respectively.

For experiments in the *ufm1* background, the pGGZ003::Ubi10_DDRGK1-GFP construct was introduced into pUbi::*RSZ22*-mCherry/*ufm1* and pUbi::*THO6*-mCherry/*ufm1* plants to obtain the respective double transgenic lines. Additionally, pUbi::DDRGK1-GFP; pUbi::mCherry double transgenic lines were generated by transforming the pGGZ003::Ubi10_DDRGK-GFP construct into pUbi::mCherry plants. All transgenic lines were confirmed by confocal microscopy or immunoblotting.

**Immunoblotting analysis in *Arabidopsis***

Total protein was extracted from 7-day-old *Arabidopsis* seedlings using Grinding Buffer (50 mM Tris-HCl, 150 mM NaCl, 1% Glycerol, 0.5% NP-40, 1.5 mM $MgCl_2$, 1 $\times$ Protease inhibitor cocktail (Roche)). Lysates were incubated on ice for 10 min and cleared by two rounds of centrifugation (16,000 $\times$ *g*, 10 min, 4 °C). Protein concentration was determined via the Bradford method using Coomassie Blue G-250 (Sigma-Aldrich). Equal amounts of proteins were mixed with SDS loading buffer (250 mM Tris-HCl pH 6.8, 10% SDS, 0.05% bromophenol blue, 30% glycerol, freshly supplied with 5% of $\beta$-mercaptoethanol), boiled at 95 °C for 10 min. 10 $\mu$g of total protein was loaded to the 4–20% Mini-PROTEAN TGX Precast Protein Gels (BioRad). Proteins were transferred to nitrocellulose membranes using a semi-dry Turbo Transfer Blot System (BioRad). Membranes were blocked with 5% skimmed milk in TBS and 0.1% Tween 20 (TBS-T) for 1 h at room temperature or overnight 4 °C and were subsequently incubated with primary antibody for 1 h at room temperature, followed by incubation with secondary antibody conjugated to horseradish peroxidase (HRP) for 1 h at room temperature. After three 10-min washes with TBS-T, signals were developed using Pierce ECL Western Blotting Substrate or ECL SuperSignal West Femto (Thermo Fisher Scientific) and visualized with a ChemiDoc Touch Imaging System (BioRad) or iBright Imaging System (Invitrogen). Images were processed using Image Lab software (BioRad).

Protein band intensities were quantified with ImageJ[54]. Rectangular regions of interest of equal size were defined around the target bands and the corresponding marker protein lanes (as internal controls for normalization). Band intensities were measured as the area under the peak from the generated profile. Target protein levels were normalized to the internal controls. Relative protein abundance was calculated from at least three biological replicates. The relative signal intensity of the control group samples was set as 1.0. The relative signal intensity of all other samples in each replicate was converted against the average signal intensity of the control sample. Data are presented as mean $\pm$ s.e.m.

Immunoblotting analyses were performed using the antibodies listed below, anti-AtC53, anti-GFP (Roche), anti-HsUFM1 (Abcam), anti-L13-1 (Agrisera), anti-UGPase (Agrisera), anti-CNX1/2 (Agrisera), anti-Nitrilase 1 (PhytoAB), anti-Histone H3 (Agrisera), anti-FLAG M2 (Sigma-Aldrich), and HRP-conjugated secondary antibodies (BioRad).

**Confocal microscopy and image analysis in *Arabidopsis***

Five-day-old *Arabidopsis* seedlings were used for confocal imaging. Seedlings were treated in liquid 1/2 MS supplemented with either DMSO (control) or 100 $\mu$M anisomycin (ANS) for 1 h prior to microscopy. *Arabidopsis* roots were imaged using a Zeiss LSM 800 upright confocal microscope equipped with an Apochromat 40$\times$ objective lens (2$\times$ digital zoom). GFP was excited at 488 nm and detected at 510 nm; mCherry was excited at 561 nm and detected at 610 nm. All imaging parameters, including laser power, pinhole diameter, and detector gain, were kept constant across samples to ensure quantitative comparability.

Confocal images were processed using the ZEN (blue edition) and ImageJ. To evaluate the spatial relationship between target proteins and ER, fluorescence intensity line profiles were generated using the Plot Profile plugin in ImageJ. For each treatment, a linear ROI (Region of Interest) was drawn across representative cellular structures. The resulting gray values for each channel were plotted against distance (pixels). Colocalization was defined by the spatial coincidence of fluorescence intensity peaks across two channels. To quantify the ER/Nucleus signal ratio, three regions of interest (ROIs) were randomly selected within the nucleus and the ER. The mean gray value was calculated for each ROI to determine the relative signal intensity. For each cell, each of the three ER values was

divided by all the nucleus values, and the mean of these three ratios was calculated as the representative signal ratio for that ROI. These three ROI-level ratios were then averaged to obtain a single value per cell. Quantification was performed on at least five representative images per treatment group, and the data are presented as mean $\pm$ s.e.m. from at least three biological replicates.

### *In planta* co-immunoprecipitation

For *in planta* Co-IP assays, 10-day-old *Arabidopsis* seedlings grown in liquid 1/2 MS medium were treated for 4 h in 1/2 MS liquid medium supplemented with DMSO (control) or 100 $\mu$M anisomycin (ANS). Approximately 1–2 g plant material was harvested, flash-frozen in liquid nitrogen, and homogenized into a fine powder. Proteins were extracted using Co-IP grinding buffer (50 mM Tris-HCl pH 7.5, 150 mM NaCl, 10 mM $MgCl_2$, 10% glycerol and 0.1% Nonidet P-40, $1\times$ Protease inhibitor cocktail) by vortexing. Plant lysates were cleared by multiple rounds of centrifugation (16,000 $\times$ *g*, 5 min, 4 °C). To minimize non-specific binding, lysates were precleared by incubation with 10 $\mu$L of Protein A Agarose (Roche) for 10 min at 4 °C. The protein concentrations were measured by Bradford assay. For each independent experiment, equal amounts of total protein across all samples and treatments were loaded for the Input analysis. For the pull-down, equal amounts of total proteins (2–3 mg) was incubated with 25 $\mu$L of RFP-Trap Magnetic Agarose beads (ChromoTek) for 2.5 h at 4 °C with gentle rotation within each experiment. Beads were washed six times with Co-IP buffer and bound proteins were eluted by boiling the beads in SDS loading buffer for 10 min at 95 °C. The resulting supernatants were analyzed by immunoblotting as described above with respective antibodies. Endogenous unmodified UFM1 (free form) was detected on the same membrane in the input fractions as an internal loading control, as its level remained stable across all treatments.

### Subcellular fractionation from Arabidopsis

*Microsome isolation*

Ten-day-old *Arabidopsis* seedlings grown in liquid 1/2 MS medium were treated for 4 h in 1/2 MS liquid medium supplemented with DMSO (control) or anisomycin (ANS) and subsequently harvested for microsome isolation using a modified protocol[55]. Briefly, 1.5–2 g seedlings were homogenized in liquid nitrogen and resuspended in 6 mL of microsome extraction buffer (MEB; 100 mM Tris-HCl pH 8.0, 5 mM EGTA, 15 mM $MgCl_2$, 2 $\mu$M DTT, 0.3 M sucrose (Sigma-Aldrich), 20 U $mL^{-1}$ SUPERase·In RNase Inhibitor (Thermo Fisher Scientific), 50 $\mu$ $mL^{-1}$ cycloheximide (Sigma-Aldrich), and $1\times$ Protease inhibitor cocktail). Homogenates were filtered with two layers of Miracloth and cleared by sequential centrifugation at 1,000 $\times$ *g* for 5 min and 8,000 $\times$ *g* for 10 min at 4 °C. Supernatant was layered on a step gradient (3 mL 0.6 M / 3 mL 1.7 M sucrose in MEB) in polyclear tubes (Laborgeraete Beranek), and centrifuged at 100,000 $\times$ *g* for 1.5 h at 4 °C using a TH-641 rotor (Sorvall Discovery SE Ultracentrifuge). The microsome fraction at the 0.6–1.7 M sucrose interface was collected into new polyclear tubes, diluted with 5 mL MEB buffer, and pelleted at 100,000 $\times$ *g* for 30 min at 4 °C to remove residue sucrose.

For mass spectrometry analysis, microsome pellets were precipitated following a trichloroacetic acid (TCA) precipitation method. Briefly, microsome pellets were resuspended in ultrapure water to a final volume of 1 mL, precipitated by adding 20 $\mu$L of 10% sodium deoxycholate (NaDOC, Sigma-Aldrich) and 100 $\mu$L of 50% TCA. Samples were vortexed thoroughly and incubated at $-20$ °C for 1 h to overnight. Proteins were pelleted by centrifugation at 16,000 $\times$ *g* for 30 min at 4 °C, washed with 1 mL of cold acetone, and pellets were air dried at room temperature. Protein pellets were further processed into peptides using the iST 96$\times$ kit (PreOmics) according to the manufacturer's instructions.

For immunoblotting, microsome pellets were first resuspended in 0.5 mL of dissolving buffer (50 mM Tris–HCl pH 7.5, 150 mM NaCl, 10 mM $MgCl_2$, 10% glycerol and 1% Nonidet P-40 supplemented with $1\times$ Protease inhibitor cocktail). Pellets were homogenized by pipetting and incubated with gentle rotation at 4 °C for 20–30 min to ensure complete protein recovery. Proteins were subsequently subjected to TCA-precipitation as described above. The resulting protein pellets were fully dissolved in the same dissolving buffer. Protein concentrations were determined using the Pierce BCA Protein Assay Kits (Thermo Fisher Scientific), and the sample pH was adjusted with Tris-HCl (pH 7.5) to ensure proper electrophoretic migration. Equal amounts of microsome protein were denatured and resolved by SDS-PAGE for subsequent immunoblotting.

*Nucleus isolation*

Subcellular fractionation of nuclei was performed with modifications based on a previously described protocol[56]. Ten-day-old *Arabidopsis* seedlings ($\sim$ 2g) grown in liquid 1/2 MS medium were treated for 4 h in the 1/2 MS liquid medium supplemented with DMSO or anisomycin. Seedlings were harvested, ground into fine powder in liquid nitrogen, and immediately resuspended in 5 mL of Honda buffer (0.44 M Sucrose, 1.25% Ficoll (Carl ROTH), 2.5% Dextran T40 (PanReac AppliChem), 20 mM HEPES, pH 7.4, 10 mM $MgCl_2$, 0.5% Triton X-100, 1 mM DTT, 1 $\times$ Protease inhibitor cocktail and RNaseOUT nuclease inhibitor (Thermo Fisher Scientific)). The homogenate was filtered through two layers of Miracloth and centrifuged at 2,000 $\times$ *g* for 5 min at 4 °C to pellet nuclei. Supernatant was further centrifuged at 14,000 $\times$ *g* for 5 min at 4 °C. This step was repeated twice to remove residual nuclear contaminants, and the final supernatant was collected as the cytoplasmic fraction.

For isolation of the nuclear fraction, the pellet obtained after the initial 2,000 $\times$ *g* centrifugation was resuspended in 15 mL Honda buffer and centrifuged again at 2,000 $\times$ *g* for 5 min at 4 °C. The pellet was resuspended and washed once more with 10 mL of Honda buffer and centrifuged. The final nuclear pellet was resuspended in 1 mL of Honda buffer and transferred to a new RNase/DNase-free 1.5 mL microcentrifuge tube, followed by centrifugation at 8,000 $\times$ *g* for 1 min at 4 °C. The resulting pellet was resuspended in 500 $\mu$L of Honda buffer for subsequent mass spectrometry and immunoblotting analyses. For nucleus mass spectrometry analysis, samples were processed using the TCA precipitation method followed by peptide purification using the iST 96$\times$ kit (PreOmics), as described above for microsome isolation.

*Sucrose gradient fractionation of ribosomes for biochemical analysis in Arabidopsis*

Sucrose gradient fractionation was performed with modifications based on previously described methods[39,57]. Seven-day-old *Arabidopsis* seedlings ($\sim 0.5$ g) grown in liquid 1/2 MS medium were harvested and ground into a fine powder in liquid nitrogen. The powder was resuspended in $150$ $\mu$L of protein extraction buffer (PEB; 0.1 M Tris–HCl pH 8.0, 40 mM KCl, 2.5 mM $MgCl_2$, 0.4% polyoxyethylene-10-tridecyl ether (PTE, Sigma-Aldrich), 0.4% detergent mix (20% Triton, 20% Tween-20, 20% Brij-35 (Sigma-Aldrich), 0.4% sodium deoxycholate, 1 mM DTT, $100$ $\mu$g mL$^{-1}$ cycloheximide). Samples were incubated on ice for 10 min with constant vortex to ensure resuspension. Cell debris was removed by centrifugation at $21,000 \times g$ for 10 min at 4 °C. The supernatant was transferred to a new tube, and the clarification step was repeated three times. Equal amounts of RNA ($\sim 200$ $\mu$g) were adjusted to a final volume of $220$ $\mu$L. RNase I (Ambion, Thermo Fisher Scientific) was added at a ratio of $1$ $\mu$L per $100$ $\mu$g of total RNA, and samples were digested for 1 h 15 min at 4 °C with gentle rotation. Digestion was terminated by centrifugation and addition of $0.5$ $\mu$L SUPERase•In RNase Inhibitor.

A total of $200$ $\mu$L of each sample was loaded onto 10–45% (w/v) sucrose gradient prepared in gradient buffer (24 mM Tris–HCl pH 8.0, 16 mM Tris–HCl pH 9.0, 40 mM KCl, 10 mM $MgCl_2$, 1 mM DTT and $100$ $\mu$g mL$^{-1}$ cycloheximide). Gradients were centrifuged at $35,000$ rpm for 3 h at 4 °C using an SW-40 Ti rotor (Beckman Coulter Optima L-90K ultracentrifuge) or at $35,700$ rpm for 3 h at 4 °C using a TH-641 rotor (Sorvall Discovery SE ultracentrifuge).

Gradients were fractionated using a top-down Biocomp Piston Gradient Fractionator (Biocomp) equipped with a Triax UV detector and flow cell. UV ($A_{260}$) absorbance across 10–45% sucrose gradients was continuously monitored, and fractions (0.5 mL per tube) were collected and stored on ice or flash-frozen in liquid nitrogen until further processing. Peaks corresponding to the 60S subunit, monosome, and disome were collected for subsequent mass spectrometry or immunoblotting analyses.

For ribosome-associated mass spectrometry, individual or pooled fractions corresponding to 60S, monosome, or disome peaks were flash frozen in liquid nitrogen and processed using TCA precipitation, followed by tryptic digestion and purification using the iST 96$\times$ kit, as described above. For ribosome SDS-PAGE and immunoblotting, each 0.5 mL fraction was adjusted to a final volume of $1$ mL with ultrapure water and subjected to TCA-precipitation. Protein pellets were resuspended and denatured. Equal volumes of ribosome-containing fractions were loaded for immunoblotting, whereas ribosome-free fractions (free) were loaded at one-fifth of the volume used for the ribosome-containing fractions.

**Mass spectrometry data acquisition and analysis**

All samples submitted for mass spectrometry were prepared using the iST 96× kit. 16 h and time-course pooled ribosome mass spectrometry samples, and the nucleus mass spectrometry samples were processed using the Orbitrap Exploris 480 mass spectrometer. 4 h ribosome mass spectrometry samples were processed using the Eclipse mass spectrometer. Orbitrap Exploris 480 and Eclipse mass spectrometer was operated in data-dependent mode, performing a full scan. Microsome mass spectrometry samples were processed using the timsTOF HT mass spectrometer. The timsTOF HT was operated in DIA mode where 1 MS1 scan was followed by 8 DIA-PASEF ramps.

*nanoLC-MS/MS Analysis for data-dependant acquisition (DDA)*

The nano HPLC system (UltiMate 3000 RSLC nano system or Vanquish Neo UHPLC-System, Thermo Fisher Scientific) was coupled to an Orbitrap Exploris 480 mass spectrometer equipped with a FAIMS pro interfaces and a Nanospray Flex ion source (all parts Thermo Fisher Scientific). Peptides were loaded onto a trap column (PepMap Acclaim C18, $5$ mm $\times$ $300$ $\mu$m ID, $5$ $\mu$m particles, $100$ Å pore size, Thermo Fisher Scientific) at a flow rate of $25$ $\mu$l min$^{-1}$ using $0.1\%$ TFA as mobile phase. After 10 minutes, the trap column was switched in line with the analytical column (PepMap Acclaim C18, $500$ mm $\times$ $75$ $\mu$m ID, $2$ $\mu$m, $100$ Å, Thermo Fisher Scientific or $\mu$Pac 110cm generation 2 micropillar column, Pharmafluidics) operated at $30$ °C (PepMap) or $50$ °C ($\mu$Pac). Peptides were eluted using a flow rate of $230$ nl/min, starting with the mobile phases $98\%$ A ($0.1\%$ formic acid in water) and $2\%$ B ($80\%$ acetonitrile, $0.1\%$ formic acid) and linearly increasing to $35\%$ B over the next 180 min.

The Orbitrap Exploris 480 mass spectrometer was operated in data-dependent mode, performing a full scan ($m/z$ range 350–1200, resolution 60,000, normalized AGC target $100\%$) at 3 different compensation voltages (CV -45, -60, -75), followed each by MS/MS scans of the most abundant ions for a cycle time of 0.8 seconds per CV. MS/MS spectra were acquired using HCD collision energy of 30, isolation width of 1.0 or 1.2 $m/z$, orbitrap resolution of 15,000, normalized AGC target $100\%$, minimum intensity of 25,000 and maximum injection time of 30 ms. Precursor ions selected for fragmentation (include charge state 2–6) were excluded for 40 s. The monoisotopic precursor selection filter and exclude isotopes feature were enabled.

The Eclipse was operated in data-dependent mode, performing a full scan ($m/z$ range 380–1500, Orbitrap resolution 120k, AGC target value 400,000, normalized AGC target $100\%$) at 4 different compensation voltages (CV -45, -55, -65, -75), followed each by MS/MS scans of the most abundant ions for a cycle time of 0.6 sec per CV. MS/MS spectra were acquired using an isolation width of 1.2 $m/z$, absolute AGC target value of 10,000, normalized AGC target $100\%$, minimum intensity of 5,000 and a maximum injection time of 35 ms, using the Iontrap for detection with HCD collision energy of 30. Precursor ions selected for fragmentation (including charge state 2–6) were excluded for 20 s. The monoisotopic precursor selection filter and exclude isotopes feature were enabled.

*Data Processing protocol for DDA Data*

For peptide identification, the RAW-files were loaded into Proteome Discoverer (version 2.5.0.400, Thermo Scientific). All MS/MS spectra were searched using MSAmanda v2.0.0.19924[58]. The peptide mass tolerance was set to $\pm 10$ ppm and fragment mass tolerance to $\pm 10$ ppm for measurements done on the Exploris and to $\pm 400$ mmu for measurements done on the Eclipse, the maximum number of missed cleavages was set to 2, using tryptic enzymatic specificity without proline restriction. Peptide and protein identification was performed in two steps. For an initial search the RAW-files were searched against the *Arabidopsis* taxonomy database (TAIR; 32,785 sequences; 14,482,855 residues), supplemented with common contaminants and sequences of tagged proteins of interest using Iodoacetamide derivative on cysteine as a fixed modification. The result was filtered to $1\%$ FDR on protein level using the Percolator algorithm integrated in Proteome Discoverer[59]. A sub-database of proteins identified in this search was generated for further processing. For the second search, the RAW-files were searched against the created sub-database using the same settings as above and considering the following additional variable modifications: oxidation on methionine, deamidation on asparagine and glutamine, glutamine to pyro-glutamate conversion at peptide N-terminal glutamine and acetylation on protein N-terminus. For some files phosphorylation on serine, threonine and tyrosine was included as variable modification in the search. The localization of the post-translational modification sites within the peptides was performed with the tool ptmRS, based on the tool phosphoRS[60]. Identifications were filtered again to $1\%$ FDR on protein and PSM level, additionally an Amanda score cut-off of at least 150 was applied. Proteins were filtered to

be identified by a minimum of 2 PSMs in at least 1 sample. Protein areas have been computed in IMP-apQuant by summing up unique and razor peptides[61]. Resulting protein areas were normalized using intensity-based absolute quantification (iBAQ) and sum normalization was applied for normalization between samples[62]. Match-between-runs (MBR) was applied for peptides with high confident peak area that were identified by MS/MS spectra in at least one run.

Proteins were required to be identified by a minimum of 2 PSMs in at least 1 sample, and quantified proteins were filtered to include at least 3 quantified peptide groups. The statistical significance of differentially expressed proteins was determined using the limma package[63].

*LC-MS/MS setup for Data independent Acquisition (DIA)*

Peptide samples were analyzed by the LC-MS/MS approach. The nano HPLC system used was an UltiMate 3000 nano HPLC RSLC (Thermo Scientific) equipped nano-electrospray source (CaptiveSpray source 1, Bruker Daltonics), coupled to a timsTOF HT mass spectrometer (Bruker Daltonics).

Peptides samples were injected on a pre-column (PepMap C18, $5$ mm $\times$ $300$ $\mu$m $\times$ $5$ $\mu$m, 100 Å pore size, Thermo Scientific) with $2\%$ ACN/water (v/v) containing $0.1\%$ TFA at a flow rate of $10$ $\mu$l min$^{-1}$ for 10 min. Peptides were then separated on the 25 cm Aurora ULTIMATE series HPLC column (CSI; $25$ cm $\times$ $75$ $\mu$m ID, $1.7$ $\mu$m C18, IonOpticks) operating at $50$ °C controlled by the Column Oven PRSO-V1-BR (Sonation), using UltiMate 3000 (Thermo Scientific Dionex). The analytical column flow was set to $300$ nL/min and the mobile phases water/$0.1\%$ FA and $80\%$ ACN/$0.08\%$ FA (A and B, respectively) were applied in the linear gradients starting from $2\%$ B: $2\%$–$10\%$ B in 10 min, $10\%$–$24\%$ B in 35 min, $24\%$–$35\%$ B in 15 min, $35\%$–$95\%$ B in 1 min, $95\%$ for 5 min, and finally the column was equilibrated in $2\%$ B for next 10 min (all % values are v/v; water and ACN solvents were purchased from Thermo Scientific at LC-MS grade).

The LC system was coupled with TIMS quadrupole time-of-flight mass spectrometer (timsTOF HT, Bruker Daltonics) and samples were measured in dia-PASEF mode. The CaptiveSpray source parameters were: $1600$ V of capillary voltage, $3.0$ L min$^{-1}$ of dry gas, and $180$ °C of dry temperature. MS data was acquired in the MS scan mode, using positive polarity, 100–1700 $m/z$ range, mobility range was set up from 0.64–1.42 V·s/cm$^2$, ramp time was set to 100 ms and estimated cycle time was 0.95 s. Collision energy was 27 eV at $1/k_0$ 0.85 V·s/cm$^2$, and 45 eV at $1/k_0$ 1.3 V·s/cm$^2$. Automatic calibration of ion mobility was set ON. The timsTOF HT was operated in DIA mode where 1 MS1 scan was followed by 8 DIA-PASEF ramps.

*Proteomics data analysis for DIA data*

DIA data was analysed in Spectronaut 18.7[64]. Trypsin/P was specified as a proteolytic enzyme and up to 2 missed cleavages were allowed in the Pulsar directDIA+ search. Dynamic mass tolerance was applied for calibration and main search. The search was performed against the *Arabidopsis* taxonomy database (TAIR; 32,785 sequences; 14,482,855 residues), with common contaminants (347 sequences) and common tags (28 sequences) appended. Here, Carbamidomethylation of cysteine was searched as fixed modification, whereas oxidation of methionine and acetylation at protein N-termini were defined as variable modifications. Peptides with a length between 7 and 52 amino acids were considered and results were filtered using Spectronaut default filtering criteria (Precursor Qvalue $< 0.01$, Precursor PEP $< 0.2$, Protein Qvalue $< 0.01$ per Experiment and $< 0.05$ per Run, Protein PEP $< 0.75$). Quantification was performed as specified in Biognosys BGS Factory Default settings, grouping Peptides by Stripped Sequence and performing protein inference using IDPicker. Cross-Run Normalization in Spectronaut was deactivated due to subsequent mode normalization.

Spectronaut results were exported using Pivot Reports on the Protein and Peptide level and converted to Microsoft Excel files using our in-house software MS2Go. For DIA data MS2Go utilizes the python library msReport (developed at the Max Perutz Labs Proteomics Facility) for data processing. Abundances were normalized by the mode of protein ratios in msReport and missing values were imputed with values obtained from a log-normal distribution with a mean of 100. To compensate for different protein lengths, protein quantification was then normalized using iBAQ[62]. Statistical significance of differentially expressed proteins was determined using limma[63].

**Subcellular enrichment shifts quantification and functional categorization from Arabidopsis mass spectrometry data**

To quantify subcellular enrichment shifts in response to anisomycin treatment, we compared $\log_2$ fold changes in normalized protein abundance between microsomal and nuclear fractions in both wild-type and *ufm1* mutant backgrounds. Only proteins detected in both compartments were retained to ensure comparability. For each protein, enrichment was defined as the difference in anisomycin-induced fold change between compartments (Anisomycin vs DMSO), calculated as: $\Delta$ enrichment = Microsome - Nuclear. This was computed separately for wild-type and *ufm1* mutants. To limit the influence of outliers, $\Delta$ enrichment values were winsorized to the range of $-1$ to $+1$. Proteins were categorized as microsome-enriched ($\Delta > 25\%$), nucleus-enriched ($\Delta < -25\%$), or no-shift ($-25\% \leq \Delta \leq 25\%$).

Gene Ontology (GO) annotations were retrieved from Ensembl Plants using the biomaRt package and filtered for RNA-related terms containing keywords including splicing, binding, export, decay, and processing. These GO terms were grouped into six RNA-related categories: RNA binding, RNA splicing, RNA processing, RNA decay and stability, RNA export, and RNA catabolic processes. Functional categories with fewer than ten proteins were not considered for statistical testing. For each category, the proportion of proteins in each enrichment class was calculated and visualized using stacked bar plots. Fisher's exact tests were used to assess whether category-specific enrichment patterns significantly deviated from the total proteome, and $P$-values were adjusted for multiple testing using the Benjamini-Hochberg method. In parallel, empirical cumulative distribution functions (ECDFs) of $\Delta$ enrichment values were generated using the base R `ecdf()` function to compare the distributional behavior of each RNA-related category against the global proteome. This allowed systematic evaluation of how protein localization patterns across RNA-associated functions are altered by stress and UFM1 pathway disruption.

**Human cell culture and cell line generation**

RKO-iCas9 cells (doxycycline-inducible Cas9) were cultured in RPMI-1640 media (Sigma) supplemented with $10\%$ fetal bovine serum (Gibco), $2$ mM L-Glutamine (Sigma), $1\%$ Penicillin-Streptomycin (Sigma), $1\times$ Non-Essential Amino Acids (Thermo Scientific), and $1$ mM sodium pyruvate (Gibco). Cell lines were grown in a humidified incubator at $37\,^{\circ}$C and $5\%$ $CO_2$ and regularly tested for *Mycoplasma* infection with the EZ-PCR™ Mycoplasma Detection Kit (Biological Industries).

RKO-iCas9 cells expressing sgRNAs against the non-coding locus *AAVS1* were generated in[65] and were a kind gift from the Gijs Versteeg lab. RKO-iCas9 cells expressing sgRNAs against *UFM1* were generated in our previous study[19]; gRNA sequences 5′-CGACGTCAGCGTGATCTTAA-3′ and 5′-ACACTTTGTACGGCAGCCGT-3′ were used to target the *UFM1* gene. The parental RKO-iCas9-GFP cell line was a kind gift from the Johannes Zuber lab[66].

**Cytoplasmic and nuclear fractionation of human cells for RNA and protein analysis**

$0.75$ million RKO-iCas9 cells were plated per 6-well plate. To induce Cas9 expression, $250$ ng mL$^{-1}$ doxycycline was added at the time of seeding. DMSO in 1:2000 dilution was used as a control. 72 h after doxycycline induction, cells were treated with $200$ nM anisomycin (ANS) for 1 h followed by fractionation of cytoplasmic and nuclear RNA according to the published protocol[67] with modifications. Cells were washed with ice-cold phosphate-buffered saline (PBS) and lysed on the plate in $335$ $\mu$L of $0.1\%$ NP-40 in $1\times$ PBS. Plates were incubated on ice for 5 min and lysates collected by scraping. Samples were pipetted 5 times, transferred to 1.5 mL Eppendorf tubes, and pipetted 2 additional times. $30$ $\mu$L were transferred to a separate tube for immunoblotting analysis (whole cell lysate).

Cell lysates were centrifuged at $3,000\times g$ for 2 min at 4 °C. $250$ $\mu$L of supernatant were transferred to 1.5 mL Eppendorf tubes for a second round of centrifugation at $3,000 \times g$ for 2 min at 4 °C. $130$ $\mu$L of supernatant (cytosolic fraction) were transferred to 1.5 mL Eppendorf tubes. $30$ $\mu$L were transferred to a separate tube for immunoblotting analysis and $100$ $\mu$L were kept for RNA extraction. The nuclear pellet was washed with $1$ mL of $0.1\%$ NP-40 in $1\times$ PBS and centrifuged at $3,000 \times g$ for 2 min at 4 °C. After removal of the supernatant, the pellet was used for RNA extraction or dissolved in $1\times$ SDS sample buffer (50 mM Tris-HCl pH 6.8, $2\%$ SDS, $0.1\%$ Bromophenol blue, $10\%$ glycerol, $20$ mM DTT) for immunoblotting analysis. The following antibodies were used for immunoblotting: anti-UFM1 (Abcam) at 1:2000, anti-lamin A/C (Santa Cruz) at 1:1000, anti-eEF2 (Proteintech) at 1:10000, and IgG (H+L), HRP Conjugates (Promega).

### Mouse lines and primary hippocampal neuronal culture

Mouse lines were maintained in the animal facility of the Max Planck Institute for Multidisciplinary Sciences. The *Ufm1*-cKO mouse line, which carries loxP sites $5'$ of exon $3$ and $3'$ of exon $5$ of the *Ufm1* gene, was obtained from GemPharmatech. The physiological consequences of Cre-induced *Ufm1*-loss in cultured neurons were described previously[28]. The line was kept in a homozygous mutant state. Animals homozygous for *Ufm1*-cKO were viable, fertile, and exhibited no overt phenotypic changes in the cage environment.

We have complied with all relevant ethical regulations for animal use and received ethical approval from the Niedersächsisches Landesamt für Verbraucherschutz und Lebensmittelsicherheit (LAVES). Mouse breeding was done with permission of the LAVES and according to European Union Directive 2010/63/EU. Mice were housed in individually ventilated cages with bedding and nesting material in specific pathogen-free conditions at $21$ °C and $55\%$ relative humidity, under a $12$ h/$12$ h light/dark cycle. Mice received food and water *ad libitum*. Health monitoring was done quarterly following FELASA recommendations with either NMRI sentinel mice or animals from the colony. All mice used for experiments were sacrificed by decapitation on their day of birth. Animals from both sexes were used without further distinctions.

Mouse primary hippocampal neuron cultures were prepared as described previously[28,68,69]. Briefly, brains of newborn mice were dissected, and hippocampi were isolated and digested for $1$ h at $37$ °C in Dulbecco's modified Eagle's medium (DMEM) containing $2.5$ U mL$^{-1}$ papain (Worthington Biomedical Corporation), $0.2$ mg mL$^{-1}$ L-cysteine, $1$ mM $CaCl_2$, and $0.5$ mM EDTA. Papain digestion was stopped by incubation with DMEM supplemented with $10\%$ (v/v) heat-inactivated fetal bovine serum (FBS), $2.5$ mg mL$^{-1}$ albumin, and $2.5$ mg mL$^{-1}$ trypsin inhibitor. Hippocampi were triturated in Neurobasal medium (Neurobasal medium-A) containing $2\%$ (v/v) B27, $2$ mM Glutamax, $100$ U mL$^{-1}$ penicillin and $100$ $\mu$g mL$^{-1}$ streptomycin and subsequently grown in this medium. Neurons were seeded in Poly-L-Lysine (PLL)-coated plates, using cells from two hippocampi ($\sim$ $150,000$ cells) per $6$ cm plate for protein and RNA extraction experiments. The day of dissection was counted as day *in vitro* 0 (DIV 0). At DIV 1, primary hippocampal neurons were infected with viruses expressing either RFP as control, or CRE-RFP to ablate UFM1 expression. Anisomycin (ANS) was obtained from SIGMA and dissolved in DMSO and flash frozen. Neurons were treated with $20$ $\mu$M ANS or DMSO for $2$ h. All other reagents were obtained from Gibco or Sigma-Aldrich, unless stated otherwise.

### Immunoblotting analysis of mouse neurons

Cells were washed with PBS, lysed in RIPA buffer ($150$ mM NaCl, $1\%$ (v/v) Triton X-100, $0.1\%$ (v/v) SDS, $20$ mM Tris pH $7.4$–$7.7$) with protease inhibitors ($1$ $\mu$g mL$^{-1}$ aprotinin, $0.5$ $\mu$g mL$^{-1}$ leupeptin, $17.4$ $\mu$g mL$^{-1}$ PMSF) and $20$ mM N-Ethylmaleimide (NEM) to prevent de-UFMylation. Protein concentration was determined using the Bradford method (Biorad). Proteins were then heated in a sample buffer at $65$ °C for $20$ min.

SDS-PAGE was performed with standard discontinuous gels or with commercially available $4\%$–$12\%$ Bis-Tris gradient gels (Invitrogen). Blot transfers were done using nitrocellulose membranes, according to standard procedures. Reversible MemCode protein staining (ThermoFisher) was performed to determine the total protein amount. Blots were blocked with a blocking buffer (PBS containing $5\%$ (w/v) milk and $1\%$ (v/v) Tween) and probed using primary and secondary antibodies diluted in blocking buffer. Blots were developed using enhanced chemiluminescence (GE Healthcare). Chemoluminescent signals were detected using the INTAS ECL Chemostar Imager. MemCode protein stain and blot images were analyzed using Fiji.

### RNA extraction and library preparation

Cytosolic and nuclear fractions from *Arabidopsis* and human RKO cells were homogenized and stored in TRIzol at $-80$ ℃ until further processing. RNA was extracted using the Direct-zol RNA Microprep Kit (Zymo Research) according to the manufacturer's instructions. Mouse neuronal cell samples stored in $300$ µL of DNA/RNA Shield were also kept at $-80$ ℃ until use. RNA from total cells of these samples was extracted using the Quick-RNA Miniprep Plus Kit (Zymo Research), following the recommended protocol. DNase I (NEB) treatment was performed during RNA isolation. Polyadenylated mRNA was enriched from total RNA using oligo(dT) magnetic beads (NEBNext Poly(A) mRNA Magnetic Isolation Module), followed by strand-specific library preparation using the NEBNext Ultra II Directional RNA Library Prep Kit for Illumina. All steps, including mRNA capture, first- and second-strand synthesis,

end repair, adaptor ligation, and library amplification, were performed according to the manufacturer's instructions. Library quality and fragment size distribution were assessed using an Agilent Fragment Analyzer. Final libraries were sequenced in single-end or paired-end $150$ bp mode on an Illumina NovaSeq X Plus system at Vienna Biocentre NGS facility.

**RNA-seq processing and splicing analysis**

Raw FASTQ files were preprocessed using Trim Galore with default settings to remove adapter sequences and low-quality bases. Trimmed reads were aligned using STAR[70] in two-pass mode to improve splice junction detection. For *Arabidopsis*, alignments were performed against a genome index generated using the TAIR10 primary assembly and the Ensembl Plants Release 56 GTF annotation. For human RKO, reads were aligned to the GRCh38 primary assembly using the GENCODE v45 annotation. For mouse, reads were aligned to the GRCm39 primary assembly using the Ensembl Release 112 annotation. Transcript-level quantification was performed using Salmon with strand-specific settings, using the aligned BAM files as input[71].

Aligned BAM files were sorted and indexed using samtools[72], and splice junction files from STAR were used as input for rMATS[73] to identify differential alternative splicing events between control and anisomycin-treated samples. rMATS was run in paired-end mode for *Arabidopsis* and human samples and in single-end mode for mouse samples, with strand-specific orientation and the variable read length option enabled. Splicing events were quantified across five canonical types: skipped exons (SE), alternative $5'$ and $3'$ splice sites (A5SS and A3SS), mutually exclusive exons (MXE), and retained introns (IR). Events were considered significant if they exhibited a false discovery rate (FDR) $< 0.05$ relative to wild-type and a difference in percent splice inclusion ($|\Delta$PSI$|$) of at least $20\%$ for SE events or $10\%$ for all other event types. To define UFM1-dependent splicing changes, we selected events that were significantly altered in wild-type (FDR $< 0.05$) but not in the UFM1 mutant background (FDR $> 0.05$) under anisomycin treatment. For downstream analysis splicing events identified by rMATS were mapped to host Ensembl gene identifiers by overlapping event coordinates with a transcript database (TxDb) constructed from species-specific GTF annotations using the GenomicRanges and GenomicFeatures R packages[74].

**Alternatively spliced transcripts characterization**

To characterize the structural and functional features of alternatively spliced transcripts, genomic coordinates of splicing events were overlapped with transcript models derived from the reference GTF. Spliced regions were classified in a strand-aware manner relative to the coding sequence (CDS): segments upstream of the CDS start were defined as $5'$ UTR, those overlapping the coding region as CDS, and those downstream of the CDS end as $3'$ UTR. In cases of isoform ambiguity, a consensus classification was assigned using a priority hierarchy (CDS $>$ $5'$ UTR $>$ $3'$ UTR $>$ non-coding $>$ intronic). Subsequently, subcellular localization and presence of signal peptide were evaluated by querying Ensembl BiomaRt[75]. The presence of signal peptides (analyzed for human and mouse) was determined by annotated "SignalP" start positions, while subcellular localization was assessed using Gene Ontology (GO) terms for major compartments (e.g., Nucleus, Mitochondria, Endoplasmic Reticulum). Enrichment odds ratios for these features were calculated using Fisher's exact test relative to the genomic background.

**Nonsense-mediated decay (NMD) susceptibility evaluation**

To predict susceptibility to Nonsense-Mediated Decay (NMD), the genomic architecture of retained introns (IR) was analyzed for Exon Junction Complex (EJC) proximity and Premature Termination Codon (PTC) density. EJC deposition sites were inferred using splice junction density as a proxy from GTF annotations; genomic distances were calculated from the IR boundaries to the centers of all other introns within the same transcript. Downstream splice junctions located $> 55$ bp from the stop codon were classified as potential NMD-triggering EJC sites[41]. Additionally, the local sequence context of the $5'$ and $3'$ splice sites ($\pm 20$ bp) was scanned for stop codon motifs (TAA, TAG, TGA) to quantify the density of potential PTCs introduced by the retention event.

**Splice site strength and motif analysis**

To evaluate the strength of splice signals, the Maximum Entropy Model implemented in MaxEntScan[76] was used to score $9$-nt $5'$ splice sites and $23$-nt $3'$ splice sites based on their adherence to position weight matrices derived from constitutive sites. Sequences flanking annotated junctions were extracted and processed using a Python wrapper.

The ggseqlogo R package[77] was used to visualize differences in consensus motif conservation between stalling-regulated retained introns and constitutive controls. Genomic sequences spanning the $5'$ donor ($20$ bp exonic, $6$ bp intronic) and $3'$ acceptor ($20$ bp intronic, $6$ bp exonic) junctions were extracted, with strand orientation computationally validated and corrected based on canonical GT-AG dinucleotides to ensure accurate alignment.

**Motif enrichment analysis**

Motif Enrichment Analysis of RNA-binding proteins (RBP) and splicing regulatory elements was performed using AME (Analysis of Motif Enrichment) from the MEME Suite[78], querying the CisBP-RNA database[79]. To establish a background control set, constitutive introns were extracted from human and mouse gene annotations. Sequences from UFM1-dependent and UFM1-independent splicing events were then individually tested for motif enrichment relative to this constitutive background. Analyses were restricted to specific genomic intervals: the 5′ splice site (spanning -20 exon/+6 intron nucleotides), the 3′ splice site (-20 intron/+6 exon nucleotides), and the remainder of the full intron body. Significant enrichment was determined based on E-values.

**Phylogenetic profiling of UFM1**

Eukaryotic proteins families co-evolving with UFM1 were identified as described previously[80,81]. Firstly, we assembled a dataset of genome-predicted proteomes representing diverse eukaryotic taxa, as described previously[21]. The resulting proteins were compared to one another using Diamond BLASTP $v2.1.11.165$ (ultra-sensitive, maximum 250 hits, percent identity $\geq 25\%$, $E < 10^{-5}$, query coverage $\geq 25\%$) and clustered based on similarity using MCL $v22.282$ using a variety of inflation parameters ($I = 1.4, 2, 4,$ and $6$)[82,83]. Initial clusters were established with an inflation value of 1.4, and clusters larger than 450 proteins were sub-divided based on higher inflation values when possible. To compensate for fragmented clusters, those with 20 assigned proteins or less were aligned using MAFFT $v7.520$ and profile hidden Markov Models (HMM) were generated[84,85]. These HMMs were used as queries to search the initial dataset using HMMER $v3.4$ ($E < 10^{-20}$) and small clusters were merged with larger clusters (at least 50 sequences) when homology was detected, resulting in a final set of protein families.

To identify protein families which correlate with the presence of UFM1, the distribution of UFM1 was assigned across taxa based on previous curation[21]. To account for taxon sampling, species represented within the database were subdivided into supergroups, and monophyletic groupings of UFM1 presence and absence were defined. To calculate phylogenetic correlations, the median protein number for protein families with representation from at least 25 species was determined across UFM1 presence/absence clades and point-biserial correlations (PBC) were used to identify correlation coefficients between binarized UFM1 presence and median protein number[86]. Correlation significance was assessed using permutation tests ($n = 100,000$) whereby protein families of equal size were generated through random sampling of the initial dataset without replacement. Given the independent generation of each test distribution, multiple test corrections were not applied. Correlating protein families were defined as those with a PBC $\geq 0.3$ and $P < 0.05$. The distribution of correlated protein families was visualized using ITOL $v6$[87].

To assess functional associations within UFM1-correlated protein families, all proteins included within the initial dataset were annotated with Gene Ontology (GO) terms. To this end, each protein was compared to the UniProt Knowledgebase using Diamond BLASTP (sensitive, maximum 100 hits, percent identity $\geq 25\%$, $E < 10^{-5}$, query coverage $\geq 50\%$) and annotated using the Pfam database using HMMER ($E < 10^{-5}$)[88,89]. Annotations were extracted from the resulting hits using Wei2Go[90]. GO-terms were assigned to individual protein families when at least $25\%$ of proteins within a given cluster received the annotation. To identify GO-enrichments, term frequencies were compared between UFM1-correlated subsets and all eukaryotic protein families, and significance was assessed using permutation tests ($P < 0.01, n = 100,000$).

**AlphaFold-Multimer Prediction**

Protein-protein interactions between the UFMylation machinery and co-evolved candidates ($P < 0.05$, PBC $\geq 0.3$) were predicted using AlphaFold-Multimer[91–93]. Predictions were executed using the ht-colabfold pipeline (`https://gitlab.com/BrenneckeLab/ht-colabfold`) on the Vienna BioCentre CLIP Batch Environment (CBE) cluster. Human protein sequences were retrieved from UniProt and supplied in FASTA format. Interaction confidence was assessed using the interface predicted TM-score (ipTM) and a custom PEAK score, calculated as the inverted and scaled (0 to 1) minimum Predicted Aligned Error (PAE) between chains, excluding intra-molecular interactions.

## Key resources

| Reagents/Resource | Source | Catalog number/ Identifier | Notes |
|---|---|---|---|
| **Experiment models** | | | |
| Col-0 | | | *A. thaliana* |
| *ufm1* | Stephani et al (2020) | AT1G77710 | *A. thaliana* |
| pUbi::*RSZ22*-mCherry | This study | | *A. thaliana* |
| pUbi::*RSZ22*-3×FLAG | This study | | *A. thaliana* |
| pUbi::*THO6*-mCherry | This study | | *A. thaliana* |
| pUbi::*THO6*-3×FLAG | This study | | *A. thaliana* |
| pUbi::*RSZ22*-mCherry; pUbi::DDRGK1-GFP/Col-0 | This study | | *A. thaliana* |
| pUbi::*RSZ22*-mCherry; pUbi::DDRGK1-GFP/*ufm1* | This study | | *A. thaliana* |
| pUbi::*THO6*-mCherry; pUbi::DDRGK1-GFP/Col-0 | This study | | *A. thaliana* |
| pUbi::*THO6*-mCherry; pUbi::DDRGK1-GFP/*ufm1* | This study | | *A. thaliana* |
| pUbi::DDRGK1-GFP; pUbi::mCherry | This study | | *A. thaliana* |
| pUbi::DDRGK1-GFP/Col-0 | Stephani et al (2020) | | *A. thaliana* |
| pUbi::mCherry | Zhao et al (2022) | | *A. thaliana* |
| HCT116 (Human colorectal carcinoma) | ATCC | CRL-2577 | Human |
| RKO-iCas9 *UFM1* KO | This study | | Human |
| RKO-iCas9 *AAVS1* control | This study | | Mouse |
| *Ufm1*-cKO | GemPharmatech | | Mouse |
| **Recombinant DNA for transgenics** | | | |
| pGGSun_Ubi10::*RSZ22*-3×FLAG | This study | | for *A. thaliana* |
| pGGSun_Ubi10::*THO6*-3×FLAG | This study | | for *A. thaliana* |
| pGGSun_Ubi10::*RSZ22*-mCherry | This study | | for *A. thaliana* |
| pGGSun_Ubi10::*THO6*-mCherry | This study | | for *A. thaliana* |
| **Antibodies** | | | |
| Rabbit polyclonal anti-AtC53 | Stephani et al (2020) | | 1:5000 |
| Goat anti-rabbit IgG HRP-Conjugate | Biorad | 1706515 | 1:10000 |
| Goat anti-mouse IgG HRP-Conjugate | Biorad | 1706516 | 1:10000 |
| Mouse monoclonal anti-GFP | Roche | 11814460001 | 1:5000 |
| Rabbit monoclonal anti-HsUFM1 | Abcam | Ab109305 | 1:3000 |
| Rabbit polyclonal anti-L13-1 | Agrisera | AS13 2650 | 1:1000 |
| Rabbit polyclonal anti-UGPase | Agrisera | AS14 2813 | 1:1000 |
| Rabbit polyclonal anti-CNX1/2 | Agrisera | AS12 2365 | 1:3000 |
| Rabbit polyclonal anti-Nitrilase 1 | PhytoAB | PHY2194S | 1:5000 |
| Rabbit polyclonal anti-Histone H3 | Agrisera | AS10 710 | 1:5000 |
| Mouse monoclonal anti-FLAG M2 | Sigma | F3165 | 1:3000 |
| Mouse monoclonal anti-lamin A/C | Santa Cruz | sc-376248 | 1:1000 |
| Rabbit polyclonal anti-eEF2 | Proteintech | 20107-1-AP | 1:10000 |
| Anti-Mouse IgG (H+L), HRP Conjugate | Promega | W4021 | 1:5000 |
| Anti-Rabbit IgG (H+L), HRP Conjugate | Promega | W4011 | 1:5000 |
| **Strains** | | | |
| DH5$\alpha$ (*E. coli*) | In-house facility | VBC | |
| GV3101 (pSoup) (*A. tumefaciens*) | In-house facility | VBC | |
| **Chemicals** / **Enzymes** | | | |
| Anisomycin | Santa Cruz | sc-3524 | |
| EDTA-free Protease Inhibitor Cocktail | Roche | 5056489001 | |
| Brilliant Blue G | Sigma | B0770 | |
| Cycloheximide | Sigma | C7698 | |
| Sucrose | Sigma | 84097 | |
| Nuclease-Free Water | Sigma | W4502 | |
| SUPERase·In RNase Inhibitor | Thermo Fisher | AM2696 | |
| Sodium deoxycholate | Sigma | 30970 | |
| Ficoll 400 | Carl ROTH | CN90.2 | |
| Dextran 40 BioChemica | PanReac | A2249 | |
| RNaseOUT Recombinant RNase Inhibitor | Thermo Fisher | 10777019 | |
| Polyoxyethylene-10-tridecyl ether | Sigma | P2393 | |
| Brij-35 | Sigma | 801962 | |
| Ambion RNase I | Thermo Fisher | AM2294 | |
| RPMI-1640 media | Sigma | R8758 | |
| Fetal bovine serum | Gibco | 10437028 | |
| L-Glutamine | Sigma | G7513 | |
| Penicillin-Streptomycin | Sigma | P0781 | |
| Non-Essential Amino Acids | Thermo Fisher | 11140050 | |
| Sodium pyruvate | Gibco | 11360070 | |
| DNase I | NEB | M0303S | |
| ERCC RNA Spike-In Mix | Thermo Fisher | 44565740 | |
| **Critical commercial assays** | | | |
| RFP-Trap Magnetic Agarose beads | ChromoTek | rtma-200 | |
| Protein A Agarose | Roche | 11719408001 | |
| Pierce BCA Protein Assay Kits | Thermo Fisher | 23227 | |
| iST 96x Kit | PreOmics | P.O.00027 | |
| Direct-zol RNA Microprep Kit | Zymo Research | R2060 | |
| Quick-RNA Miniprep Plus Kit | Zymo Research | R1507 | |
| NEBNext Poly(A) mRNA Magnetic Isolation | NEB | E7490L | |
| NEBNext Ultra II RNA Library Prep | NEB | E7760L | |

| Reagents/Resource | Source | Catalog number/ Identifier | Notes |
|---|---|---|---|
| **Software and algorithms** | | | |
| CLC main work bench 7 | Qiagen | | Cloning |
| Zen Software | Carl Zeiss | | Microscopy |
| Image J (Fiji) | NIH | | Quantification |
| Image Lab | BioRad | | Western Blotting |
| Adobe Illustrator 2022 | Adobe Inc. | | Graphics editing |
| MS2Go | Inhouse | ms.imp.ac.at | |
| RStudio 1.2.5019 | RStudio | | Graphics editing |
| AlphaFold-Multimer | Jumper et al., 2021 | github.com/alphafold | PPI prediction |
| ht-colabfold | | gitlab.com/ht-colabfold | AlphaFold pipeline |
| Trim Galore | Babraham | babraham.ac.uk | Adapter trimming |
| Python 3.10.13 | Python | python.org | Analysis |
| Numpy 1.26.4 | NumPy | numpy.org | Statistics |
| Scipy 1.12.0 | SciPy | scipy.org | Statistics |
| Pandas 2.2.3 | Pandas | pandas.pydata.org | Data processing |
| Profiling.py | In house | | Phylogeny script |
| Go_enrichment.py | In house | | GO-enrichment |
| STAR | Dobin et al., 2013 | github.com/STAR | RNA-seq align |
| Salmon | Patro et al., 2017 | github.com/salmon | Transcript quant |
| samtools | Danecek et al., 2021 | github.com/samtools | BAM processing |
| rMATS | Shen et al., 2014 | github.com/rmats | Splicing analysis |
| MaxEntScan | Yeo & Burge, 2004 | hollywood.mit.edu | Splice site scoring |
| MEME Suite (AME) | McLeay & Bailey, 2010 | meme-suite.org | Motif enrichment |
| biomaRt | Durinck et al., 2005 | Bioconductor | GO retrieval |
| GenomicRanges | Lawrence et al., 2013 | Bioconductor | Genomic intervals |
| GenomicFeatures | Lawrence et al., 2013 | Bioconductor | Transcript DB |
| ggseqlogo | Wagih, 2017 | CRAN/Bioconductor | Sequence logo |
| Diamond BLASTP v2.1.11 | Buchfink et al., 2021 | github.com/diamond | Seq comparison |
| MCL v22.282 | Enright, 2002 | micans.org/mcl/ | Protein clustering |
| MAFFT v7.520 | Katoh & Standley | mafft.cbrc.jp | Alignment |
| HMMER v3.4 | Mistry et al., 2013 | hmmer.org | HMM search |
| ITOL v6 | Letunic & Bork, 2024 | itol.embl.de | Tree visualization |
| Wei2Go | Reijnders, 2022 | N/A | GO extraction |
| **Databases and reference genomes** | | | |
| UniProt | UniProt Consortium | uniprot.org | Protein seqs |
| Ensembl Plants | Ensembl | plants.ensembl.org | *Arabidopsis* (Rel 56) |
| GENCODE | GENCODE Consortium | gencodegenes.org | Human (v45) |
| Ensembl | Ensembl | ensembl.org | Mouse (Rel 112) |
| CisBP-RNA | Rosado-Tristani 2025 | cisbp-rna | RBP motif DB |
| Gene Ontology (GO) | GO Consortium | geneontology.org | Func annotation |
| TAIR10 | Ensembl Plants | *A. thaliana* primary assembly | *Arabidopsis* ref |
| GRCh38 | GENCODE | *H. sapiens* primary assembly | Human ref |
| GRCm39 | Ensembl | *M. musculus* primary assembly | Mouse ref |
| Pfam | Mistry et al., 2021 | pfam.xfam.org | Domain annotation |

## Code availability

All custom code generated in this study for visualization, statistical analysis, and feature analysis is available at https://github.com/Papareddy/UFMylation_Ribosome_stalling_RNA_Splicing. Primary bioinformatics scripts were developed using human intelligence and subsequently streamlined via the Antigravity agentic framework (using Gemini or Claude Code) for redundancy mitigation.

## Data availability

All RNA sequencing data generated in this study are available at the National Center for Biotechnology Information Gene Expression Omnibus (NCBI GEO, https://www.ncbi.nlm.nih.gov/geo/) under accession number GSE325905. The mass spectrometry proteomics data have been deposited to the ProteomeXchange Consortium via the PRIDE[94] partner repository with the dataset identifier PXD075540. All the raw data are available via Zenodo https://doi.org/10.5281/zenodo.19305729.

## Acknowledgements

We thank Vienna Biocenter Core Facilities (VBCF), particularly Proteomics, NGS, BioOptics and Plant Sciences. Proteomics analyses were performed by the Proteomics Facility at IMP/IMBA/GMI using the VBCF instrument pool. We acknowledge the use of high-performance computing resources provided by the bwHPC initiative and the Vienna CLIP computing cluster. The computational results reported within this publication were made possible by these infrastructures. We acknowledge funding from Austrian Academy of Sciences, Austrian Science Fund (FWF, P34944, I 6760, SFB F79), Vienna Science and Technology Fund (WWTF, LS21-009), European Research Council Grant (Project number: 101043370), DFG Heisenberg Program (Project number: 541762498) and Research Grants (Project numbers: 566190050, 568404408), the German research Foundation (DFG; SFB1286-A09 to N.B and M.T.). Ni Zhan was supported by a Marie Skłodowska-Curie Individual Fellowship (Project number: 101028611). We thank Adrian Söderholm (Versteeg lab) for his assistance with cytoplasmic and nuclear RNA fractionation. We are grateful to D. Warnecke, C. Harenberg, and F. Benseler for their expert technical assistance in mouse genotyping, and the staff of the Max Planck Institute for Multidisciplinary Sciences Transgenic Animal Facility for the generation and maintenance of mouse colonies. We also thank Sally Wenger for her technical support in confocal imaging. We thank Marion Clavel for helpful comments on the draft. We thank all members of the Dagdas lab for their support and helpful discussions for this project.

## Author contributions

N.Z., R.K.P., and Y.D. conceived and designed the project. N.Z. generated and characterized *Arabidopsis* transgenic lines, optimized the ribosome fractionation approach, and performed plant-based experiments including stress treatments, western blotting, co-immunoprecipitation, microsome, nuclei, and ribosome isolations. N.Z. prepared all samples for LC-MS/MS, conducted initial proteomics data analysis and target identification and validation, integrated datasets, and wrote the manuscript with input from all the authors. R.K.P. and H.A. established the plant microsome isolation pipeline and N.Z. continued to optimize it. R.K.P. optimized the *Arabidopsis* nuclei and cytosol isolation workflow. R.K.P. and N.Z. performed *Arabidopsis* nuclei and cytosol isolation for RNA sequencing. R.K.P. prepared RNA samples and libraries and led the RNA sequencing and analysis workflow. B.E. performed *Arabidopsis* root confocal imaging analysis and assisted with *Arabidopsis* transgenic line characterization and western blotting. A.S.A. and M.M. generated the human knockout lines, purified the cytoplasmic and nuclear fractions, and performed western blotting. A.S.A. prepared RNA from human samples for RNA sequencing. M.T. and C.P. performed mouse primary neuron experiments; N.B. supervised the mouse neural cell project. N.A.T.I. performed phylogenetic profiling and analysis. R.K.P. designed the rest of the software for data analysis and data visualization. R.K.P. and N.Z. assembled the figures. G.E.K. supervised the human cell work and provided input on the manuscript. Y.D. supervised the project, secured funding, and led the manuscript preparation and revision. All authors reviewed and edited the manuscript.

## References

1. Hetz, C., Zhang, K. & Kaufman, R. J. Mechanisms, regulation and functions of the unfolded protein response. *Nat. Rev. Mol. Cell Biol.* **21**, 421–438, doi:10.1038/s41580-020-0250-z (2020).
2. van Anken, E., Bakunts, A., Hu, C.-C. A., Janssens, S. & Sitia, R. Molecular evaluation of endoplasmic reticulum homeostasis meets humoral immunity. *Trends Cell Biol.* **31**, 529–541, doi:10.1016/j.tcb.2021.02.004 (2021).
3. Wiseman, R. L., Mesgarzadeh, J. S. & Hendershot, L. M. Reshaping endoplasmic reticulum quality control through the unfolded protein response. *Mol. Cell* **82**, 1477–1491, doi:10.1016/j.molcel.2022.03.025 (2022).
4. Stephani, M. *et al.* A cross-kingdom conserved ER-phagy receptor maintains endoplasmic reticulum homeostasis during stress. *eLife* **9**, e58396, doi:10.7554/eLife.58396 (2020).
5. Mochida, K. & Nakatogawa, H. ER-phagy: selective autophagy of the endoplasmic reticulum. *EMBO Rep.* **23**, e55192, doi:10.15252/embr.202255192 (2022).
6. Karagöz, G. E., Acosta-Alvear, D. & Walter, P. The unfolded protein response: detecting and responding to fluctuations in the protein-folding capacity of the endoplasmic reticulum. *Cold Spring Harb. Perspect. Biol.* **11**, doi:10.1101/cshperspect.a033886 (2019).
7. Ferro-Novick, S., Reggiori, F. & Brodsky, J. L. ER-phagy, ER homeostasis, and ER quality control: implications for disease. *Trends Biochem. Sci.* **46**, 630–639, doi:10.1016/j.tibs.2020.12.013 (2021).
8. Brandman, O. & Hegde, R. S. Ribosome-associated protein quality control. *Nat. Struct. Mol. Biol.* **23**, 7–15, doi:10.1038/nsmb.3147 (2016).
9. Joazeiro, C. A. P. Mechanisms and functions of ribosome-associated protein quality control. *Nat. Rev. Mol. Cell Biol.* **20**, 368–383, doi:10.1038/s41580-019-0118-2 (2019).

10. Yip, M. C. J. & Shao, S. Detecting and rescuing stalled ribosomes. *Trends Biochem. Sci.* **46**, 731–743, doi:10.1016/j.tibs.2021.03.008 (2021).
11. Komatsu, M., Noda, N. N. & Inada, T. The mechanistic basis and cellular functions of UFMylation. *Nat. Rev. Mol. Cell Biol.*, doi:10.1038/s41580-025-00944-y (2026).
12. Millrine, D., Peter, J. J. & Kulathu, Y. A guide to UFMylation, an emerging posttranslational modification. *FEBS J.* **290**, 5040–5056, doi:10.1111/febs.16730 (2023).
13. Peter, J. J. *et al.* A non-canonical scaffold-type E3 ligase complex mediates protein UFMylation. *EMBO J.* **41**, e111015, doi:10.15252/embj.2022111015 (2022).
14. Ishimura, R. *et al.* Mechanistic insights into the roles of the UFM1 E3 ligase complex in ufmylation and ribosome-associated protein quality control. *Sci. Adv.* **9**, eadh3635, doi:10.1126/sciadv.adh3635 (2023).
15. Walczak, C. P. *et al.* Ribosomal protein RPL26 is the principal target of UFMylation. *Proc. Natl. Acad. Sci. USA* **116**, 1299–1308, doi:10.1073/pnas.1816202116 (2019).
16. Wang, L. *et al.* UFMylation of RPL26 links translocation-associated quality control to endoplasmic reticulum protein homeostasis. *Cell Res.* **30**, 5–20, doi:10.1038/s41422-019-0236-6 (2020).
17. DaRosa, P. A. *et al.* UFM1 E3 ligase promotes recycling of 60S ribosomal subunits from the ER. *Nature* **627**, 445–452, doi:10.1038/s41586-024-07073-0 (2024).
18. Makhlouf, L. *et al.* The UFM1 E3 ligase recognizes and releases 60S ribosomes from ER translocons. *Nature* **627**, 437–444, doi:10.1038/s41586-024-07093-w (2024).
19. Mihailovic, M. *et al.* The coordinated action of UFMylation and the RQC pathways clears arrested polypeptides at the ER. *EMBO J.*, doi:10.1038/s44318-026-00753-9 (2026).
20. Penchev, I. *et al.* UFMylation orchestrates spatiotemporal coordination of RQC at the ER. *Sci. Adv.* **11**, eadv0435, doi:10.1126/sciadv.adv0435 (2025).
21. Picchianti, L. *et al.* Shuffled ATG8 interacting motifs form an ancestral bridge between UFMylation and autophagy. *EMBO J.* **42**, e112053, doi:10.15252/embj.2022112053 (2023).
22. Wang, L. *et al.* SAYSD1 senses UFMylated ribosome to safeguard co-translational protein translocation at the endoplasmic reticulum. *Cell. Rep.* **42**, 112028, doi:10.1016/j.celrep.2023.112028 (2023).
23. Li, B. *et al.* Ufmylation reconciles salt stress-induced unfolded protein responses via ER-phagy in Arabidopsis. *Proc. Natl. Acad. Sci. USA* **120**, e2208351120, doi:10.1073/pnas.2208351120 (2023).
24. Ishimura, R. *et al.* The UFM1 system regulates ER-phagy through the ufmylation of CYB5R3. *Nat. Commun.* **13**, 7857, doi:10.1038/s41467-022-35501-0 (2022).
25. Xu, X. *et al.* The ufmylation cascade controls COPII recruitment, anterograde transport, and sorting of nascent GPCRs at ER. *Sci. Adv.* **10**, eadm9216, doi:10.1126/sciadv.adm9216 (2024).
26. Zhu, H. *et al.* Ufbp1 promotes plasma cell development and ER expansion by modulating distinct branches of UPR. *Nat. Commun.* **10**, 1084, doi:10.1038/s41467-019-08908-5 (2019).
27. Gerakis, Y., Quintero, M., Li, H. & Hetz, C. The UFMylation system in proteostasis and beyond. *Trends Cell Biol.* **29**, 974–986, doi:10.1016/j.tcb.2019.09.005 (2019).
28. Perdigão, C. *et al.* Encephalopathy-linked UFM1 variants impede neuronal protein translation, development, and function. *EMBO Mol. Med.*, doi:10.1038/s44321-026-00389-6 (2026).
29. Parra Bravo, C. *et al.* Human iPSC 4R tauopathy model uncovers modifiers of tau propagation. *Cell* **187**, 2446–2464.e2422, doi:10.1016/j.cell.2024.03.015 (2024).
30. Samelson, A. J. *et al.* CRISPR screens in iPSC-derived neurons reveal principles of tau proteostasis. *Cell* **189**, 1517–1534.e1519, doi:10.1016/j.cell.2025.12.038 (2026).
31. Tsaban, T. *et al.* CladeOScope: functional interactions through the prism of clade-wise co-evolution. *NAR Genom. Bioinform.* **3**, doi:10.1093/nargab/lqab024 (2021).
32. Chen, C., Itakura, E., Weber, K. P., Hegde, R. S. & de Bono, M. An ER complex of ODR-4 and ODR-8/Ufm1 specific protease 2 promotes GPCR maturation by a Ufm1-independent mechanism. *PLoS Genet.* **10**, e1004082, doi:10.1371/journal.pgen.1004082 (2014).
33. Rausin, G., Tillemans, V., Stankovic, N., Hanikenne, M. & Motte, P. Dynamic nucleocytoplasmic shuttling of an Arabidopsis SR splicing factor: role of the RNA-binding domains. *Plant Physiol.* **153**, 273–284, doi:10.1104/pp.110.154740 (2010).
34. Cáceres, J. F., Screaton, G. R. & Krainer, A. R. A specific subset of SR proteins shuttles continuously between the nucleus and the cytoplasm. *Genes Dev.* **12**, 55–66, doi:10.1101/gad.12.1.55 (1998).
35. Twyffels, L., Gueydan, C. & Kruys, V. Shuttling SR proteins: more than splicing factors. *FEBS J.* **278**, 3246–3255, doi:10.1111/j.1742-4658.2011.08274.x (2011).
36. Stankovic, N. *et al.* Dynamic distribution and interaction of the Arabidopsis SRSF1 subfamily splicing factors. *Plant Physiol.* **170**, 1000–1013, doi:10.1104/pp.15.01338 (2016).
37. Tillemans, V., Leponce, I., Rausin, G., Dispa, L. & Motte, P. Insights into nuclear organization in plants as revealed by the dynamic distribution of Arabidopsis SR splicing factors. *Plant Cell* **18**, 3218–3234, doi:10.1105/tpc.106.044529 (2006).
38. Pisareva, V. P., Skabkin, M. A., Hellen, C. U. T., Pestova, T. V. & Pisarev, A. V. Dissociation by Pelota, Hbs1 and ABCE1 of mammalian vacant 80S ribosomes and stalled elongation complexes. *EMBO J.* **30**, 1804–1817, doi:10.1038/emboj.2011.93 (2011).
39. Sinha, N. K. *et al.* EDF1 coordinates cellular responses to ribosome collisions. *eLife* **9**, e58828, doi:10.7554/eLife.58828 (2020).

40. Kertész, S. *et al.* Both introns and long 3′-UTRs operate as cis-acting elements to trigger nonsense-mediated decay in plants. *Nucleic Acids Res.* **34**, 6147–6157, doi:10.1093/nar/gkl737 (2006).

41. Nagy, E. & Maquat, L. E. A rule for termination-codon position within intron-containing genes: when nonsense affects RNA abundance. *Trends Biochem. Sci.* **23**, 198–199, doi:10.1016/S0968-0004(98)01208-0 (1998).

42. Hetz, C. & Glimcher, L. H. Fine-tuning of the unfolded protein response: assembling the IRE1$\alpha$ interactome. *Mol. Cell* **35**, 551–561, doi:10.1016/j.molcel.2009.08.021 (2009).

43. Walter, P. & Ron, D. The unfolded protein response: from stress pathway to homeostatic regulation. *Science* **334**, 1081–1086, doi:10.1126/science.1209038 (2011).

44. Bradley, T., Cook, M. E. & Blanchette, M. SR proteins control a complex network of RNA-processing events. *Rna* **21**, 75–92, doi:10.1261/rna.043893.113 (2015).

45. Monteuuis, G., Wong, J. J. L., Bailey, C. G., Schmitz, U. & Rasko, J. E. J. The changing paradigm of intron retention: regulation, ramifications and recipes. *Nucleic Acids Res.* **47**, 11497–11513, doi:10.1093/nar/gkz1068 (2019).

46. Pandit, S. *et al.* Genome-wide analysis reveals SR protein cooperation and competition in regulated splicing. *Mol. Cell* **50**, 223–235, doi:10.1016/j.molcel.2013.03.001 (2013).

47. Komatsu, M., Inada, T. & Noda, N. N. The UFM1 system: Working principles, cellular functions, and pathophysiology. *Mol. Cell* **84**, 156–169, doi:10.1016/j.molcel.2023.11.034 (2024).

48. Yan, T. *et al.* The UFMylation pathway is impaired in Alzheimer's disease. *Mol. Neurodegener.* **19**, 97, doi:10.1186/s13024-024-00784-y (2024).

49. Fanara, S. *et al.* The Arabidopsis SR45 splicing factor bridges the splicing machinery and the exon–exon junction complex. *J. Exp. Bot.* **75**, 2280–2298, doi:10.1093/jxb/erae002 (2024).

50. Lopato, S. *et al.* Network of interactions of a novel plant-specific Arg/Ser-rich protein, atRSZ33, with atSC35-like splicing factors. *J. Biol. Chem.* **277**, 39989–39998, doi:10.1074/jbc.M206455200 (2002).

51. Lampropoulos, A. *et al.* GreenGate - a novel, versatile, and efficient cloning system for plant transgenesis. *PLOS ONE* **8**, e83043, doi:10.1371/journal.pone.0083043 (2013).

52. Clough, S. J. & Bent, A. F. Floral dip: a simplified method for Agrobacterium-mediated transformation of Arabidopsis thaliana. *Plant J.* **16**, 735–743, doi:10.1046/j.1365-313x.1998.00343.x (1998).

53. Zhao, J. *et al.* Plant autophagosomes mature into amphisomes prior to their delivery to the central vacuole. *J. Cell Biol.* **221**, doi:10.1083/jcb.202203139 (2022).

54. Schindelin, J. *et al.* Fiji: an open-source platform for biological-image analysis. *Nat. Methods* **9**, 676–682, doi:10.1038/nmeth.2019 (2012).

55. Li, S. *et al.* MicroRNAs Inhibit the Translation of Target mRNAs on the Endoplasmic Reticulum in Arabidopsis. *Cell* **153**, 562–574, doi:10.1016/j.cell.2013.04.005 (2013).

56. Liu, C. *et al.* Arabidopsis ARGONAUTE 1 binds chromatin to promote gene transcription in response to hormones and stresses. *Dev. Cell* **44**, 348–361.e347, doi:10.1016/j.devcel.2017.12.002 (2018).

57. Song, P. *et al.* Methyltransferase ATMETTL5 writes m6A on 18S ribosomal RNA to regulate translation in Arabidopsis. *New Phytol.* **244**, 571–587, doi:10.1111/nph.20034 (2024).

58. Dorfer, V. *et al.* MS Amanda, a universal identification algorithm optimized for high accuracy tandem mass spectra. *J. Proteome Res.* **13**, 3679–3684, doi:10.1021/pr500202e (2014).

59. Käll, L., Canterbury, J. D., Weston, J., Noble, W. S. & MacCoss, M. J. Semi-supervised learning for peptide identification from shotgun proteomics datasets. *Nat. Methods* **4**, 923–925, doi:10.1038/nmeth1113 (2007).

60. Taus, T. *et al.* Universal and confident phosphorylation site localization using phosphoRS. *J. Proteome Res.* **10**, 5354–5362, doi:10.1021/pr200611n (2011).

61. Doblmann, J. *et al.* apQuant: accurate label-free quantification by quality filtering. *J. Proteome Res.* **18**, 535–541, doi:10.1021/acs.jproteome.8b00113 (2019).

62. Schwanhäusser, B. *et al.* Global quantification of mammalian gene expression control. *Nature* **473**, 337–342, doi:10.1038/nature10098 (2011).

63. Smyth, G. K. Linear models and empirical bayes methods for assessing differential expression in microarray experiments. *Stat. Appl. Genet. Mol. Biol.* **3**, Article3, doi:10.2202/1544-6115.1027 (2004).

64. Bruderer, R. *et al.* Extending the limits of quantitative proteome profiling with data-independent acquisition and application to acetaminophen-treated three-dimensional liver microtissues. *Mol. Cell. Proteomics* **14**, 1400–1410, doi:10.1074/mcp.M114.044305 (2015).

65. Schwartz, I. *et al.* SPOP targets the immune transcription factor IRF1 for proteasomal degradation. *eLife* **12**, doi:10.7554/eLife.89951 (2023).

66. de Almeida, M. *et al.* AKIRIN2 controls the nuclear import of proteasomes in vertebrates. *Nature* **599**, 491–496, doi:10.1038/s41586-021-04035-8 (2021).

67. Jahn, J. *et al.* Preparation of cytoplasmic and nuclear long RNAs from primary and cultured Cells. *J. Vis. Exp.*, doi:10.3791/64199 (2023).

68. Burgalossi, A. *et al.* Analysis of neurotransmitter release mechanisms by photolysis of caged $Ca^{2+}$ in an autaptic neuron culture system. *Nat. Protoc.* **7**, 1351–1365, doi:10.1038/nprot.2012.074 (2012).

69. Ripamonti, S. *et al.* SUMOylation controls the neurodevelopmental function of the transcription factor Zbtb20. *J. Neurochem.* **154**, 647–661, doi:10.1111/jnc.15008 (2020).

70. Dobin, A. *et al.* STAR: ultrafast universal RNA-seq aligner. *Bioinformatics* **29**, 15–21, doi:10.1093/bioinformatics/bts635 (2013).

71. Patro, R., Duggal, G., Love, M. I., Irizarry, R. A. & Kingsford, C. Salmon provides fast and bias-aware quantification of transcript expression. *Nat. Methods* **14**, 417–419, doi:10.1038/nmeth.4197 (2017).

72. Danecek, P. *et al.* Twelve years of SAMtools and BCFtools. *GigaScience* **10**, doi:10.1093/gigascience/giab008 (2021).
73. Shen, S. *et al.* rMATS: Robust and flexible detection of differential alternative splicing from replicate RNA-Seq data. *Proc. Natl. Acad. Sci. USA* **111**, E5593–E5601, doi:10.1073/pnas.1419161111 (2014).
74. Lawrence, M. *et al.* Software for computing and annotating genomic ranges. *PLoS Comput. Biol.* **9**, e1003118, doi:10.1371/journal.pcbi.1003118 (2013).
75. Durinck, S. *et al.* BioMart and Bioconductor: a powerful link between biological databases and microarray data analysis. *Bioinformatics* **21**, 3439–3440, doi:10.1093/bioinformatics/bti525 (2005).
76. Yeo, G. & Burge, C. B. Maximum entropy modeling of short sequence motifs with applications to RNA splicing signals. *J. Comput. Biol.* **11**, 377–394, doi:10.1089/1066527041410418 (2004).
77. Wagih, O. ggseqlogo: a versatile R package for drawing sequence logos. *Bioinformatics* **33**, 3645–3647, doi:10.1093/bioinformatics/btx469 (2017).
78. McLeay, R. C. & Bailey, T. L. Motif Enrichment Analysis: a unified framework and an evaluation on ChIP data. *BMC Bioinformatics* **11**, 165, doi:10.1186/1471-2105-11-165 (2010).
79. Rosado-Tristani, D. A. *et al.* CisBP-RNA: a web resource for eukaryotic RNA-binding proteins and their motifs. *Nucleic Acids Res.* **54**, D98–D105, doi:10.1093/nar/gkaf1081 (2025).
80. Husremović, T. *et al.* PHLPP2 is a pseudophosphatase that lost activity in the metazoan ancestor. *Proc. Natl. Acad. Sci. USA* **122**, e2417218122, doi:10.1073/pnas.2417218122 (2025).
81. Irwin, N. A. T. *et al.* The function and evolution of motile DNA replication systems in ciliates. *Curr. Biol.* **31**, 66–76.e66, doi:10.1016/j.cub.2020.09.077 (2021).
82. Buchfink, B., Reuter, K. & Drost, H.-G. Sensitive protein alignments at tree-of-life scale using DIAMOND. *Nat. Methods* **18**, 366–368, doi:10.1038/s41592-021-01101-x (2021).
83. Enright, A. J., Van Dongen, S. & Ouzounis, C. A. An efficient algorithm for large-scale detection of protein families. *Nucleic Acids Res.* **30**, 1575–1584, doi:10.1093/nar/30.7.1575 (2002).
84. Katoh, K. & Standley, D. M. MAFFT multiple sequence alignment software version 7: improvements in performance and usability. *Mol. Biol. Evol.* **30**, 772–780, doi:10.1093/molbev/mst010 (2013).
85. Mistry, J. *et al.* Pfam: The protein families database in 2021. *Nucleic Acids Res.* **49**, D412–D419, doi:10.1093/nar/gkaa913 (2021).
86. Tate, R. F. Correlation between a discrete and a continuous variable. point-biserial correlation. *Ann. Math. Stat.* **25**, 603–607 (1954).
87. Letunic, I. & Bork, P. Interactive Tree of Life (iTOL) v6: recent updates to the phylogenetic tree display and annotation tool. *Nucleic Acids Res.* **52**, W78–W82, doi:10.1093/nar/gkae268 (2024).
88. Consortium, T. U. UniProt: a worldwide hub of protein knowledge. *Nucleic Acids Res.* **47**, D506–D515, doi:10.1093/nar/gky1049 (2019).
89. Mistry, J. *et al.* Pfam: The protein families database in 2021. *Nucleic Acids Res.* **49**, D412–D419, doi:10.1093/nar/gkaa913 (2021).
90. Reijnders, M. Wei2GO: weighted sequence similarity-based protein function prediction. *PeerJ* **10**, e12931, doi:10.7717/peerj.12931 (2022).
91. Hohmann, U. *et al.* An ATP-gated molecular switch orchestrates human mRNA export. *Nature* **649**, 1042–1050, doi:10.1038/s41586-025-09832-z (2026).
92. Jumper, J. *et al.* Highly accurate protein structure prediction with AlphaFold. *Nature* **596**, 583–589, doi:10.1038/s41586-021-03819-2 (2021).
93. Mirdita, M. *et al.* ColabFold: making protein folding accessible to all. *Nat. Methods* **19**, 679–682, doi:10.1038/s41592-022-01488-1 (2022).
94. Perez-Riverol, Y. *et al.* The PRIDE database at 20 years: 2025 update. *Nucleic Acids Res.* **53**, D543–D553, doi:10.1093/nar/gkae1011 (2025).

# Supplemental figures

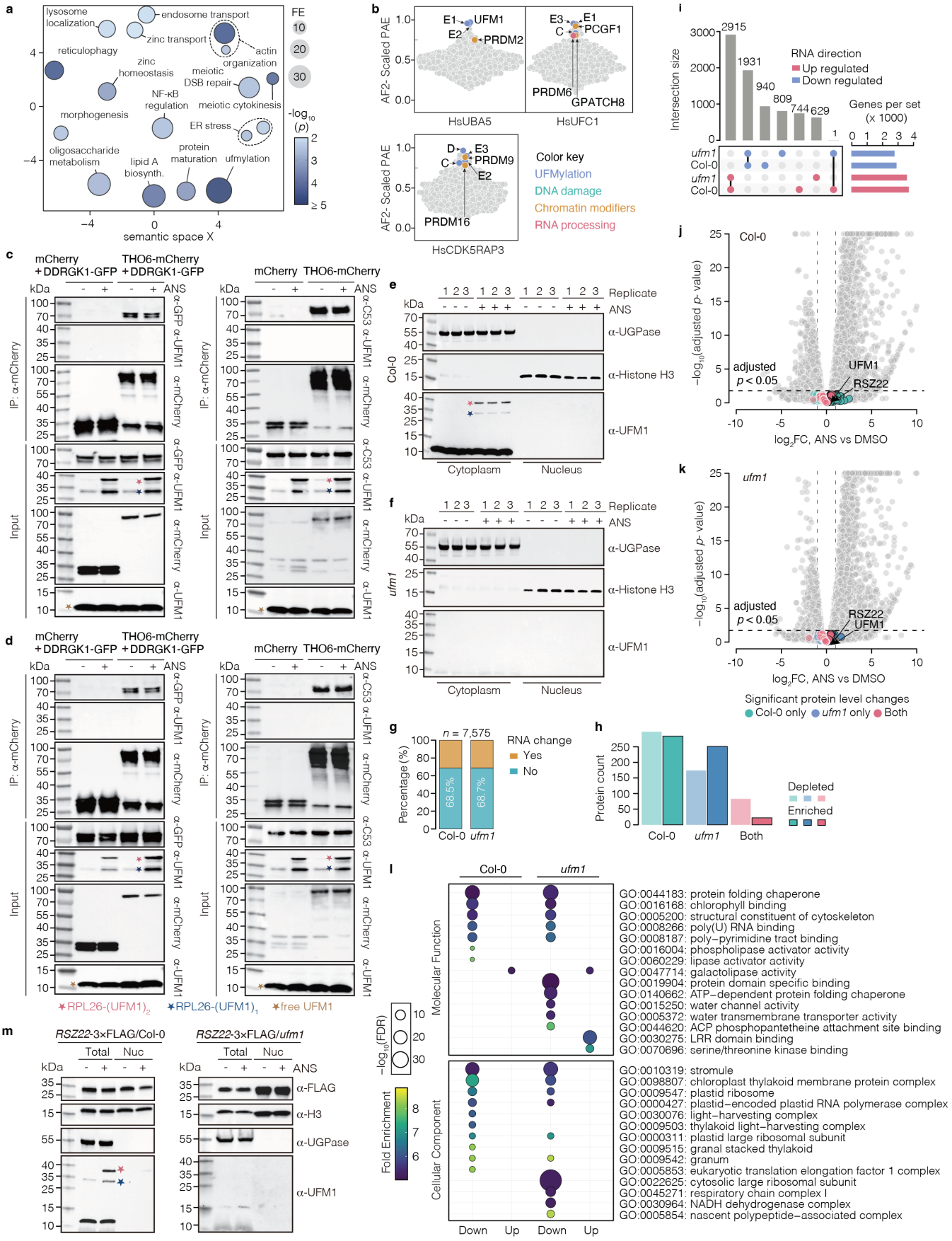


**Fig. S1** | **Validation of UFM1 co-evolutionary candidates and transcriptomic-proteomic integration.** **a,** Semantic clustering of GO terms for UFM1 co-evolutionary candidates (point-biserial correlation $> 0.3$, $P < 0.05$). Dot size and color indicate fold enrichment and $-\log_{10}(P)$. **b,** Dot plot illustrating AlphaFold2 (AF2) Multimer interaction predictions of coevolved genes against UFMylation machinery. The Y-axis represents the average protein interaction score across the top three ranked models, calculated from domain-specific Predicted Aligned Error (PAE) values rescaled from 0 to 1. Abbreviations: P1, P2: UFSP1 and 2; E1, E2, E3: UBA5, UFC1, and UFL1; C: CDK5RAP3; D: DDRGK1. Coevolved genes with Scaled PAE $\geq 0.75$ are colored according to key. **c,** *In vivo* co-immunoprecipitation (Co-IP) of THO6 interactions with DDRGK1-GFP and UFMylated RPL26 (left panel) or with endogenous C53 and UFMylated RPL26 (right panel) under DMSO or ANS (4 h) treatment. Proteins were extracted from the *Arabidopsis* lines co-expressing DDRGK1-GFP with either mCherry (control) or THO6-mCherry in Col-0 background seedlings (left panel), or from mCherry (control) and THO6-mCherry seedlings (right panel). Input samples were normalized by Bradford assay prior to loading. The consistent level of endogenous free UFM1 (unconjugated) in input fractions serves as an internal loading control to show equal protein loading across all lanes. THO6-mCherry was immunoprecipitated with RFP-Trap magnetic agarose, bound proteins detected by immunoblotting ($n = 2$). Mono- (1), di- (2) UFMylated RPL26 and free UFM1 are indicated. **d,** Biological replicate of (c). **e, f,** Immunoblotting of nuclear fractionation quality in 10-day-old Col-0 and *ufm1* seedlings (4 h ANS treatment). H3 and UGPase are nuclear and cytosolic markers, respectively. UFM1 blot confirms genotype-specific conjugates upon ANS as indicated ($n = 3$). **g,** Proportion of proteins showing RNA-dependent versus RNA-independent abundance changes in Col-0 and *ufm1* after ANS treatment based on integrated proteomic and RNA-seq analysis. **h,** Counts of proteins significantly enriched or depleted ($P < 0.05$) upon ANS treatment in indicated genotypes. **i,** UpSet plot showing intersections of nuclear DEGs (ANS versus DMSO) in Col-0 and *ufm1*. Bar heights indicate shared and genotype-specific upregulated (red) and downregulated (blue) gene set sizes, defining shared and genotype-specific transcriptional responses. **j, k,** Volcano plots of nuclear RNA-seq DEGs (ANS versus DMSO) in Col-0 (j) and *ufm1* (k). Genes with adjusted $P > 0.05$ are highlighted, indicating stable transcript levels and that many UFMylation-dependent proteomic changes are RNA-independent. **l,** GO enrichment of upregulated and downregulated DEGs in Col-0 and *ufm1*. Dot size and color denote $-\log_{10}(\text{FDR})$ and fold enrichment, respectively. Distinct transcriptional programs indicate that UFMylation dependent proteomic responses are primarily post-transcriptional. **m,** Immunoblot analysis of RSZ22-3×FLAG in total (whole-cell lysates) and nuclear fractions (replicate for Fig. 1i). 10-day-old RSZ22-3×FLAG seedlings (Col-0 and *ufm1* backgrounds) were treated with DMSO or ANS (4 h). H3 and UGPase serve as nuclear and cytosolic markers, respectively. Mono- (1) and di- (2) UFMylated RPL26 are indicated.

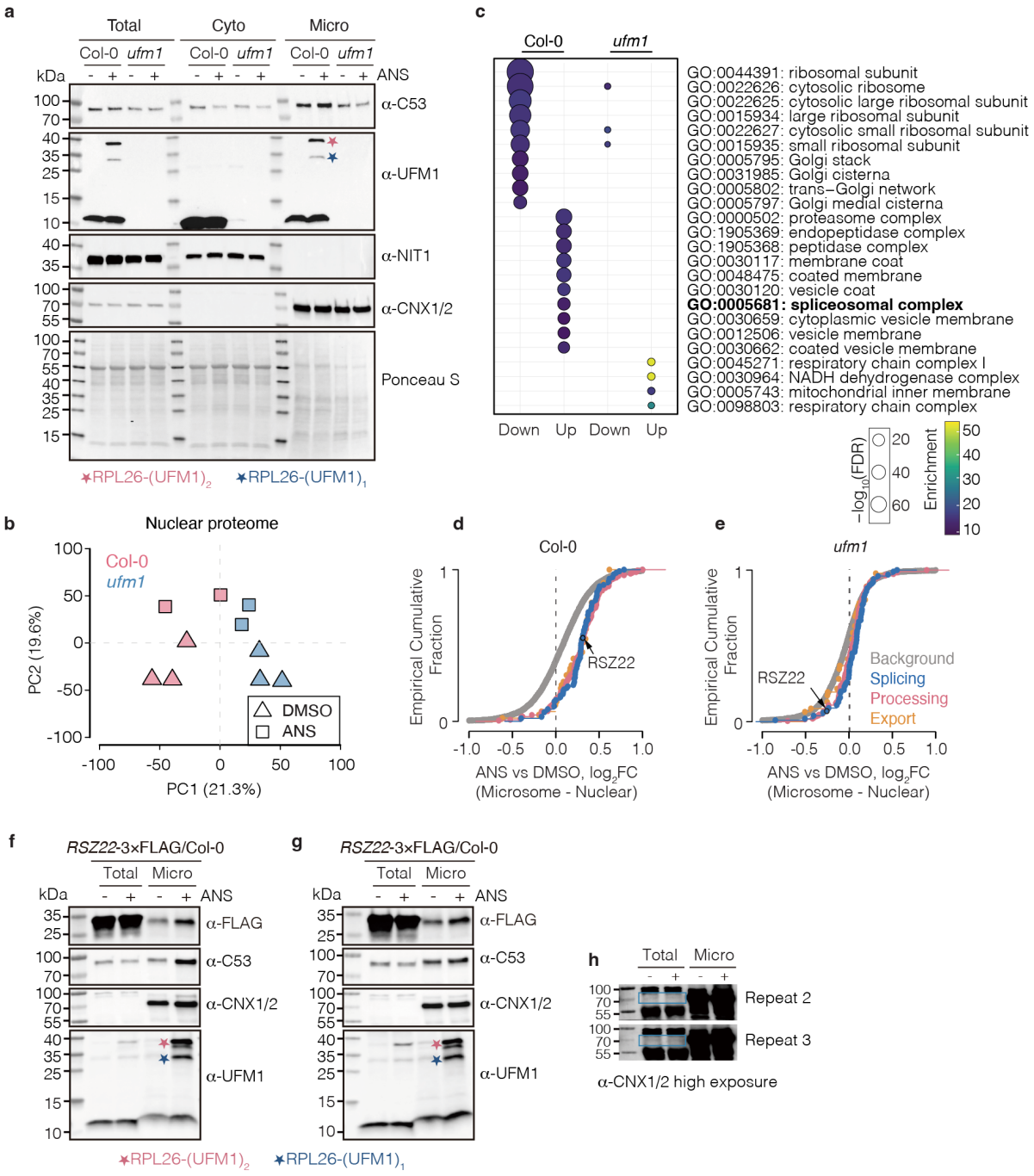



**Fig. S2** | **Validation of microsomal enrichment and analysis of microsome-associated proteome.** **a,** Validation of microsome isolation quality. Markers CNX1/2 (ER) and NIT1 (cytosol) confirm fraction purity. UFMylated RPL26 is enriched in the microsomal fraction. Mono- (1) and di- (2) UFMylated RPL26 are indicated. Ponceau S indicates total protein loading. **b,** PCA of nuclear proteomes ($n = 3$ for DMSO; $n = 2$ for ANS). PC1 and PC2 segregation reflects separation by genotype and treatment. **c,** GO enrichment analysis of proteins significantly altered in microsomal fraction upon ANS treatment in Col-0 and *ufm1*. Dot size and color denote $-\log_{10}$(FDR) and fold enrichment. **d, e,** Empirical cumulative distribution function (ECDF) plots showing subcellular redistribution. Δenrichment is defined as the difference in $\log_2$ fold change (ANS versus DMSO) between microsomal and nuclear fractions, for total proteome (grey) and RNA-related categories (colored) in Col-0 (d) and *ufm1* (e). RSZ22 is indicated as a representative example. **f–h,** Additional biological replicates for Fig. 2h. Immunoblot analysis of RSZ22-3×FLAG in total lysates and microsomal fractions. Mono- (1) and di- (2) UFMylated RPL26 are indicated. **h,** High exposure immunoblots of CNX1/2. $n = 3$ total biological replicates used for Fig. 2j quantification.

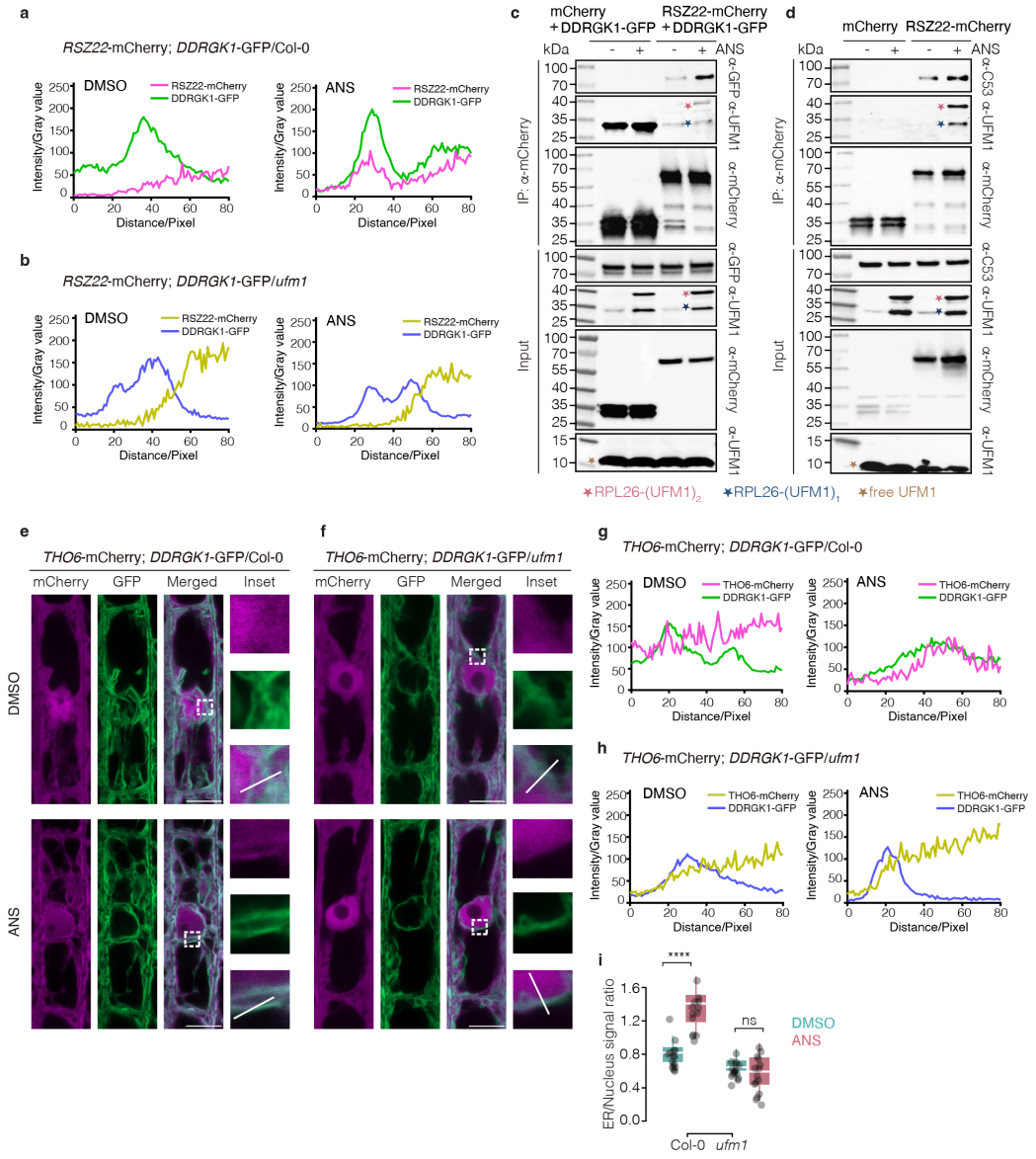



**Fig. S3** | **UFMylation-dependent subcellular redistribution of RSZ22 and THO6, and RSZ22-UFMylation interactions.** **a, b,** Fluorescence intensity profiles (line-scans) of RSZ22-mCherry and DDRGK1-GFP along the regions indicated in Fig. 2k, l. In Col-0 background (a), RSZ22 and DDRGK1 signals are shown in magenta and green, respectively, and ANS induces synchronized shifts and overlapping peaks. In *ufm1* background (b), RSZ22 and DDRGK1 signals are shown in yellow-green and purple, respectively, and the two signals remain spatially distinct regardless of ANS treatment. **c, d,** Representative biological replicates for Fig. 2n, o. *In vivo* Co-IP analysis of RSZ22 interactions with DDRGK1 and UFMylated RPL26 (c), or with endogenous C53 and UFMylated RPL26 (d), under DMSO or ANS (4 h) treatment. Lysates were incubated with RFP-Trap magnetic agarose, input and bound proteins were analyzed by immunoblotting. Mono- (1), di- (2) UFMylated RPL26 and free UFM1 are indicated. **e, f,** Confocal microscopy of THO6–mCherry and DDRGK1–GFP (ER marker) in roots from Col-0 (e) and *ufm1* (f) backgrounds. Five-day-old seedlings were treated with DMSO or ANS (1–2 h). ANS induces UFM1-dependent spatial overlap between THO6 and the ER in Col-0 but not in *ufm1*. Enlarged views and white lines indicate line-scan regions. Scale bars, 10 $\mu$m. **g, h,** Fluorescence intensity profiles along the regions indicated in (e), (f). In Col-0 background roots (g), THO6 and DDRGK1 signals show overlapping peaks after ANS treatment, indicating co-localization. In *ufm1* background (h), the two signals remain spatially separated after ANS treatment. **i,** Quantification of ER-to-nucleus THO6 signal ratios from e, f. Data are mean $\pm$ SD from 3 biological replicates. Each dot represents an individual cell ($n = 15$ cells from 3 biological replicates). Statistical significance was determined by two-tailed unpaired $t$-test **** $P \leq 0.0001$; ns, not significant.

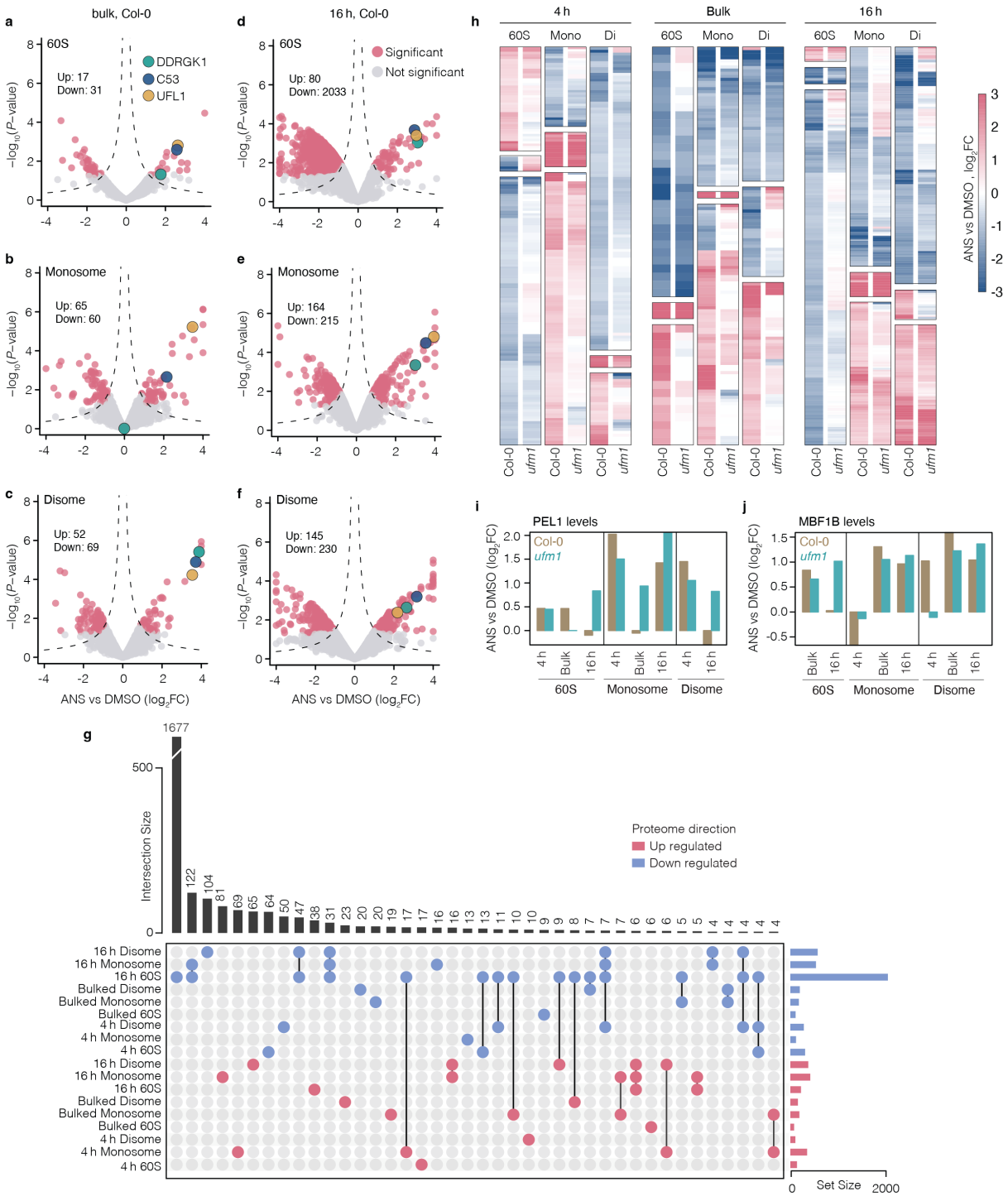



**Fig. S4** | **Ribosomal proteomics evaluation and cytosolic RQC factor recruitment.** **a–c,** Volcano plots from the bulk ribosome proteomics dataset (pooled from 1, 4, 8, 16 h treatments), showing ANS-induced recruitment of UFMylation components (UFL1, C53 and DDRGK1) to 60S (a), monosome (b), disome (c) fractions. x-axis, $\log_2$ fold change (ANS versus DMSO). y axis, $-\log_{10}(P\text{-value})$. **d–f,** Volcano plots from the 16 h ribosome proteomics dataset, showing recruitment of UFL1, C53, and DDRGK1 to 60S (d), monosomes (e), and disomes (f). **g,** UpSet plot showing the intersections of significantly up-regulated (red) and down-regulated (blue) proteins across the indicated fractions (60S, Monosome, Disome) and conditions (Bulk, 4h, 16h). Vertical bars represent the size of the intersection; horizontal bars represent the total set size. **h,** Heatmap showing $\log_2$ fold changes (ANS versus DMSO) for proteins identified as significantly differentially abundant in Col-0 (WT). These same proteins are visualized in *ufm1* mutants to compare abundance patterns across time points (4h, Bulk, 16h) and ribosomal fractions (60S, Mono, Di). **i, j,** MS abundance profiles for PEL1 (i, plant homolog of mammalian PELO) and MBF1B (j, plant homolog of mammalian EDF1) across ribosomal fractions. Bars represent $\log_2$ fold change (ANS versus DMSO) in Col-0 (olive) and *ufm1* (cyan) from three datasets (4 h, bulk and 16 h). Both Col-0 and *ufm1* show comparable ribosomal recruitment of these two proteins.

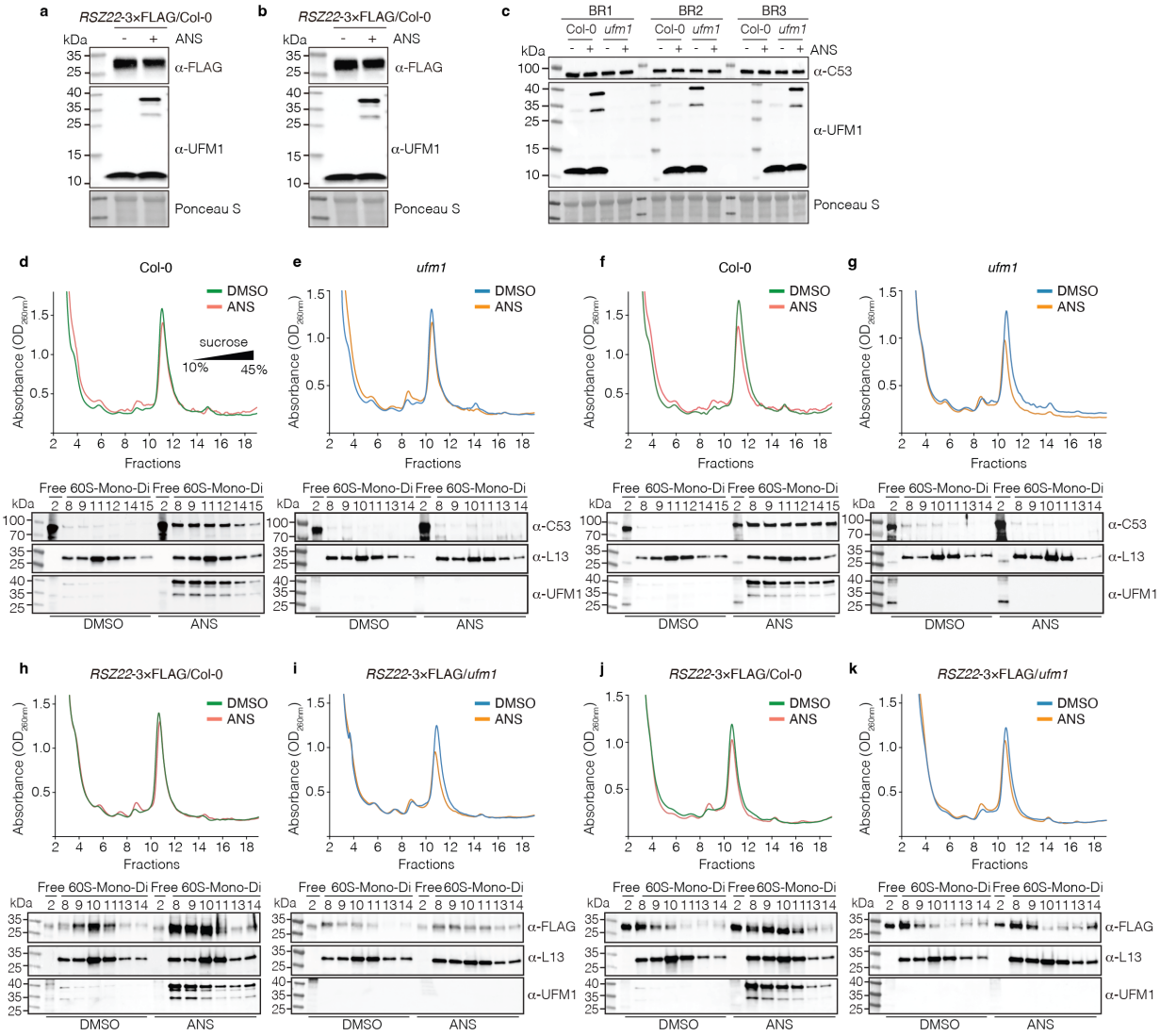



**Fig. S5** | **Supporting evidence for the ribosomal recruitment of C53 and RSZ22.** **a, b,** Immunoblot analysis of RSZ22-3×FLAG in total lysates of 7-day-old RSZ22-3×FLAG seedlings (Col-0 background) treated with DMSO or ANS (4 h). Lysates were probed using anti-FLAG and anti-UFM1 antibodies; Ponceau S indicates loading ($n = 2$ independent biological replicates). **c,** Immunoblot analysis of endogenous C53 in total lysates from Col-0 and *ufm1* seedlings treated with DMSO or ANS (4 h) ($n = 3$ independent biological replicates). **d–g,** Additional biological replicates of sucrose gradient sedimentation and immunoblot analysis of endogenous C53 in Col-0 (d), (f) and *ufm1* (e), (g). UV absorbance ($A_{260}$) profiles (top) indicate ribosome distribution across 10%–45% gradients. Fractions were immunoblotted for C53, L13 (60S marker), and UFM1. Free: ribosome-free fractions. Results correspond to the second (d), (e) and third (f), (g) independent experiments, complementing Fig. 3f, g. **h–k,** Additional biological replicates of sucrose gradient sedimentation and immunoblot analysis of RSZ22-3×FLAG in Col-0 (h), (j) and *ufm1* (i), (k) backgrounds. UV absorbance ($A_{260}$) profiles (top) indicate ribosome distribution. Fractions were immunoblotted for FLAG, L13, and UFM1. Results correspond to the second (h), (i) and third (j), (k) independent experiments, complementing Fig. 3h, i.

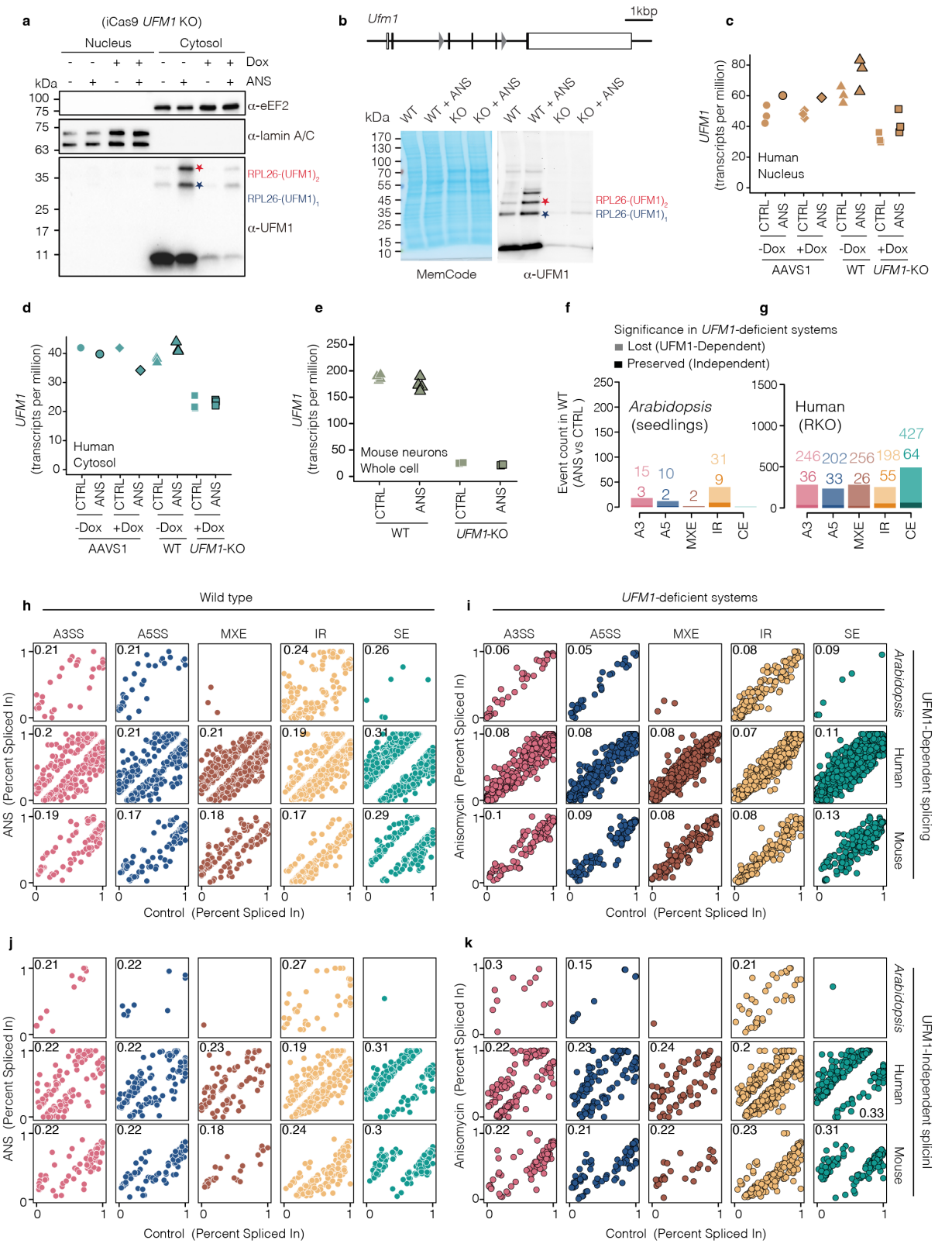

a
(iCas9 UFM1 KO)
Nucleus
Cytosol
Dox
ANS
kDa
α-eEF2
α-lamin A/C
RPL26-(UFM1)2
RPL26-(UFM1)1
α-UFM1
b
Ufm1
1kbp
kDa
WT
WT + ANS
KO
KO + ANS
MemCode
α-UFM1
c
UFM1 (transcripts per million)
Human
Nucleus
CTRL
ANS
-Dox
+Dox
AAVS1
WT
UFM1-KO
d
UFM1 (transcripts per million)
Human
Cytosol
e
UFM1 (transcripts per million)
Mouse neurons
Whole cell
f
Significance in UFM1-deficient systems
Lost (UFM1-Dependent)
Preserved (Independent)
Event count in WT (ANS vs CTRL)
Arabidopsis (seedlings)
Human (RKO)
A3
A5
MXE
IR
CE
h
Wild type
i
UFM1-deficient systems
A3SS
A5SS
MXE
IR
SE
ANS (Percent Spliced In)
Anisomycin (Percent Spliced In)
Control (Percent Spliced In)
Arabidopsis
Human
Mouse
UFM1-Dependent splicing
j
k
UFM1-Independent splicing

**Figure S6** | **Validation of subcellular fractionation and cross-species analysis of UFM1-dependent splicing. a,** Immunoblot analysis of nuclear and cytosolic fractions in iCas9 *UFM1* KO cells treated as in Fig. 4b. Membranes were probed for eEF2, Lamin A/C, and UFM1. eEF2 and Lamin A/C serve as cytosolic and nuclear markers, respectively. Mono- (1) and di- (2) UFMylated RPL26 are indicated. **b,** Schematic and validation of the *Ufm1* conditional allele. (Top) Schematic representation of the *Ufm1* targeting strategy, indicating LoxP sites (grey triangles), coding exons (black boxes), and non-coding exons (white boxes); diagram is drawn to scale. (Bottom) Immunoblots (right) and total protein stain (left) of lysates from primary cortical neurons. Neurons were infected at DIV1 with lentiviruses expressing either RFP (WT) or Cre-RFP (KO) and treated at DIV12 with 20 $\mu$M anisomycin (ANS) or DMSO vehicle for 2 h. Mono- (1) and di- (2) UFMylated RPL26 are indicated. **c, d,** *UFM1* transcript abundance (transcripts per million, TPM) in human nuclear (c) and cytosolic (d) fractions across AAVS1, WT, and *UFM1*-KO cell lines under control (CTRL) or ANS treatment conditions. **e,** *Ufm1* transcript abundance in whole cell lysates from mouse neurons comparing WT and *Ufm1*-KO under CTRL or ANS conditions. **f, g,** Quantification of ANS-induced alternative splicing events from the cytoplasmic fractions in WT *Arabidopsis* (f) and Human RKO cells (g), classified by event type. Lighter bars indicate UFM1-dependent events lost in UFM1-deficient systems; darker bars indicate UFM1-independent events retained. **h–k,** Scatter plots comparing PSI values between CTRL and ANS treatment for UFM1-dependent and independent events across *Arabidopsis*, human, and mouse transcriptomes. UFM1-dependent splicing events shown in WT backgrounds (h), and in UFM1-deficient systems (i) to demonstrate loss of splicing shift. UFM1-independent splicing events are shown in WT (j) and UFM1-deficient systems (k), demonstrating preserved splicing changes. Mean Absolute Error (MAE) values summarizing the global splicing shifts are indicated in each panel.

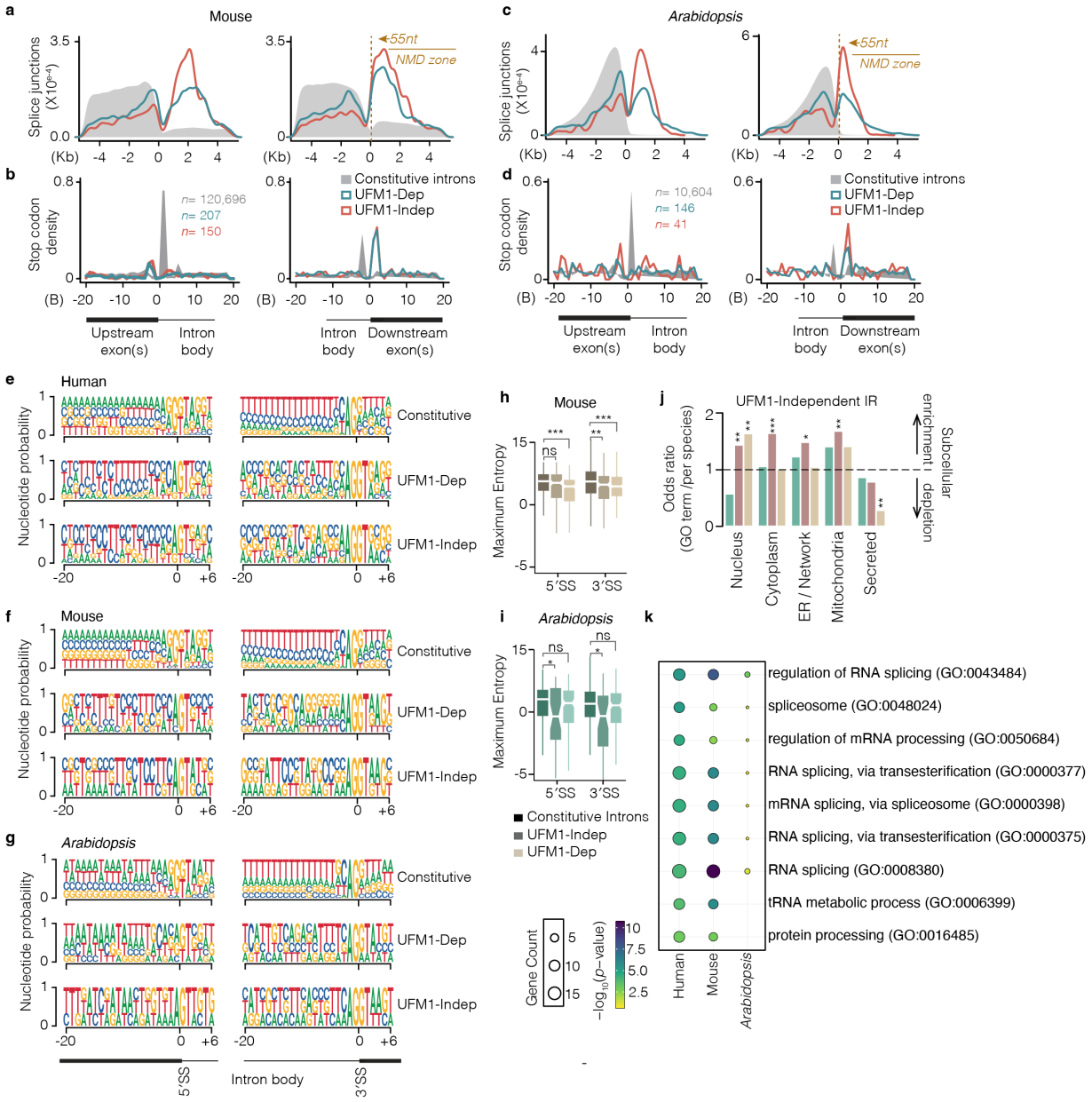



**Figure S7** | **Molecular features and functional enrichment of UFM1-associated splicing events.** **a, c,** Metagene profiles showing the splice junction distribution relative to the stop codon in mouse (a) and *Arabidopsis* (c). Constitutive introns are shown in grey, UFM1-dependent events in blue, and UFM1-independent events in red. The 55-nt NMD zone is indicated by dashed lines and arrows. **b, d,** Density of stop codons in upstream exons, intron bodies, and downstream exon regions for mouse (b) and *Arabidopsis* (d). Comparison includes constitutive introns (grey), UFM1-dependent events (blue), and UFM1-independent events (red). Sample sizes ($n$) are provided for each category. **e–g,** Sequence logos displaying nucleotide probabilities at the -20 to +6 positions for 5′SS and 3′SS. Profiles are shown for constitutive, UFM1-dependent, and UFM1-independent introns in human (e), mouse (f), and *Arabidopsis* (g). **h, i,** Maximum entropy (MaxEnt) scores for 5′SS and 3′SS in mouse (h) and *Arabidopsis* (i). Box plots compare constitutive (black), UFM1-independent (dark green/grey), and UFM1-dependent (beige) introns. Statistical significance: *** $P < 0.001$; ** $P < 0.01$; * $P < 0.05$; ns, not significant. **j,** Odds ratios for subcellular localization (nucleus, cytoplasm, ER/Network, mitochondria, secreted) associated with UFM1-independent retained introns across three species. **k,** GO enrichment analysis UFM1-independent target transcripts, highlighting RNA splicing and protein processing functions in human, mouse, and *Arabidopsis*. Dot size indicates gene count; color gradient indicates significance ($-\log_{10} P$-value). **l,** Comparison of RNA-binding protein (RBP) motif enrichment in UFM1-dependent versus UFM1-independent introns relative to constitutive introns from mouse neurons. Dot size denotes motif enrichment in UFM1-dependent introns compared to UFM1-independent introns.

## 7.2. Confirmation of manuscript status for “Dual regulation of the unfolded protein response by IGF2BP3 during ER stress

**Subject:** Fwd: Fwd: [EXTERN] GENESDEV/2025/353291 -- Source Files Reminder
**From:** Aleksandra Anisimova <aleksandra.anisimova@univie.ac.at>
**Date:** 21-Apr-26, 11:22 AM
**To:** Milica Mihailovic <milicam97@univie.ac.at>

> **From:** genesdev@cshlbp.org
> **Date:** March 19, 2026 at 21:08:35 GMT+1
> **To:** guelsuen.karagoez@meduniwien.ac.at
> **Subject: [EXTERN] GENESDEV/2025/353291 -- Source Files Reminder**

> MS ID#: GENESDEV/2025/353291/(US 32020)
> MS TITLE: Dual regulation of the unfolded protein response by IGF2BP3 during ER stress
>
> March 19, 2026
>
> Dear Gulsun Elif Karagoz,
>
> We are contacting you regarding the above manuscript, which has just been accepted for publication in G&D. If you need to make changes, please log in to your Author Area in G&D's submission system (Bench Press) and upload your new files.
>
> In order to proceed with production of the paper, we require the following items:
>
> 1. A clean word document of the main text and figure legends. Please remove the supplemental figures legends.
>
> 2. High-quality individual electronic figure files (as TIFF, EPS, JPEG, AI or PDF files in RGB color mode).
>
> 3. A single PDF file containing the Supplemental methods, Supplemental figures and Supplemental figure legends. Supplemental tables, if any, may be uploaded as individual files.
>
> 4. Supplemental filenames MUST include underscores. Do not include spaces between words, for example, Supplemental_Data.pdf, etc.
>
> 5. Supplemental citations within the Word document MUST be cited as (Supplemental Fig. S1, etc.).
>
> 6. A signed license to publish (this can be found in your Author Area) form uploaded as supplemental file in Bench Press.

You will be prompted to notify the editorial office once you have uploaded these files. In this e-mail, please include your standard UPS delivery address (including street address) so that we can send you one complimentary copy of the journal issue in which your manuscript appears.

If you will not be making any changes at this time, please e-mail our office right away genesdev@cshlbp.org so we may proceed with the processing of your paper.

If the accepted article includes direct NIH funding, please be aware that according to the NIH Public Access Policy, authors may be required to submit a copy of the Author Accepted Manuscript to PubMed Central themselves. Please include the DOI provided here when doing so: 10.1101/gad.353291.125.

Best wishes,

Genes & Development
Editorial Office

## 7.3. Confirmation of manuscript status for “UFMylation anchors splicing factors at the ER to reprogram nuclear splicing”

**Subject:** Fwd: Fwd: Nature 2026-03-09429 out to review; possible response required
**From:** Milica Mihailovic <milicam97@univie.ac.at>
**Date:** 29-Apr-26, 10:00 AM
**To:** milicam97@univie.ac.at

Begin forwarded message:

**From:** jie.wang@nature.com
**Subject: Nature 2026-03-09429 out to review; possible response required**
**Date:** 24. April 2026 at 09:02:27 CEST
**To:** yasin.dagdas@cos.uni-heidelberg.de
**Cc:** romy.zhou@springernature.com
**Reply-To:** jie.wang@nature.com

Dear Professor Dagdas,

Thank you for submitting your manuscript, "UFMylation anchors splicing factors at the ER to reprogram nuclear splicing", to Nature. I am pleased to tell you that we are sending your paper out for review.

CHECKLISTS: We are continually improving the quality of methods, statistics reporting and code availability in our papers. To that end, we require that for all life sciences papers, a reporting summary that collates information on experimental design and reagents is provided. In addition, a code and software checklist that ensures the availability of code to referees and includes details of its potential release on publication must be supplied if any novel code is used. Please send the completed form(s) within 48 hr to the Editorial Assistant copied to this email. These forms are 'smart pdfs' and must therefore be downloaded and completed in Adobe Reader (i.e. they cannot be opened in a web browser); see here for guidance. Because the forms will be accessible to the referees to aid in their evaluation of your work, if you have selected double-blind peer review, you should ensure that they do not contain any information that could potentially identify you.

RAW DATA (GELS): The original source images for all data obtained by electrophoretic separation (e.g., EMSA, northern/Southern/western blots, etc) must be provided. The raw images must be assembled into a single .pdf or .tif file (multiple gels on a single page is encouraged). The full scanned images must be in uncropped form and contain labeled size/molecular weight markers and loading controls. There should be an accurate indication of how the gels were cropped for the final figure. The figure legends and raw data files should indicate whether controls (such as beta-actin) were run on the same gel as loading controls, or on separate gels as sample processing controls (see here for guidance).

STRUCTURAL DATA: Papers reporting structural data must use the standard Nature templates; there are separate links to tables for X-ray crystallography, NMR and cryoEM structures. In addition, all structures must be submitted to an appropriate database (e.g. PDB) before review,

and validation reports provided (required for crystallography and NMR; strongly suggested for cryoEM), before the paper can be sent to referees. We also now require that authors provide the raw data for X-ray crystallography and cryoEM structures.

CO-REVIEWS: We offer referees the opportunity to enlist a single co-reviewer to aid in preparing their review. This process allows the co-reviewer to receive credit for doing so. Functionally, this workflow involves adding the co-reviewer separately in our system, although there will be one joint review submitted. We mention this to alert you that the number of reviews may be less than the number of referees.

TRANSPARENT PEER REVIEW: We support transparent peer review of original research manuscripts, in which we publish the referees' comments to the authors and the authors' rebuttal letters as a supplementary peer review file. Upon your request, confidential information and data can be removed from the referee reports and rebuttal letters prior to publication. More information can be found at our https://www.nature.com/documents/nature-transparent-peer-review.pdf target="new">FAQ page.

We would like to ask you that you please provide a link to a code repository and complete the following software and custom code submission checklist:

Software supplement: https://www.nature.com/documents/nr-software-policy.pdf
(Please note that the form is a dynamic 'smart pdf' and must therefore be downloaded and completed in Adobe Reader.)

Alternatively, or as an additional resource, please consider setting up an executable compute capsule for your code on the cloud-based platform Code Ocean, to facilitate the review process as well as the reproducibility and re-usability of your code. Code Ocean staff will assist you in generating a compute capsule for your code and provide a working copy of this compute capsule for use in the peer review process (after a brief review by Code Ocean staff, to ensure that everything runs). If you have selected Double Blind Peer Review, we will make sure the capsule contains no information about your identity.

Please let us know as soon as possible if you wish to participate and we will provide you with further information about setting up a compute capsule. An overview of the process can be found here: https://help.codeocean.com/publishing-on-code-ocean/peer-review-on-code-ocean.

If you do not opt for setting a Code Ocean capsule, please fill in the software and custom code submission checklist.

Some further information about using Code Ocean for peer review and publication of code can be found in this blog post and in Code Ocean's user guide here/.

We will be in touch again once we have received comments from our referees. In the meantime, the status of your manuscript can be followed in the manuscript tracking system.

Yours sincerely,

Jie Wang, PhD
Senior Editor
Nature
ORCID ID: 0000-0001-7797-6472

* Nature Portfolio's author website contains information about and links to policies and resources.

This email has been sent through the Springer Nature Manuscript Tracking System NY-610A-SN&MTS

*Confidentiality Statement:*

*This e-mail is confidential and subject to copyright. Any unauthorised use or disclosure of its contents is prohibited. If you have received this email in error please notify our Manuscript Tracking System Helpdesk team at http://platformsupport.nature.com .*

*Details of the confidentiality and pre-publicity policy may be found here http://www.nature.com/authors/policies/confidentiality.html*

Privacy Policy | Update Profile